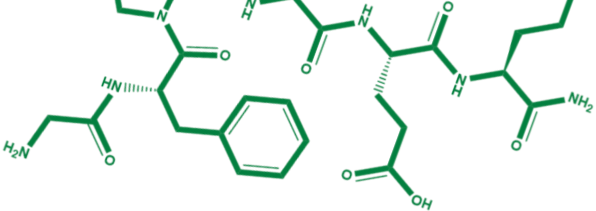

Preparation and Characterisation of Peptide-Decorated Nanomaterials

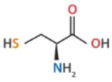

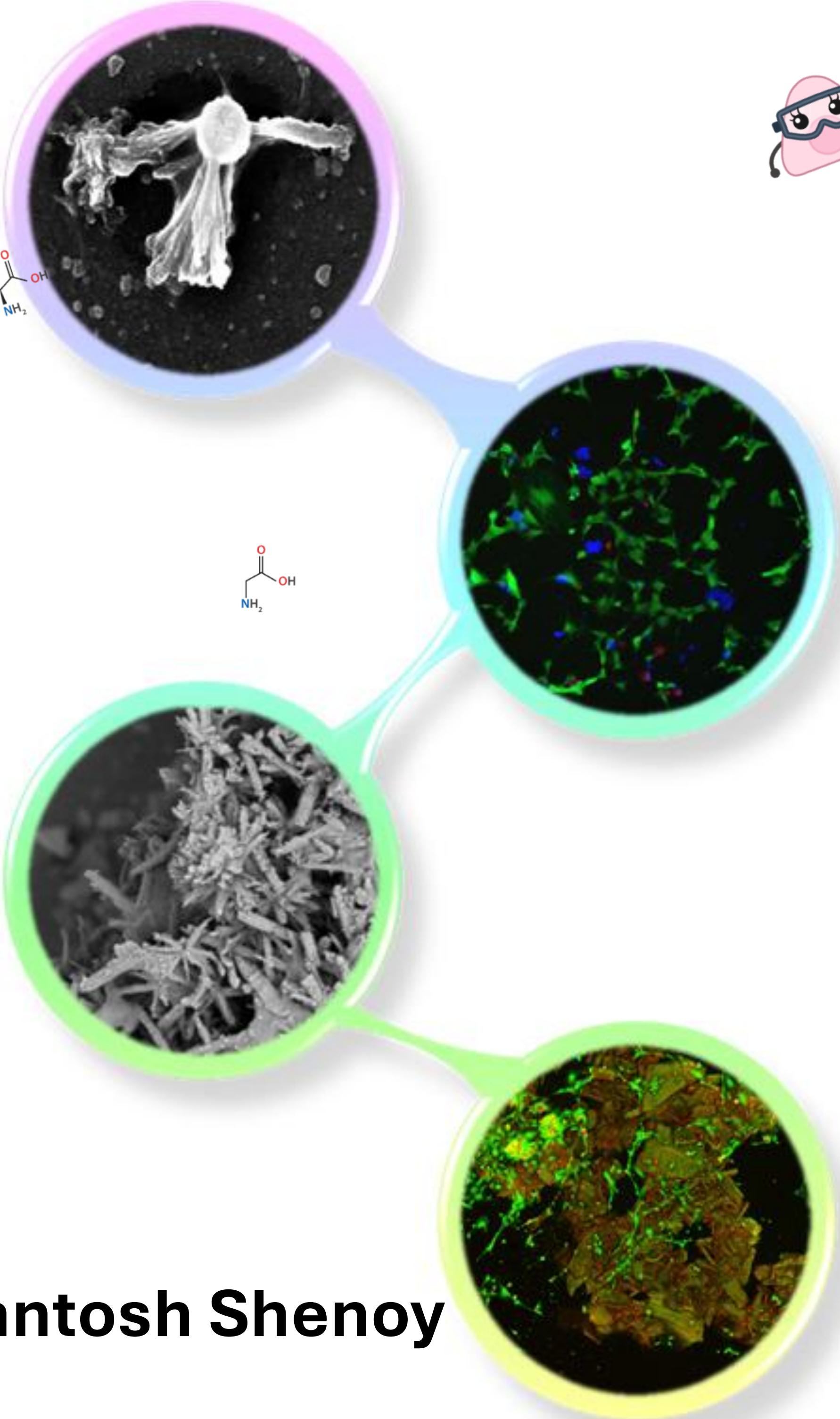

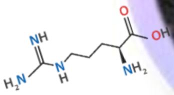

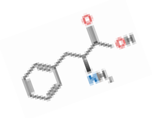

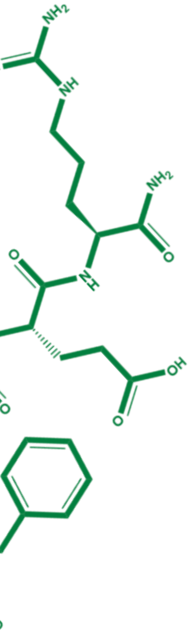

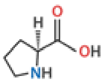

Dhriti Santosh Shenoy

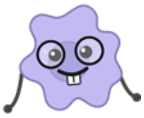

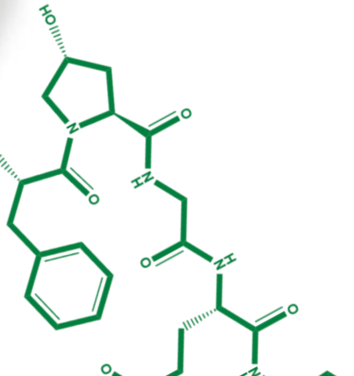

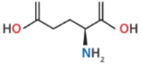

UNIVERSITÀ DEGLI STUDI DI MILANO

TESI DI DOTTORATO DI RICERCA IN CO-TUTELA

UNIVERSITÀ DEGLI STUDI DI MILANO *UNIVERSITÉ DE MONTPELLIER*

CORSO DI DOTTORATO ed eventuale curriculum

Pharmaceutical Sciences, XXXVIII cycle

DIPARTIMENTO

DISFARM, Department of Pharmaceutical Sciences

TESI DI DOTTORATO DI RICERCA

Preparation and characterisation of peptide-decorated nanomaterials

CHIM/06

Dhriti Santosh Shenoy

Matr. R14176

ORCID n.0000-0002-7709-3757

TUTOR: prof. SARA PELLEGRINO

CO-TUTOR: prof. GILLES SUBRA

COORDINATORE DEL DOTTORATO: prof. GIULIO VISTOLI

A.A. 2022/2023

THÈSE POUR OBTENIR LE GRADE DE DOCTEUR DE L'UNIVERSITÉ DE MONTPELLIER

En Ingénierie Biomoléculaire

École doctorale ED 459 Sciences Chimiques Balard

Unité de recherche UMR 5247- Institut des Biomolécules Max Mousseron

En partenariat international avec Università degli Studi di Milano, Italie

Développement de nanomatériaux décorés par des peptides

Présentée par Dhriti Santosh SHENOY
Le 16 Juin 2026

Sous la direction de M. Gilles SUBRA, Mme. Sara PELLEGRINO
et Mme. Cécile ECHALIER

Devant le jury composé de

M. Steven BALLET, Professeur, Vrije Universiteit Brussel	Président du Jury
M. Andrey KLYMCHENKO, DR CNRS, Université de Strasbourg	Rapporteur
Mme. Muriel AMBLARD, DR CNRS, Université de Montpellier	Examinatrice
Mme. Alessandra ROMANELLI, Maître de conférences, Università degli Studi di Milano	Examinatrice
Mme. Sara PELLEGRINO, Maître de conférences, Università degli Studi di Milano	Directrice de thèse
M. Gilles SUBRA, Professeur, Université de Montpellier	Directeur de thèse

UNIVERSITÉ DE MONTPELLIER

This PhD is part of Marie Skłodowska-Curie Actions. It was funded by the HORIZON-TMA-MSCA-DN-Joint Doctorate "Functional Nano-Scaffolds for Regenerative Medicine", named with the acronym NanoReMedi, Grant agreement No: 101072645

UNIVERSITÀ
DEGLI STUDI
DI MILANO

UNIVERSITÉ DE
MONTPELLIER

NANOREMEDI
Functional Nano-Scaffolds for Regenerative Medicine

www.nanoremedi.eu

MARIE CURIE ACTIONS

Acknowledgement:

The beauty of the journey lies not in the destination but in the company, and I would like to express my sincere gratitude to everyone who helped and supported me throughout my PhD.

First, I would like to thank the NanoReMedi network and our project coordinator, Professor Maria Luisa Gelmi, for this programme and for warmly welcoming me into the team. I am also grateful to our project managers—Benedetta, Roberta, and Pasquale—and our project consultant, Samuele, for organising everything and helping with all aspects of the project.

I would like to thank my supervisors, Professor Sara Pellegrino, Professor Gilles Subra, and Dr Cécile Echalier, for accepting me into their groups and giving me this opportunity. Without Sara's patient guidance and support through all the academic and bureaucratic challenges, I would not have completed this work. Her encouraging words during moments of self-doubt and the trust and freedom she granted me to explore unconventional ideas were invaluable. I am also grateful for her unwavering support during the initial period of my PhD, which made me feel genuinely cared for as both a researcher and an individual. Gilles, I thank you for the numerous discussions and the endless advice you so generously offered; I always valued the opportunity to ask you questions. Cécile, I thank you for your patience in listening, for meticulously structuring my work plans, explaining the rationale behind them, and managing the administrative responsibilities. My time in Montpellier was memorable and enjoyable, largely because of your efforts in making the journey smooth and pleasant.

I would like to thank my NanoReMedi colleagues and collaborators—Emeline, Nursu, Enrica, Ida, Meital, and Sowmya—for all the intensive meetings we held to write our reviews and articles. Working with all of you has greatly enriched my experience and knowledge as a scientist. I am also thankful to Ali, Baran, Merve, Dulce, Lauren, and Nicolas for making the NanoReMedi experience enjoyable. The post-meeting gatherings, where we discussed both professional and personal matters, made the journey memorable and stimulated many interesting scientific conversations.

I would like to thank my postdoctoral mentors, Antonia and Kali. Antonia, your guidance and training on work organisation during the initial phase of my PhD have been of lasting benefit, and the coffee breaks and light-hearted moments we shared were greatly appreciated. Kali, you are the heart of the laboratory; I recognise how much your presence contributed to a lively and positive working environment. You established a connection with me from the time Sara introduced us, and it always felt as though we had been close friends for years. Michela, thank you for explaining experiments to me and for sharing your experiences. It has been a pleasure working alongside you and discussing our research, the TPE molecules and your BFF. I wish you continued success with your PhD. Zoe, Leti, Raffa, Crash, Fra, Matteo, and Bea—you were amazing and fun colleagues. Whenever I encountered difficulties in understanding or felt frustrated, you all provided help and support, for which I am truly grateful.

I would also like to extend a warm thanks to Lavinia, Michele, and Benedetta from Deloitte Officine Innovazione for patiently showing me the ropes of consultancy. Your support and Lavinia's great guidance helped me learn so much about start-ups and biotech innovations in such a short time. The warm and friendly environment not only helped me expand my horizons but also gave me a great experience of the world beyond academia. My time in Milan would be incomplete without mentioning my amazing roommates, who made life in Milan so fun and lively. Ifi, Hiba, Alessandro—you were wonderful roommates, and the experience with all of you was so great that I feel lucky to have met you. Also, thank you, Cheshta. Our friendship feels like the ultimate girl-friend goal—so honest, full of support and love. I hope you also have a fantastic end to your PhD.

I am grateful to Pascal, Luc, Anthony, and Baptiste for training me on various instruments and techniques. I also extend my sincere thanks to Christopher for training me on the instruments at Cartigen and for listening to my ambitious experimental designs and offering advice. I thank Anthony, Maxime, Anaïs, Jules, François, Hugo, and Gaëtan for warmly welcoming me into the group and assisting me with laboratory work and data analysis. My time in the F9 laboratory would not have been as memorable without Penthip, Jonas, and Dhyana. From finding the best desserts during lunch breaks, to taking leftover desserts to the office after events, to cooking together and playing card games after lunch—every moment I spent with you was memorable and enjoyable. I am deeply grateful to have found such excellent colleagues and even more wonderful friends in both of my laboratories.

Throughout the PhD, projects and countries changed, but what remained constant was the unconditional support of Dulce, Lauren and Nicolas. The best outcome of this PhD has not been the work itself but the enduring friendships I have formed with you guys. Dulce, from my very first day in Milan, you were there, helping me with everything—administrative matters and laboratory tasks alike. I never had to worry about anything in Milan because you were always present, guiding me and looking after me. You listened to all my concerns and even organised enjoyable trips so that I could relax and feel less stressed. I feel truly blessed to have found a friend as wonderful as you during this PhD. Lauren, you have been like a sister to me. I am immensely happy to have met you. You brought a wonderful spark of energy to our group. I would have been quite lost in Montpellier without you—from teaching me biological techniques to introducing me to friends so I am not left alone, you were exceptionally kind. Whether in Milan or Montpellier, you ensured that I had the best possible time. Nicolas, you joined later, but you quickly became an integral part of the group. Thank you for listening to my concerns and for calmly offering your perspectives. Your suggestions, especially during my thesis writing when I felt uncertain about how to proceed, were instrumental in helping me complete this work.

I would like to thank Karen, Joseph, Apurva, Sayali, Jérémie, and Malte. The time spent in your company felt like being at home. Whether discussing my work, listening to your experiences, or receiving your advice, I always felt a sense of calm. With supportive friends like all of you by my side, I felt that nothing could go wrong. I cannot conclude without thanking ZooZoo and Ragini for being just a phone call away, regardless of the time. You are more than best friends—you are integral parts of my life. No matter how long it has been since we last spoke, it always feels as though we are continuing a conversation from yesterday. I look forward to seeing you both soon.

Last but not least, I would never have dreamed of undertaking this PhD without the unconditional support of my family. Years ago, I said that I idolise my mother because she is the strongest person I know, and years later, I reaffirm that sentiment. Whether fighting against people for me or fighting cancer, my amma remains undefeated. I am also grateful to my mamu for supporting my decisions and offering sound advice during moments of uncertainty. Pachi, Bappa, Shekhar Ajja, Amit Anna, and Aruna Akka—thank you for always being ready to help, just a phone call away. Finally, I would like to thank Vinayak. You have proven yourself to be a thoughtful advisor and a patient listener. Your advice, whether on financial or personal matters, has been consistently valuable. I am proud and fortunate to have you.

Abstract:

Peptide-based nanomaterials offer exceptional tunability through sequence control and chemical modification. Within the NanoReMedi framework, this work establishes a structure–property paradigm wherein the hydrophobic domain—aliphatic lipidation, amphiphilic β-sheet extension, or AIE conjugation—deterministically governs assembly, mechanics, and bioactivity across three complementary strategies.

Strategy I established that stearic acid (C18) conjugation dominates morphological outcome, overriding peptide sequence to drive spherical or vesicular architectures. Under physiological ionic strength, colloidal stability was dictated by net electrostatic charge rather than β-sheet propensity. **Strategy II** extended these findings to macroscopic hydrogel formation using the GFOGER epitope functionalised with three distinct domains: an amphiphilic hexapeptide (FQFQFK), its lipidated analogue, and the AIE luminogen TPE. Spectroscopic and rheological studies revealed that lipidation acts as a conformational switch, yielding high modulus β-sheet networks with enhanced early adhesion but poor shear recovery. In contrast, AIE conjugation produced softer, intrinsically fluorescent matrices, with hydroxyproline content being a critical determinant of supramolecular packing density. **Strategy III**, conducted with the University of Pavia, demonstrated that, following covalent immobilisation of bioactive peptides onto electrospun PLGA scaffolds via thiol-maleimide chemistry, the peptide hydropathy index exerts greater control over surface wettability and endothelial selectivity than grafting density.

Collectively, this thesis establishes a predictive framework for the rational design of peptide-decorated biomaterials, balancing mechanical robustness against dynamic reversibility. It also demonstrates that subtle sequence modifications—like proline

hydroxylation—offer control over supramolecular architecture, providing a molecular roadmap for targeted regenerative therapies.

List of Figures and Tables

Figure 1 Interplay of intrinsic (thermodynamic) and extrinsic (kinetic) factors affecting peptide self-assembly. Adapted from the reference [10] 4
Figure 2 Peptide Amphiphile Design Strategies 6
Figure 3 Schematic illustration of TPE-driven self-assembly of fatty acid–AIE peptide hybrids. 11
Figure 4 Late-stage peptide functionalisation. Adapted from the reference [47] 12
Figure 5 Aim of PhD 17
Figure 6 PhD timeline 17
Figure 7 General mechanism of integrin-mediated signalling pathways of bioactive peptides mentioned in the thesis 18
Figure 8 Workflow of DLS analysis 27
Figure 9 SEM Images of Lipopeptides a) DS02, b) DS04, c) DS08, d) DS10, e) DS12, and f) DS14 29
Figure 10 Peptide amphiphile designs (focused on in this work) 35
Figure 11 Fluorescence Emission Spectra of 5% AIE hydrogels 41
Figure 12 Rheology of all six hydrogels at the same w/v concentration of 6% (a-e) a) frequency sweep at 1% strain, b) amplitude sweep at 1Hz frequency, c) time sweep at 1% strain and 1Hz frequency, d) flow sweep and e) thixotropy 43
Figure 13 Circular dichroism of peptide hydrogels at (a-c) different concentrations: a) 0.05 mM, b) 0.1 mM, c) 0.2 mM and different solvent ratios (d-f) CD of TPE peptides in d)95:5 water:MeOH, e)9:1 water:MeOH, f)8:2 water:MeOH, g)7:3 water:MeOH, h)1:1 water:MeO 48
Figure 14 SEM Images of Xerogels Derived from Peptide Hydrogels a)DS33, b)DS34, c)DS35, d)DS36, e)TPE08 and f)TPE38 49
Figure 15 Transwell setup used for the LDH assay 50
Figure 16 LDH Assay a) graph of cell viability results, (b-g) live/dead image of the cells incubated with different hydrogels b)DS33(6%) c)DS34(4%) d)DS35(6%) e)DS36(2%) f) TPE08 (5%) g)TPE38(5%) h) negative control and i) positive control 51
Figure 17 a)graph showing cell adhesion at different time points; (b-e) Confocal image after 4 hours of b)DS33, c)DS34, d)DS35 and e)DS36 53
Figure 18 Confocal image of cells encapsulated in peptide hydrogels. Z stack top view of a)DS33 b)DS34 c)DS35 d)DS36 hydrogel and side view of e)DS33 f)DS34 g)DS35 h) DS36 hydrogel 55
Figure 19 Structures printed using the DS36 hydrogel on a 3D printer a)0.41mm nozzle and b)........ 56
Figure 20 Schematic representation of peptide immobilisation on electrospun PLGA scaffold 64
Figure 21 SEM image of a representative plain PLGA scaffold (before peptide immobilisation)........ 65

Figure 22 SEM images of (a) P1-scaffold, (b) P2-scaffold, (c) P3-scaffold, (d) P4-scaffold, (e) P5-scaffold 68
Figure 23 Cell viability of peptide (P1, P2, P3, P5) solutions in complete cell culture media at various concentrations (8–400 μM) 70
Figure 24 Live and Dead assay on peptide-immobilised scaffolds after 72 h of incubation. 71
Figure 25 DAPI and phalloidin staining on peptide-immobilised scaffolds 72
Figure 26 Relative water absorption capacity and surface wettability of peptide-conjugated PLGA scaffolds. 73
Figure 27 HUVECs viability at 24h and 72h after P1, P2 and P3 treatment at varied concentrations 74
Figure 28 HUVEC viability at 24h and 72h after peptide conjugated scaffold extraction treatment 75
Figure 29 Deconvoluted ATR-FTIR Spectra of the Amide Region (1750–1500 cm^{-1}) of lipopeptides: a) DS02, b) DS04, c)DS08, d) DS10, e)DS12, and f)DS14 89
Figure 30 (a-f) DLS intensity vs. size graphs of 25 μM peptides: (a) DS02, (b) DS04, (c) DS08, (d) DS10, (e) DS12, and (f) DS14 in 95:5 (v/v) water:DMSO solution. (g–l) DLS intensity vs. size graphs of 25 μM peptides: (g) DS02, (h) DS04, (i) DS08, (j) DS10, (k) DS12 and (l) DS14 in 95:5 (v/v) PBS: DMSO solution. 91
Figure 31 Scheme for synthesis of TPE acid- for late-stage peptide functionalisation .. 94
Figure 32 Deconvoluted ATR-FTIR Spectra of the Amide Region (1750–1500 cm^{-1}) of Peptide Hydrogels: a)DS33, b)DS34, c)DS35, d) DS36, e)TPE 08 and f)TPE 38 96
Figure 33 (a-f) DLS intensity vs. size graphs of 50 μM peptides: (a) DS33, (b) DS34, (c) DS35, (d) DS36, (e) TPE 08, and (f) TPE 38 in 9:1 (v/v) water:DMSO solution. (g–l) DLS intensity vs. size graphs of 50 μM peptides: (g) DS33, (h) DS34, (i) DS35, (j) DS36, (k) TPE 08, and (l) TPE 38 in 9:1 (v/v) PBS:DMSO solution. 98
Figure 34 UV chromatogram and ESI-MS spectrum of DS02. Gradient: 20-100% of B in A in 20 min. 0.8 mL/min. A: 0.1% TFA in 100% H2O: B: 0.1% TFA in CH_3CN. The peaks signed correspond to: [M+H]+ (795.06 m/z) .... a
Figure 35 UV chromatogram and ESI-MS spectrum of DS04. Gradient: 20-100% of B in A in 20 min. 0.8 mL/min. A: 0.1% TFA in 100% H2O: B: 0.1% TFA in CH_3CN. The peaks signed correspond to: [M+H]+ (784.32 m/z) .... b
Figure 36 UV chromatogram and ESI-MS spectrum of DS08. Gradient: 20-100% of B in A in 20 min. 0.8 mL/min. A: 0.1% TFA in 100% H2O: B: 0.1% TFA in CH_3CN. The peaks signed correspond to: [M+H]+ (943.18 m/z) c
Figure 37 UV chromatogram and ESI-MS spectrum of DS10. Gradient: 20-100% of B in A in 20 min. 0.8 mL/min. A: 0.1% TFA in 100% H2O: B: 0.1% TFA in CH_3CN. The peaks signed correspond to: [M+H]+ (781.73 m/z) .... d
Figure 38 UV chromatogram and ESI-MS spectrum of DS12. Gradient: 20-100% of B in A in 20 min. 0.8 mL/min. A: 0.1% TFA in 100% H2O: B: 0.1% TFA in CH_3CN. The peaks signed correspond to: [M+2H]2+ (1089.55 m/z) and [M+3H]3+ (727.60 m/z) .... e

Figure 39 UV chromatogram and ESI-MS spectrum of DS14. Gradient: 20-100% of B in A in 20 min. 0.8 mL/min. A: 0.1% TFA in 100% H2O: B: 0.1% TFA in CH_3CN. The peaks signed correspond to: [M+2H]+2 (884.68 m/z) and [M+3H]+3 (589.62 m/z) .... f

Figure 40 UV chromatogram and ESI-MS spectrum of DS33. Gradient: 5-70% of B in A in 20 min. 0.8 mL/min. A: 0.1% TFA in 100% H2O: B: 0.1% TFA in CH_3CN. The peaks signed correspond to: [M+2H]2+ (744.41 m/z).. g

Figure 41 UV chromatogram and ESI-MS spectrum of DS34. Gradient: 20-100% of B in A in 20 min. 0.8 mL/min. A: 0.1% TFA in 100% H2O: B: 0.1% TFA in CH_3CN. The peaks signed correspond to: [M+2H]2+ (877.69 m/z) .... h

Figure 42 UV chromatogram and ESI-MS spectrum of DS35. Gradient: 5-70% of B in A in 20 min. 0.8 mL/min. A: 0.1% TFA in 100% H2O: B: 0.1% TFA in CH_3CN. The peaks signed correspond to: [M+H]+ (1503.62 m/z), [M+2H]2+ (752.56 m/z), and [M+3H]3+ (502.19 m/z) i

Figure 43 UV chromatogram and ESI-MS spectrum of DS36. Gradient: 20-100% of B in A in 20 min. 0.8 mL/min. A: 0.1% TFA in 100% H2O: B: 0.1% TFA in CH_3CN. The peaks signed correspond to: [M+2H]2+ (885.97 m/z) .... j

Figure 44 UV chromatogram and ESI-MS spectrum of TPE 08. Gradient: 20-100% of B in A in 20 min. 0.8 mL/min. A: 0.1% TFA in 100% H2O: B: 0.1% TFA in CH_3CN. The peaks signed correspond to: [M+H]+ (1247.67 m/z) .... k

Figure 45 UV chromatogram and ESI-MS spectrum of TPE 38. Gradient: 20-100% of B in A in 20 min. 0.8 mL/min. A: 0.1% TFA in 100% H2O: B: 0.1% TFA in C_H3CN. The peaks signed correspond to: [M+H]+ (1231.58 m/z) l

Figure 46 UV chromatogram and ESI-MS spectrum of P1. Gradient: 5-70% of B in A in 20 min. 0.8 mL/min. A: 0.1% TFA in 100% H2O: B: 0.1% TFA in CH_3CN. The peaks signed correspond to: [M+H]+ (631.79 m/z) and [M+Na]+ (653.80 m/z) .... m

Figure 47 UV chromatogram and ESI-MS spectrum of P2. Gradient: 5-70% of B in A in 20 min. 0.8 mL/min. A: 0.1% TFA in 100% H2O: B: 0.1% TFA in CH_3CN. The peaks signed correspond to: [M+H]+ (620.08 m/z) and [M+2H]2+ (310.66 m/z) .... n

Figure 48 UV chromatogram and ESI-MS spectrum of P3. Gradient: 5-70% of B in A in 20 min. 0.8 mL/min. A: 0.1% TFA in 100% H2O: B: 0.1% TFA in CH_3CN. The peaks signed correspond to: [M+H]+ (780.96 m/z) and [M+2H] 2+ (391.93 m/z)................................ o

Figure 49 UV chromatogram and ESI-MS spectrum of P4. Gradient: 5-70% of B in A in 20 min. 0.8 mL/min. A: 0.1% TFA in 100% H2O: B: 0.1% TFA in CH_3CN. The peaks signed correspond to: [M+H]+ (619.39 m/z) and [M+2H]2+ (310.93 m/z) .... p

Figure 50 UV chromatogram and ESI-MS spectrum of P5. Gradient: 5-70% of B in A in 20 min. 0.8 mL/min. A: 0.1% TFA in 100% H2O: B: 0.1% TFA in CH_3CN. The peaks signed correspond to: [M+H]+ (1604.11 m/z), [M+2H]2+ (803.05 m/z) and [M+3H]3+ (536.01 m/z) .... q

Figure 51 ATR-FTIR spectra of DS02(Stearic acid-IKVAV-NH_2) in solid state .... r

Figure 52 ATR-FTIR spectra of DS04 (Stearic acid-REDV-NH_2) in solid state .... s

Figure 53 ATR-FTIR spectra of DS08(Stearic acid-GFOGER-NH_2) in solid state .... s

Figure 54 ATR-FTIR spectra of DS10(Stearic acid-fPRP-NH$_2$) in solid state......................t
Figure 55 ATR-FTIR spectra of DS12 (Stearic acid-KLTWQELYQLKYKGI-NH$_2$) in solid state ....t
Figure 56 ATR-FTIR spectra of DS14 (Stearic acid-KAFDITYVRLKF-NH$_2$) in solid state..... u
Figure 57 ATR-FTIR spectra of DS33 (FQFQFKGFPGER-NH$_2$) in solid state..................... u
Figure 58 ATR-FTIR spectra of DS34 (Stearic acid-FQFQFKGFPGER-NH$_2$) in solid state .. u
Figure 59 ATR-FTIR spectra of DS35 (FQFQFKGFOGER-NH$_2$) in solid state v
Figure 60 ATR-FTIR spectra of DS36 (Stearic acid-FQFQFKGFOGER-NH$_2$) in solid state.. v
Figure 61 ATR-FTIR spectra of TPE 08(TPE acid-GFOGER-NH$_2$) in solid state .... w
Figure 62 ATR-FTIR spectra of TPE 38 (TPE acid-GFPGER-NH$_2$) in solid state .... w

Table 1: List of bioactive peptides used during the course of the PhD 19
Table 2: Library of lipopeptides.. 25
Table 3: Percentages of secondary structure for each peptide at the solid state, calculated with OriginPro [107]... 26
Table 4:DLS of lipopeptide library at 95:5 solvent ratio(water:DMSO and PBS:DMSO) and 25 μM peptide concentration 27
Table 5: GFOGER peptide conjugate library 36
Table 6: Percentages of secondary structure for each peptide at the solid state, calculated with OriginPro[107] 37
Table 7: DLS and pH of GFOGER peptide library.. 39
Table 8:Minimum Gelation Concentration (MGC) of Peptide Hydrogels 40
Table 9: Mechanical characterisation of plain scaffold (average ± standard deviation). 65
Table 10: Cysteine-Modified Peptide Library Synthesised for SDVG Functionalisation . 66
Table 11:Quantification of Peptide Conjugation onto PLGA Scaffolds......................... 69
Table 12:List of lipopeptide sequences synthesised by MW-SPPS, their corresponding linear gradient used for purification using semi-preparative RP-HPLC 87
Table 13:Peptide Amphiphile Library and RP-HPLC Purification Gradients 95
Table 14:Cysteine-Modified Peptide Library and RP-HPLC Purification Gradients 105

Table of Contents

v

Acknowledgement: i

Abstract: v

List of Figures and Tables vii

Abbreviations xiv

1. Introduction 1
  1.1. Peptide Self-Assembly 2
  1.2. Self-Assembling Peptide Nanomaterials 4
    1.2.1. Peptide amphiphiles 5
2. Aim of the PhD 13
  2.1. Investigated Peptide Architectures 15
    2.1.1. Lipopeptides- Nanocolloids 15
    2.1.2. Amphiphilic Peptide Hydrogels 15
  2.2. Peptide-Polymer Conjugate (collaborative project) 16
  2.3. Selection and Biological Rationale of Bioactive Peptides 17
    2.3.1. Cell adhesive peptides 19
    2.3.2. Triple helical peptides 20
    2.3.3. Anticoagulant sequence 21
    2.3.4. Angiogenic sequence 21
3. Lipopeptides 23
  3.1. Results 24
    3.1.1. Synthesis of Lipopeptides 24
    3.1.2. Conformational analysis - FTIR 25
    3.1.3. Self-assembly studies - DLS 26
    3.1.4. Scanning Electron Microscopy (SEM) 28
  3.2. Discussion 29
4. Peptide hydrogels 32
  4.1. Results 35
    4.1.1. Synthesis of Peptide Amphiphiles 35
    4.1.2. Conformational Analysis - ATR-FTIR 36
    4.1.3. Self-Assembly Studies -DLS 38
    4.1.4. Hydrogel Evaluation 39

- 4.1.5. Biological evaluations 49
- 4.1.6. 3D printing 55
- 4.2. Discussion 56
  - 4.2.1. Mechanical insights and summary of DS33, DS34, DS35 and DS36 56
  - 4.2.2. AIE-conjugated peptides 58
- 5. Peptide-Decorated Vascular Graft 61
  - 5.1. RESULTS 64
    - 5.1.1. Characterisations of Plain PLGA Scaffolds (before peptide immobilisation) 64
    - 5.1.2. Synthesis of Cysteine-Modified Peptides 66
    - 5.1.3. Peptide Immobilisation and Scaffold Morphology 67
    - 5.1.4. Quantification of peptide immobilisation onto plain scaffold 68
    - 5.1.5. Cytotoxicity of Soluble Peptides on Fibroblasts (nHDFs) 69
    - 5.1.6. Fibroblast Response to Peptide-Immobilised Scaffolds 70
    - 5.1.7. Water Absorption and Surface Wettability 72
    - 5.1.8. Endothelial Cell (HUVEC) Response to Soluble Peptides 73
    - 5.1.9. Endothelial Cell Response to Scaffold Extracts 74
  - 5.2. Discussion: 75
- 6. Conclusion 78
  - 6.1. Lipopeptide Nanocolloids 79
  - 6.2. Amphiphilic Peptide Hydrogels 80
  - 6.3. Peptide-Decorated Vascular Grafts 82
  - 6.4. Future Perspectives 83
- 7. Experimental section 85
  - 7.1. Materials: 86
  - 7.2. Project 1 : Lipopeptides-nanocolloids (DS02, DS04, DS08, DS10, DS12, and DS14) 86
    - 7.2.1. Synthesis and purification of lipopeptides 86
    - 7.2.2. Conformational analysis using ATR-FTIR 88
    - 7.2.3. Self-Assembly Studies using DLS 89
    - 7.2.4. SEM 91
  - 7.3. Amphiphilic Peptide Hydrogels (DS33, DS34, DS35, DS36, TPE 08 and TPE 38) 92
    - 7.3.1. Synthesis and Purification of Peptide Amphiphiles 92
    - 7.3.2. Conformational analysis of peptides – ATR-FTIR 96
    - 7.3.3. Self-Assembly Studies using DLS 97
    - 7.3.4. Hydrogel formation 98
    - 7.3.5. Biological evaluation 101
    - 7.3.6. 3D printing (DS36) 102

7.4. Peptide-decorated modular SDVG 103
  7.4.1. Electrospun Scaffold Fabrication 103
  7.4.2. Synthesis and purification of cysteine peptides 104
  7.4.3. Peptide Immobilisation 106
  7.4.4. Physiochemical Characterisations of Peptide Immobilised Scaffolds 106
  7.4.5. *In Vitro* Biological Evaluation on Normal Human Dermal Fibroblasts (nHDFs) 108
  7.4.6. *In Vitro* Biological Evaluation on Human Umbilical Vein Endothelial Cells (HUVECs) 110
7.5. Instrumentation and Software 112
  7.5.1. Analytical and Semi-Preparative RP-HPLC 112
  7.5.1. Mass Spectrometry (ESI-MS) 112
  7.5.2. Fourier-Transform Infrared Spectroscopy (FTIR) 112
  7.5.3. Dynamic Light Scattering (DLS) 112
  7.5.4. Circular Dichroism (CD) Spectroscopy 112
  7.5.5. Rheology 113
  7.5.6. Scanning Electron Microscopy (SEM) 113
  7.5.7. Confocal Microscopy 113
  7.5.8. 3D Bioprinting 113
  7.5.9. Mechanical Testing 113
7.6. Statistical Analysis 113
8. References: 115
9. Supplementary Data .... a
RP-HPLC chromatograms and MS-ESI analyses .... a
ATR-FTIR spectra .... r

Abbreviations

Abbreviations	Full Forms
Acn	Acetonitrile
AIE	Aggregation-Induced Emission
ATR-FTIR	Attenuated Total Reflection Fourier Transform Infrared
C18	Stearic Acid (18-carbon alkyl chain)
CD	Circular Dichroism
DAPI	4',6-Diamidino-2-phenylindole
DCM	Dichloromethane
DIC	N,N-Diisopropylcarbodiimide
DIEA	N,N,N-Diisopropylethylamine
DLS	Dynamic Light Scattering
DMAP	P-Dimethylaminopyridine
DMEM	Dulbecco's Modified Eagle Medium
DMF	N,N-Dimethylformamide
DMSO	Dimethyl Sulfoxide
DODT	3,6-Dioxa-1,8-Octanedithiol
EC	Endothelial Cell
ECM	Extracellular Matrix
EDC	1-Ethyl-3-(3-dimethylaminopropyl)carbodiimide
ESI-MS	Electrospray Ionisation-Mass Spectrometry
EtOAc	Ethyl acetate
FA	Fatty Acid
FBS	Fetal Bovine Serum
Fmoc	9-Fluorenylmethoxycarbonyl
HBTU	2-(1H-Benzotriazol-1-yl)-1,1,3,3-tetramethyluronium hexafluorophosphate
HOBt	Hydroxy Benzotriazole
HUVEC	Human Umbilical Vein Endothelial Cell
LDH	Lactate Dehydrogenase
MeOH	Methanol
MES	2-(N-Morpholino)ethanesulfonic acid
MGC	Minimum Gelation Concentration
MTT	3-(4,5-Dimethylthiazol-2-yl)-2,5-diphenyltetrazolium bromide
MW-SPPS	Microwave assisted Solid Phase Peptide Synthesis
NBD	Nitrobenzoxadiazole
nHDF	Normal Human Dermal Fibroblast
NHS	N-Hydroxy succinimide
Oxyma	Ethyl cyanoglyoxylate-2-oxime (coupling additive)
PB(S)	Phosphate Buffer (Saline)
PLGA	Poly(Lactic-Co-Glycolic Acid) / Poly(Lactide-Co-Glycolide)
RP-HPLC	Reversed-Phase High Performance Liquid Chromatography
rt	Room Temperature
SDVGs	Small-Diameter Vascular Grafts

SEM	Scanning Electron Microscopy
SPPS	Solid Phase Peptide Synthesis
TCEP	Tris(2-carboxyethyl)phosphine
TFA	Trifluoroacetic Acid
THF	Tetrahydrofuran
THP	Triple Helical Peptide
TIPS	Triisopropylsilane
TPE	Tetraphenylethylene
VEGF	Vascular Endothelial Growth Factor

List of amino acids

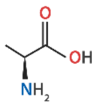

Alanine
Ala - A

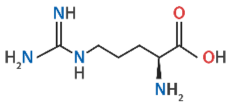

Arginine
Arg - R

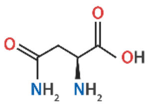

Asparagine
Asn - N

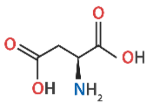

Aspartate
Asp - D

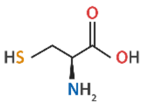

Cysteine
Cys - C

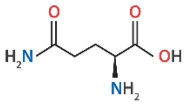

Glutamine
Gln - Q

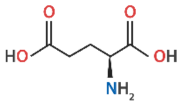

Glutamate
Glu - E

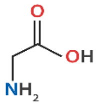

Glycine
Gly - G

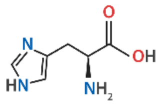

Histidine
His - H

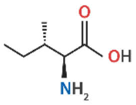

Isoleucine
Ile - I

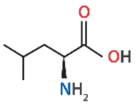

Leucine
Leu - L

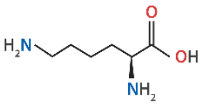

Lysine
Lys- K

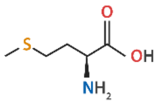

Methionine
Met - M

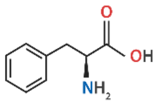

Phenylalanine
Phe - F

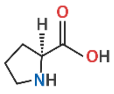

Proline
Pro - P

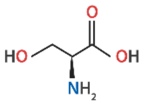

Serine
Ser - S

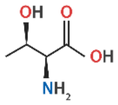

Threonine
Thr - T

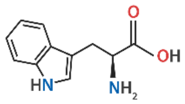

Tryptophan
Trp - W

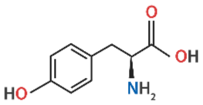

Tyrosine
Tyr - Y

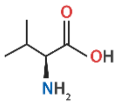

Valine
Val - V

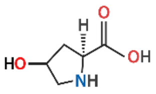

Hydroxyproline
Hyp - O

1. Introduction

Supramolecular Peptide Nanomaterials & Sequence Designing

In nature, proteins represent some of the most sophisticated functional materials, displaying multiscale hierarchical assembly largely through non-covalent interactions (alongside covalent crosslinks such as disulfide bonds), making complex structures that act as molecular machinery at the cellular and tissue level. Inspired by this, the recent years have seen an increase in the design and application of functional materials using short bioactive domains of proteins or bioactive peptides, whose properties can be tuned at the molecular level to enhance efficiency and the material's capacity to execute a specific function. [1] [2]

1.1. Peptide Self-Assembly

Molecular self-assembly is an intrinsic process by which molecules spontaneously organise into ordered, energetically favourable architectures through the cooperative action of multiple weak non-covalent interactions. Unlike covalent bonds, these interactions are inherently reversible, enabling assembled structures to dynamically reorganise in response to environmental stimuli, conferring both structural coherence and adaptive functionality.

This bottom-up fabrication strategy has emerged as a powerful tool in the engineering of nano-biomaterials, offering precise control over the hierarchical organisation of the structure through controlling the design rationale of the building blocks. [3,4] Among the diverse range of self-assembling systems investigated, peptides and peptidomimetics are particularly interesting choice as modular building blocks for nano-biomaterials. This interest stems from three key attributes of peptide materials:

- First, peptide-based systems have inherent self-assembly behaviour. This behaviour is the foundation of various native structural complexes, making peptide-derived nanomaterials, biocompatible and easily integrated with living tissues. [5]

- Second, peptide sequences can be precisely engineered at the amino acid level to incorporate specific biological signals (receptor-binding motifs, extracellular matrix ligands, and growth factor–mimetic domains), allowing programmed presentation of bioactive cues that regulate cell behaviour. Such tunability is particularly advantageous in tissue regeneration, where spatial and biochemical control over cell–material interactions is essential. [6–8]
- Third, peptides offer significant advantages in terms of synthetic control and reproducibility. They are synthesised using well-established methods - solid-phase peptide synthesis (SPPS), liquid-phase chemistry, enzymatic synthesis, or recombinant expression- enabling precise regulation over sequence length, composition, and chemical modification. Unlike full-length proteins, peptides lack higher-order structural heterogeneity, which facilitates high purity and consistent batch-to-batch production. [9]

This molecular precision enables systematic investigation of structure–function relationships and rational design optimisation of supramolecular assemblies tailored to specific biomedical applications.

The peptide self-assembly arises from a complex interplay between intrinsic and extrinsic factors, which gives rise to a plethora of cooperative non-covalent interactions that form thermodynamically favourable structures with free-energy minima. Intrinsic material properties reflect the collective contribution of multiple weak non-covalent interactions rather than any single dominant force. These properties are often estimated statistically from available peptide datasets and interpreted as generalised sequence-dependent trends. Importantly, the position of amino acids within a sequence strongly influences structural behaviour. Peptides with identical amino acid compositions but different sequence arrangements may exhibit similar overall polarity yet display markedly different structural and morphological properties.

In addition to intrinsic non-covalent interactions, external stimuli—including pH, temperature, ionic strength, solvent polarity, enzymatic activity, and concentration—can introduce kinetic control over peptide assembly pathways (Figure 1). Such stimuli may lead to kinetically trapped states and metastable morphologies rather than thermodynamically favoured structures. Understanding the interplay between sequence design, thermodynamic stability, and kinetic regulation is therefore essential for the rational development of stable peptide-based nanomaterials. [6]

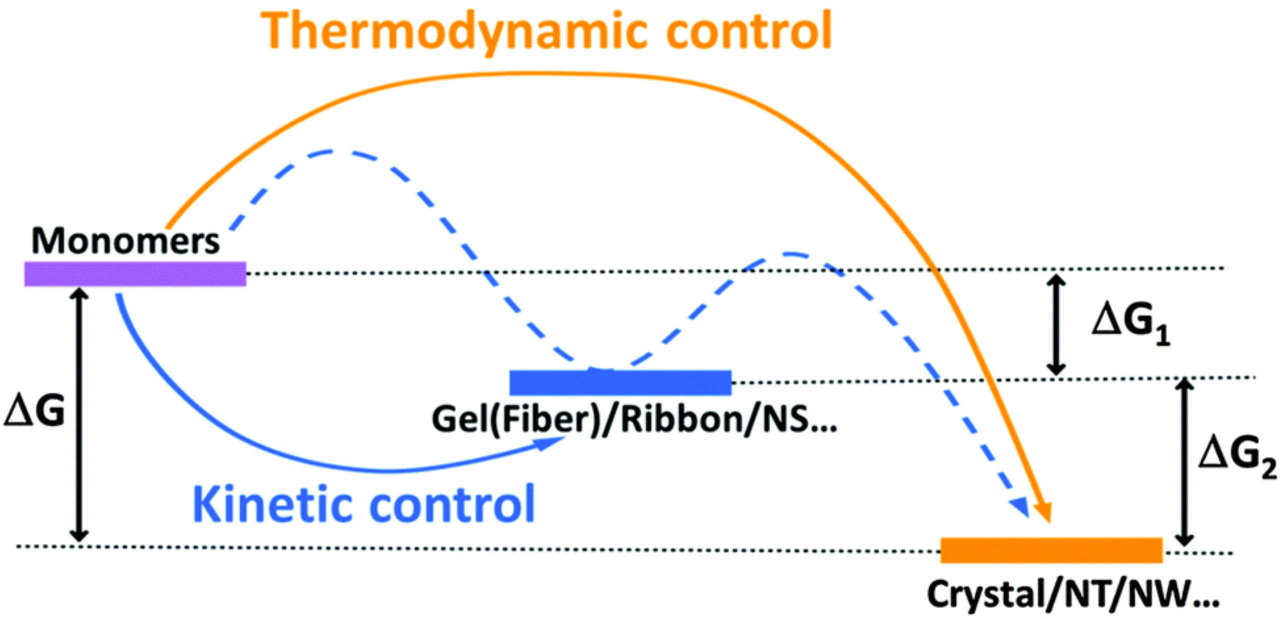

Figure 1 Interplay of intrinsic (thermodynamic) and extrinsic (kinetic) factors affecting peptide self-assembly. Adapted from the reference [10]

1.2. Self-Assembling Peptide Nanomaterials

Beyond intrinsic and extrinsic variables, the primary sequence design remains the most fundamental determinant of the self-assembly pathway. By strategically organising amino acids, one can precisely modulate non-covalent interactions to favour specific folding patterns. In the presence of external triggers, these designed building blocks undergo hierarchical organisation into well-defined secondary structures—such as α-helices, β-sheets, β-turns, or collagen-like triple helices—or assemble into spherical and cylindrical micellar architectures.

This level of control is achieved by systematically varying the amino acid composition, the specific sequence order, and the incorporation of chemical modifications. Such precision allows for the fabrication of peptide-based nanomaterials with tailored mechanical stiffness, sophisticated hierarchical complexity, and targeted biological functionality. [22]

One of the most prevalent sequence-design strategies used to generate peptide nanomaterials, particularly hydrogels, is a peptide amphiphile:

1.2.1. Peptide amphiphiles

Peptide amphiphiles (PAs) represent an important class of self-assembling biomaterials that combine molecular recognition properties of peptides with the self-assembly behaviour of amphiphilic molecules. Amphiphilic materials typically consist of a hydrophobic tail and a hydrophilic head group, which impart surfactant-like behaviour and allow them to form organised supramolecular structures in aqueous environments. In peptide amphiphiles, amphiphilicity can be introduced through several design strategies like short hydrophobic peptide segments, aromatic groups, or lipid moieties. These molecular architectures promote self-assembly into nanofibres, ribbons, belts, or micellar structures. Under controlled conditions, these structures can form highly ordered supramolecular fibrillar networks and entrap large amounts of water, forming hydrogels (Figure 2). [23]

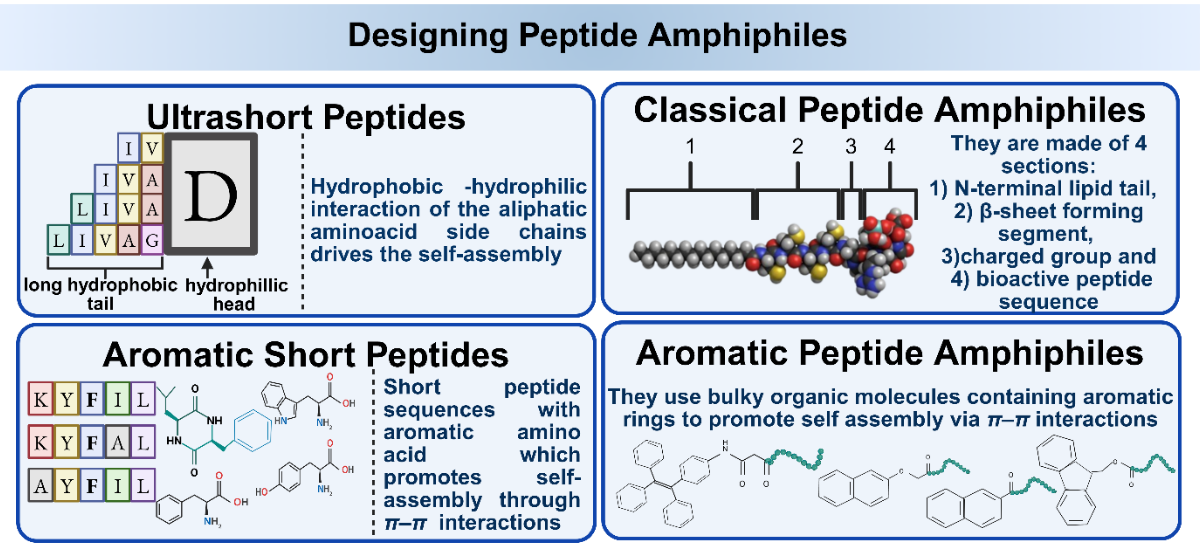

Figure 2 Peptide Amphiphile Design Strategies

1.2.1.1. *Ultra-Short Peptide Amphiphiles*

This peptide amphiphile design strategy involves the use of 3–6 aliphatic amino acids. In these systems, a relatively hydrophilic amino acid head group is combined with a more hydrophobic peptide segment that acts as the tail. For instance, non-aromatic linear peptides with a dominant hydrophobic nature -composed of amino acid residues such as valine, leucine, isoleucine, alanine and glycine - are conjugated to a polar amino acid such as aspartic acid, glutamic acid, lysine, serine, or threonine. Despite their minimal size, these molecules self-assemble into helical supramolecular fibres in water, which align in parallel or antiparallel arrangements to produce stable fibrillar hydrogels. [23]

1.2.1.2. *Intrinsically Aromatic & Amphipathic Sequences*

Aromatic amino acids enhance self-assembly through π–π stacking interactions. One of the earliest examples of ultra-short aromatic peptide hydrogels involved diphenylalanine (FF) motifs. Conjugation of D-leucine or D-valine to the FF dipeptide showed fibrous hydrogel networks under physiological pH due to the peptide chirality of D-amino acids. In these systems, the D-amino acids promote tighter packing and extended β-sheet conformations, aligning phenylalanine residues via π–π stacking, unlike the L-amino acids, thereby acting as a molecular zipper, stabilising the supramolecular assembly and promoting hydrogel formation. [24–26] In another approach, long peptide sequences (6 amino acid long) containing alternating phenylalanine and aspartate residues were used to create extended anionic amphiphilic chains that were further functionalised with bioactive peptides at the C-terminus to enhance cell adhesion and biological interactions. [27]

A hybrid design strategy was reported by Ballet et al., which integrated aromatic amino acids with amphipathic sequences to combine π–π stacking with hydrophobic–hydrophilic segregation. The short amphipathic hexapeptide, FQFQFK (H-FQFQFK-NH_2), inspired by amyloid-like nanofiber assembly, follows an iterative design with alternating residues of phenylalanine and glutamine, creating an amphipathic character similar to an ultra-short peptide. amphiphiles. Despite having only a single charged residue at the C-terminus (lysine), this compact design exhibits excellent gel properties, making it suitable for injectable and drug delivery applications. [28] Subsequent studies focused on improving the mechanical and physiochemical properties of the hydrogels using sequence length and amino acid modifications. [29–31]

1.2.1.3. Classical Lipidated Peptide Amphiphiles

A major advancement in the design of peptide amphiphiles was introduced by Stupp and co-workers, who developed a modular architecture consisting of four distinct structural segments:

1) a hydrophobic fatty acid tail at the N-terminus,

2) a hydrophobic β-sheet-forming region,

3) a charged amino acid region, and

4) a bioactive motif at the C-terminus to interact with cells.

A representative example of this design is the peptide amphiphile $CH_3(CH_2)_{14}$CONH-CCCCGGG-PSRGD, in which the RGD motif promotes cell adhesion, the fatty acid tail drives the hydrophobic collapse, while the β-sheet forming segment promotes nanofibre formation through hydrogen bonding. The charged region stabilises the assembly in aqueous environments and allows the nanofibres to interact with biological systems. [32]

Over time, several β-sheet-forming sequences such as AAAAGGG, AAALLL, and VVVAAA were developed to improve hydrophobicity and enhance supramolecular assembly. [33–35] Recent studies have demonstrated that even shorter peptide segments containing only four amino acids can form functional peptide amphiphiles. These studies revealed that the supramolecular dynamics of the assembled nanofibres strongly influence biological activity. Systems with highly dynamic fibrils exhibited enhanced bioactivity, including axonal growth, neuronal survival, angiogenesis, and functional recovery following spinal cord injury, whereas systems with restricted supramolecular motion showed reduced biological performance. [36]

Variations of this strategy have also been reported in which the fatty acid tail is retained, but the peptide segment is shortened considerably. For example, the lipopeptide NH_2-kMF-$C_{12}H_{25}$ has been shown to self-assemble into nanostructures that exhibit dual antibacterial and anticancer activity. Such simplified amphiphilic designs demonstrate that even minimal peptide sequences can produce biologically functional supramolecular materials. [37]

1.2.1.4. Aromatic Conjugate-Modified Peptide Amphiphiles

The conjugation of aromatic groups to peptides is used to enhance supramolecular assembly. Aromatic molecules can be attached directly to peptide sequences or connected through linkers. The resulting molecules assemble through π–π stacking interactions, forming parallel, antiparallel, or interlocked stacked arrangements that produce fibrous supramolecular structures capable of forming hydrogels. [38]

Among the most widely studied examples are Fmoc-based peptide hydrogels. The 9-fluorenyl methoxycarbonyl (Fmoc) protecting group, commonly used in peptide synthesis, also acts as a hydrophobic aromatic moiety that promotes self-assembly. The classic example is Fmoc-FF, which forms hydrogels through an antiparallel β-sheet arrangement in which the Fmoc groups interlock through π-π stacking interactions. This arrangement produces cylindrical supramolecular assemblies that further organise into nanofibre networks. [39]

Hybrid systems have also been developed by combining Fmoc-based peptides with other amphiphilic components. For example, Fmoc-FF has been combined with cationic amphiphilic peptides such as $(GK)_3$ linked to a fatty acid tail to generate hydrogels capable of delivering negatively charged drugs. [39]

1.2.1.4.1. Aggregation-Induced Emission (AIE) Luminogen-Based Peptide Amphiphiles

In recent years, aggregation-induced emission (AIE) luminogens have emerged as powerful tools for designing fluorescent peptide amphiphiles. Unlike conventional fluorophores that emit strongly in solution but become quenched upon aggregation, AIE molecules exhibit enhanced fluorescence in the aggregated state. This unique property makes them particularly useful for studying supramolecular self-assembly processes and for monitoring the formation and degradation of supramolecular aggregates in real time. AIE luminogens are also advantageous because their emission is highly photostable, making them useful for long-term imaging of biomaterials. The ability to combine fluorescence imaging with supramolecular self-assembly provides valuable insights into the structural dynamics of peptide hydrogels.

One of the most widely studied AIE luminogens is tetraphenylethylene (TPE). TPE contains four phenyl rings arranged around a central ethylene core, which makes it highly hydrophobic. In solution, the free rotation of these phenyl rings leads to non-radiative energy dissipation and weak fluorescence. However, upon aggregation, the rotational motion of the phenyl rings becomes restricted, a phenomenon known as restriction of intramolecular motion (RIM). This restriction suppresses non-radiative decay pathways and results in strong fluorescence emission. [40–42]

An early example of AIE-based peptide amphiphiles involved diglycine (GG) conjugated to a TPE moiety at the N-terminus. The hydrophobic TPE unit promoted aggregation in aqueous environments, while the peptide segment contributed hydrogen bonding and electrostatic interactions. These combined interactions resulted in the formation of supramolecular nanobelts, which further assembled into hydrogel networks. Because fluorescence arises only after aggregation, these systems enable direct visualisation of the self-assembly process. [43]

Another AIE luminogen used in the development of peptide amphiphile is nitrobenzoxadiazole (NBD). The design involved the conjugation of NBD to a hexapeptide through an alkyl linker. The resulting hydrogel exhibited fluorescence intensities nearly ten times greater than the free NBD molecule and showed pH-responsive fluorescence switching, enabling reversible monitoring of environmental changes. [44] Apart from these systems, 1,8-naphthalimide and naphthalene diimide (NDI) derivatives have also been explored as AIE-active building blocks. For example, Bertouille et al. replaced the phenylalanine residue adjacent to lysine with 1,8-naphthalimide-derived amino acids, thereby forming β-sheet nanofibre-based hydrogels. The incorporation of the fluorescent aromatic moiety enhanced π–π stacking interactions, enabling stable gel formation at lower peptide concentrations in physiological saline conditions. The strengthened intermolecular interactions also improved the rheological properties of the hydrogel, making the system promising for injectable biomaterials, real-time fluorescence tracking, and sustained drug delivery applications. [45]

Building on these developments, the Pellegrino group previously synthesised fatty acid–TPE conjugated peptide hybrids, where fatty acid spacers of varying lengths were introduced between the TPE luminogen and a bioactive peptide sequence to investigate how spacer length influences peptide self-assembly. This work demonstrated that the use of longer fatty acid chains helped in the formation of more stable fibrillar aggregates with better emission, yielding supramolecular gels with promising rheological features (Figure 3). [46]

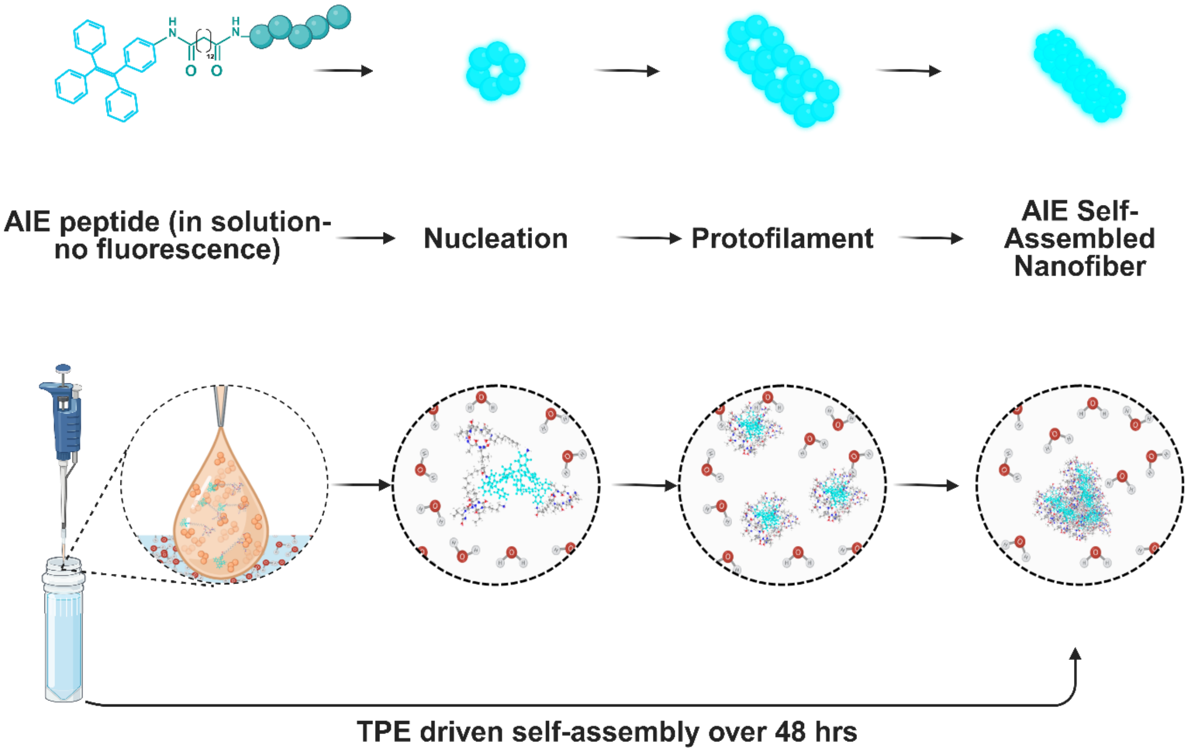

Figure 3 Schematic illustration of TPE-driven self-assembly of fatty acid–AIE peptide hybrids.

In a subsequent study, a TPE–phenylalanine-derived fluorescent amino acid was synthesised via Suzuki–Miyaura cross-coupling and used for late-stage peptide functionalisation through solution-phase and solid-phase peptide synthesis. [47] Coupling this AIE-active amino acid to a Leu-Val dipeptide in solid-phase transformed the self-assembly morphology from the needle-like structures characteristic of the parent aliphatic dipeptide [48]; to spherical aggregates in aqueous-organic solvent mixtures. Out of the two AIE amino acids synthesised, the asymmetrically extended TPE π-system exhibited stronger and brighter fluorescence emission compared to conventional TPE systems, highlighting its potential for designing highly emissive peptide-based biomaterials. [47]

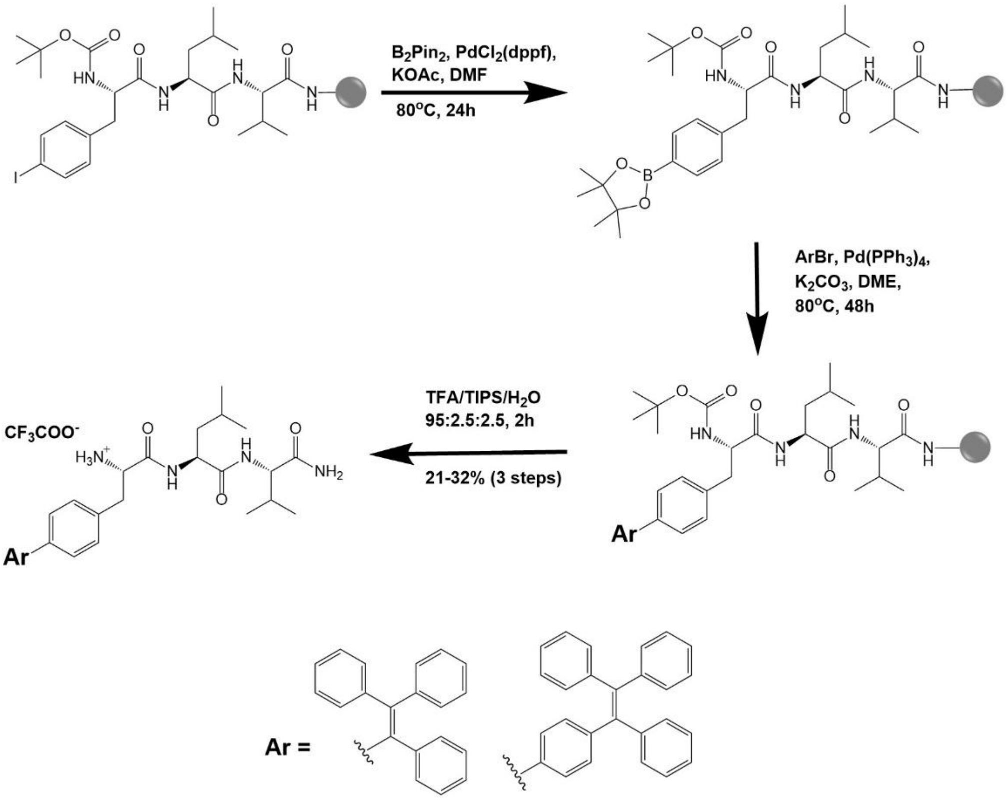

Figure 4 Late-stage peptide functionalisation. Adapted from the reference [47]

2. Aim of the PhD

PhD Overview

Regenerative medicine requires materials that can combine the mechanical integrity of synthetic scaffolds with bioactivity of native tissue – a combination that remains difficult to achieve. While polymers like PLGA offer excellent processability and mechanical integrity, they fail to actively direct cell fate. Conversely, decellularised tissues provide innate bioactivity but lack molecular programmability and batch-to-batch consistency. [49] Bioactive peptide motifs—short sequences derived from the extracellular matrix (ECM)—offer a solution: they can be displayed on robust synthetic scaffolds to direct specific cellular responses such as adhesion, migration, and differentiation. [50]

However, the translation of a peptide sequence into a functional material is not straightforward. The presentation of the bioactive ligand to the cell surface receptor is governed by the molecular architecture of the carrier. Simply conjugating a peptide to a polymer chain does not guarantee bioactivity; the local nano-environment, peptide mobility, and supramolecular packing dictate whether the sequence is accessible or buried.

The central hypothesis of this thesis is that the nature and structural properties of the hydrophobic domain in a peptide amphiphile predictably govern three critical material properties:

a. Structural Hierarchy: Whether the system forms fluid nanocolloids, rigid nanofibers, or entangled hydrogels.

b. Mechanical Rigidity: The resulting storage modulus (G') and gelation efficiency.

c. Functional Bioactivity: The accessibility of the bioactive epitope to integrin receptors.

By systematically varying the hydrophobic "anchor" (alkyl chain, AIE luminogen, or structured β-sheet peptide) while maintaining a constant set of bioactive sequences (IKVAV, REDV, GFOGER), this work aims to establish quantitative structure–property relationship. The objective is to generate design rules that predict whether a new peptide conjugate will self-assemble into a soft colloid suitable for injection or a stiff gel suitable for cell encapsulation. This work is embedded within the NanoReMedi Consortium, which targets three specific clinical needs: vascular graft endothelialisation, osteochondral repair, and preventing implant failure. In all cases, the material must actively communicate with host cells via integrin-mediated signalling.

2.1. Investigated Peptide Architectures

The experimental strategy is bifurcated into two distinct material classes designed to test the limits of hydrophobic driving forces.

2.1.1. Lipopeptides- Nanocolloids

This strategy focused on minimalist lipopeptide design, and it isolates the fundamental effect of lipidation on self-assembly behaviour and colloidal stability across a diverse library of clinically relevant six bioactive peptide sequences (IKVAV, REDV, GFOGER, (D-Phe)PRP, KLTWQELYQLKYKGI, and KAFDITYVRLKF). The objective was to understand how variations in peptide length, charge, and hydrophilicity modulate the driving force of the hydrophobic C18 alkyl chain to dictate the formation of stable nanocolloids in aqueous environments.

2.1.2. Amphiphilic Peptide Hydrogels

Building on the principles established with simple lipopeptide nanocolloids, this second investigation sought to translate self-assembly into the formation of macroscopic, self-supporting hydrogels. This study focuses specifically on the collagen-mimetic bioactive sequence GFOGER, exploring how the incorporation of additional aromatic and structured amphiphilic domains at the N-terminus influences hierarchical assembly. Three distinct molecular design strategies were employed to systematically vary the nature of the hydrophobic driving force:

1. Amphipathic β-Sheet Peptide Conjugate: Direct extension of the bioactive sequence with the self-assembling hexapeptide FQFQFK.
2. Lipidated β-Sheet Peptide Conjugate: Combination of the FQFQFK hexapeptide with an N-terminal stearic acid tail to maximise hydrophobic collapse and hydrogen bonding potential.
3. AIE Luminogen Conjugate: Conjugation of 4-amino-tetraphenylethene (TPE) via a fatty acid spacer to induce self-assembly while enabling intrinsic fluorescence.

The impact of these different N-terminal amphiphilic groups on the secondary structure, gelation efficiency, mechanical rigidity, and ultimate bioactivity of the GFOGER-presenting hydrogels was systematically evaluated.

2.2. Peptide-Polymer Conjugate (collaborative project)

In addition, in collaboration with another NanoReMedi Doctoral Candidate, Nursu Erdogan (University of Pavia and CICNanoGune), we developed peptide-decorated modular small-diameter vascular grafts. Here, bioactive peptides with a Cysteine on the N-terminus were covalently conjugated to electrospun maleimide-functionalised poly(lactic-co-glycolic acid) (PLGA) scaffolds via Michael addition reaction. The resulting peptide-decorated scaffolds were designed to serve as the bioactive inner layer of multilayer small-diameter vascular grafts (SDVGs), combining the mechanical integrity of PLGA with the biological activity of peptides to improve endothelialisation and hemocompatibility.

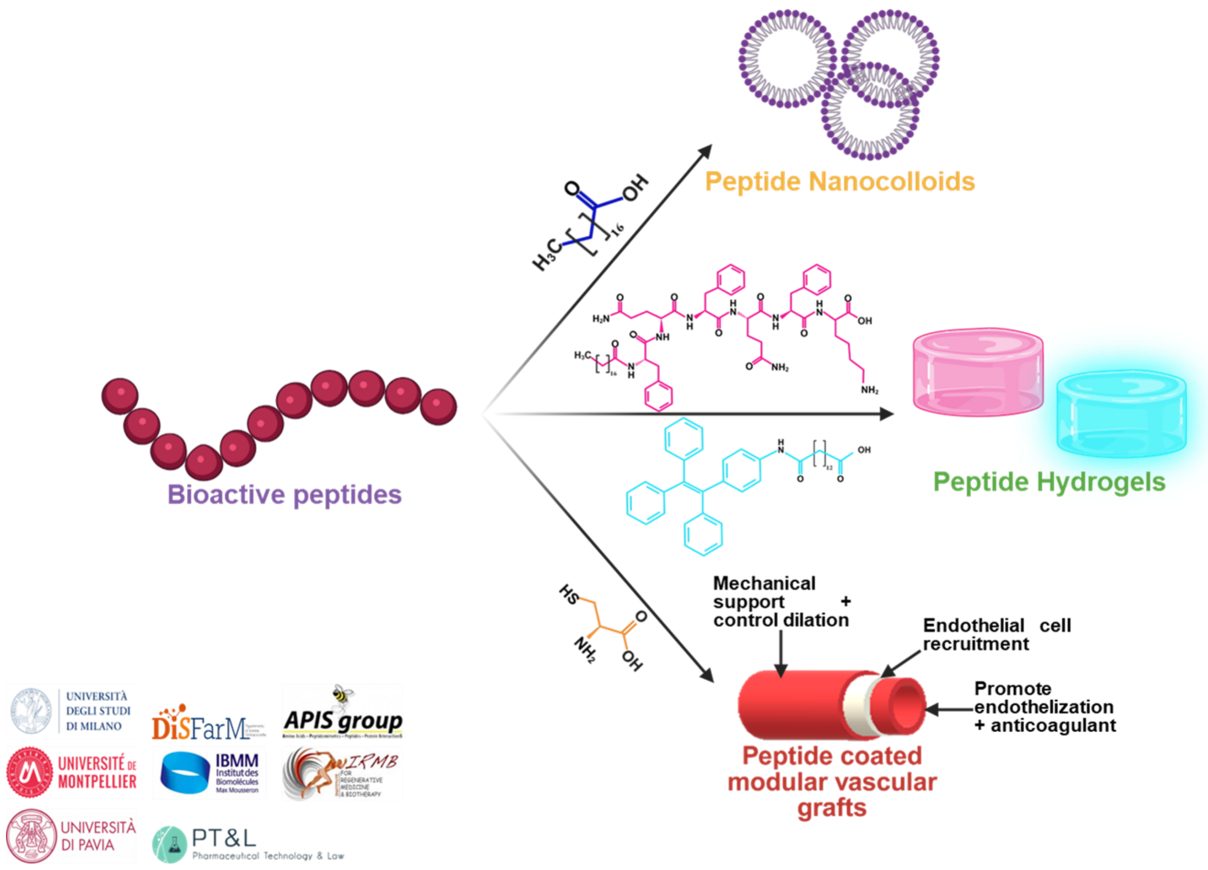

Figure 5 Aim of PhD

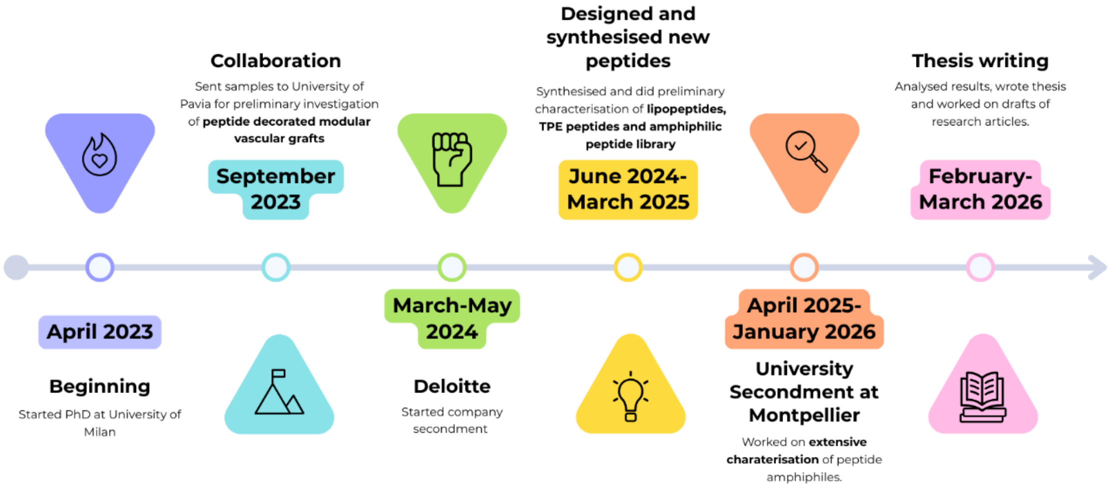

Collaboration
Sent samples to University of Pavia for preliminary investigation of **peptide decorated modular vascular grafts**
September 2023

Designed and synthesised new peptides
Synthesised and did preliminary characterisation of **lipopeptides, TPE peptides and amphiphilic peptide library**
June 2024-March 2025

Thesis writing
Analysed results, wrote thesis and worked on drafts of research articles.
February-March 2026

April 2023
Beginning
Started PhD at University of Milan

March-May 2024
Deloitte
Started company secondment

April 2025-January 2026
University Secondment at Montpellier
Worked on **extensive charaterisation** of peptide amphiphiles.

Figure 6 PhD timeline

2.3. Selection and Biological Rationale of Bioactive Peptides

Functional bioactive peptide motifs serve as minimal mimics of the extracellular matrix (ECM), providing the biochemical cues necessary to direct tissue regeneration. These short sequences bind specifically to integrins—transmembrane receptors that lack intrinsic enzymatic activity—triggering a conformational shift that promotes the recruitment of intracellular signalling complexes. This outside-in signalling cascade governs critical cellular functions, including adhesion, migration, proliferation, differentiation, and apoptosis (Figure 7). [51–53]

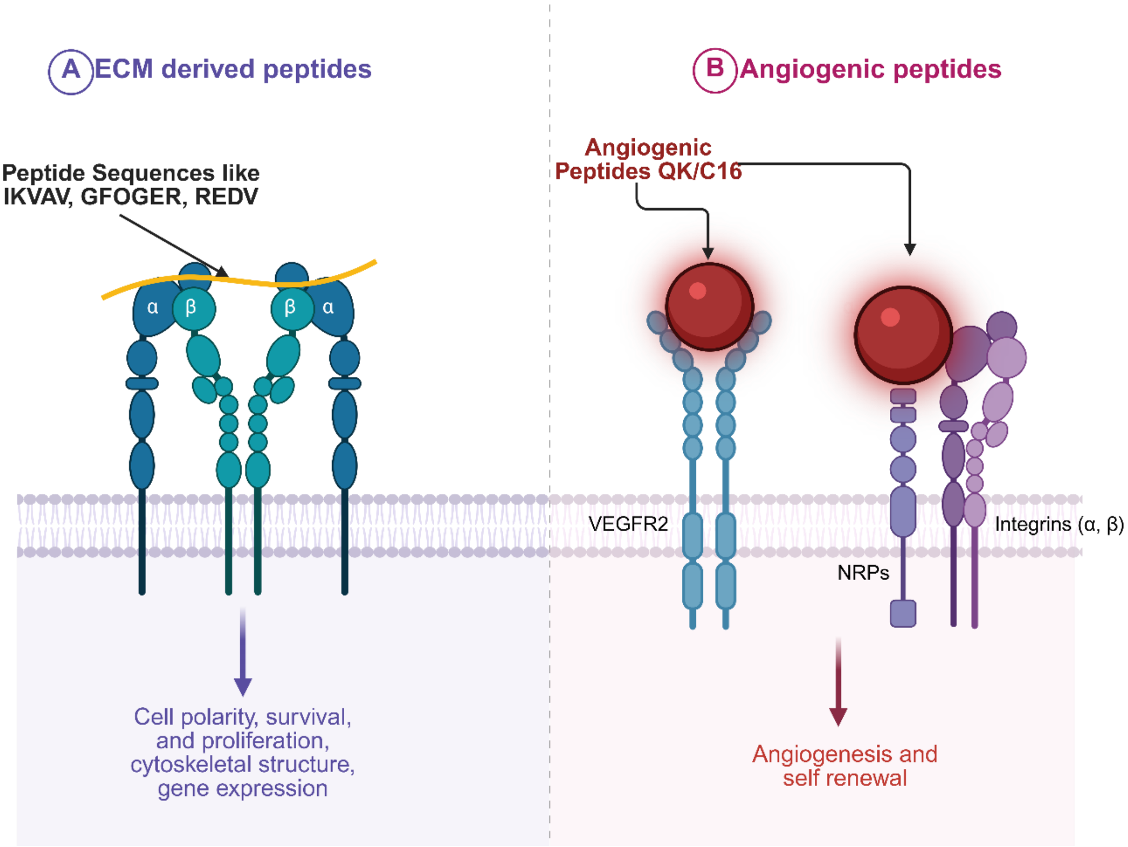

Figure 7 General mechanism of integrin-mediated signalling pathways of bioactive peptides mentioned in the thesis

As the main aim of this work was to obtain peptide-decorated nanomaterials for tissue regeneration within the NanoReMedi consortium framework, we selected peptide sequences able to promote cell adhesion, proliferation, differentiation, vascularisation and angiogenesis. In addition, an anticoagulant peptide was also synthesised (Table 1).

Table 1: List of bioactive peptides used during the course of the PhD

Peptide sequence	Source	Functions
IKVAV	Laminin	Encourage vascularisation and differentiation factors [54]
REDV	CS5 site of fibronectin	Promotes endothelial cell adhesion and proliferation [55]
GFOGER	Collagen I	Promotes cell adhesion, proliferation and differentiation [56]
(D-Phe) PRP	Fragment of Bivalirudin	Anticoagulant properties [57]
KLTWQELYQLKYKGI	17–25 α-helical region of VEGF	Vascular endothelial growth factor (VEGF) mimicking peptide [58]
KAFDITYVRLKF	γ1 chain of laminin-1	pro-angiogenic peptide C16 [59]

2.3.1. Cell adhesive peptides

Among the bioactive peptide sequences widely explored for their ability to regulate cellular behaviour, IKVAV, a laminin-derived peptide, stands out due to its strong bioactivity and broad integrin-binding profile. IKVAV primarily interacts with the β1 integrin subunit and can engage multiple integrin heterodimers, including α3β1, α4β1, and α6β1. This versatility enables IKVAV to influence a wide range of cellular processes such as adhesion, migration, proliferation, and differentiation. Integrin α3β1, one of the key receptors for IKVAV, is expressed in tissues such as the lung, kidney, skin, and stomach, and plays a crucial role in the development of several organs, including the brain, liver, and muscle. [60–63] Similarly, α6β1, another important IKVAV-binding integrin, is found in epithelial cells, platelets, leukocytes, and gametes, and is involved in nervous system development as well as reproductive processes such as follicle growth and luteal formation. [60,64,65] Through these interactions, IKVAV facilitates cell–matrix adhesion and modulates cell–cell communication, both of which are essential for tissue organisation and regeneration. Due to its ability to bind multiple integrin subtypes across diverse cell types, IKVAV has emerged as a highly promising functional motif in biomaterial design. [54,66] Incorporation of IKVAV into material surfaces enhances their bioactivity and promotes favourable cellular responses. For example, surface functionalisation of TiO_2 with IKVAV has been shown to significantly improve endothelial cell adhesion, proliferation, viability, and angiogenic potential. These effects highlight the strong potential of IKVAV-containing materials in tissue engineering and regenerative medicine applications, particularly where vascularisation and multi-tissue integration are critical. [67]

Another minimal bioactive sequence is REDV, derived from the CS5 site of the alternatively spliced type III connecting segment of fibronectin. [106] This peptide selectively binds to α4β1 integrin, which is expressed on the cytomembranes of endothelial cells (ECs), making it more specific than sequences such as IKVAV. This specificity makes REDV a promising ligand for EC adhesion, promoting rapid endothelialisation. [69–72] In regenerative medicine, REDV can be used as a complementary strategy to prevent thrombosis in vascular grafts, as rapid endothelialisation inhibits initial thrombus formation and facilitates improved long-term patency. [73,74]

2.3.2. Triple helical peptides

Another category of peptides widely studied includes triple helical peptides(THPs) or collagen-mimetic sequences. The most common of these sequences is GFOGER (where O represents hydroxyproline). GFOGER is a linear sequence derived from the α1(I) chain of collagen I. When presented in the correct three-dimensional conformation, it interacts with integrins α2β1 and α11β1. The addition of this peptide increases the mean cell surface area, which significantly improves the functional association of the cells with the scaffold, thereby enhancing cell proliferation. Integrin-THP binding is accompanied by filopodia/lamellipodia projection and actin polymerisation [11,12]. The GFOGER sequence has also been shown to self-assemble into nanofibres under specific pH conditions. This is due to the molecular interaction of the peptide sequence with the surrounding conditions. [75] In addition to enhancing cell adhesion and proliferation, GFOGER promotes mineral deposition in the tissue scaffold, serving as a late functional marker of osteoblastic differentiation. [76,77]

2.3.3. Anticoagulant sequence

The integration of anti-thrombotic agents is crucial for ensuring the long-term functionality of engineered cardiovascular tissues. While vascular grafts can be immobilised with biochemical cues to promote endothelialisation, [78,79] Preventing acute thrombosis at the graft-blood interface remains a major challenge. Bivalirudin, a short peptide sequence (fPRPGGGGNGDFEEIPEEYL, in one-letter code) derived from hirudin, has been used as an alternative to heparin to overcome limitations such as thrombocytopenia and osteopenia. [80–82] This peptide binds to both the active site and exosite of thrombin, thereby preventing the conversion of fibrinogen to fibrin and zymogen FXIII to transglutaminase FXIIIa. Bivalirudin has also been shown to inhibit thrombin-mediated platelet activation and adhesion. [83,84] In this thesis, the shorter bioactive fragment (D-Phe)PRP was employed as a model anticoagulant sequence. [57]

2.3.4. Angiogenic sequence

Angiogenesis is pivotal for cardiac regeneration, ensuring the crucial supply of nutrients and oxygen, facilitating a faster immune response, and aiding in the disposal of metabolic waste. [85]

This process is driven by the rapid migration and proliferation of ECs. While ECs proliferate rapidly during the embryonic stage, their proliferation is extremely low in adults, a process mediated by interactions between vascular growth factors and their cell-surface receptors. [86] To address this, Pal et al. developed injectable vasculogenic hydrogels by conjugating the pro-angiogenic peptide QK with a copolymer hydrogel of poly(N-isopropylacrylamide) and thiol-modified gelatine. QK, a 15-amino-acid peptide (KLTWQELYQLKYKGI), is a VEGF-mimicking sequence with better stability than the VEGF molecule itself and exhibits superior angiogenic bioactivity by binding to VEGF receptors (VEGFR-1 and -2). [87]

Another peptide C16 (KAFDITYVRLKF), derived from the γ1 chain of laminin-1, has been shown to promote angiogenesis and reduce blood vessel leakiness by binding to integrins αvβ3 and α5β1. αvβ3 integrin is expressed in the mesenchyme, blood vessels, smooth muscle cells, fibroblasts, and platelets, and plays an important role in angiogenesis, ECM regulation, vascular smooth muscle cell migration, osteoclast adhesion to bone matrix, and the regulation of inflammation. [88–90] However, its overexpression has been linked to various cancers, including bone metastasis, breast cancer, non-small cell lung cancer, cervical cancer, ovarian cancer, glioblastoma, melanoma, pancreatic cancer, prostate cancer, colon cancer, and lung cancer. [52] While α5β1 integrin promotes cell migration, invasion, proliferation, and ageing, and plays a critical role in bone formation, its upregulation can lead to a loss of bone-forming capacity in adipose-derived stromal/stem cells. [91–95] A cooperative effect between these two integrins supports focal adhesion maturation, which is vital for mechanosensing, cell migration, and cell-ECM adhesion. [96]

3. Lipopeptides

Role of Peptide Sequence on C18-Driven Self-Assembly

My contribution: Peptide Synthesis, characterisation, DLS, and ATR-FTIR.

All work was done at the University of Milan.

Dr Lucia Feni & Dr Stefania Crespi helped with Mass Spectroscopy & SEM analysis.

Lipidation—the covalent attachment of fatty acid chains to peptides or proteins—is a naturally occurring modification that governs critical biological processes, including membrane trafficking, protein synthesis, and cellular signalling. [7,97] This has inspired the development of synthetic lipopeptides as therapeutic molecules, where the lipid tail promotes self-assembly, enhances stability and *in vivo* half-life through carrier protein binding and delayed renal clearance. [98]

Designing effective scaffold materials using these molecules requires a clear understanding of how the peptide sequence modulates the hydrophobic driving force of the lipid tail and, consequently, dictates aggregate size, morphology, and secondary structure. These parameters directly impact biological interactions, biodistribution, and therapeutic efficacy. [99,100]

In this work, we investigated the effect of bioactive sequence length on the self-assembly of lipopeptides. Stearic acid was conjugated at the N-terminus of the six peptides with different lengths, hydrophilicity and bioactivity (Table 1). The C18 alkyl chain provides a significantly higher driving force for self-assembly—particularly for longer peptide sequences—ensuring sufficient hydrophobicity in the resulting lipopeptides. [101–103]

This study aims to advance understanding of how peptide sequence dictates self-assembly in lipopeptides and to identify a sequence suitable for future development as a self-assembling peptide hydrogel.

3.1. Results

3.1.1. Synthesis of Lipopeptides

All peptides were synthesised using microwave-assisted 9-Fluorenylmethoxycarbonyl/tert-Butyl (Fmoc/tBu) SPPS on Rink amide resin (100–200 mesh, 0.69 mmol/g) with Liberty Blue instrument (CEM). The microwave-assisted method employed rapid in situ coupling using N, N'-Diisopropylcarbodiimide/ Ethyl cyanoglyoxylate-2-oxime (DIC/Oxyma) for 2 minutes at 90 °C, eliminating the need for an additional base. Microwave heating accelerated both acylation and deprotection steps while mitigating aggregation commonly observed in self-assembling sequences. [104,105]

Following microwave-assisted chain assembly, stearic acid was manually coupled to the N-terminus of each peptide to generate fatty acid–peptide conjugates. After cleavage and purification, all final products were obtained in good yields and high purity, as confirmed by reversed-phase high-performance liquid chromatography (RP-HPLC) and mass spectrometry (MS).

Table 2: Library of lipopeptides

Code	Peptide sequence	Purity (%)	Mg obtained
DS02	Stearic acid-IKVAV-NH_2	92.7%	12.6 mg
DS04	Stearic acid-REDV-NH_2	94.6%	10 mg
DS08	Stearic acid-GFOGER-NH_2	98.9%	15.5 mg
DS10	Stearic acid-fPRP-NH_2	94.0%	29.8 mg
DS12	Stearic acid-KLTWQELYQLKYKGI-NH_2	92.9%	9 mg
DS14	Stearic acid-KAFDITYVRLKF-NH_2	93.8%	8.6 mg

3.1.2. Conformational analysis - FTIR

Solid-state Attenuated Total Reflection Fourier Transform Infrared spectroscopy (ATR_FTIR) was used to assess the secondary structure of the lipopeptides in the bulk state, avoiding interference from water vibrations in the amide I region. [106]

Deconvolution of the amide I band spectra (Figure 29) revealed that all peptides adopted a mixed conformation. DS02, DS14 and DS10 predominantly exhibited β-sheet character, with characteristic peaks at 1623.11 cm^{-1}, 1622.41 cm^{-1} and 1622.58 cm^{-1}, respectively. In contrast, DS04, DS08, and DS12 showed a major α-helical contribution (1660.42 cm^{-1}, 1660.99 cm^{-1} and 1653.99 cm^{-1}, respectively). The quantified secondary structure percentages are presented in Table 3.

Table 3: Percentages of secondary structure for each peptide at the solid state, calculated with OriginPro [107]

Code	β-sheet	β-turn	α-helix	Random
DS02	49.49%	31.27 %	-	-
DS04	13.11 %	4.02 %	82.87 %	
DS08	24.24 %	-	49.57 %	26.19 %
DS10	54.36 %	45.64 %	-	-
DS12	34.41 %	-	65.59 %	-
DS14	56.39 %	36.28 %	7.33	-

3.1.3. Self-assembly studies - DLS

Self-assembly behaviour of lipopeptides was assessed via nanoprecipitation, wherein lipopeptides were dissolved in a water-miscible organic solvent and rapidly injected into excess aqueous buffer (poor solvent). This creates a transient solvent gradient at the mixing interface, which modulates lipopeptide–solvent and lipopeptide-lipopeptide interactions, leading to kinetically trapped, non-equilibrium nanostructures – such as particles, fibres, or vesicles – whose morphology is dictated by the kinetic pathway of aggregation (Figure 8).

The hydrodynamic diameter (D_h) of the resulting nanoparticles was characterised by dynamic light scattering (DLS). In DLS spectroscopy, fluctuations in scattered light intensity arising from Brownian motion of nanoparticles are measured over time, and the autocorrelation function is fitted to extract the translational diffusion coefficient. This helps to understand how processing conditions steer the kinetically controlled self-assembly of lipopeptides.

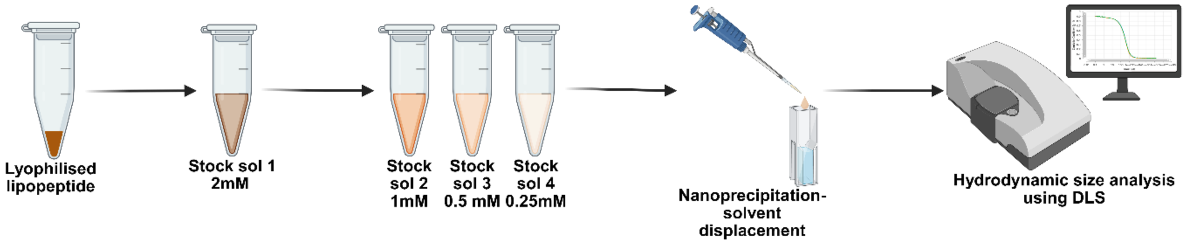

Figure 8 Workflow of DLS analysis

All lipopeptides formed nanoscale aggregates under both solvent conditions, though their size and uniformity varied significantly by sequence and environment. In water: Dimethyl sulfoxide (DMSO), DS12 and DS14 formed the smallest aggregates, while DS04 formed the largest. Most peptides exhibited bimodal distributions, except DS02 and DS08. In Phosphate-Buffered Saline (PBS):DMSO (physiological pH and ionic strength), DS02, DS08, DS10, and DS12 show massive aggregation (micron-scale), whereas DS04 remains remarkably stable, forming slightly smaller aggregates in PBS than in water. DS10 exhibits a highly polydisperse or potentially unstable system in PBS (polydispersity index/PDI ~1; indicative of a polydisperse suspension approaching precipitation rather than a stable colloidal dispersion). Overall, DS04 is the most physiologically compatible candidate, whereas DS12 and DS14 are optimal for low-ionic-strength applications.

Results for the 95:5 water: DMSO and PBS:DMSO ratios at 25 μM are summarised in Table 4.

Table 4:DLS of lipopeptide library at 95:5 solvent ratio(water:DMSO and PBS:DMSO) and 25 μM peptide concentration

Code	Peptide sequences	H_2O:DMSO (pH between 6 and 7)		PBS:DMSO (pH 7.4)	
		Size (nm)	PDI	Size (nm)	PDI
DS02	Stearic acid-IKVAV-NH_2	299±9.1	0.28±0.1	1558±52.7	0.61±0.2
DS04	Stearic acid-REDV-NH_2	589.6±69.3	0.56±0.2	492.1±44.1	0.66±0.1
DS08	Stearic acid-GFOGER-NH_2	379±15.3	0.5±0.02	1920±98.9	0.47±0.04
DS10	Stearic acid-fPRP-NH_2	246.5±81.4	0.34±0.1	Unstable/ Aggregated	1
DS12	Stearic acid-KLTWQELYQLKYKGI-NH_2	102.4±4.4	0.19±0.02	2862±546.4	0.72±0.1
DS14	Stearic acid-KAFDITYVRLKF-NH_2	122.3±13.0	0.39±0.1	1288±28.71	0.5±0.04

3.1.4. Scanning Electron Microscopy (SEM)

SEM imaging was performed to visualise the nanostructure of the lipopeptides (from section 3.1.3), which formed stable aggregates under in 95:5 water:DMSO solvent mixture at 25 µM concentration. The micrographs revealed diverse morphologies across the library, consistent with the varying secondary structures and aggregation behaviours observed by FTIR and DLS. DS08 and DS14 formed discrete, spherical aggregates. DS10 and DS12 exhibited elongated sphere-like to cuboidal aggregates. In contrast, DS02 and DS04 showed a mixed morphology, presenting both spherical aggregates and fibre-like structures.

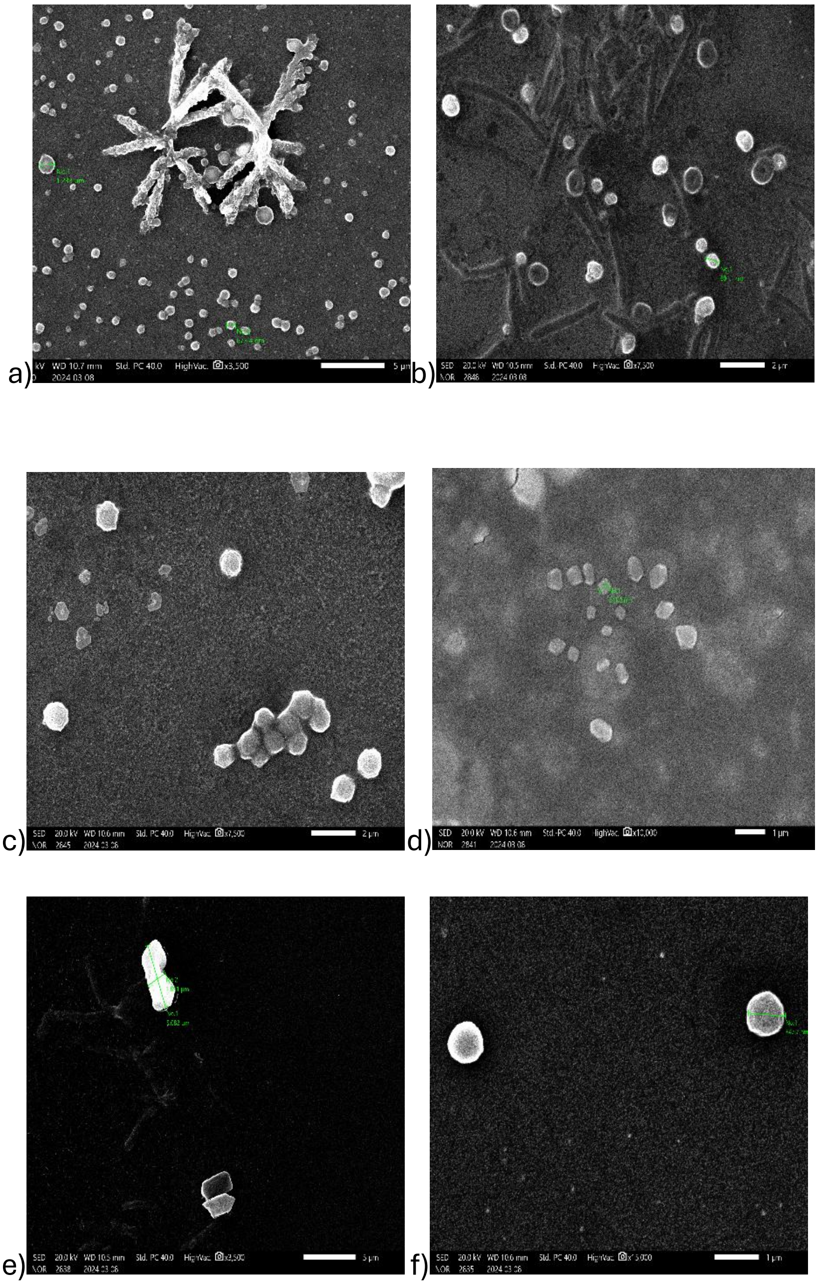

Figure 9 SEM Images of Lipopeptides a) DS02, b) DS04, c) DS08, d) DS10, e) DS12, and f) DS14

3.2. Discussion

The successful synthesis of the lipopeptides, confirmed by mass spectrometry and RP-HPLC with high purity (≥92.7%), enabled a detailed structure–function investigation focusing on how variations in the peptide headgroup sequence influence secondary structure, self-assembly, and resulting nanostructures.

A notable diversity in secondary structure was observed through ATR-FTIR analysis in the solid state, which appeared to correlate with the self-assembly behaviour measured by DLS. DS02 (IKVAV), DS10 (fPRP) and DS14 (KAFDITYVRLKF) exhibited predominantly β-sheet conformations (49.5%, 54.4% and 56.4%, respectively). Classically, β-sheet forming peptides are typically associated with nanofibre formation via intermolecular hydrogen bonding along the peptide backbone. However, SEM images of these lipopeptides in water:DMSO mixture indicated the formation of spherical aggregates. This apparent discrepancy highlights the dominant influence of the hydrophobic stearic acid tail, in combination with the peptide sequence, promotes curvature that favours spherical micelles or vesicular assemblies rather than extended fibrillar structures, overriding the intrinsic propensity of the peptide headgroup to minimise the hydrophobic surface area. [108]

Interestingly, in the case of DS02, some spherical nanoparticles were observed to aggregate and form tube-like structures. This suggests that while the primary assembly unit is spherical, the IKVAV headgroup retains sufficient β-sheet character to facilitate secondary aggregation, a precursor state to nanotube formation observed in related peptide amphiphile systems. [109] The DLS data for DS10 in PBS (PDI = 1.0; Size > 2 μm) further highlights the sensitivity of these β-sheet systems to ionic strength. This behaviour can be attributed to the specific amino acid arrangement within the sequence. The placement of D-phenylalanine (f) and arginine (R) adjacent to proline forces these residues into a rigid orientation. Combined with the charge-shielding effect of ions in PBS, this rigidity allows very little conformational freedom for the amino acids to reorient upon a change in solvent environment. In pure water, Coulombic repulsion between arginine side chains maintains small, positively charged aggregates in a dispersed state. [110,111] In PBS, however, the ions shield the arginine side chains, permitting the hydrophobic phenylalanine residues to associate and induce aggregation.

For lipopeptides DS04(REDV), DS08(GFOGER and DS12(KLTWQELYQLKYKGI) with α-helical conformations, a length-dependent trend in assembly behaviour was observed. While the α-helical conformation has a strong tendency to self-assemble into coil-coil structures or elongated assemblies, the fatty acid tail favours smaller, curved assemblies. The balance between these competing driving forces explains the morphological progression observed. Despite the highest α-helical content (82.9%), DS04 exhibited the largest hydrodynamic diameter in water (590 nm) and a high polydispersity, presented random fibril and spherical assemblies in SEM, suggesting that the hydrophobic tail dominates in shorter sequences. The system becomes kinetically trapped in a heterogeneous state where micelles and short, disordered fibrils coexist. Notably, DS04 was the only peptide to show improved colloidal stability in PBS (size reduction to 492 nm). This suggests that the high charge density of the arginine residue in REDV effectively stabilises the nanoparticles against salt-induced aggregation, making DS04 the most promising candidate for physiological applications from a formulation standpoint. [112]

As the peptide sequence lengthens (GFOGER: 6 residues; KLTWQELYQLKYKGI: 15 residues), the morphological transition toward elongated assemblies becomes evident. SEM revealed a shift from spheres (DS08) to cuboidal/elongated spheres (DS12). The DLS data corroborates this trend: DS12 formed the smallest and most monodisperse aggregates in pure water (102.4 nm, PDI 0.19). This suggests that the longer peptide sequence of DS12 provides sufficient amphiphilic balance and intermolecular cohesive energy to stabilise a well-defined, thermodynamically favoured nanostructure. However, the massive aggregation observed for DS08 and DS12 upon transfer to PBS (sizes >1.9 μm) indicates that the longer sequences, despite their ordered structure in water, lack sufficient electrostatic or steric repulsion to prevent flocculation in high ionic strength environments. [113,114]

4. Peptide hydrogels

Role of N-Terminal Domains on GFOGER Self-Assembly

My contribution: All the experiments were carried out by me.

Work done at the University of Milan: Peptide Synthesis, Purification, DLS, ATR-FTIR

Work Done at the University of Montpellier:

i. F9 group & SynBio: Peptide Purification, CD, UV-Visible & Fluorescence spectroscopy

ii. C5 group: Rheology

iii. Cartigen & IRMB: Cell Biology, 3D Printing & SEM

Scaffold materials, bioactive molecules and cells work together to create a suitable environment for tissue repair in regenerative medicine. Among the various scaffold materials, hydrogels have emerged as a promising material due to their unique structural and functional similarities to natural extracellular matrix (ECM). ECM is a dynamic tissue microenvironment with a complex structure and exists in a symbiotic relationship with cells: it supports cells, facilitates their growth, supplies nutrients, and disposes of waste, while cells, in turn, produce ECM components within their organelles. Due to their diverse functionalities, there is a growing demand for ECM-like or ECM-mimicking hydrogels for tissue engineering applications. [115–117]

Although hydrogels derived from natural and synthetic polymers offer tunable viscoelastic properties, they often lack essential biochemical cues and are unable to achieve the functional complexity required to direct complex cellular behaviours. A promising strategy involves the use of functional peptides, which can serve both as bioactive signals and structural scaffolds. [118,119]

Self-assembling peptide amphiphiles are one such class of functional biomaterials. These molecules consist of a bioactive peptide headgroup conjugated to a hydrophobic tail that drives self-assembly in aqueous environments, enabling the formation of controlled nanostructures with the hydrophilic bioactive peptide displayed on their surface. This self-assembly process can be modulated by environmental stimuli such as pH, ionic strength, temperature, and concentration. [120–123]

In this study, we focused on the collagen-mimetic peptide GFOGER, a short sequence derived from type I collagen [124,125] with a high affinity for the α2β1 integrin. This integrin is abundantly expressed on osteoblasts and mesenchymal stem cells (MSCs) and plays a crucial role in promoting osteogenic differentiation and supporting bone regeneration. [56] In addition, GFOGER peptide also has been reported to enhance mineralisation. [126]

We also investigated GFPGER, a similar sequence encoded by the *scl* gene of A. S*treptococcus*. Since bacterial cells cannot perform post-translational proline hydroxylation, GFPGER contains proline in place of hydroxyproline. [127–130] By comparing hydrogels functionalised with GFOGER and GFPGER, we aimed to investigate whether the proposed peptide amphiphile design can compensate for the difference in the ligand affinity between the two sequences within a 3D microenvironment.

Both these collagen mimic sequences were investigated using three different peptide amphiphile designs (Figure 10):

1. **Conjugation to amphipathic hexapeptide FQFQFK** - This sequence exhibits an amyloid-like design and self-assembles into β-sheet structures, forming nanofibres that entangle into hydrogels in phosphate-buffered saline (PBS) at pH 7.4. [28,30,131]
2. **Conjugation to FQFQFK and lipidation with Stearic acid** - Addition of stearic acid to FQFQFK conjugate increases the hydrophobicity of the resulting lipopeptide, providing a significantly higher driving force for self-assembly and enhancing *in vivo* stability. [101–103]
3. **Conjugation to an AIE moiety(TPE) via a fatty acid spacer** - An amino-TPE derivative was added to the N-terminus of peptide via a fatty acid spacer. The spacer ensured that the bioactive segment of the peptide remained accessible for receptor binding, avoiding steric hindrance from the bulky TPE group. [132] The AIE -functionalisation offers additional advantage of real-time monitoring of cell–peptide interactions without additional dyes.

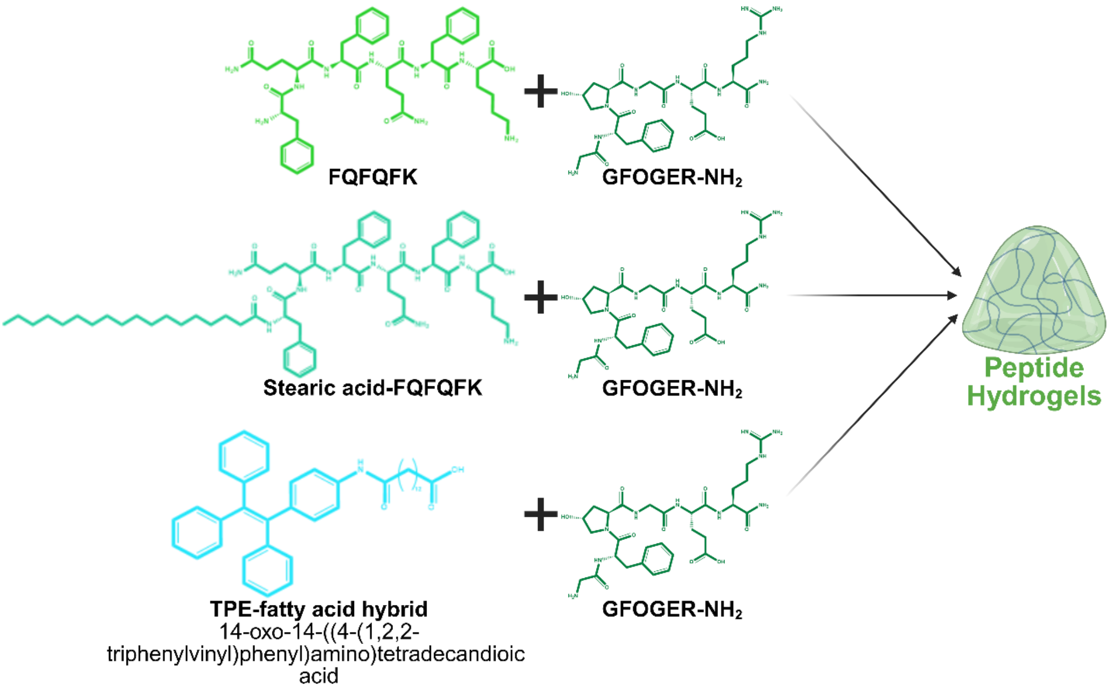

Figure 10 Peptide amphiphile designs (focused on in this work)

4.1. Results

4.1.1. Synthesis of Peptide Amphiphiles

We designed and synthesised six peptide amphiphiles based on the collagen-mimetic sequence GFOGER (where O = hydroxyproline) and its non-hydroxylated analogue GFPGER. All peptides were successfully synthesised on a 0.05 mmol scale via microwave-assisted Fmoc/tBu SPPS and purified by RP-HPLC. The TPE-fatty acid hybrid was synthesised and characterised according to previously established protocols in our laboratory (7.3.1). [46,133] Purity was assessed by analytical RP-HPLC, confirming >94% purity for all six conjugates, with isolated yields ranging from 20.4 mg to 83 mg, which was sufficient for subsequent characterisation (Table 5).

Table 5: GFOGER peptide conjugate library

Code	Peptide sequence	Purity (%)	Quantity obtained (mg)
DS33	FQFQFKGFPGER-NH_2	95.90%	20.4 mg
DS34	Stearic acid-FQFQFKGFPGER-NH_2	97.30%	83 mg
DS35	FQFQFKGFOGER-NH_2	95.20%	34.8 mg
DS36	Stearic acid-FQFQFKGFOGER-NH_2	98.50%	64.4 mg
TPE 08	TPE acid-GFOGER-NH_2	95%	49mg
TPE 38	TPE acid-GFPGER-NH_2	94%	50mg

4.1.2. Conformational Analysis - ATR-FTIR

Deconvoluted FTIR spectra for all lipopeptides are provided in the Experimental Data (Figure 29), with calculated secondary structure percentages summarised in (Table 6). [134,135]

The lipopeptides DS34 and DS36 majorly adopted β-sheet conformation (1625 cm^{-1} and 1623.09 cm^{-1}, respectively). The non-lipidated peptide DS33 exhibited predominantly β-turn conformation (1663.34 cm^{-1}), while DS35 showed an unordered conformation (1649.35 cm^{-1}). For the TPE conjugates, TPE 08 was predominantly β-turn (sum of peaks at 1674.51 cm^{-1} and 1666.15 cm^{-1}), whereas TPE 38 showed mainly α-helix (1661.37cm^{-1}). These results reflect the intrinsic conformation of the peptides in the absence of external stimuli.

Table 6: Percentages of secondary structure for each peptide at the solid state, calculated with OriginPro[107]

Code	β-sheet	β-turn	α-helix	Random
DS33	39.33%	60.67%	-	-
DS34	55.07%	27.16%	17.77%	-
DS35	13.38%	-	-	86.62%
DS36	50.72%	39.26%	10.02%	-
TPE 08	42.76%	57.24%	-	-
TPE 38	41.63%	-	58.37%	-

The peptides were synthesised according to the established PA design principles that favour a well-defined secondary structure that can form a hydrogel, such as β-sheet. This was observed in the case of lipopeptides DS34 and DS36. Other sequences showed other conformations: DS33 and TPE 08 exhibited β-turns, while TPE 38 adopted an α-helical confirmation alongside minor β-sheet contributions. The most unexpected result was seen with DS35, which adopted 86.6% random conformation and only about 13.4% β-sheet-a striking deviation from the intended design.

Notably, these FTIR measurements were performed on lyophilised solids. It is anticipated that under physiologically relevant conditions, these peptides may undergo conformational reorganisation into β-sheet or β-turn structures capable of supporting hydrogel formation.

4.1.3. Self-Assembly Studies -DLS

The self-assembly behaviour of the peptide amphiphiles was evaluated via nanoprecipitation (solvent displacement) in a 9:1 water:DMSO and PBS:DMSO mixture (similar work flow as mentioned in section 3.1.3). The comparative results are summarised in Table 7.

In the water:DMSO environment, all peptides exhibited strong scattering intensity. The FQFQFK-containing peptides (DS33–DS36) all formed large aggregates in water:DMSO, with mean diameters ranging from approximately 1800 nm to 3100 nm. The non-lipidated peptide DS35 (FQFQFKGFOGER) exhibited the highest polydispersity (PDI 0.85) among the FQFQFK series. Lipidation of the hexapeptide scaffold (DS34 and DS36) resulted in slightly more uniform size distributions. The AIE conjugate TPE08 (GFOGER) exhibited excellent colloidal uniformity in water:DMSO, with a low polydispersity index (PDI = 0.17 ± 0.02) and a mean diameter of 212 nm, indicating formation of a monodisperse, kinetically stable aggregate population. In contrast, its non-hydroxylated analogue TPE38 (GFPGER) formed aggregates over ten times larger (2826 nm) with high polydispersity (PDI 0.69).

Upon transfer to PBS:DMSO (9:1), a striking divergence in colloidal stability was observed. Among the FQFQFK-based peptides, the non-lipidated peptides DS33 and DS35 exhibited a marked decrease in hydrodynamic size upon transfer to PBS. DS33 reduced from ~3094 nm to ~721 nm, while DS35 decreased from ~1805 nm to ~1267 nm. In contrast, the lipidated peptides DS34 and DS36 maintained their large, micron-scale aggregates in PBS (sizes remaining >2500 nm). DS34 exhibited the greatest colloidal resilience, with its size and PDI remaining virtually unchanged between water (2818 nm, PDI 0.46) and PBS (2594 nm, PDI 0.33). The AIE conjugates TPE08 and TPE38 both underwent significant aggregation in PBS. TPE 08 aggregated into large structures (2551 nm, PDI 0.38), while TPE 38 maintained a similar size (~2579 nm) but with a reduced PDI (0.51).

All peptides were designed to favour formation of fibre-like aggregates. Large, polydisperse micron-sized aggregates detected by DLS are consistent with the presence of nanofibers- either as discrete bundles or entangled networks- which typically yield micron-scale hydrodynamic measurements under these measurement conditions. In PBS, a change in aggregate size and distribution was anticipated, given that these sequences undergo hydrogelation exclusively in PBS and not in deionised water. This behaviour suggests that phosphate ions participate in the self-assembly process, likely through charge screening or specific ion–peptide interactions that promote structural reorganisation.

Table 7: DLS and pH of GFOGER peptide library

Code	**Solvent (Water:DMSO 9:1)**			**Solvent (PBS:DMSO 9:1)**	
	pH	**Size (nm)**	**PDI**	**Size (nm)**	**PDI**
DS33	6.48	3094±458.6	0.44±0.07	721.3±45.5	0.34±0.17
DS34	6.45	2818±368.1	0.46±0.14	2594±179.1	0.33±0.08
DS35	6.36	1805±158.9	0.85±0.09	1267±202.7	0.89±0.09
DS36	6.48	2942±261.9	0.43±0.05	2529±472.3	0.75±0.22
TPE 08	7.63	212.1±13.64	0.17±0.02	2551±10.6	0.38±0.07
TPE 38	7.21	2826±104	0.69±0.19	2579±173.3	0.51±0.16

4.1.4. Hydrogel Evaluation

Hydrogels were prepared by adding phosphate-buffered saline (PBS, pH 7.4) to lyophilised peptide powder, followed by alternating sonication and vortexing for 3 min at room temperature. This procedure induced rapid hydrogelation.

The minimum gelation concentration (MGC) – the lowest concentration (w/v%) yielding a self-supporting gel by vial inversion—was determined for each peptide (Table 8). Non-lipidated peptides DS33 and DS35 formed gels at 10% but not at 5%; subsequent testing at 6% confirmed gelation, establishing an MGC of 6%. The AIE conjugates TPE08 and TPE38 required 5% for gelation, failing to gel at 4%. Among the lipidated peptides, DS34 gelled at 4% but not at 3% (MGC = 4%), whereas DS36 gelled at all concentrations down to 2% (MGC = 2%).

The MGC values revealed a clear hierarchy of gelation efficiency: DS36 (2%) > DS34 (4%) > TPE08 = TPE38 (5%) > DS33 = DS35 (6%).

Table 8:Minimum Gelation Concentration (MGC) of Peptide Hydrogels

Peptide code and sequence	Minimum Gelation conc. (w/v %)	Hydrogel
DS33 FQFQFKGFPGER-NH_2	6%	
DS34 Stearic acid-FQFQFKGFPGER-NH_2	4%	
DS35 FQFQFKGFOGER-NH_2	6%	
DS36 Stearic acid-FQFQFKGFOGER-NH_2	2%	
TPE08 TPE acid-GFOGER-NH_2	5%	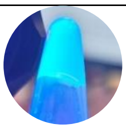
TPE38 TPE acid-GFPGER-NH_2	5%	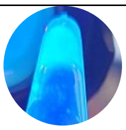

The lowest MGC observed for DS36 is attributed to the strong hydrophobic driving force conferred by the stearic acid tail, which promotes hydrophobic collapse and dense nucleation even at low concentrations. The additional hydroxyl group in the GFOGER sequence may also contribute to holding the structure more tightly, thereby reducing the concentration of peptide required. In contrast, the non-lipidated peptides DS33 and DS35 rely on weaker π–π stacking and triple-helical interactions, necessitating higher concentrations for network formation.

The AIE-functionalised peptides form hydrogels via π–π stacking of the TPE moiety, which simultaneously restricts intramolecular motion and leads to fluorescence emission. At 5% w/v, both hydrogels exhibited bluish emission (Figure 11), with the GFOGER-containing TPE08 displaying approximately 25% higher emission intensity than the GFPGER analogue TPE38. This difference correlates directly with assembly efficiency—tighter packing enhances RIM and intensifies fluorescence rather than causing quenching—and indicates that the hydroxyproline residue in GFOGER likely strengthens intermolecular hydrogen bonding, promoting more compact packing compared to the proline-containing GFPGER sequence.

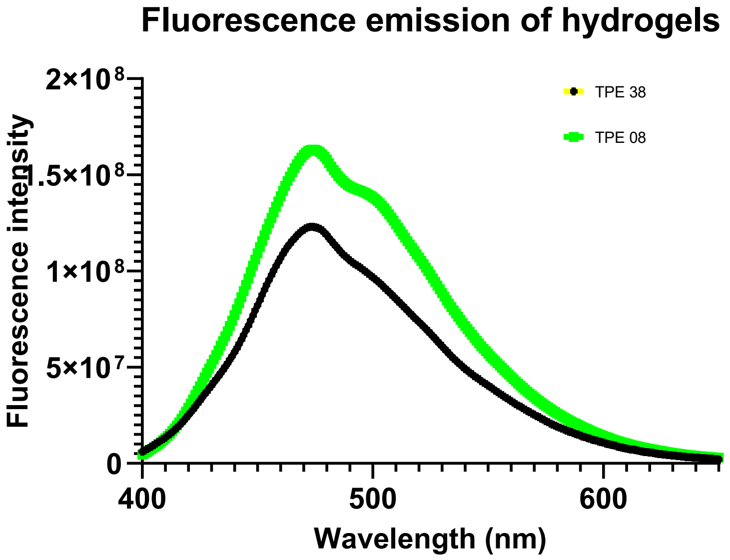

Figure 11 Fluorescence Emission Spectra of 5% AIE hydrogels

4.1.4.1. Rheology

Rheological measurements were performed on all hydrogels at 37 °C and a standardised concentration of 6% w/v to enable direct comparison. Frequency sweeps (1% strain), amplitude sweeps (1 Hz), time sweeps, flow sweeps, and thixotropy tests are presented in Figure 12.

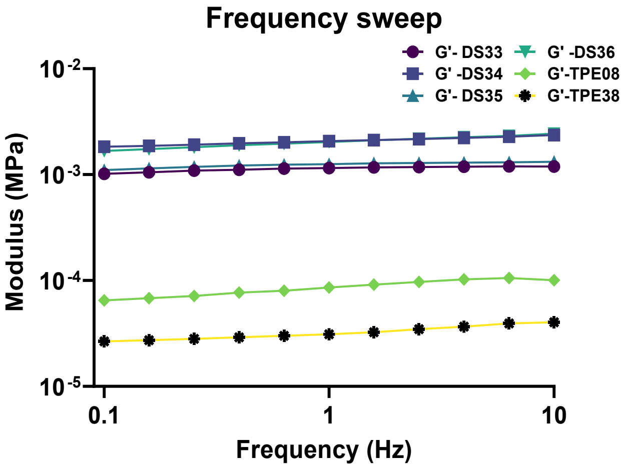

a)

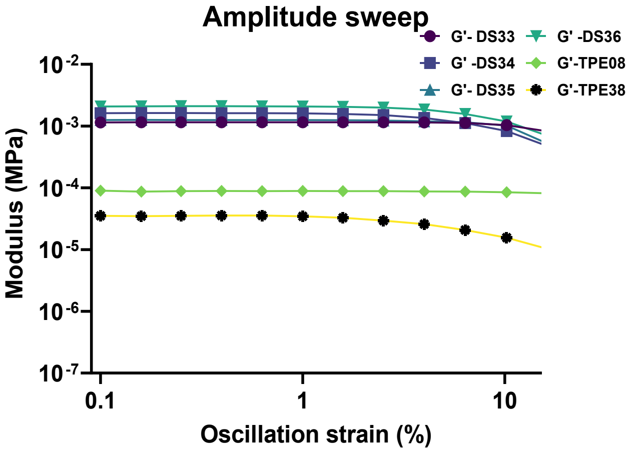

b)

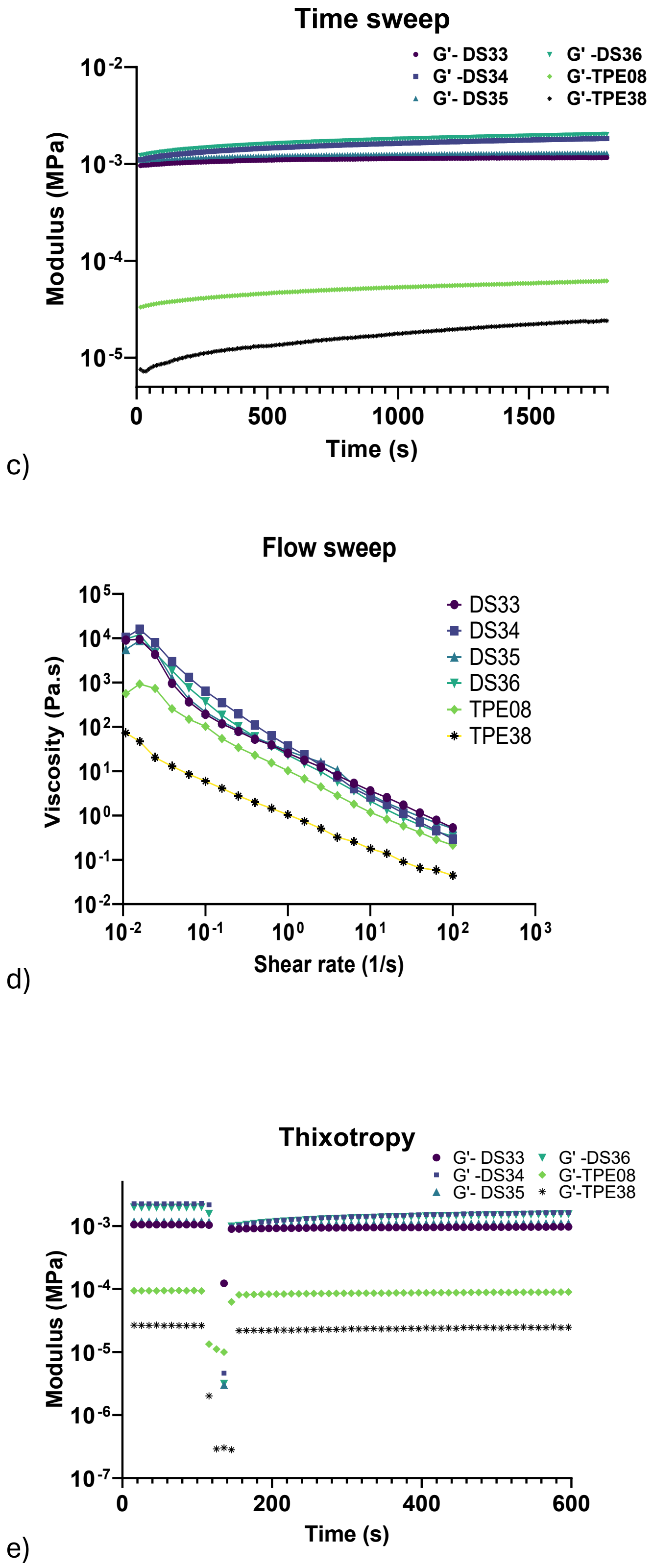

Figure 12 Rheology of all six hydrogels at the same w/v concentration of 6% (a-e) a) frequency sweep at 1% strain, b) amplitude sweep at 1Hz frequency, c) time sweep at 1% strain and 1Hz frequency, d) flow sweep and e) thixotropy

At 6% w/v, the lipidated peptides exhibited substantially higher storage moduli (G') than their non-lipidated and AIE-functionalised counterparts, consistent with the expectation that the stearic acid tail provides a dominant hydrophobic driving force for network assembly. The lipopeptide DS36 displayed the highest G' (2.09 kPa), followed by DS34 (1.60 kPa), while the non-lipidated peptides DS35 and DS33 yielded intermediate moduli of 1.24 kPa and 1.14 kPa, respectively. The AIE-functionalised peptides TPE08 and TPE38 produced the weakest gels, with G' values of 0.09 kPa and 0.04 kPa, respectively. The G' values obtained for the lipidated peptides (~1–2 kPa) fall within the lower range of reported elastic moduli for native soft tissues—such as brain (0.1–1 kPa) and adipose tissue (~2 kPa)—and are comparable to other short peptide-based hydrogels in the literature (e.g., Fmoc-FF, ~1.7 - 5.7 kPa depending on pH).[136]

Although the lipidated peptides DS34 and DS36 exhibit favourable stiffness, their limited thixotropic recovery following high-strain deformation may compromise their performance in 3D printing applications. In contrast, DS33, DS35, TPE08, and TPE38 demonstrated near-complete recovery of G'. Blending the lipidated peptides with one of these more recoverable sequences, or with a secondary biopolymer such as xanthan gum, represents a potential strategy to improve post-extrusion recovery—a hypothesis that warrants further investigation.

The very low viscoelastic moduli of AIE gels TPE 08 and TPE 38 make them unsuitable for load-bearing applications. However, their weak gel nature, shear-thinning behaviour and intrinsic fluorescence can be leveraged in a composite approach, by using them as a real-time activity monitor to visualise the gel properties without compromising their mechanical properties.[137–139]

4.1.4.2. Circular Dichroism (CD) experiments

CD spectroscopy was performed on the peptides under two sets of experimental conditions: (i) diluting the peptide hydrogels to obtain varying concentrations in aqueous solution (0.05, 0.1, and 0.2 mM), and (ii) varying solvent composition (water/methanol mixtures) at a fixed peptide concentration of 0.25 mM.

4.1.4.2.1. Concentration-Dependent Studies of Diluted Hydrogel

The lipopeptides DS34 and DS36 displayed robust β-sheet signatures across all concentrations examined, with a characteristic positive band near 195–198 nm and a negative band centered around 215–218 nm (Figure 13: a-c). This signature persisted even at the lowest concentration tested, confirming that the stearic acid provides sufficient hydrophobic driving force to nucleate β-sheet assembly spontaneously, without requiring high peptide density. In contrast, the non-lipidated analogues DS33 and DS35 exhibited spectra more consistent with a β-turn conformation, suggesting that without the strong driving force and stabilising effect of the lipid tail, the peptides cannot transition further to β-sheet. [140,141] At low concentration (0.05 mM), DS35 showed a small maximum at 204 nm; this spectral shift may reflect a concentration-dependent structural transition, with the peptide likely existing as a disordered monomer below this threshold. [142]

The AIE peptide TPE 08 exhibited a non-canonical CD spectrum with a positive maximum near 200 nm, minima at ~210 and 225 nm, and additional TPE-derived bands at ~260 and 300 nm. This pattern suggests a mixed origin: partial α-helical backbone combined with exciton coupling between closely packed TPE chromophores in the aggregate. TPE 38 showed qualitatively similar but significantly weaker signals under equivalent conditions, indicating reduced chiral order or lower assembly efficiency. This difference underscores the influence of the peptide sequence—specifically the presence of hydroxyproline in GFOGER—on the extent of chromophore coupling and supramolecular packing, corroborating the higher emission intensity observed for TPE08 relative to TPE38 (section 4.1.4.).

4.1.4.2.2. Solvent-Dependent Studies: Effect of Water/Methanol composition

To further probe the contributions of hydrophobic driving forces and backbone hydrogen bonding, CD spectra were recorded at 0.25 mM across a series of water/MeOH mixtures ranging from 95:5 to 0:100 (v/v)(Figure 13: d-f). Increasing MeOH content produced a monotonic increase in spectral signal amplitudes and improved resolution of spectral features for all compounds. This behaviour is consistent with two concurrent effects: (i) reduction of competitive water–backbone hydrogen bonding, which promotes intramolecular and intermolecular hydrogen bond formation; and (ii) attenuation of light scattering from large aqueous aggregates, which can artificially suppress or distort CD signals. Data obtained in 100% MeOH therefore represents the maximum achievable structural order for each compound under these conditions, although such non-aqueous structures may not fully recapitulate the physiologically relevant hydrogel state. DS35 showed the strongest solvent-dependent transition: weak/featureless spectra in water-rich conditions, progressive β-turn emergence at 1:1 MeOH, and a well-defined profile in 100% MeOH. This is due to the high dependence of the peptide sequence solely on the H-bonding of the backbone structure for the self-assembly, making the peptides DS33 and DS35 more sensitive to solvent conditions. The requirement for a critical peptide density to achieve stable networks—evidenced by their higher MGC values—is consistent with this hydrogen-bond-driven assembly mechanism. In contrast, DS36 exhibited the largest amplitude increase in 100% MeOH, while DS34 displayed modest variation across solvent conditions. The strong hydrophobic driving force conferred by the stearic acid tail in these lipidated peptides promotes the formation of a stable, solvent-excluded hydrophobic core, rendering the assembly largely insensitive to changes in solvent polarity and peptide concentration. This insensitivity aligns with the low MGC and robust β-sheet signatures observed for DS36 and DS34.

For TPE peptides, 1:1 MeOH induced a broad ~220–225 nm minimum with a positive ~260 nm feature, while in 100% MeOH, both TPE compounds showed complex multi-band spectra (195–215 nm). This is because the aromatic rings of the TPE dictate the chiroptical assembly of the peptides, which is solvent sensitive, making this design more amphiphilic than the non-lipidated peptides DS33 and DS35 but having a weaker cooperative driving force than the hydrophobic collapse of the lipopeptide DS34 and DS36. This explains why the MGC of the TPE peptides was between the lipidated and non-lipidated peptide sequences.

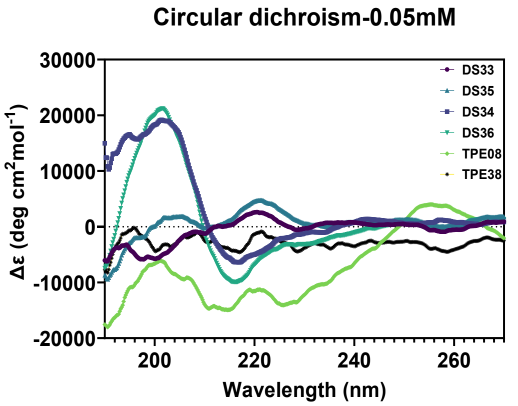

a)

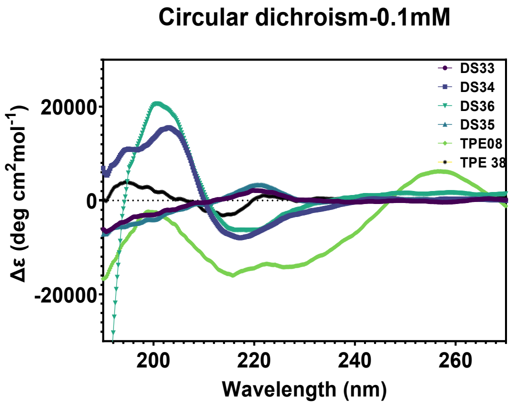

b)

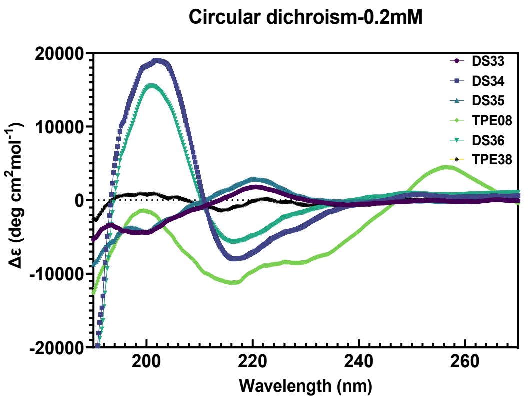

c)

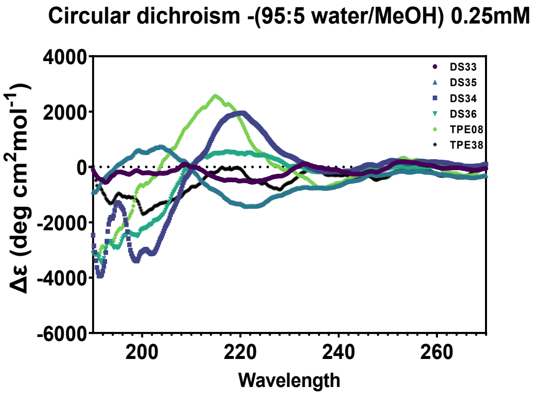

d)

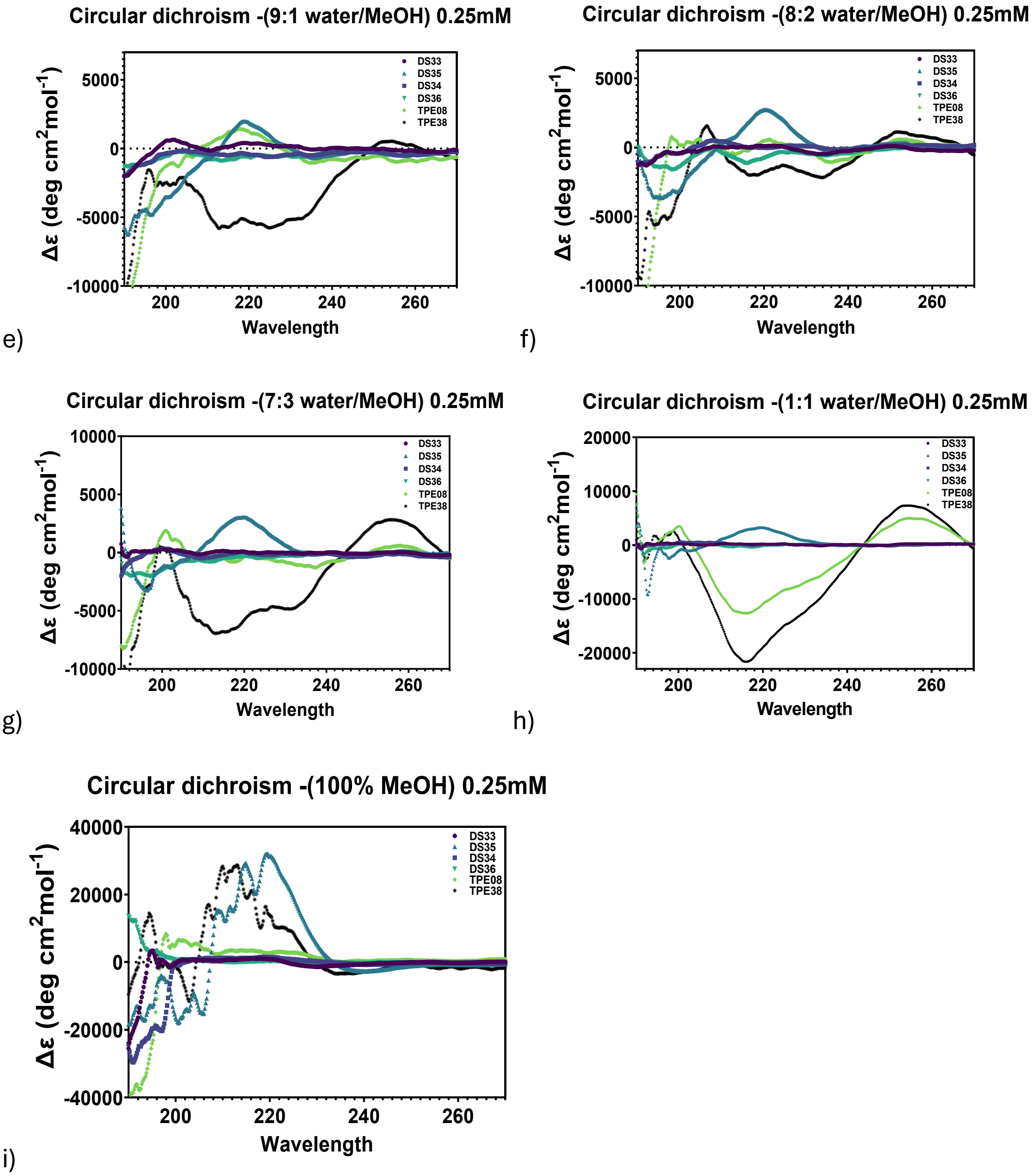
Circular dichroism -(9:1 water/MeOH) 0.25mM

Circular dichroism -(8:2 water/MeOH) 0.25mM

Circular dichroism -(7:3 water/MeOH) 0.25mM

Circular dichroism -(1:1 water/MeOH) 0.25mM

Circular dichroism -(100% MeOH) 0.25mM

Figure 13 Circular dichroism of peptide hydrogels at (a-c) different concentrations: a) 0.05 mM, b) 0.1 mM, c) 0.2 mM and different solvent ratios (d-f) CD of TPE peptides in d)95:5 water:MeOH, e)9:1 water:MeOH, f)8:2 water:MeOH, g)7:3 water:MeOH, h)1:1 water:MeO

4.1.4.3. Scanning Electron Microscopy (SEM)

In SEM images (Figure 14) the observed pore sizes appeared sufficiently large (>10 µm) to support cell encapsulation and nutrient diffusion. In contrast, DS35 and TPE 08 exhibited noticeably smaller pore dimensions in the dried state. However, it is important to note that lyophilisation can induce significant shrinkage and collapse of the hydrogel network; therefore, the pore sizes observed by SEM may not accurately represent the architecture of the fully hydrated hydrogels.

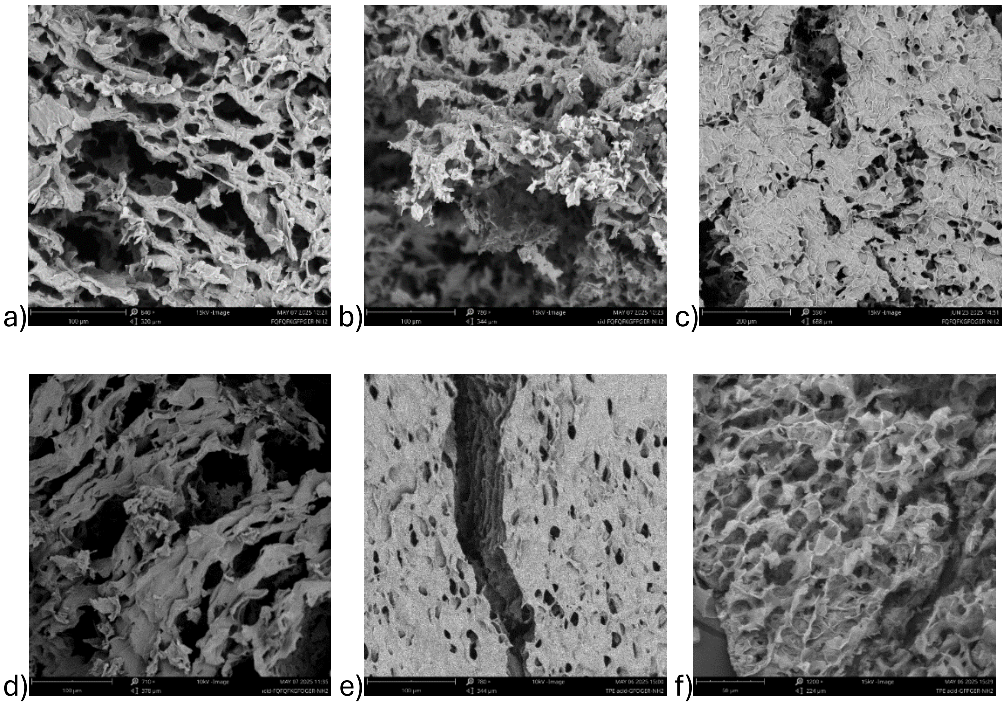

Figure 14 SEM Images of Xerogels Derived from Peptide Hydrogels a)DS33, b)DS34, c)DS35, d)DS36, e)TPE08 and f)TPE38

4.1.5. Biological evaluations

4.1.5.1. LDH Cytotoxicity

The mouse mesenchymal stromal cell line ($C_3H_{10}T_{1/2}$) was cultured in indirect contact with the hydrogels (concentrations mentioned in Table 8) via transwell inserts (Figure 15). All hydrogels exhibited very low to negligible cytotoxicity and maintained high cell viability.[143]

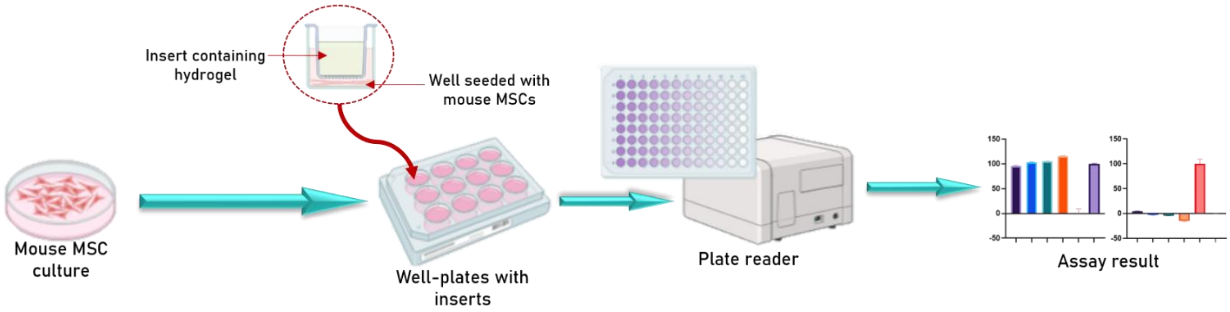

Figure 15 Transwell setup used for the LDH assay

Live/dead staining revealed a high viability across all conditions. Morphological analysis revealed subtle design-dependent differences. Cells exposed to the non-lipidated GFOGER conjugate (DS35) displayed pronounced elongation and alignment, consistent with α2β1 integrin-mediated cytoskeletal organisation induced by the collagen-mimetic motif. [144] The corresponding GFPGER analogue (DS33) exhibited less alignment, supporting the functional importance of hydroxyproline for integrin engagement. Lipopeptides (DS34, DS36) maintained well-spread morphologies and high viability, confirming that stearic acid conjugation does not compromise cytocompatibility; the modestly reduced cell density observed for DS36 relative to DS35 likely reflects altered nutrient diffusion rather than cytotoxicity. AIE-functionalised peptides (TPE08, TPE38) also supported healthy cell spreading with negligible red signal, establishing that the tetraphenylethylene luminogen is non-cytotoxic. The rounder morphology noted for TPE38 may be attributed to its lower storage modulus, consistent with known stiffness-dependent MSC spreading behaviour. [56,145]

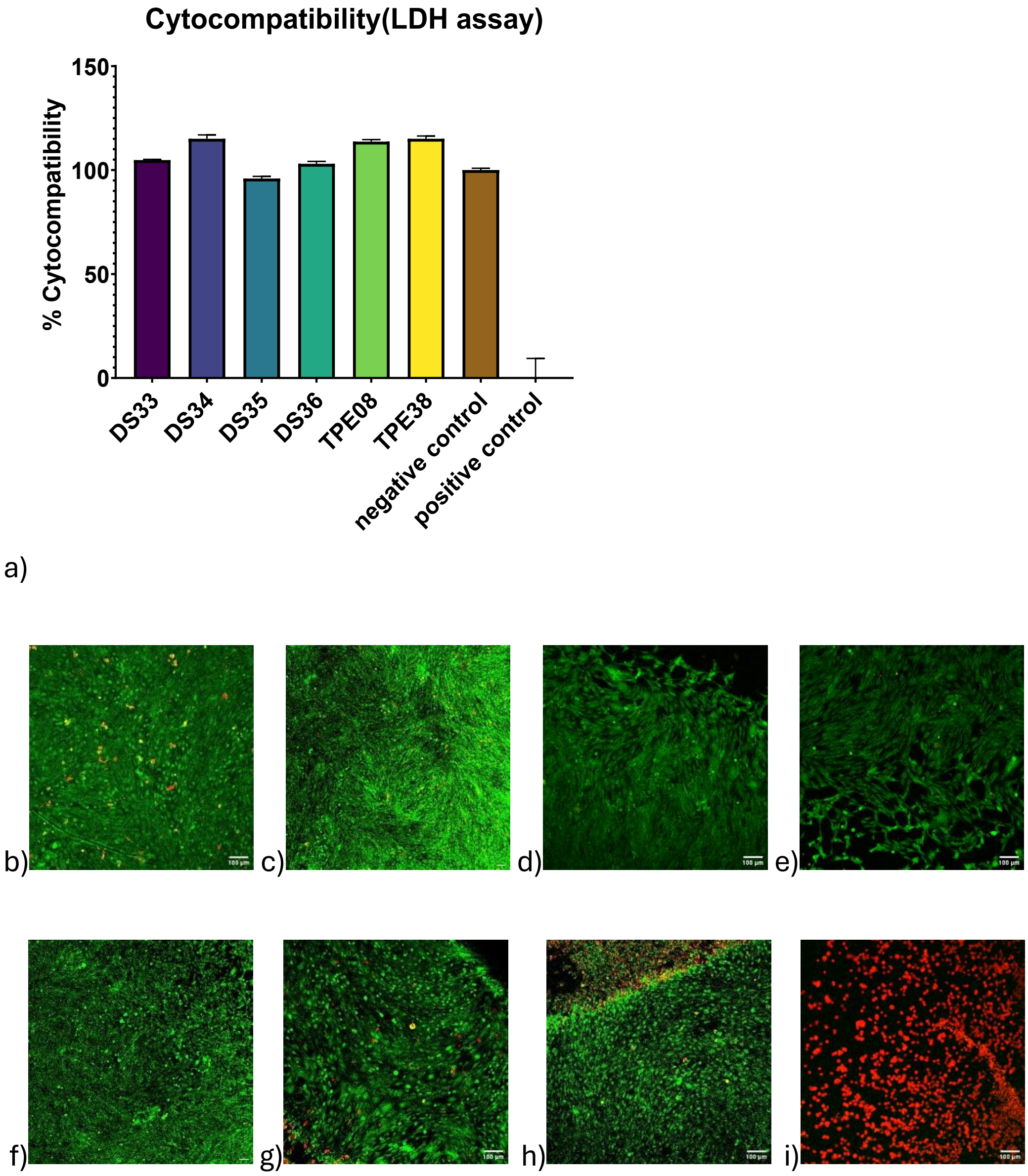

Figure 16 LDH Assay a) graph of cell viability results, (b-g) live/dead image of the cells incubated with different hydrogels b)DS33(6%) c)DS34(4%) d)DS35(6%) e)DS36(2%) f) TPE08 (5%) g)TPE38(5%) h) negative control and i) positive control

4.1.5.2. Cell Adhesion

Cell adhesion assays were performed to evaluate the bioactivity of the peptide sequences on hydrogel surfaces. $C_3H_{10}T_{1/2}$ cells were seeded onto the hydrogels prepared in the well-plate and cultured for 30 min, 1 h, 2 h, and 4 h at 37 °C; adherent cells were quantified via the CellTiter-Glo® assay. The TPE peptides hydrogels (TPE08, TPE38) disintegrated under the assay conditions, precluding reliable adhesion measurements—a limitation attributable to their low mechanical integrity (G' ≤ 0.09 kPa) and weak gel character. Among the tested peptide hydrogels, DS34 and DS36 promoted the highest levels of cell adhesion at the early time points (30 min to 2 h). Confocal microscopy supported these quantitative findings, though background staining of the hydrogels by the live/dead dyes reduced image contrast, making the difference in adhesion between hydrogels less apparent visually (Figure 17 b-e).

Morphological analysis revealed sequence-dependent differences. DS33 displayed rounded, partially spread cells with mixed viability, whereas DS35 supported rounded cell spreading with predominantly green fluorescence. This disparity confirms that hydroxyproline is essential for high-affinity α2β1 integrin engagement, consistent with the established collagen-mimetic bioactivity of GFOGER. [144] DS34 yielded moderate adhesion with rounded cell clusters, indicating that lipidation does not compensate for the intrinsically lower integrin affinity of GFPGER. Notably, DS36 formed large crystalline surface aggregates alongside rounded green cells, suggesting that the strong hydrophobic driving force of the stearic acid tail promotes surface precipitation, which may occlude the bioactive epitope in a 2D format. [146]

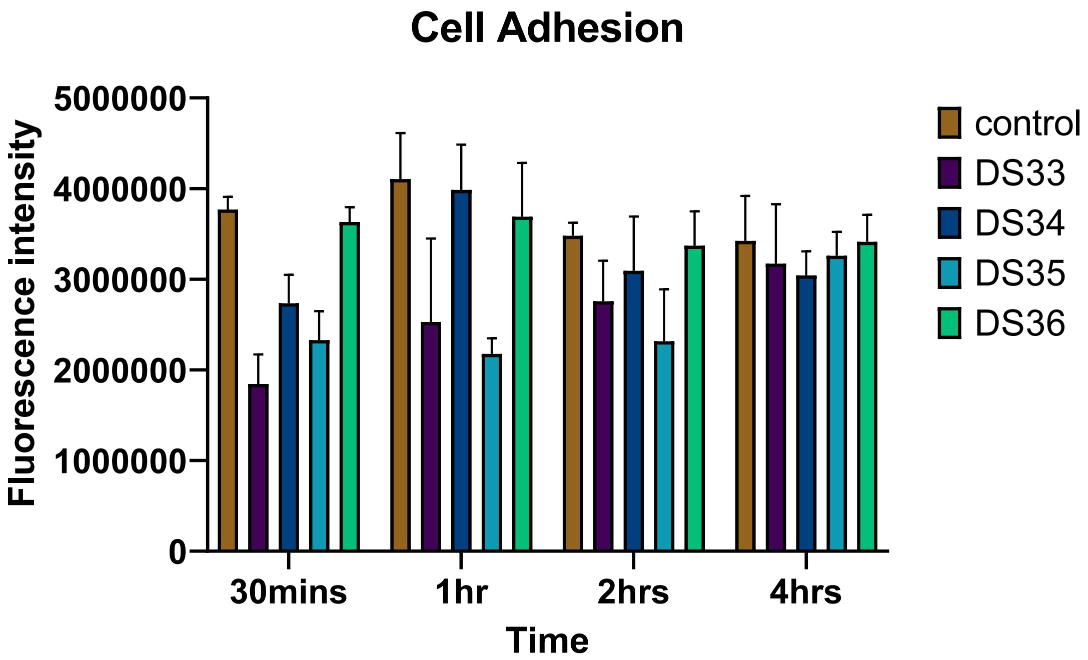

a)

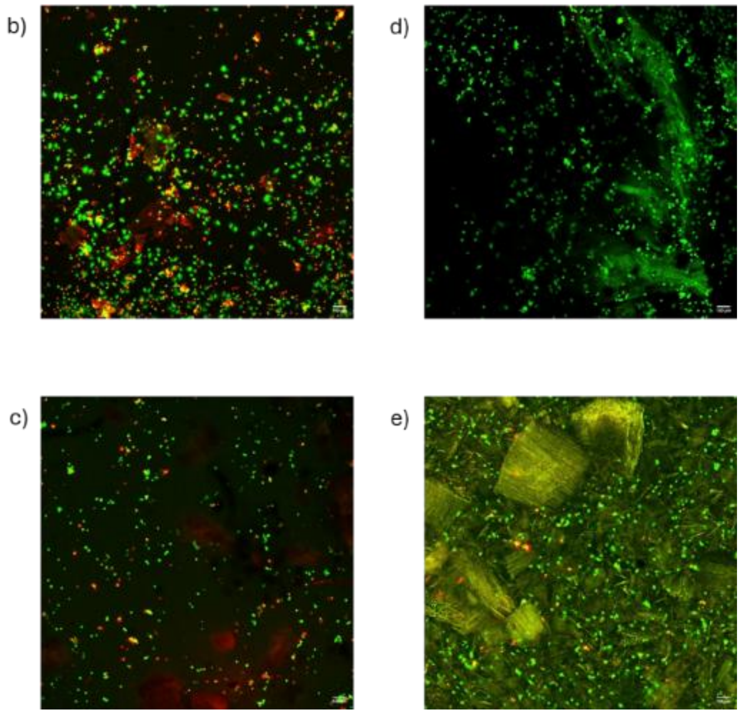

Figure 17 a)graph showing cell adhesion at different time points; (b-e) Confocal image after 4 hours of b)DS33, c)DS34, d)DS35 and e)DS36

4.1.5.3. Cell Encapsulation

The potential of the hydrogels as bioinks was evaluated via 3D cell encapsulation. $C_3H_{10}T_{1/2}$ cells were suspended in peptide solutions prior to gelation, ensuring homogeneous distribution, and cultured for 7 days. All hydrogels remained macroscopically intact throughout the culture period. Live/dead staining and confocal z-section imaging confirmed that cells were distributed throughout the gel interior, validating true volumetric encapsulation rather than surface seeding. [147]It should be noted that, as with the 2D adhesion assays, some background fluorescence from the hydrogel matrix was observed, which slightly reduced image contrast; however, the qualitative trends in viability and cell morphology between peptide formulations remained clearly distinguishable.

Sequence-dependent differences in viability were evident. The non-lipidated GFPGER peptide DS33 exhibited substantial red clustering and mixed viability, consistent with insufficient integrin-mediated pro-survival signalling in the absence of hydroxyproline. In contrast, DS35

(GFOGER) supported robust, elongated cell morphologies with minimal red signal, confirming that the collagen-mimetic motif promotes α2β1 integrin engagement and downstream survival cues even within a 3D matrix. Lipidated variants presented a more heterogeneous picture. DS34 (Stearic acid–GFPGER) displayed healthy, spread cells interspersed with yellow aggregates, while DS36 (Stearic acid–GFOGER) showed well-distributed, viable green cells alongside large green crystalline precipitates. These aggregates, likely arising from kinetically trapped precipitation or phase separation during cell mixing—possibly exacerbated by the omission of sonication prior to encapsulation—created localised dense peptide pockets through which cells navigated. This heterogeneity suggests that while lipidation enhances bulk gelation and cytocompatibility, it may also introduce microstructural inhomogeneities when processed in the presence of cells. [146]

Cross-sectional imaging further revealed that GFOGER-containing gels maintained uniform green fluorescence throughout the gel depth, whereas GFPGER gels displayed localised red foci, indicative of a viability gradient. This spatial pattern may reflect oxygen or nutrient diffusion limitations compounded by the absence of pro-survival integrin signaling at the gel core.

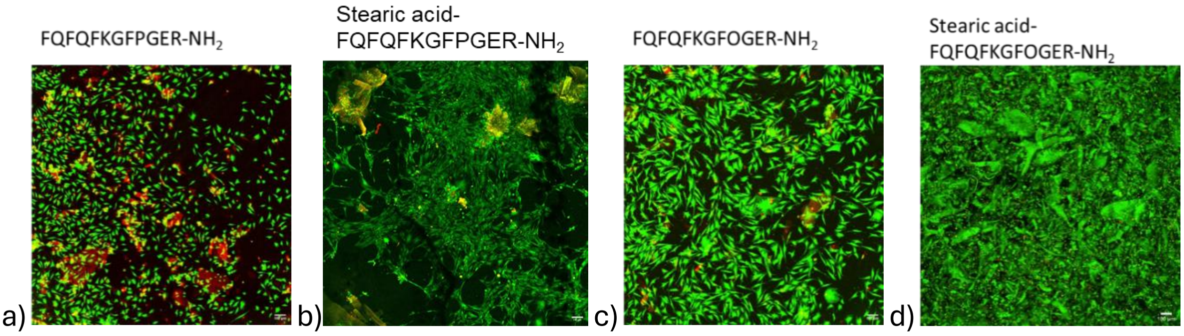
a) FQFQFKGFPGER-NH_2

b) Stearic acid-FQFQFKGFPGER-NH_2

c) FQFQFKGFOGER-NH_2

d) Stearic acid-FQFQFKGFOGER-NH_2

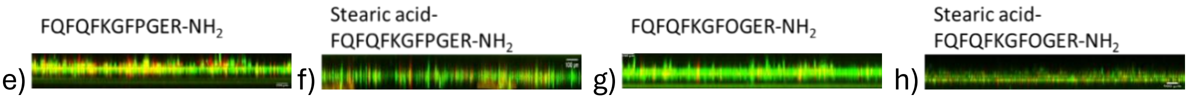

Figure 18 Confocal image of cells encapsulated in peptide hydrogels. Z stack top view of a)DS33 b)DS34 c)DS35 d)DS36 hydrogel and side view of e)DS33 f)DS34 g)DS35 h) DS36 hydrogel

4.1.6. 3D printing

The hydrogel was extruded smoothly without blockage, indicating that macroscopic aggregation does not impede flow through the nozzle. Printability was evaluated using a Bio X pneumatic extrusion bioprinter at a fixed print speed of 12 mm s^{-1} across varying nozzle diameters and pressures. Extrusion through a standard conical nozzle (0.41mm inner diameter) at 4 kPa yielded continuous but over-extruded filaments of irregular thickness and poor dimensional fidelity. Multilayer deposition under these conditions resulted in immediate fusion of successive layers, indicating insufficient elastic recovery. Substitution with 21G Cellink needle (0.51 mm internal diameter) at 4 kPa did not ameliorate over-extrusion, confirming that extrusion pressure, rather than nozzle geometry, governs filament diameter under these conditions. Reducing pressure to 2 kPa with the same needle produced thinner filaments but introduced discontinuous deposition and void formation, characteristic of under-extrusion.

These findings delineate an inoperable pressure window between 2 and 4 kPa for the current formulation: 4 kPa yields over-extrusion and poor layer fidelity, whereas 2 kPa results in filament discontinuity. This behaviour reflects a mismatch between the gel's rheological profile—specifically its viscosity and yield stress—and the printer's operational envelope. Future optimisation should prioritise systematic rheological characterisation to define target viscoelastic properties, followed by fine pressure titration (2.5–3.5 kPa), evaluation of elevated print speeds to mitigate filament spreading, and exploration of temperature-controlled extrusion to modulate gelation kinetics.

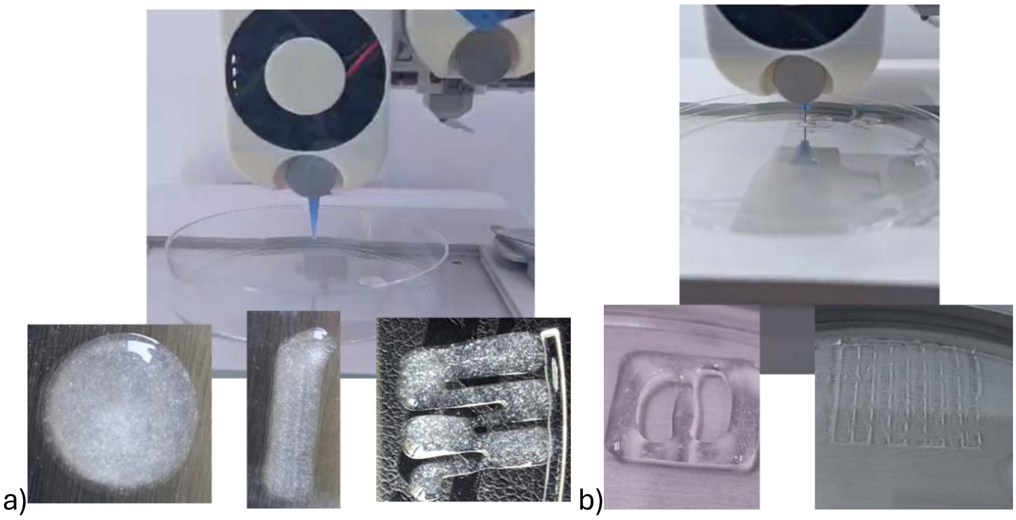

Figure 19 Structures printed using the DS36 hydrogel on a 3D printer a)0.41mm nozzle and b)

4.2. Discussion

4.2.1. Mechanical insights and summary of DS33, DS34, DS35 and DS36

This study demonstrates that incorporating a stearic acid tail into the amphiphilic sequence serves as a structural switch, transitioning self-assembly from a flexible to a more rigid conformation. The identical signature of the secondary structure of the peptide in both ATR-FTIR and CD spectroscopy (dilute state) reveals a clear dichotomy: lipopeptides (DS34, DS36) are governed by hydrophobic collapse, while non-lipidated analogues (DS33, DS35) are governed by H-bonding equilibria. For non-lipidated peptides (DS33 and DS35), the ATR-FTIR data (Table 6) and CD concentration-dependence (Figure 13: a-c) confirm that lipidation shifts the equilibrium from unordered or β-turn structures toward robust β-sheet networks.

For lipopeptides DS34 and DS36, the stearic acid tail creates a low-dielectric hydrophobic core that pre-organises the peptide backbone for intermolecular β-sheet hydrogen bonding. This is evidenced by the persistence of a β-sheet signal even at 0.05 mM, indicating a critical aggregation concentration well below the testing range. [148–151] In contrast, DS33 and DS35 lack this entropic driving force. Their assembly is driven primarily by π-π stacking of the FQFQFK segment, resulting in more flexible Type I β-turns (FTIR) that are highly sensitive to concentration and solvent polarity. [140,141]

The DLS data (Table 7) provide a critical insight into the dynamic behaviour of these assemblies, which is essential for understanding hydrogelation. The non-lipidated peptides DS33 and DS35 undergo a striking reduction in hydrodynamic size upon transfer from water to PBS (e.g., DS33 from ~3100 nm to ~720 nm). This is not merely aggregation; it represents a salt-induced compaction. In pure water, electrostatic repulsion between charged lysine residues forces the FQFQFK assemblies into loose, highly hydrated clusters. The phosphate ions in PBS effectively screen this repulsion, allowing the peptides to collapse into denser, more stable nuclei that are precursors to gelation. Conversely, the lipidated peptides DS34 and DS36 maintain micron-scale sizes in both water and PBS. The hydrophobic core of the stearic acid assembly is essentially impervious to ionic strength changes—the structure is "locked in" from the moment of nanoprecipitation. This explains the lower MGC (2-4%) and higher G' (1.6-2.1 kPa) of the lipopeptides: they form rigid, kinetically trapped networks rather than dynamic equilibrium gels. [152]

The rheological analysis (Figure 12) demonstrates a classic trade-off in supramolecular materials. The extensive, rigid β-sheet network of DS36 yields high stiffness (G' ~2.1 kPa) but poor thixotropic recovery (~30-40% loss). The high-energy hydrogen bonds in the β-sheet are brittle; once broken by shear, the stearic acid domains cannot rapidly re-anneal on the timescale of the experiment. [153] In contrast, the non-lipidated DS33 and DS35 exhibit near-complete recovery. Their weaker, more dynamic β-turn interactions allow for rapid re-association post-shear. [154] This distinction is critical for bioprinting applications and directly explains the 3D printing outcome described in section 4.1.6. The DS36 filament exhibited non-uniform extrusion ("thick and non-uniform") precisely because it lacks the rapid shear-thinning recovery necessary to flow smoothly through a nozzle and reform a stable strand instantly. It behaves as a yield-stress fluid with a long recovery time constant.

The differences directly translate to the biological observations (Section 4.1.5). The highly structured instantaneous assembly of lipopeptides facilitates presentation of the bioactive GFOGER/GFPGER motif on the surface of the nanostructure, which leads to a high density of bioactive groups being presented on the surface. Since the potency of the GFOGER motif is density-dependent, this assembly increases local peptide concentration and enhances interaction with cell-surface receptors, improving biocompatibility and cell adhesion at early time points. [66,148,150,155] By contrast, the non-lipidated FQFQFK hexapeptide, though amphiphilic, requires more time to cluster and achieve a comparable surface density of the bioactive peptide, accounting for the initial differences in cell adhesion on the hydrogel. [156] However, the heterogeneity observed in DS34 and DS36 3D encapsulation —specifically the crystalline precipitates—highlights a potential drawback of this strong driving force. Rapid, uncontrolled hydrophobic collapse in the presence of cells can lead to phase separation and the formation of peptide-rich "pockets" that limit uniform nutrient diffusion, despite the overall high viability (LDH).

4.2.2. AIE-conjugated peptides

The TPE conjugates (TPE08 and TPE38) validate the design principle of using aggregation-induced emission (AIE) as both a structural probe and a functional readout. The comparison between GFOGER (TPE08) and GFPGER (TPE38) provides a stark illustration of how a single hydroxyl group (Hyp vs. Pro) dictates supramolecular chirality and photophysical output. [157]

While TPE38 has an α-helical character and TPE08 has β-turn/β-sheet, the mechanistic link is the hydrogen bonding capacity of hydroxyproline. The hydroxyl group of O facilitates inter-strand water-bridged networks that stabilise extended β-sheet-like packing of the GFOGER sequence. In GFPGER, the absence of this group favours a more compact, intramolecularly stabilised α-helical conformation. [158]

The DLS data (Table 7) reinforces these structural findings. In water:DMSO, TPE 08 (GFOGER) forms small, monodisperse particles (~212 nm, PDI 0.17), indicative of a well-ordered, kinetically stable assembly. In contrast, TPE 38 (GFPGER) forms aggregates over ten times larger (~2826 nm) with high polydispersity (PDI 0.69), reflecting a less controlled, heterogeneous aggregation process driven by weaker intermolecular interactions. Upon transfer to PBS, both TPE conjugates undergo significant aggregation, indicating that electrostatic repulsion plays a key role in stabilising the smaller TPE 08 nanostructures in low ionic strength environments. The fluorescence emission data further corroborate this relationship (Figure 11): the GFOGER hydrogel exhibits approximately 25% greater emission intensity than GFPGER. The hydroxyproline residue promotes tighter molecular packing and the formation of smaller, more uniform aggregates. The resultant steric confinement restricts intramolecular rotation of the TPE moiety—the mechanistic basis of AIE—thereby yielding enhanced fluorescence. [158]

Rheological characterisation reveals soft gels with storage modulus (G’) values ranging between 10 and 100 Pa. Compared to amphiphilic sequences (stearic acid-FQFQFK and FQFQFK peptide), TPE incorporation, while beneficial for fluorescence, does not provide the same structural stiffness. It should be noted, however, that the low mechanical strength and the observed tendency to disintegrate in cell culture media (section 4.1.5.2) currently limit the standalone application of these AIE hydrogels as load-bearing scaffolds. These materials may be better suited as injectable, space-filling gels or as sensing/diagnostic platforms where their fluorescent properties can be exploited. These observations align with recent reviews on peptide-AIEgen hybrids, which note that the characteristic twisted or propeller-shaped molecular conformation of TPE can present a challenge for achieving densely packed, rigid assemblies, although this can be addressed through strategic peptide design. [157,159]

5. Peptide-Decorated Vascular Graft (NanoReMedi Collaboration)

Bioactive PLGA Scaffolds for Small-Diameter Vascular Grafts.

My contribution: Peptide synthesis and Purification (done at the University of Milan)

Journal: Discover Materials

Title: **A Peptide Library Approach to Biofunctionalized Electrospun PLGA Scaffolds for Vascular Regeneration**

Nursu Erdogan, Enrica Chiesa, Mariella Rosalia, Dhriti Santosh Shenoy, Kaliroi Peqini, Sara Pellegrino, Ida Genta

While self-assembled peptide nanomaterials offer exceptional biocompatibility and inherent bioactivity, their translation to load-bearing tissue engineering applications is often constrained by limited mechanical strength. [160] This limitation can be addressed by blending or conjugating peptides with synthetic polymers, thereby synergising the biological functionality of the peptides with the tunable mechanical integrity of the polymers. [161,162] In this approach, the synthetic polymer provides a robust, three-dimensional structural framework, while surface-immobilised peptides confer the specific biochemical cues necessary to direct cellular adhesion, proliferation, and differentiation.

This collaborative study aimed to develop a peptide-decorated modular vascular graft by combining electrospinning technology with precisely designed bioactive peptide motifs presented on the surface of the vascular graft. Electrospun scaffold composed of poly-lactide-co-glycolide (PLGA) (a copolymer of 88% lactic acid and 12 % glycolic acid), an FDA approved polymer, was selected as the structural foundation due to its excellent biocompatibility, mechanical integrity, and biodegradability. [163] Peptide immobilisation was done in 2 steps: first, surface modification of the electrospun graft with 1-(2-aminoethyl)maleimide hydrochloride; second, immobilisation of cysteine-terminated peptides via Michael addition reaction. This approach ensures the uniform immobilisation of the bioactive peptide without burying them within the nanofibre bulk. [164]

Despite extensive studies on individual cell-adhesive peptides, a systematic, side-by-side comparison of multiple peptide motifs presented on an identical biomaterial interface remains limited, particularly for sdvg applications. This work presents a small but functionally diverse peptide library (Table 1) designed to systematically investigate how distinct peptide sequences direct the behaviour of fibroblasts and endothelial cells at the biomaterial interface. The library comprised of five bioactive peptide motifs: 1) laminin-derived IKVAV [165–169], 2) fibronectin-derived REDV [170–173], 3) collagen mimicking GFOGER [174–179], 4) bivalirudin-derived (D-Phe)PRP [180–182], and 5) laminin-1-derived KAFDITYVRLKF [183–188].

The functionalised scaffolds were systematically characterised for conjugation efficiency, surface physicochemical properties, and their capacity to modulate cell-specific responses in both fibroblasts and human umbilical vein endothelial cells (HUVECs). The resulting structures are intended to serve as the bioactive inner layer of a multilayer small-diameter vascular graft (SDVG), combining the mechanical integrity of PLGA with the biological activity of peptides to improve endothelialisation and hemocompatibility. A representative example of the conjugation strategy employed (Figure 20). The maleimide-functionalised PLGA scaffold undergoes Michael addition with cysteine-terminated peptides. This figure illustrates the general approach; a family of five distinct peptide sequences (P1–P5, see Table 10) was immobilised using this methodology, enabling systematic comparison of peptide sequence effects on scaffold properties.

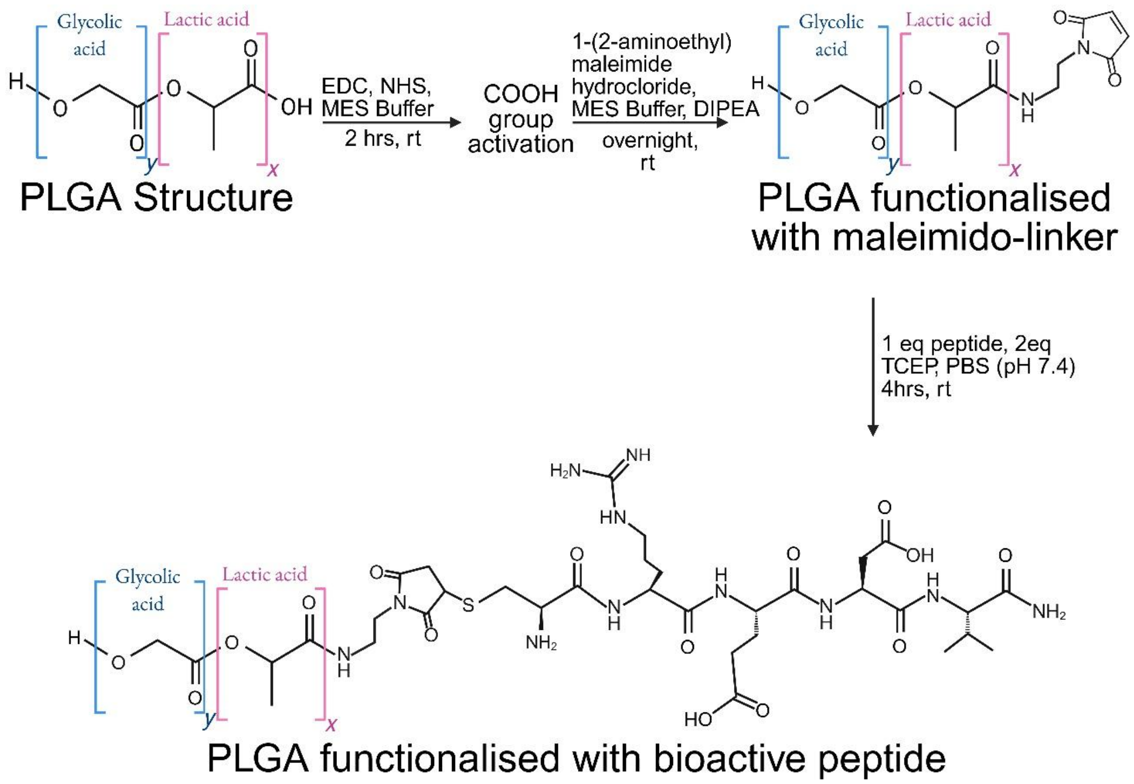

Figure 20 Schematic representation of peptide immobilisation on electrospun PLGA scaffold

5.1. RESULTS

5.1.1. Characterisations of Plain PLGA Scaffolds (before peptide immobilisation)

SEM imaging confirmed the successful fabrication of randomly oriented, bead-free electrospun fibres of PLGA with a mean diameter of 2.9 ± 0.2 μm (Figure 21). The scaffold thickness was measured at 107.2 ± 18.2 μm. Mechanical testing (

Table 9) yielded an ultimate tensile strength (UTS) of 2.9 ± 0.1 MPa and a Young's modulus of 54.2 ± 14.6 MPa. The scaffolds exhibited high ductility, with an elongation at break of 442.7 ± 48.7%, indicative of a strain-hardening fibrous network capable of significant deformation before failure.

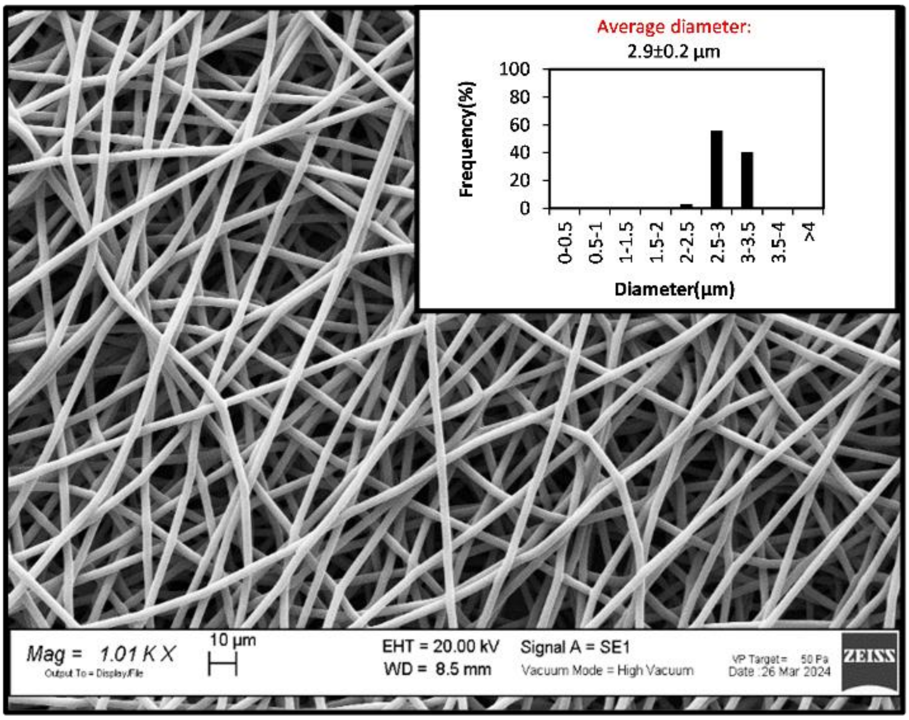

Figure 21 SEM image of a representative plain PLGA scaffold (before peptide immobilisation)

Table 9: Mechanical characterisation of plain scaffold (average ± standard deviation)

Property	Value
Ultimate Tensile Strength (UTS)	2.9 ± 0.1 MPa
Young's Modulus	54.2 ± 14.6 MPa
Yield Strength	1.8 ± 0.2 MPa
Yield Strain	3.1 ± 0.3%
Breaking Point Stress	2.6 ± 0.1 MPa
Elongation at Break	442.7 ± 48.7%

5.1.2. Synthesis of Cysteine-Modified Peptides

Following the promising design reported by Bai et. al., all five peptide sequences were successfully synthesised via microwave-assisted Fmoc/tBu solid-phase peptide synthesis (SPPS) with an N-terminal cysteine residue to facilitate subsequent conjugation. After cleavage and purification by semi-preparative RP-HPLC, all peptides were obtained with high purity (≥94%) and good yields. The correct molecular weights were confirmed by electrospray ionisation mass spectrometry (ESI-MS). The physicochemical properties of each peptide - including net charge at physiological pH, and grand average of hydropathy (GRAVY) index- are summarised in Table 10, as these parameters are known to influence both conjugation efficiency and subsequent cell–material interactions.

Table 10: Cysteine-Modified Peptide Library Synthesised for SDVG Functionalisation

Code	Peptide Sequence	Origin (Function)	Purity (%)	Mass (mg)	Net Charge (pH 7.4)	GRAVY* Index
P1	CIKVAV-NH_2	Laminin α1 (adhesion/angiogenesis)	94%	41.2	+1	+2.21
P2	CREDV-NH_2	Fibronectin CS5 (selective cell adhesion of endothelial cells)	99%	58.8	0	-0.96
P3	CGFOGER-NH_2	Collagen I (cell adhesion, proliferation)	99%	69.8	+1	-0.70

P4	C(D-Phe)PRP-NH$_2$	Bivalirudin fragment (anticoagulant)	99%	77.5	+1	-0.82
P5	CKAFDITYVRLKF-NH$_2$	Laminin γ1 (pro-angiogenic)	95%	27.5	+2	-0.28

*** GRAVY index calculated using the Kyte-Doolittle scale. Positive values indicate hydrophobicity; negative values indicate hydrophilicity.** [189]

5.1.3. Peptide Immobilisation and Scaffold Morphology

Peptides were covalently immobilised onto maleimide-functionalised electrospun PLGA scaffolds via thiol–maleimide Michael addition (Figure 20). [164] Plain scaffolds were cut into circular discs (diameter 15 mm), weighed and activated with 1-Ethyl-3-(3-dimethylaminopropyl)carbodiimide (EDC 2mM) and N-Hydroxysuccinimide (NHS 5mM) in 2-(N-Morpholino)ethanesulfonic acid buffer (MES buffer 0.1 M, pH 5-6) for 2 hours at room temperature. Activated scaffolds were then incubated overnight (16–18 h) with 1-(2-aminoethyl)maleimide hydrochloride (10 equivalents relative to scaffold mass) in MES buffer containing 5 μL DIPEA. After washing with Milli-Q water, maleimide-functionalised scaffolds were incubated with peptide solutions (3 equivalents relative to PLGA) in PBS (pH 7.4) containing Tris(2-carboxyethyl)phosphine (TCEP 2 equivalents relative to peptide) as a reducing agent. Conjugation proceeded for 4 h at room temperature. Scaffolds were subsequently washed twice with PBS, and the peptide solutions before and after immobilisation were retained for quantification. Peptide-conjugated scaffolds are hereafter designated P1-scaffold, P2-scaffold, P3-scaffold, P4-scaffold, and P5-scaffold.

SEM analysis of the peptide-immobilised scaffolds (Figure 22 P1–P5) confirmed that the conjugation procedure did not alter fibre morphology or induce swelling/degradation. Mean fibre diameters ranged from 2.0 to 2.8 μm. Occasional surface particulates were attributed to residual salt crystals from washing steps rather than peptide aggregation.

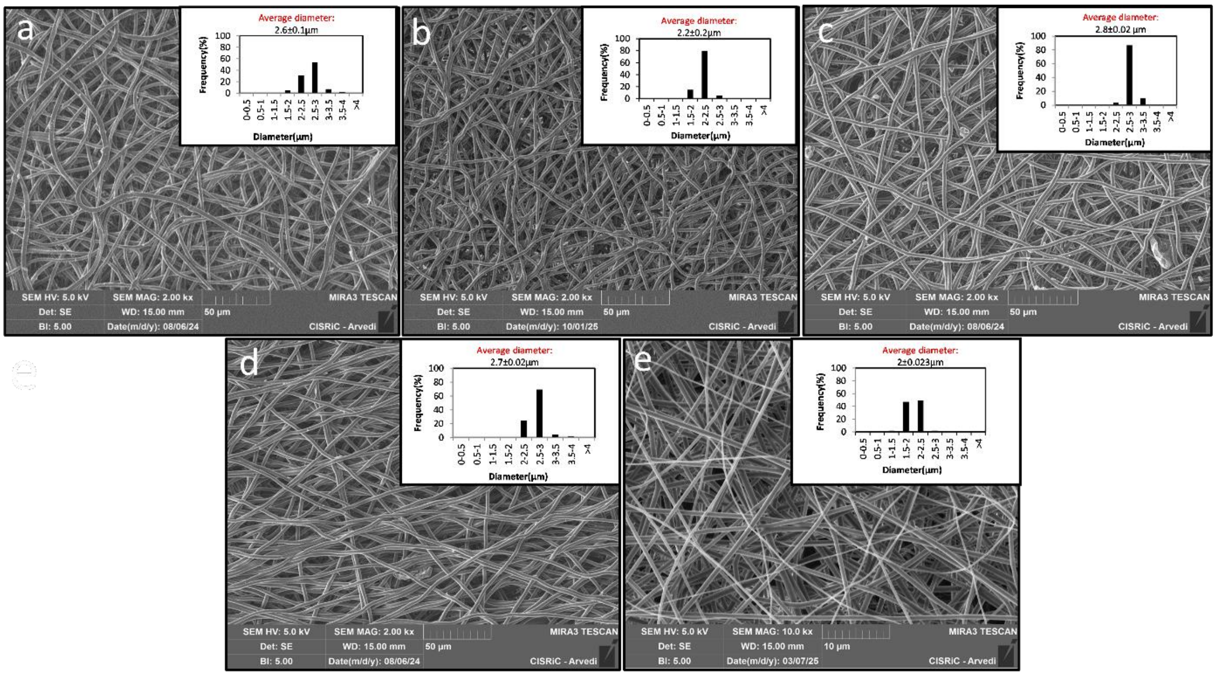

Figure 22 SEM images of (a) P1-scaffold, (b) P2-scaffold, (c) P3-scaffold, (d) P4-scaffold, (e) P5-scaffold

5.1.4. Quantification of peptide immobilisation onto plain scaffold

HPLC quantification of the peptide remaining in the conjugation supernatant revealed variable immobilisation efficiencies across the peptide library (Table 11). The P1-scaffold (CIKVAV) exhibited the highest conjugation efficiency (36.8 ± 6.4%), corresponding to a surface density of 6.6 ± 1.1 μg peptide per mg of PLGA fibres. Conversely, the P4-scaffold (C(D-Phe)PRP) displayed the lowest efficiency (10.4 ± 3.1%), likely due to steric hindrance from the bulky D-Phe residue adjacent to the anchoring cysteine. [190,191] Due to this low conjugation yield, the P4-scaffold was excluded from subsequent biological evaluations.

Table 11:Quantification of Peptide Conjugation onto PLGA Scaffolds

Name	Peptide conjugation (nmol)	Peptide conjugation (µg/mg fibres)	Conjugation efficiency (%)
P1-scaffold	18.9 ± 0.30	6.6 ± 1.1	36.8 ± 6.4
P2-scaffold	15.7 ± 0.58	4.7 ± 1.6	26.8 ± 9.3
P3-scaffold	28.5±1.68	4.6±1.8	21.1± 8.3
P4-scaffold	22.3±6.9	1.8±0.5	10.4±3.1
P5-scaffold	12.9 ± 0.66	9.1 ± 2.7	24.9 ± 11.1

5.1.5. Cytotoxicity of Soluble Peptides on Fibroblasts (nHDFs)

Prior to scaffold evaluation, the intrinsic cytotoxicity of the soluble peptides (P1, P2, P3, P5) was assessed on normal human dermal fibroblasts (nHDFs) across a concentration gradient of 8–400 µM in complete cell culture media for 24 hrs (Figure 23). Peptides P1, P2, and P3 exhibited no significant cytotoxic effects, with cell viability remaining above 80% at most tested concentrations. Notably, P3 (CGFOGER) consistently promoted fibroblast proliferation, yielding viability values exceeding 100% of the untreated control. In contrast, P5 (CKAFDITYVRLKF) exhibited pronounced, dose-dependent cytotoxicity, reducing fibroblast viability to approximately 50–60% at higher concentrations (≥100 µg/mL). This effect may arise from soluble C16 acting as an antagonist, disrupting endogenous integrin-mediated adhesion and inducing anoikis-like apoptosis.

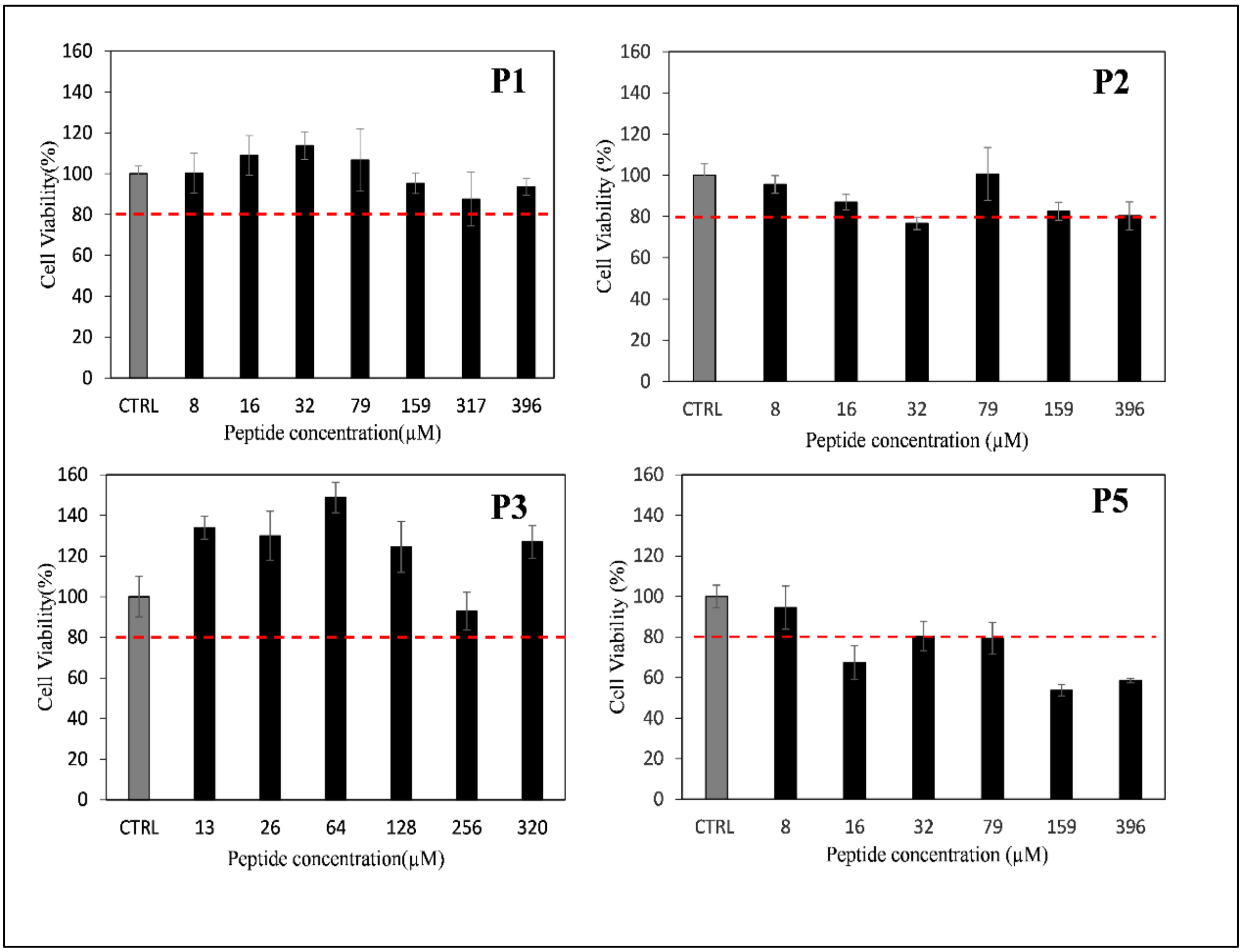

Figure 23 Cell viability of peptide (P1, P2, P3, P5) solutions in complete cell culture media at various concentrations (8–400 µM)

5.1.6. Fibroblast Response to Peptide-Immobilised Scaffolds

Based on the low conjugation efficiency of P4 (section 5.1.4) and the cytotoxicity of soluble P5 (section 5.1.5), only peptides P1, P2, and P3 were advanced for scaffold-based studies. nHDFs were cultured directly on the peptide-immobilised scaffolds for 72 hrs. Live/Dead staining (Figure 24) revealed predominantly viable cells across all scaffold types, though some non-viable cells were observed on the P2-scaffold (CREDV). Given that soluble P2 was non-cytotoxic to fibroblasts (Figure 23), this effect likely arises from time-dependent stress or the presentation of a surface that is suboptimal for fibroblast adhesion, consistent with the known endothelial selectivity of the REDV motif. [170,171,173] After 72 hrs of incubation on scaffolds, 4',6-Diamidino-2-phenylindole (DAPI) and phalloidin staining (Figure 25) further confirmed extensive cell spreading, well-defined actin stress fibres, and elongated fibroblastic morphologies on all peptide-immobilised scaffolds, comparable to the plain PLGA control.

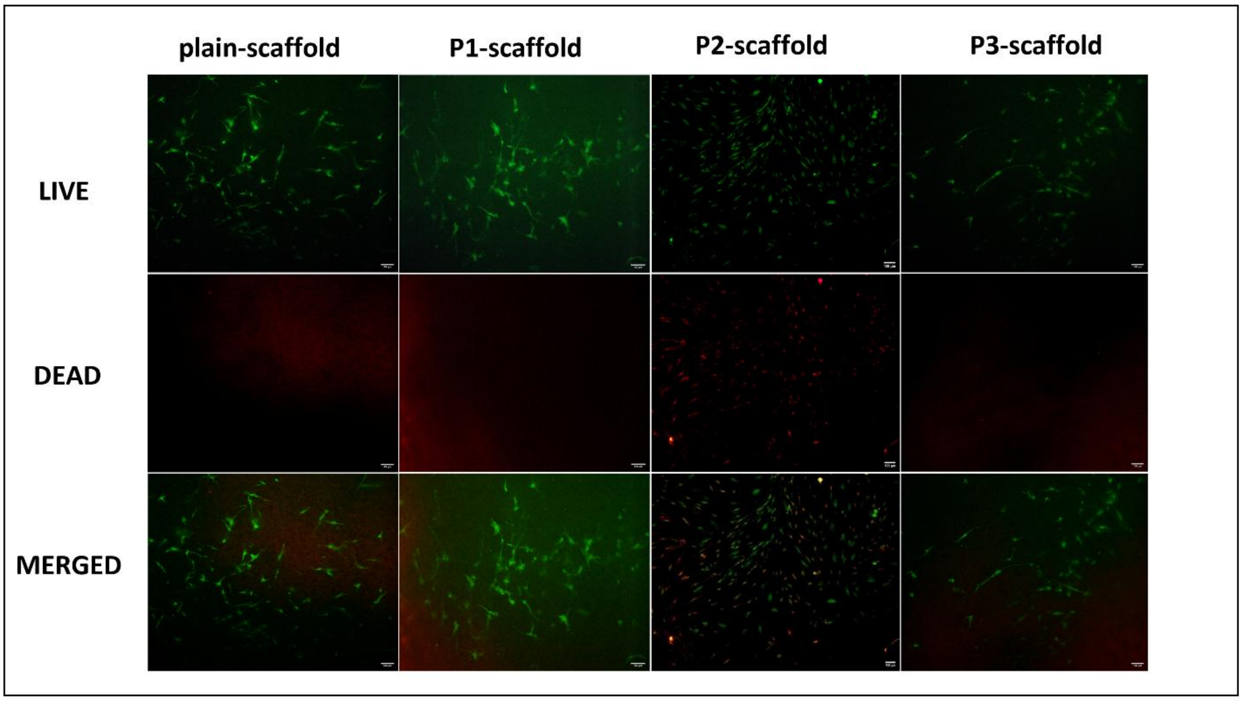

Figure 24 Live and Dead assay on peptide-immobilised scaffolds after 72 h of incubation.

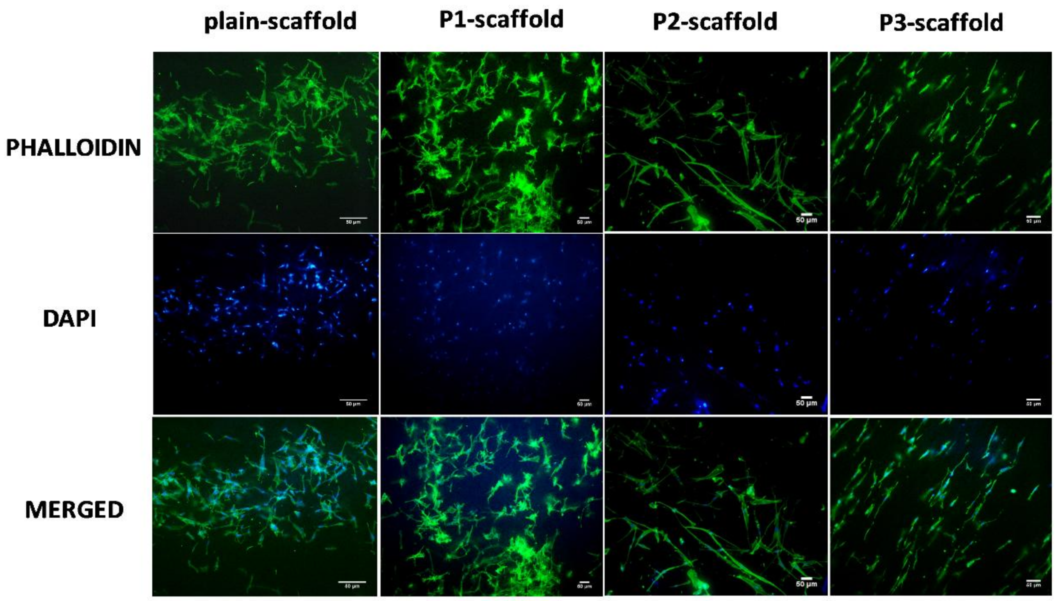

Figure 25 DAPI and phalloidin staining on peptide-immobilised scaffolds

5.1.7. Water Absorption and Surface Wettability

Relative water absorption capacity showed a modest descending trend following peptide conjugation compared to plain PLGA (Figure 26). Static water contact angle measurements revealed that the plain PLGA scaffold was highly hydrophobic, with a contact angle of 121.3 ± 3.8°. Peptide immobilisation produced sequence-dependent changes in surface wettability. Notably, only the modification with P2 (CREDV) resulted in a statistically significant reduction in contact angle to 104.2 ± 3.9°, indicating improved surface hydrophilicity. This observation correlates strongly with the physicochemical properties of the peptides, particularly the GRAVY index (

Table 9). P2 possesses the lowest (most negative) GRAVY index (–0.96) of the library, consistent with its enhanced capacity to increase surface wettability.

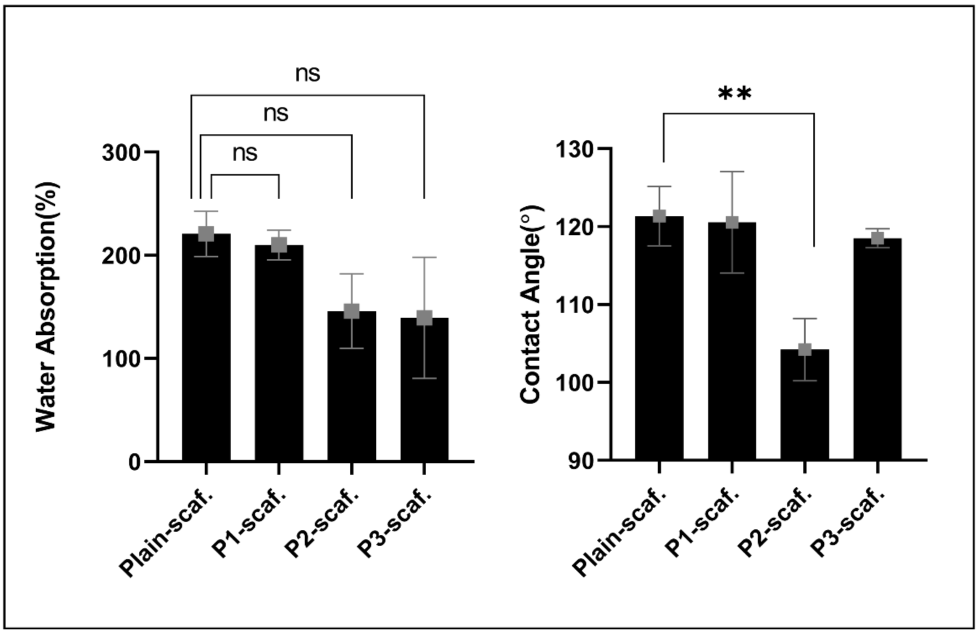

Figure 26 Relative water absorption capacity and surface wettability of peptide-conjugated PLGA scaffolds.

[Statistical significance was defined as follows: ns (p ≥ 0.05); *p < 0.05; **p < 0.01; ***p < 0.001; and ****p < 0.0001.]

5.1.8. Endothelial Cell (HUVEC) Response to Soluble Peptides

The effect of soluble peptides P1, P2, and P3 on human umbilical vein endothelial cell (HUVEC) viability was assessed at 24 and 72 hours across a range of concentrations (Figure 27). All three peptides exhibited dose- and time-dependent effects. An optimal concentration window was identified at approximately 50 µg/mL, where all three peptides promoted proliferation without inducing cytotoxicity. At concentrations outside this optimal range (both lower and higher), reduced cellular responses were observed. Among the three peptides, P2 (CREDV) demonstrated the highest compatibility with HUVECs at elevated concentrations, maintaining high viability even at 100 µg/mL.

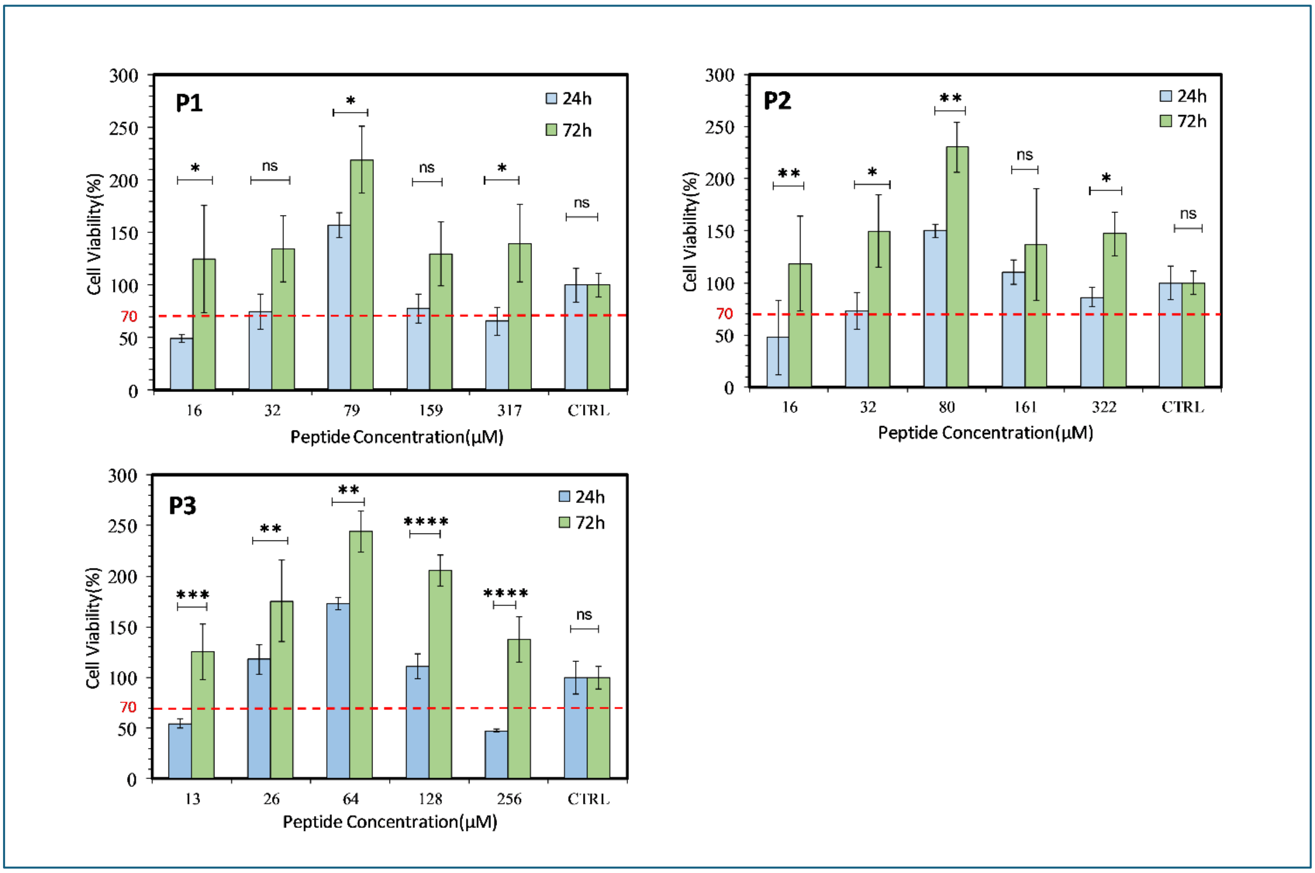

Figure 27 HUVECs viability at 24h and 72h after P1, P2 and P3 treatment at varied concentrations

Statistical significance was defined as follows: ns, not significant ($p \geq 0.05$); *$p < 0.05$, significant; **$p < 0.01$, very significant; ***$p < 0.001$, extremely significant; and ****$p < 0.0001$, extremely significant

5.1.9. Endothelial Cell Response to Scaffold Extracts

To evaluate potential cytotoxicity arising from scaffold degradation products or leachable, HUVECs were cultured in medium conditioned by incubation with the peptide-immobilised scaffolds (extract method). At 24 hours, scaffold extracts induced no acute cytotoxicity (Figure 28). However, prolonged exposure (72 hours) resulted in a measurable reduction in cell viability across all scaffold types, including the plain PLGA control. This effect is attributed to the well-documented accumulation of acidic degradation by-products (lactic and glycolic acid) from hydrolytic PLGA degradation. Notably, the peptide-functionalised scaffolds, particularly the P2-scaffold, partially mitigated this reduction in viability compared to the plain PLGA control.

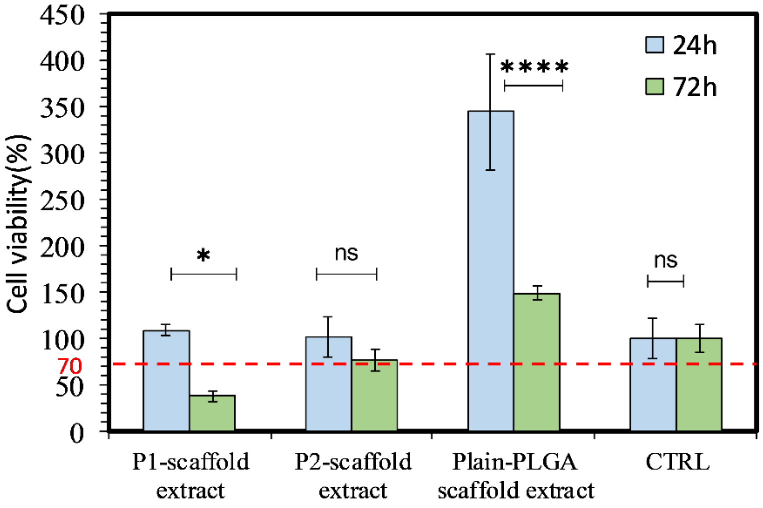

Figure 28 HUVEC viability at 24h and 72h after peptide conjugated scaffold extraction treatment

Statistical significance was defined as follows: ns, not significant ($p \geq 0.05$); *$p < 0.05$, significant; **$p < 0.01$, very significant; ***$p < 0.001$, extremely significant; and ****$p < 0.0001$, extremely significant.

5.2. Discussion:

This collaborative study successfully demonstrates the rational design, synthesis, and biological evaluation of a peptide-decorated PLGA scaffold platform intended for small-diameter vascular graft applications. The discussion focuses on structure–property relationships linking peptide physicochemical characteristics to conjugation efficiency, surface properties, and cell-specific biological responses.

All five cysteine-modified peptides were obtained with high purity (≥94%), confirming the robustness of the microwave-assisted SPPS protocol. However, conjugation efficiencies varied substantially (10.4% to 36.8%), underscoring the critical influence of peptide sequence on surface immobilisation chemistry. The highest efficiency was observed for P1 (CIKVAV, 36.8%) and the lowest for P4 (C(D-Phe)PRP, 10.4%). These differences arise from a combination of cysteine accessibility, peptide physicochemical properties, and steric hindrance. P1 is highly hydrophobic (GRAVY +2.21); in aqueous buffer, hydrophobic peptides may adsorb nonspecifically to the hydrophobic PLGA surface prior to covalent reaction, increasing local concentration and apparent conjugation efficiency. Conversely, the moderately efficient hydrophilic P2 (GRAVY –0.96) remains well-solvated but uncharged, allowing diffusion to the surface. The bulky D-Phe residue in P4 likely hinders the adjacent cysteine thiol from approaching surface-bound maleimide, explaining its poor yield. [190,191]

Contact angle measurements confirmed that peptide immobilisation can tune the hydrophilicity of inherently hydrophobic PLGA (CA ~121°), but this effect was highly sequence dependent. Only P2 (CREDV) produced a statistically significant reduction in contact angle (to ~104°). This aligns precisely with GRAVY indices: P2 has the most negative index (–0.96), indicating the highest density of hydrophilic side chains (Arg, Glu, Asp). Notably, the hydrophobic P1 (GRAVY +2.21) failed to improve wettability despite a higher conjugation density (~6.6 µg/mg). Thus, peptide sequence identity—specifically its hydropathy profile—is a more potent determinant of wettability than surface density alone.

Soluble peptide screening revealed a dichotomy in fibroblast response. P1, P2, and P3 were well-tolerated, consistent with their ECM protein origins (laminin, fibronectin, collagen). P3 (CGFOGER) actively promoted fibroblast viability above control levels. While GFOGER is classically an α2β1 integrin ligand associated with osteogenesis, [178,179] this data suggests it may also engage fibroblast integrins to stimulate survival or proliferative signalling pathways, independent of a 3D collagen matrix context.

In contrast, P5 (CKAFDITYVRLKF) exhibited dose-dependent cytotoxicity. C16 is a known pro-angiogenic sequence signalling through αvβ3 and α5β1 integrins. [183,184,188] Although fibroblasts express αvβ3, its activation can trigger divergent effects depending on ligand presentation. Soluble C16 may act as an antagonist, disrupting endogenous integrin-mediated adhesion and inducing anoikis-like apoptosis. This underscores a critical principle: a peptide motif that is bioactive when immobilised may be cytotoxic in soluble form. This finding justified excluding P5 from endothelial studies.

Fibroblasts cultured directly on peptide-immobilised scaffolds showed generally favourable responses, with extensive spreading and actin organisation across all surfaces, confirming that covalent immobilisation preserves cell-adhesive functionality. Conversely, a subtle cell-selective response was observed for the P2-scaffold (CREDV). Despite soluble P2 being non-cytotoxic, some fibroblast death occurred on the P2-immobilised surface. REDV is renowned for endothelial cell selectivity, binding preferentially to α4β1 integrin, which is enriched on endothelial cells but expressed at lower levels on fibroblasts. [170,171,173] Fibroblasts rely more heavily on α5β1 (RGD-binding) and αv-containing integrins. Thus, a high local density of REDV may present a surface suboptimal for fibroblast adhesion, validating the intended specificity of this motif.

HUVEC studies revealed an optimal concentration window for bioactivity. For all three peptides tested (P1, P2, P3), the most favourable endothelial response occurred at an intermediate concentration (~50 μg/mL in solution; corresponding surface densities of 4–9 μg/mg on scaffolds). At lower densities, bioactive cues may be insufficient for robust integrin clustering; at higher densities, receptor saturation or steric crowding may paradoxically reduce bioactivity. Among the peptides, P2 (CREDV) demonstrated the most favourable profile for endothelial cells, maintaining high viability even at elevated concentrations. This aligns with its established role in promoting endothelialisation [172,173] and positions the P2-scaffold as the most promising candidate for the luminal surface of a vascular graft. The partial protective effect of peptide functionalisation against PLGA degradation product toxicity further supports this conclusion, suggesting that a healthy endothelial layer may be more resilient to the acidic microenvironment generated during scaffold resorption.

6. Conclusion

Key Insights

The rational design of peptide-decorated nanomaterials has emerged as a powerful strategy for bridging the gap between biologically inert synthetic scaffolds and the complex, dynamic signalling environment of the native extracellular matrix. Over the course of this thesis, three distinct yet complementary approaches were systematically investigated to establish structure–property relationships governing the self-assembly, mechanical performance, and biological activity of peptide-functionalised biomaterials.

6.1. Lipopeptide Nanocolloids

The first project established a minimalist platform to isolate the effect of lipidation on self-assembly. The successful synthesis of high-purity library of stearic acid-conjugated bioactive peptides (DS02, DS04, DS08, DS10, DS12, DS14) enabled a critical demonstration that both the peptide headgroup sequence and the hydrophobic stearic acid tail collaboratively—and sometimes competitively—dictate the final nanostructure. Solid-state ATR-FTIR analysis revealed the expected secondary structure propensities: β-sheet for IKVAV (DS02), (D-Phe)PRP (DS10), and C16 (DS14); α-helical character for REDV (DS04), GFOGER (DS08), and QK (DS12).

However, these conformations did not directly translate into the anticipated fibrillar morphologies. Instead, the hydrophobic C18 tail exerted a dominant influence, promoting interfacial curvature that favoured spherical or vesicular assemblies over extended fibres. This was particularly evident for β-sheet-forming lipopeptides (DS02, DS10 and DS14), which formed spherical aggregates in water:DMSO mixtures despite their known fibril propensity. Among α-helical lipopeptides, a length-dependent trend emerged: the shorter DS04 was dominated by tail-induced curvature, yielding mixed spherical and fibrillar assemblies, while the longer DS12 achieved a better balance, forming more uniform, elongated sphere-like or cuboid structures.

Further, the DLS studies in physiological media PBS buffer highlighted that colloidal stability is heavily dictated by electrostatic charge shielding. In high ionic strength media, the short, highly charged DS04 outperformed longer, more ordered sequences, suggesting that environmental ionic strength is a critical determinant of assembly persistence.

Key Structure-Property Insight: *Secondary structure alone is insufficient to predict self-assembly outcomes in lipopeptides. The interplay between peptide length, net charge, and the hydrophobic tail dictates the final morphology. Short, highly charged sequences confer superior colloidal stability in physiological saline, whereas longer, amphiphilic sequences are optimal for generating uniform, low-dispersity carriers in low-ionic-strength formulations.*

6.2. Amphiphilic Peptide Hydrogels

Building on the finding that the hydrophobic tail dictates morphology, the second project compared two distinct molecular design strategies—lipidation and aggregation-induced emission (AIE) conjugation—to control the structure, mechanics, and bioactivity of peptide-based hydrogels. Critically, the work demonstrated that the nature of the hydrophobic drive dictates the rigidity, reversibility, and functional presentation of the final supramolecular assembly.

For the stearic acid lipopeptides (DS34, DS36), the lipid tail acts as a dominant structural switch, forcing a persistent and thermodynamically stable β-sheet conformation across all concentrations and solvent conditions examined. This architecture produced highly organised, rigid networks with superior storage moduli, ideal for presenting bioactive motifs (e.g., GFOGER) at high density to enhance early-stage cell adhesion. However, this mechanical robustness comes at the cost of poor shear recovery and irreversible disruption under high strain.

On the other hand, for the non-lipidated peptides (DS33, DS35), the absence of the lipid tail yields flexible, conformationally labile structures (Type I β-turns) that are highly sensitive to their solvation environment. While mechanically weaker, these analogues exhibit excellent shear recovery and rapid re-association, making them suitable for applications requiring dynamic restructuring. The measurable critical aggregation concentration of DS35 (0.05 mM) provides a valuable direct window into the monomer-aggregate transition.

The AIE-conjugated peptides (TPE 08 and TPE38) revealed a striking structure–property relationship: a single post-translational modification—the hydroxylation of proline to hydroxyproline—profoundly altered both the supramolecular organisation and photophysical output. TPE 08 (GFOGER) formed smaller, more uniform β-sheet/β-turn assemblies that effectively restricted intramolecular rotation of TPE, resulting in enhanced fluorescence via the AIE mechanism. In contrast, TPE 38 (GFPGER) adopted a mixed α-helical conformation, yielding larger, more polydisperse aggregates with reduced emission intensity. Rheologically, both AIE hydrogels are softer (G' = 10–100 Pa) and more flexible than the lipopeptide systems, reflecting the looser packing enabled by the twisted AIEgen conformation.

Key Structure-Property Insight: *Overall, the lipopeptide strategy prioritised rigidity and stable bioactivity presentation at the expense of dynamic reversibility, whereas the AIE strategy prioritised real-time fluorescence monitoring and conformational flexibility at the expense of mechanical stiffness. Both designs are promising; but, the choice of hydrophobic tail (stearic acid vs. AIE luminogen) and the presence of hydroxyproline depend on the target application. For load-bearing scaffolds requiring stable cell adhesion, the lipopeptide approach is advantageous. For injectable or shear-thinning systems where structural monitoring is* *essential, the AIE-conjugated design offers a label-free, structure-sensitive alternative. Together, these findings provide a clear design rulebook for tuning peptide hydrogel properties through strategic selection of the hydrophobic driving force and minor sequence variations.*

6.3. Peptide-Decorated Vascular Grafts

While the first two projects focused on self-assembled soft materials, the final collaborative project examined the translation of peptide bioactivity to a solid, electrospun PLGA scaffold intended for small-diameter vascular graft applications. A focused library of five cysteine-modified peptides (P1: CIKVAV; P2: CREDV; P3: CGFOGER; P4: C(D-Phe)PRP; P5: CKAFDITYVRLKF) was successfully synthesised and covalently immobilised via thiol–maleimide chemistry.

Conjugation efficiency varied significantly (10–37%), governed primarily by cysteine accessibility and the physicochemical properties of the peptide sequence. The highly hydrophobic P1 (CIKVAV) achieved the highest surface density, while P4 (C(D-Phe)PRP) was poorly conjugated and excluded from further study. Surface wettability was significantly improved only by the most hydrophilic peptide, P2 (CREDV), demonstrating that peptide sequence identity is a more potent determinant of surface hydrophilicity than peptide surface density alone.

Biological screening revealed peptide-dependent and cell-type-specific responses. Soluble P5 (C16) exhibited dose-dependent cytotoxicity towards fibroblasts, underscoring the critical principle that a peptide motif bioactive when surface-immobilised may act as an antagonist in soluble form. The REDV-modified scaffold (P2) emerged as the lead candidate for the luminal surface of a vascular graft, demonstrating selective support for endothelial cell viability, even at elevated concentrations, and partially mitigating the time-dependent cytotoxicity associated with acidic PLGA degradation products. The collagen-mimetic P3 (GFOGER) promoted fibroblast proliferation, suggesting utility for the adventitial layer of a multi-layered graft.

Key Structure-Property Insight: *For peptide-functionalised solid scaffolds, the peptide sequence governs not only the intended biological response but also the efficiency of surface conjugation, the resulting surface wettability, and the cell-type specificity of the interaction. Covalent immobilisation of endothelial-selective peptides (e.g., REDV) can buffer the local cytotoxic effects of polymer degradation while promoting targeted cell adhesion.*

6.4. Future Perspectives

Collectively, the work presented in this thesis establishes a coherent and predictive framework for the rational design of peptide-decorated nanomaterials. The transition from self-assembled lipopeptide nanocolloids to supramolecular hydrogels and, finally, to peptide-functionalised solid scaffolds demonstrates a unifying principle: the molecular architecture of the hydrophobic domain and the physicochemical identity of the bioactive peptide sequence jointly govern the structural, mechanical, and functional properties of the resulting biomaterial.

Future work should focus on several key areas to further translate these findings towards clinical application:

i. Dynamic Hydrogel Systems: Combining the mechanical robustness of the lipopeptide hydrogels with the shear-recovery properties of the non-lipidated or AIE-based systems could yield hybrid materials with optimised properties for 3D bioprinting.

ii. In Vivo Evaluation: The promising in vitro performance of the REDV-functionalised PLGA scaffold and the GFOGER-presenting hydrogels warrants progression to preclinical animal models to assess their efficacy in promoting vascular integration and osteochondral regeneration, respectively.

iii. AIE-Based Biosensing: The intrinsic fluorescence of the TPE-conjugated hydrogels should be exploited for real-time, label-free monitoring of cell-mediated hydrogel remodelling and degradation in vitro and potentially in vivo.

iv. Mixed Peptide Surfaces: The vascular graft platform would benefit from the co-immobilisation of multiple synergistic peptides (e.g., REDV for endothelialisation combined with (D-Phe)PRP for thromboresistance) to more closely mimic the multifunctional nature of the native ECM.

In conclusion, this thesis contributes a comprehensive set of design rules that connect molecular-level peptide engineering to macroscopic material performance, providing a valuable roadmap for the development of next-generation peptide-based biomaterials for regenerative medicine.

7. Experimental section

Materials, Methods & Protocols

7.1. Materials:

All reagents, solvents and consumables were purchased from the companies IRIS Biotech GmbH, Sigma-Aldrich, VWR BDH, and Fluorochem. The purity of all materials fulfilled at least the specifications required for synthesis quality. Anhydrous solvents were used where indicated.

7.2. Project 1 : Lipopeptides-nanocolloids (DS02, DS04, DS08, DS10, DS12, and DS14)

7.2.1. Synthesis and purification of lipopeptides

7.2.1.1. Synthesis of lipopeptides

The precursor peptides (IKVAV, REDV, GFOGER, (D-Phe)PRP, KLTWQELYQLKYKGI, and KAFDITYVRLKF) were synthesised via microwave-assisted Fmoc/tBu solid-phase peptide synthesis (SPPS) on Rink amide resin (100–200 mesh, 0.69 mmol/g). Following chain elongation and final Fmoc deprotection, stearic acid was coupled to the N-terminus of each resin-bound peptide. Initial manual couplings were performed overnight using standard carbodiimide chemistry (Oxyma Pure and DIC). Subsequently, stearic acid coupling was optimised and performed on a Liberty Blue automated microwave peptide synthesiser (CEM Corporation) following the technical procedure published by CEM for fatty acid coupling. The coupling was performed in two steps: (i) 75 °C, 170 W, 15 s, $\Delta T = 2$ °C; (ii) 90 °C, 30 W, 300 s, $\Delta T = 1$ °C. The coupling cycle was repeated twice to maximise yield.

Upon completion, the resin was transferred into a syringe reactor equipped with a fritted filter, washed sequentially with DMF (5 × 4 mL), DCM (5 × 4 mL), and Et_2O (3 × 4 mL), and then dried under a stream of compressed air.

7.2.1.2. Cleavage and Deprotection

The dried resin was treated with a cleavage cocktail solution of Trifluoroacetic acid/TFA (3 mL) with phenol (450 mg), Triisopropylsilane/TIPS (150 µL), thioanisole (150 µL), and deionised water (150 µL). The suspension was agitated on an orbital shaker for 3 h at room temperature. The cleavage solution was then filtered through the syringe frit directly into 40 mL of ice-cold tert-butyl methyl ether/hexane (1:1 v/v) to precipitate the crude peptide. The suspension was centrifuged (4 °C, 6500 rpm, 20 min), the supernatant was discarded, and the peptide pellet was washed twice with ice-cold diethyl ether (Et_2O). The crude peptide was dried under a stream of compressed air. A small aliquot (~1 mg) was dissolved in H_2O/acetonitrile (acn) (1:1 v/v) for analysis by ESI-MS and analytical RP-HPLC.

7.2.1.3. RP-HPLC of lipopeptides

Crude lipopeptides were purified by semi-preparative reverse-phase high-performance liquid chromatography (RP-HPLC) using a Sepachrom Vydamas RP-C8 column (5 µm, 250 × 21.2 mm) on a Jasco LC-NetII/ADC system equipped with a PU-4180 pump and MD-4010 PDA detector. A linear gradient of 20–100% Solvent B in Solvent A over 20 min was employed for all lipopeptides, at a flow rate of 20 mL/min, with detection at λ = 220 nm. Solvent A: H_2O + 0.1% (v/v) TFA; Solvent B: ACN + 0.1% (v/v) TFA. The purified fractions were pooled, frozen, and lyophilised. Purified peptides were stored at –20 °C.

Table 12:List of lipopeptide sequences synthesised by MW-SPPS, their corresponding linear gradient used for purification using semi-preparative RP-HPLC

Code	sequence	RP-HPLC semi-prep gradient*
DS 02	Stearic acid-IKVAV-NH_2	20-100% of B in A over 20 mins
DS 04	Stearic acid-REDV-NH_2	20-100% of B in A over 20 mins
DS 08	Stearic acid-GFOGER-NH_2	20-100% of B in A over 20 mins

DS10	Stearic acid-fPRP-NH_2	20-100% of B in A over 20 mins
DS 12	Stearic acid-KLTWQELYQLKYKGI-NH_2	20-100% of B in A over 20 mins
DS 14	Stearic acid-KAFDITYVRLKF-NH_2	20-100% of B in A over 20 mins

***Solvent system: A: 0.1% (v/v) TFA in 100% H_2O; B: 0.1% (v/v) TFA in 100% CH_3CN. Column: Sepachrom Vydamas RP-C8 column (5 µm, 250 x 21.2 mm). Flow rate: 20 mL/min. λ 220 nm.**

7.2.2. Conformational analysis using ATR-FTIR

FTIR spectroscopy measurements were made on a Perkin Elmer Spotlight 400 FT-IR spectrophotometer equipped with a diamond crystal Attenuated Total Reflection (ATR) accessory. All the samples were analysed at room temperature in the solid state. A total of 32 scans were performed for all measurements with a resolution of 4 cm^{-1} in the 4000-650 cm^{-1} spectral region. Data processing was performed using OriginPro software. The deconvolution of the spectra was done in the spectral region between 1560-1750 cm^{-1}, using the Fit Peaks (Pro) function.

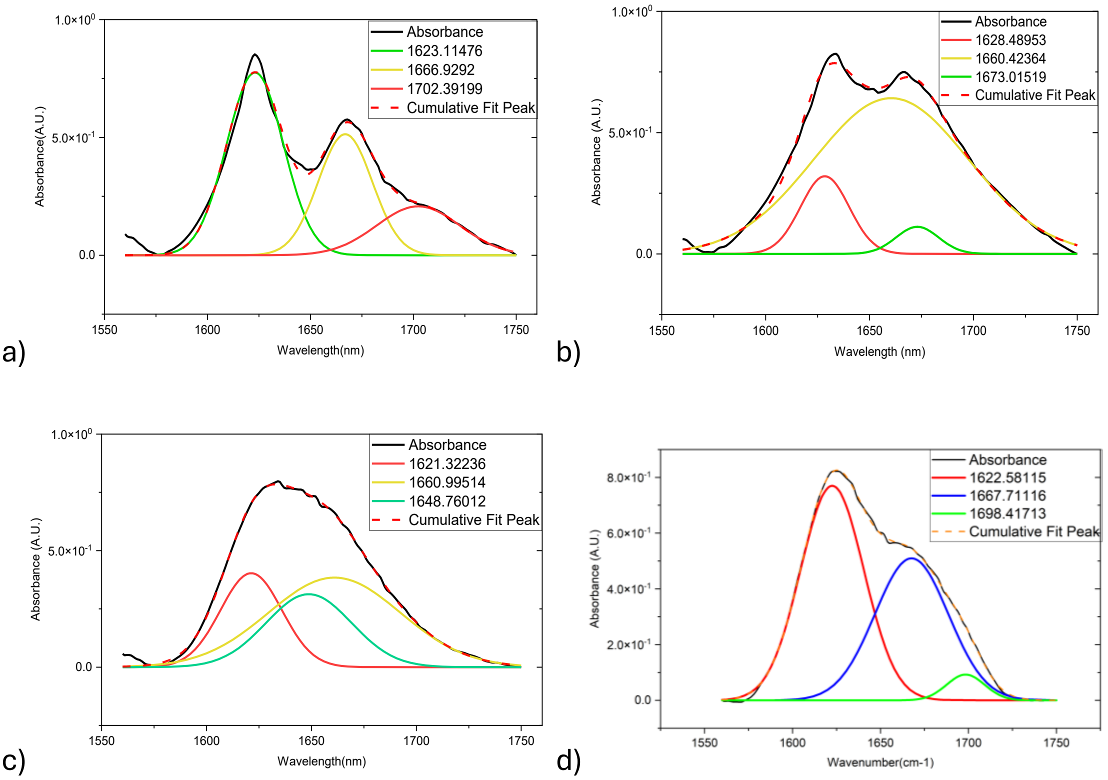

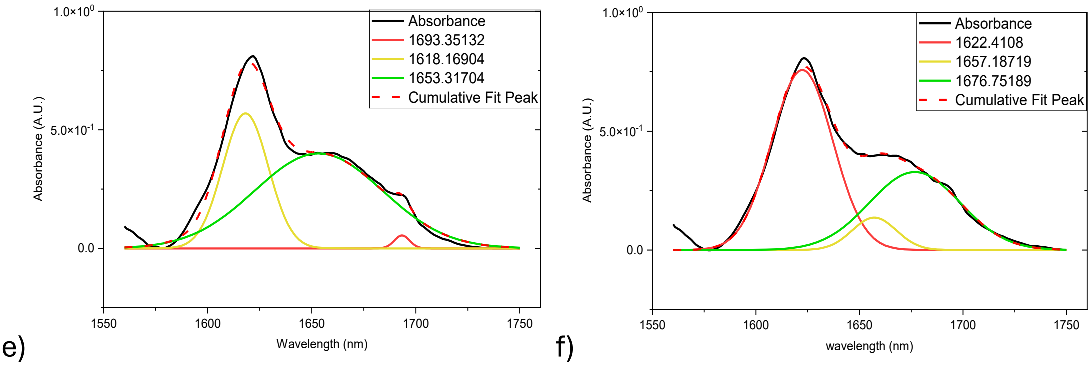

Figure 29 Deconvoluted ATR-FTIR Spectra of the Amide Region (1750–1500 cm^{-1}) of lipopeptides: a) DS02, b) DS04, c)DS08, d) DS10, e)DS12, and f)DS14

7.2.3. Self-Assembly Studies using DLS

Stock solutions of each lipopeptide were prepared in DMSO at a concentration of 2 mM (Stock 1). Serial dilutions were performed with DMSO to obtain Stock 2 (1 mM), Stock 3 (0.5 mM), and Stock 4 (0.25 mM). Nanoprecipitation was performed by adding the DMSO stock solution dropwise to either deionised water or PBS (pH 7.4) under gentle vortexing to achieve final solvent ratios of 1:9 and 0.5:9.5 (DMSO:aqueous v/v), corresponding to final peptide concentrations of 50 μM and 25 μM, respectively. [132]

Dynamic Light Scattering (DLS) measurements were performed using a Malvern Zetasizer Nano ZS instrument (Malvern Panalytical Ltd.) equipped with a 633 nm He–Ne laser operating at a scattering angle of 173° (backscatter detection). Measurements were conducted at 25 °C after the nanocolloid dispersions had been aged for 24–48 h at room temperature. Viscosity and refractive index values for the DMSO/water and DMSO/PBS mixtures were obtained from literature data. [192] Hydrodynamic diameters (Z-average) and polydispersity indices (PDI) were averaged from at least three independent measurements, each consisting of 12–15 sub-runs.

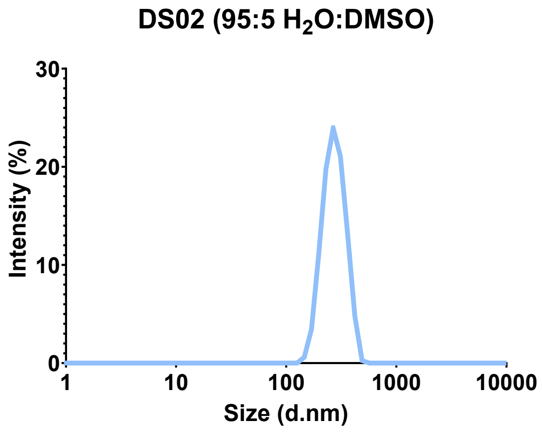
DS02 (95:5 H_2O:DMSO)
Intensity (%)
0
10
20
30
1
10
100
1000
10000
Size (d.nm)

a)

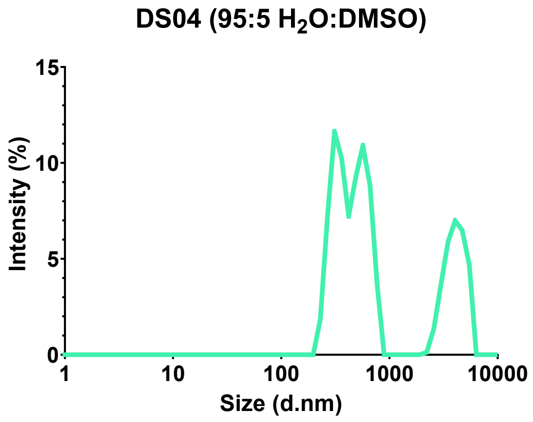
DS04 (95:5 H_2O:DMSO)
Intensity (%)
0
5
10
15
1
10
100
1000
10000
Size (d.nm)

b)

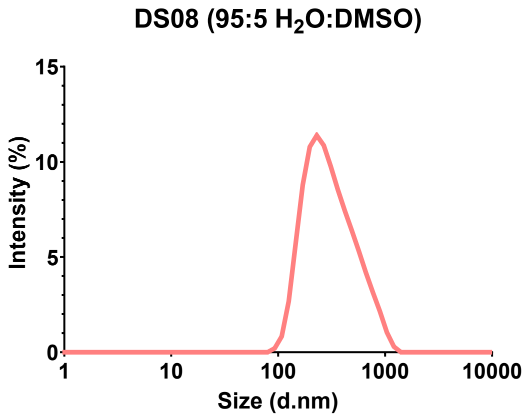
DS08 (95:5 H_2O:DMSO)
Intensity (%)
0
5
10
15
1
10
100
1000
10000
Size (d.nm)

c)

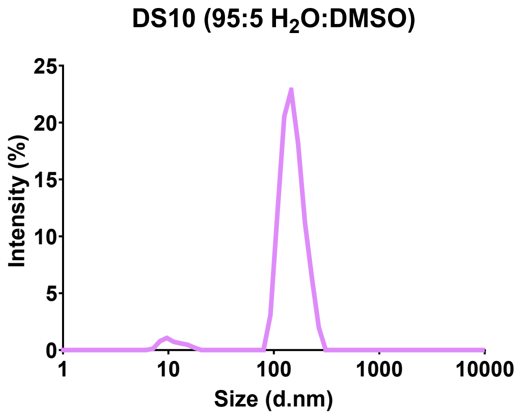
DS10 (95:5 H_2O:DMSO)
Intensity (%)
0
5
10
15
20
25
1
10
100
1000
10000
Size (d.nm)

d)

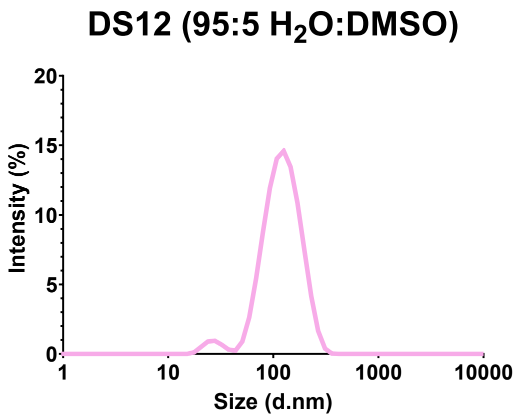
DS12 (95:5 H_2O:DMSO)
Intensity (%)
0
5
10
15
20
1
10
100
1000
10000
Size (d.nm)

e)

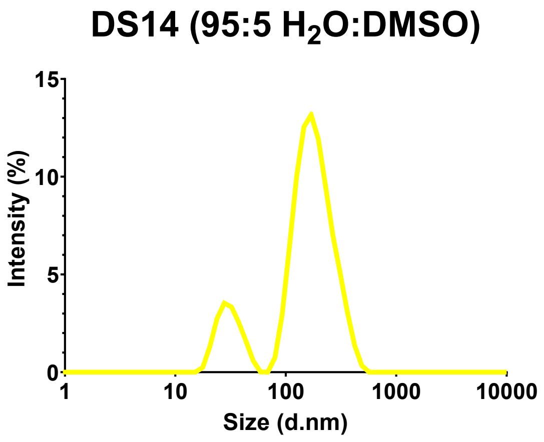
DS14 (95:5 H_2O:DMSO)
Intensity (%)
0
5
10
15
1
10
100
1000
10000
Size (d.nm)

f)

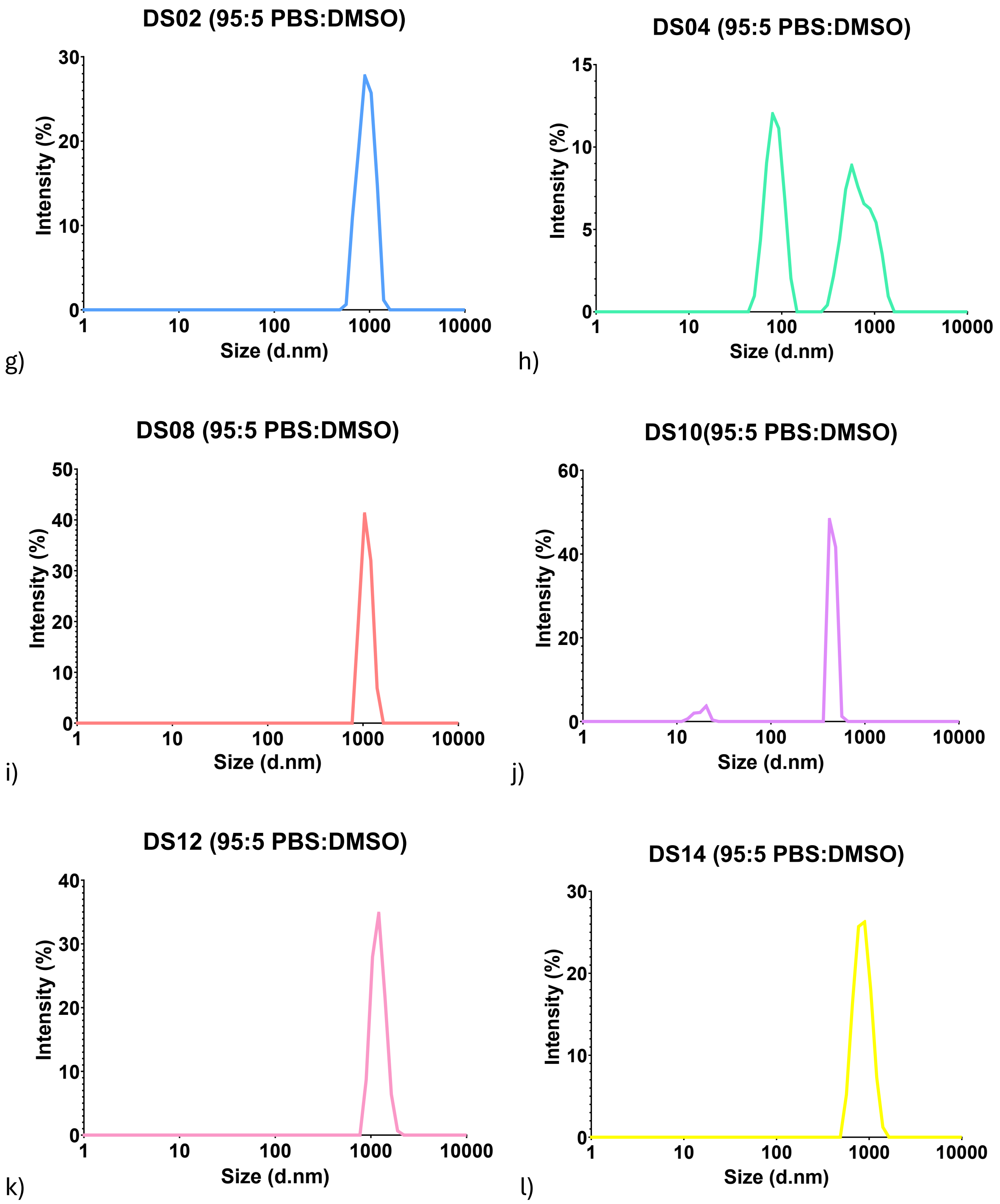

Figure 30 (a-f) DLS intensity vs. size graphs of 25 μM peptides: (a) DS02, (b) DS04, (c) DS08, (d) DS10, (e) DS12, and (f) DS14 in 95:5 (v/v) water:DMSO solution. (g–l) DLS intensity vs. size graphs of 25 μM peptides: (g) DS02, (h) DS04, (i) DS08, (j) DS10, (k) DS12 and (l) DS14 in 95:5 (v/v) PBS: DMSO solution.

7.2.4. SEM

Nanocolloid dispersions were prepared via solvent displacement as described in Section 8.2.3, using a 95:5 water:DMSO ratio and a final peptide concentration of 25 μM. Dispersions were aged for 24 h at room temperature. An aliquot of each dispersion was deposited onto a silicon wafer or aluminium SEM stub and allowed to air-dry completely. The dried samples were sputter-coated with a thin layer of gold (approx. 10 nm) to enhance conductivity. Imaging was performed using a JEOL JSM-IT500 scanning electron microscope operating under high vacuum at an accelerating voltage of 5–10 kV.

7.3. Amphiphilic Peptide Hydrogels (DS33, DS34, DS35, DS36, TPE 08 and TPE 38)

7.3.1. Synthesis and Purification of Peptide Amphiphiles

7.3.1.1. Synthesis of 4-amino TPE

4-Amino-tetraphenylethene was synthesised via a McMurry coupling reaction following a previously published protocol. [193] Briefly, $TiCl_4$ (2.63 mL, 24 mmol, 5 eq) was added dropwise to a stirred suspension of zinc dust (3.2 g, 48 mmol, 10 eq) in anhydrous THF (30 mL) cooled to –10 °C in an ice-salt bath. The mixture was stirred for 10 min, allowed to warm to room temperature, and then heated under reflux at 66 °C for 2 h. The mixture was then cooled to –10 °C, and a solution of benzophenone (1.05 g, 5.76 mmol, 1.2 eq) and 4-aminobenzophenone (0.95 g, 4.8 mmol, 1 eq) in anhydrous THF (80 mL) was added slowly. The reaction was heated under reflux for a further 2 h under an inert atmosphere. After cooling to room temperature, the reaction was quenched by slow addition to 10% (w/w) aqueous K_2CO_3 (100 mL) and stirred vigorously overnight. The mixture was filtered, extracted with EtOAc, and the combined organic layers were washed with brine and dried over anhydrous Na_2SO_4. After filtration, the solvent was removed under reduced pressure, and the crude residue was purified by flash column chromatography (silica gel, eluent gradient) to afford the title compound as a pale yellow solid. To increase the yield, the reaction was repeated on a larger scale, as the $TiCl_4$ reagent is extremely sensitive to moisture, which can adversely affect the yield in small-scale synthesis.

7.3.1.2. Synthesis of (14-oxo-14-((4-(1,2,2-triphenylvinyl)phenyl)amino)tetradecandioic acid))

Tetradecandioic acid (0.87 g, 3.38 mmol, 3 eq) was dissolved in a mixture of anhydrous DCM/DMF (2:1 v/v). HBTU (0.47 g, 1.24 mmol, 1.1 eq relative to TPE-NH_2) was added under a nitrogen atmosphere. The solution was cooled in an ice bath, and anhydrous DIPEA (1.175 mL, 6.75 mmol, 6 eq) was added slowly. The reaction mixture was removed from the ice bath, and a solution of TPE-NH_2 (0.39 g, 1.125 mmol, 1 eq) in a minimum volume of anhydrous DCM was added slowly. The reaction was stirred overnight at room temperature under an inert atmosphere. The solvent was evaporated under reduced pressure, and the residue was diluted with DCM and washed with brine. The organic layer was dried over Na_2SO_4, filtered, and concentrated in vacuo. The crude product was purified by flash column chromatography (DCM/MeOH gradient) to yield the pure TPE-acid linker as confirmed by previous characterisation. The stoichiometric ratio was strictly adhered to as it had been previously optimised to ensure selective activation of only one carboxyl group. [132]

The analytical characterisations (^{1}H and ^{13}C NMR) of the TPE-fatty acid hybrid was consistent with the previously published data from our laboratory. [46,133]

^{1}H NMR (400 MHz, DMSO-*d*$_6$) δ = 11.93 (1 H, s), 9.78 (1 H, s), 7.34 (2 H, d, J 8.3), 7.22 – 7.04 (10 H, m), 6.97 (5 H, dd, J 13.6, 7.0), 6.86 (2 H, d, J 8.2), 2.21 (4 H, dt, J 23.1, 7.4), 1.52 (4 H, dt, J 25.9, 6.9), 1.25 (16 H, d, J 7.4)

^{13}C NMR (100 MHz, DMSO-*d*$_6$) δ= 174.96, 171.65, 143.89, 143.80, 143.74, 140.73, 140.49, 138.18, 138.16, 131.49, 131.17, 131.12, 128.33, 128.24, 128.22, 126.97, 126.91, 126.87, 118.75, 36.86, 34.15, 29.46, 29.43, 29.38, 29.25, 29.20, 29.12, 29.01, 25.56, 24.97

ESI-MS (m/z) calculated for $C_{40}H_{45}NO_3$ 588.34, found 587.32 [M-H]-.

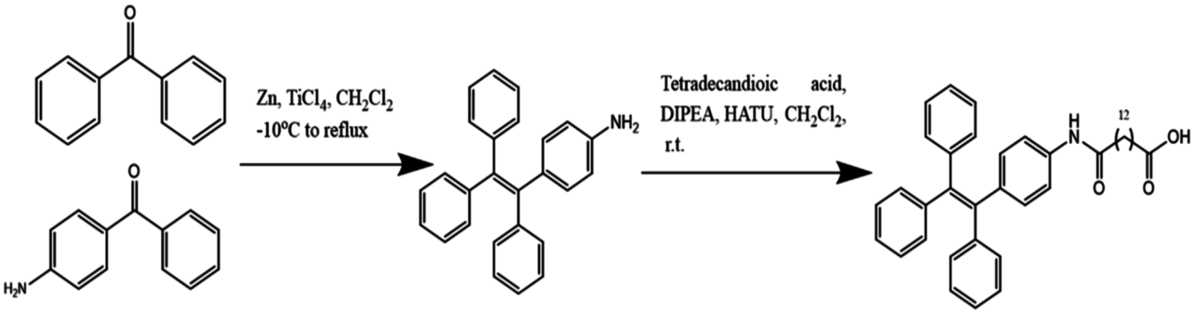

Figure 31 Scheme for synthesis of TPE acid- for late-stage peptide functionalisation

7.3.1.3. General Procedure for Microwave-Assisted SPPS of Peptide Precursors

All linear peptide precursors (DS33, DS35 and the peptide segments of DS34, DS36) were synthesised on a Liberty Blue automated microwave peptide synthesiser (CEM Corporation) using the Fmoc/tBu strategy. Syntheses were performed on a 0.05 mmol scale using Fmoc-Rink amide AM resin (100–200 mesh, loading 0.7 mmol/g). The resin was pre-swollen in DMF (1 mL) for 30 min before synthesis.

Deprotection: Fmoc deprotection was performed using 20% (v/v) piperidine in DMF in two stages: (i) 80 °C, 200 W, 30 s, ΔT = 2 °C; (ii) 90 °C, 50 W, 70 s, ΔT = 1 °C. The resin was then washed with DMF (4 × 5 mL).

Coupling: Amino acid couplings were performed using a five-fold molar excess of Fmoc-AA-OH (0.2 M in DMF), DIC (0.25 M in DMF), and Oxyma Pure (0.5 M in DMF). The standard coupling cycle consisted of two stages: (i) 75 °C, 170 W, 15 s, ΔT = 2 °C; (ii) 90 °C, 30 W, 70 s, ΔT = 1 °C. For sterically hindered or Arg residues, a double-coupling protocol was employed.

Upon completion of the linear sequence and final Fmoc deprotection, the resin was washed with DMF (5 × 5 mL), DCM (5 × 5 mL), and Et_2O (3 × 5 mL) and dried under a stream of nitrogen.

7.3.1.4. Coupling of Stearic acid (DS34 and DS36)

Stearic acid was coupled to the N-terminus of the resin-bound FQFQFKGFPGER and FQFQFKGFOGER sequences directly on the Liberty Blue instrument. The coupling protocol followed the CEM technical procedure for fatty acid coupling: (i) 75 °C, 170 W, 15 s, $\Delta T = 2$ °C; (ii) 90 °C, 30 W, 300 s, $\Delta T = 1$ °C. The coupling cycle was repeated twice. Following coupling, the resin was washed and dried as described above.

7.3.1.5. Manual Coupling of TPE -Acid Linker (TPE 08 and TPE 38)

For the AIE peptides, the TPE-acid linker was coupled manually to the N-terminus of the resin-bound GFOGER and GFPGER sequences. The coupling was performed using a solution of TPE-acid/HBTU/HOBt/DIPEA (2.5:3:3:6 molar equivalents relative to resin loading) in 1:1 DCM:DMF. The reaction was agitated overnight at room temperature. Completion of the coupling was confirmed by a negative Kaiser test. The resin was then washed thoroughly with DMF, DCM, and Et_2O, and dried under nitrogen flow.

7.3.1.6. Cleavage, Deprotection and Purification

Cleavage and side chain deprotection were performed using the same procedure described in Section 7.2.1.2. Crude peptides were purified by semi-preparative RP-HPLC using the same instrumentation and column described in Section 7.2.1.3. Peptide-specific linear gradients are detailed in Table 13. Purified fractions were lyophilised and stored at –20 °C.

Table 13:Peptide Amphiphile Library and RP-HPLC Purification Gradients

Code	Sequence	RP-HPLC semi-prep gradient*
DS33	FQFQFKGFPGER-NH_2	15-35% of B in A over 20 mins
DS34	Stearic acid-FQFQFKGFPGER-NH_2	70-90% of B in A over 20 mins
DS35	FQFQFKGFOGER-NH_2	18-38% of B in A over 20 mins
DS36	Stearic acid-FQFQFKGFOGER-NH_2	55-75% of B in A over 20 mins
TPE 08	TPE acid-GFOGER-NH_2	60-80% of B in A over 20 mins
TPE 38	TPE acid-GFPGER-NH_2	55-75% of B in A over 20 mins

***Solvent system: A: 0.1% (v/v) TFA in 100% H_2O; B: 0.1% (v/v) TFA in 100% CH_3CN. Column: Sepachrom Vydamas RP-C8 column (5 µm, 250 x 21.2 mm). Flow rate: 20 mL/min. λ 220 nm.**

7.3.2. Conformational analysis of peptides – ATR-FTIR

FTIR spectroscopy was performed as described in Section 7.2.2 on lyophilised peptide powders.

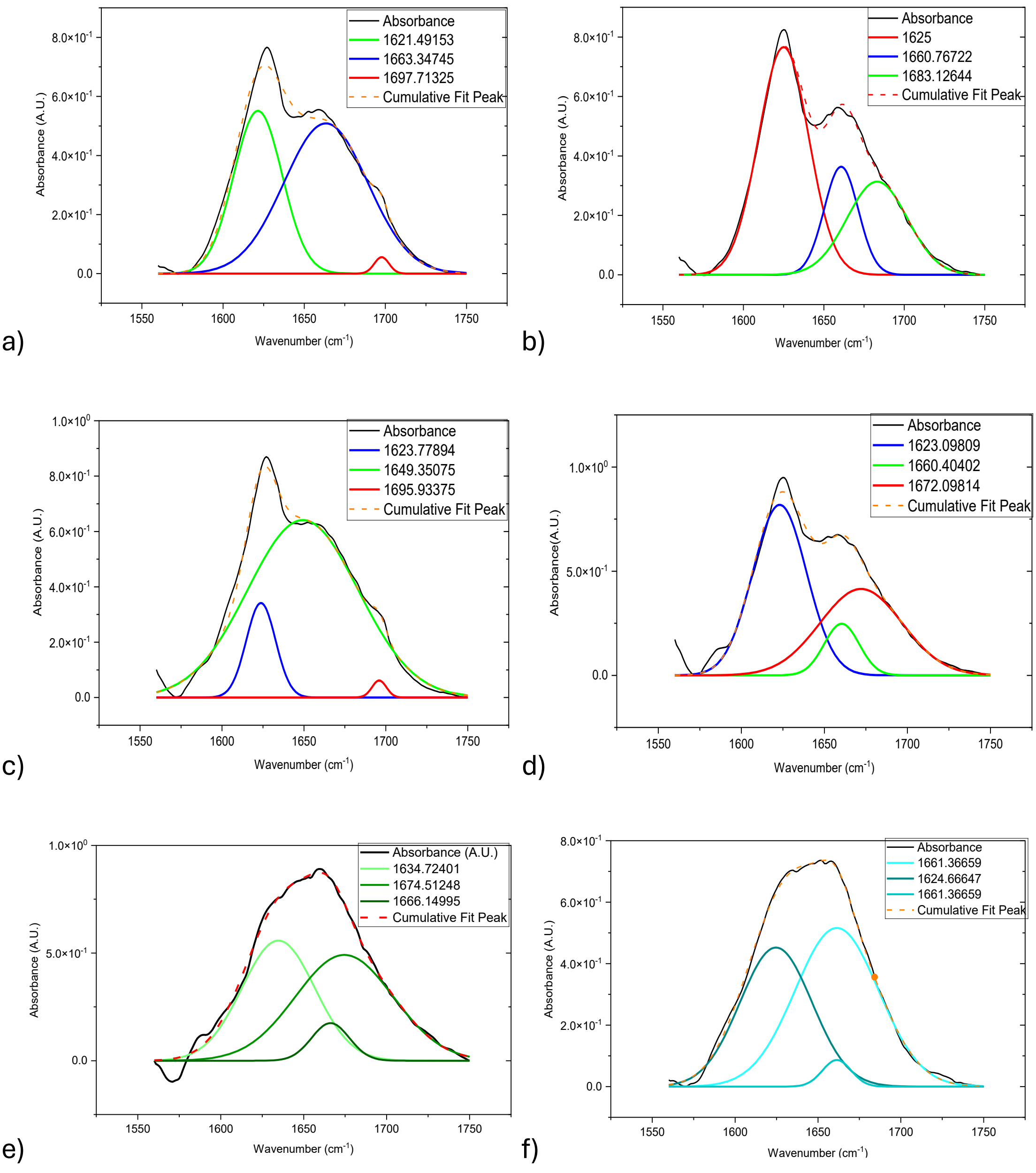

Figure 32 Deconvoluted ATR-FTIR Spectra of the Amide Region (1750–1500 cm^{-1}) of Peptide Hydrogels: a)DS33, b)DS34, c)DS35, d) DS36, e)TPE 08 and f)TPE 38

7.3.3. Self-Assembly Studies using DLS

DLS sample preparation and measurements were performed as described in Section 7.2.3, using a final peptide concentration of 50 µM in 9:1 (v/v) water:DMSO and PBS:DMSO mixtures.

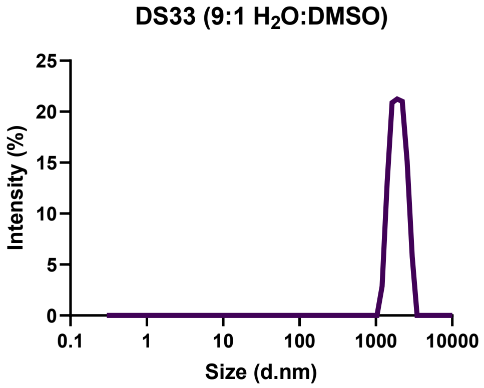

a)

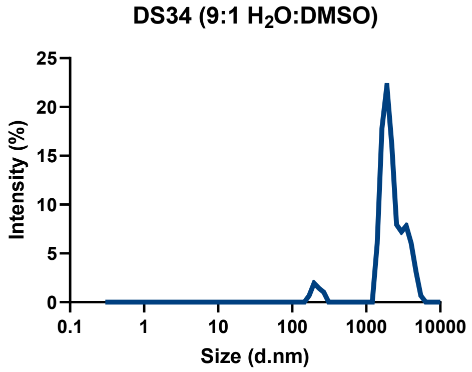

b)

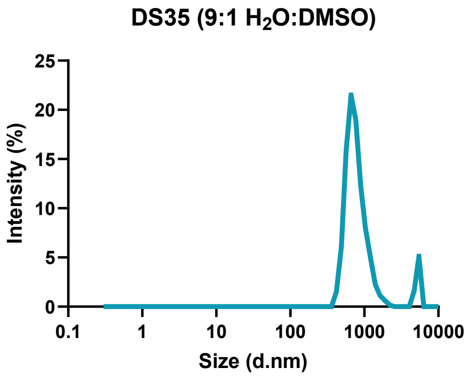

c)

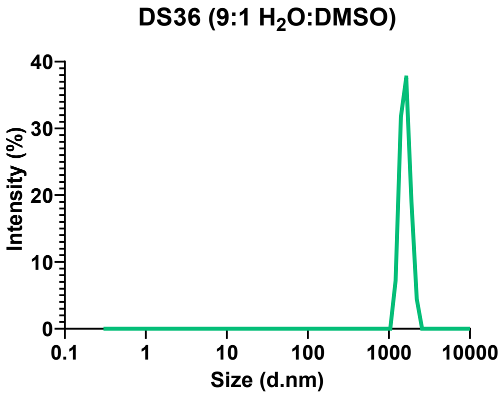

d)

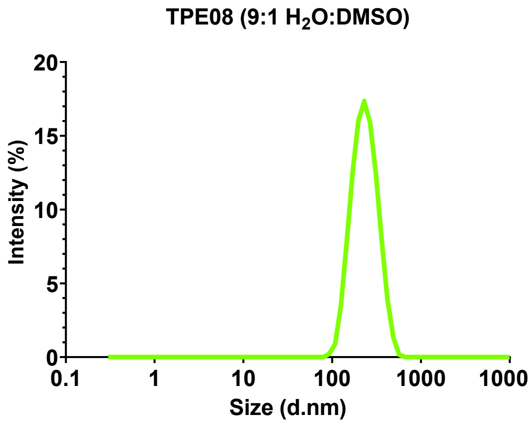

e)

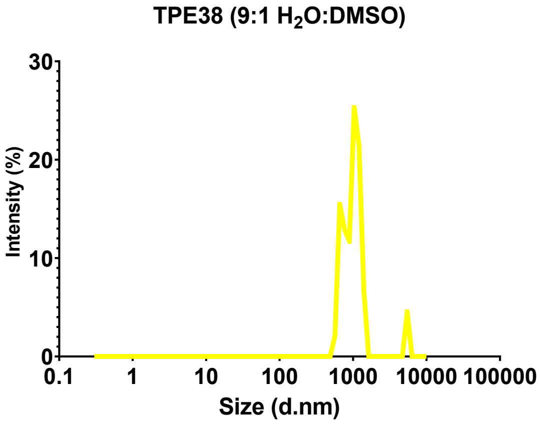

f)

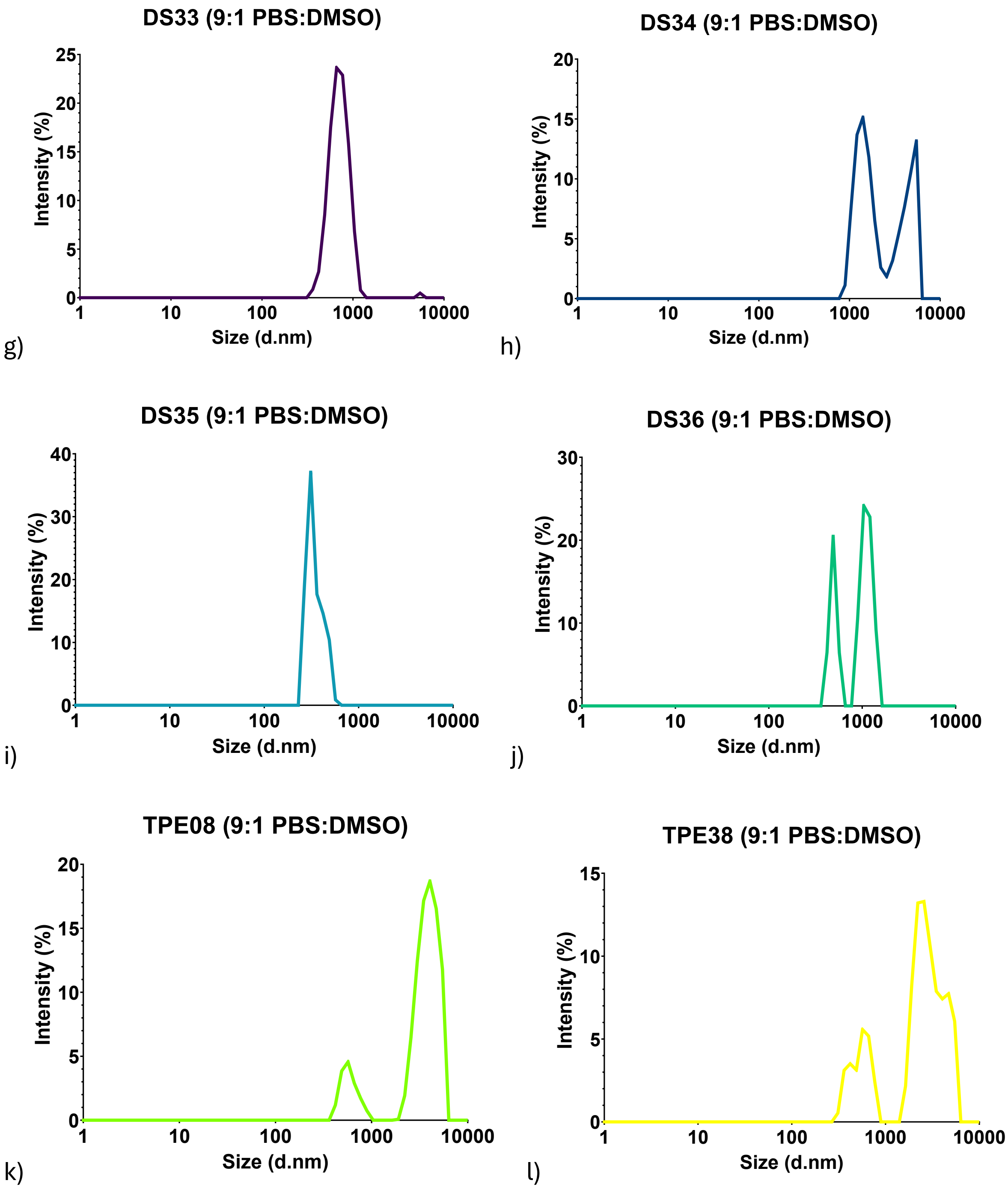

Figure 33 (a-f) DLS intensity vs. size graphs of 50 µM peptides: (a) DS33, (b) DS34, (c) DS35, (d) DS36, (e) TPE 08, and (f) TPE 38 in 9:1 (v/v) water:DMSO solution. (g–l) DLS intensity vs. size graphs of 50 µM peptides: (g) DS33, (h) DS34, (i) DS35, (j) DS36, (k) TPE 08, and (l) TPE 38 in 9:1 (v/v) PBS:DMSO solution.

7.3.4. Hydrogel formation

Hydrogels were prepared by dissolving the lyophilised peptide in 1× PBS (pH 7.4) to the desired final concentration (w/v %). The mixture was alternately vortexed and sonicated in a room-temperature water bath for 3 min to ensure complete dissolution and initiation of self-assembly. Hydrogel formation was confirmed by the vial inversion test after incubation at room temperature for a minimum of 30 min.

7.3.4.1. Rheology

Rheological measurements were performed using a TA Instruments Discovery HR-30 rheometer equipped with a stainless steel 20 mm parallel plate geometry. The temperature was maintained at 37 °C throughout all experiments using a Peltier plate. Freshly prepared hydrogels were loaded onto the Peltier plate, the geometry was lowered to a gap of 0.5 mm, and the sample perimeter was covered with a solvent trap to prevent evaporation. Samples were allowed to equilibrate for 5 min prior to measurement.

- Frequency Sweep: Performed at a constant oscillatory strain of 1% (within the linear viscoelastic region, LVER) over a frequency range of 10 to 0.1 Hz (log scale, 5 points per decade).
- Amplitude Sweep: Performed at a constant frequency of 1 Hz over an oscillatory strain range of 0.1% to 100% (log scale, 5 points per decade).
- Time Sweep: Performed at a constant frequency of 1 Hz and strain of 1% for a duration of 1 h (sampling interval: 10 s/point).
- Flow Sweep: Performed using a logarithmic shear rate ramp from 0.01 to 100 s^{-1} (5 points per decade).
- Thixotropy (Step-Strain): Performed at a constant frequency of 1 Hz with alternating strain intervals: (i) 1% strain for 60 s, (ii) 100% strain for 30 s, (iii) 1% strain for 1800 s (sampling interval: 3 s/point during all steps).

7.3.4.2. Circular Dichroism

Circular dichroism spectra were recorded on a Jasco J-815 spectropolarimeter equipped with a Peltier temperature controller set to 37 °C. A quartz cuvette with a path length of 0.05 cm was used for all measurements. Spectra were acquired from 190 to 300 nm with a data pitch of 0.2 nm, a scanning speed of 500 nm/min, and a response time of 1 s. Three consecutive scans were accumulated and averaged for each sample. The spectrum of the corresponding blank solvent was subtracted from each sample spectrum. Data were converted to mean residue ellipticity (θ, degree·cm^2·dmol^{-1}) using the following formula

$$\boldsymbol{\theta} = \frac{(\boldsymbol{\theta_{Obs}} \times \boldsymbol{MRW})}{(\mathbf{10} \times \boldsymbol{c} \times \boldsymbol{l})}$$

where θ_obs is the measured ellipticity in millidegrees, MRW is the mean residue weight, c is the peptide concentration in mg/mL, and l is the path length in cm.

7.3.4.2.1. Concentration-Dependent CD in Aqueous Solution

Hydrogels were initially prepared in PBS at their respective MGCs (DS33 and DS35: 6% w/v; DS34: 4% w/v; DS36: 2% w/v). These stock hydrogels were diluted with deionised water to obtain a 1 mM stock solution (based on peptide concentration). This stock was further diluted with deionised water to yield final peptide concentrations of 0.2, 0.1, and 0.05 mM for CD analysis.

7.3.4.2.2. Solvent-Dependent CD in Water/Methanol Mixtures

Stock solutions of each peptide were prepared in methanol (MeOH) at a concentration of 10 mM. These stocks were diluted with appropriate mixtures of MeOH and deionised water to achieve a final peptide concentration of 0.25 mM in the following solvent compositions (v/v): A) 100% MeOH; B) 1:1 MeOH/water; C) 3:7 MeOH/water; D) 2:8 MeOH/water; E) 1:9 MeOH/water; F) 0.5:9.5 MeOH/water. [194]

7.3.4.3. SEM

Hydrogels prepared at their respective minimum gelation concentrations (MGC) were flash-frozen in liquid nitrogen and lyophilised for 48 h to obtain xerogels. The dried xerogels were carefully fractured to expose the internal porous structure, mounted onto aluminium SEM stubs using carbon adhesive tape, and sputter-coated with a 10 nm layer of gold. Imaging was performed using a Phenom-World ProX scanning electron microscope operating at an accelerating voltage of 10 or 15 kV.

7.3.5. Biological evaluation

The $C_3H_{10}T_{1/2}$ mouse mesenchymal stromal cell line was cultured in complete proliferation medium consisting of DMEM low glucose supplemented with 10% (v/v) fetal bovine serum (FBS), 1% (v/v) penicillin/streptomycin, and 1% (v/v) L-glutamine. Cells were maintained at 37 °C in a humidified incubator with 5% CO_2 and passaged at 70–80% confluency.

7.3.5.1. Cytotoxicity Evaluation (LDH Assay)

Cytotoxicity of the hydrogels was evaluated using an indirect contact method (transwell inserts) and quantified via the Lactate Dehydrogenase (LDH) assay. $C_3H_{10}T_{1/2}$ cells were seeded in the lower compartment of a 24-well transwell plate and allowed to adhere overnight. Hydrogels were prepared in situ within the transwell inserts and placed into the wells, ensuring no direct contact between the hydrogel and the cell monolayer. After 72 h of incubation, aliquots of the culture medium were collected from the lower compartment and analysed for LDH release using a commercial LDH cytotoxicity assay kit according to the manufacturer's instructions. Luminescence was measured using a plate reader. Cell viability was also qualitatively assessed by staining the cell monolayer in the lower compartment with Invitrogen™ Live/Dead™ viability/cytotoxicity stain and imaging by confocal microscopy [143,194]

7.3.5.2. Cell Adhesion Assay

Cell adhesion to the hydrogel surfaces was quantified using the CellTiter-Glo® luminescent cell viability assay. Hydrogels were prepared directly in the wells of a 96-well plate. $C_3H_{10}T_{1/2}$ cells were seeded onto the surface of the pre-formed hydrogels at a density of 1×10^4 cells per well. After incubation for predetermined time points (30 min, 1 h, 2 h, and 4 h) at 37 °C, non-adherent cells were removed by gentle washing with DPBS. Adherent cells were quantified by adding CellTiter-Glo® reagent directly to the wells and measuring luminescence. Adhesion was expressed as a percentage of the luminescence signal from a 100% adhesion control (cells seeded directly onto tissue culture-treated plastic without a washing step). For qualitative visualisation, parallel samples were stained with Invitrogen™ Live/Dead™ stain after 4 h of incubation and imaged by confocal microscopy.

7.3.5.3. Cell Encapsulation:

To assess the cytocompatibility of the hydrogels in a 3D environment, a cell encapsulation assay was performed. $C_3H_{10}T_{1/2}$ cells were harvested and gently resuspended in the peptide solution (prepared in PBS) prior to the initiation of gelation. The cell-laden solution was then transferred to a suitable culture vessel and allowed to undergo gelation at 37 °C. After 7 days of culture, with a medium change every 2–3 days, cell viability was assessed by staining the cell-laden hydrogels with Invitrogen™ Live/Dead™ stain and imaging by confocal microscopy. Z-stack images were acquired to visualise cell distribution and viability throughout the depth of the hydrogel. [147]

7.3.6. 3D printing (DS36)

A DS36 hydrogel was prepared at 2% w/v in PBS as described in Section 8.3.4 and loaded into a 3 mL syringe barrel. Printing tests were performed using a BioX 3D bioprinter (CELLINK). Printing parameters were optimised by systematically varying extrusion pressure (starting from

1 kPa) and printhead speed (starting from 1 mm/s). Two different extrusion tips were evaluated: a 0.41 mm conical nozzle and a 0.21-inch (approx. 27G) blunt needle. The optimal parameters identified for filament extrusion were a pressure of 4 kPa and a print speed of 12 mm/s.

7.4. Peptide-decorated modular SDVG

7.4.1. Electrospun Scaffold Fabrication

7.4.1.1. Fabrication of PLGA Electrospun Scaffolds

Poly(lactide-co-glycolide) (PLGA, 50:50 lactide:glycolide ratio, Mw ~66 kDa, PURASORB®) was dissolved in 1,1,1,3,3,3-hexafluoro-2-propanol (HFIP) at a concentration of 25% w/v by stirring overnight in a tightly sealed glass vial. Electrospinning was performed using a NANON 01A vertical electrospinning device (MECC Co. Instruments Ltd.). The polymer solution was loaded into a syringe fitted with a 22G blunt-type needle and dispensed at a flow rate of 0.1 mL/h. A voltage of 15 kV was applied between the needle tip and a flat aluminium collector plate positioned at a distance of 15 cm. Electrospinning was conducted for 2 h. The resulting fibrous scaffolds were dried overnight in a fume hood to evaporate residual HFIP. Scaffold thickness was measured using a digital calliper.

7.4.1.2. Morphological Characterisation of Plain Scaffolds

The morphology and fibre uniformity of the plain PLGA scaffolds were evaluated by scanning electron microscopy (SEM, Mira3 XMU, Tescan). Samples were sputter-coated with gold prior to imaging at an accelerating voltage of 20 kV. Fibre diameter distributions were quantitatively analysed using ImageJ software, measuring at least 100 individual fibres per sample. [195]

7.4.1.3. Mechanical Characterisations of Plain Scaffolds

The mechanical properties of the plain PLGA scaffolds were evaluated using a uniaxial tensile testing machine (Mark-10 Tensile Testers). Scaffolds were cut into dog-bone shaped specimens using a calibrated cutter conforming to ASTM D-882 standard dimensions. Tests were performed in triplicate at a crosshead speed of 20.1 mm/min. Stress and strain values were calculated according to the standard equations:

Stress (MPa) = Load (N) / Cross-sectional Area (mm^2)

Strain = Extension (mm) / Initial Gauge Length (mm)

The ultimate tensile strength (UTS), Young's modulus, yield strength, yield strain, breaking point stress, and elongation at break were determined from the resulting stress–strain curves.

7.4.2. Synthesis and purification of cysteine peptides

7.4.2.1. MW-assisted solid phase peptide synthesis of bioactive peptides with cysteine: (P1, P2, P3, P4, and P5)

Peptides P1 (CIKVAV-NH_2), P2 (CREDV-NH_2), P3 (CGFOGER-NH_2), P4 (C(D-Phe)PRP-NH_2), and P5 (CKAFDITYVRLKF-NH_2) were synthesised using the Liberty Blue automated microwave peptide synthesiser following the general Fmoc/tBu SPPS procedure described in Section 7.2.1.1. An N-terminal cysteine residue was incorporated as the final coupling step. Upon completion of the synthesis, the peptide-bound resins were washed sequentially with DMF (5 × 5 mL), DCM (5 × 5 mL), and Et_2O (3 × 5 mL), and subsequently dried under a gentle stream of nitrogen. This drying step is essential to prevent oxidation of the free cysteine thiol group, which would otherwise form disulfide bonds and render the peptide unreactive towards the maleimide-functionalised scaffold surface.

7.4.2.2. Cleavage of cysteine-containing peptides

Upon completion of the synthesis, the resin was transferred to a syringe reactor and washed/dried as previously described. Cleavage and global deprotection were achieved using a modified cocktail optimised for cysteine-containing peptides to minimise oxidation and side reactions. The cleavage solution consisted of TFA (3.6 mL), thioanisole (280 µL), and DODT

(120 µL). The reaction was agitated for 3 h at room temperature. The cleavage solution was filtered into 40 mL of ice-cold tert-butyl methyl ether/hexane (1:1 v/v). The precipitated peptide was collected by centrifugation (4 °C, 6500 rpm, 20 min), washed twice with ice-cold Et_2O, and dried under nitrogen flow.

7.4.2.3. RP-HPLC of cysteine peptides

Crude peptides were purified by semi-preparative RP-HPLC using a Sepachrom Robusta C18 column (10 µm, 250 × 21.2 mm). A linear gradient of 5–70% Solvent B in Solvent A over 20 min was employed for all peptides (flow rate: 10 mL/min, λ = 220 nm). Purified fractions were pooled, lyophilised, and stored at –20 °C. Peptide purity was assessed by analytical RP-HPLC using a Phenomenex Gemini-NX C18 column (5 µm, 150 × 4.6 mm) with a flow rate of 0.8 mL/min and identical solvent system. Peptide identity was confirmed by ESI-MS on a Finnigan LCQ Fleet ion trap spectrometer (Thermo Scientific).

Table 14:Cysteine-Modified Peptide Library and RP-HPLC Purification Gradients

Code	Sequence	RP-HPLC semi-prep gradient*
P1	CIKVAV-NH_2	5-70% of B in A over 20 mins
P2	CREDV-NH_2	5-70% of B in A over 20 mins
P3	CGFOGER-NH_2	5-70% of B in A over 20 mins
P4	CfPRP-NH_2	5-70% of B in A over 20 mins
P5	CKAFDITYVRLKF-NH_2	5-70% of B in A over 20 mins

***Solvent system: A: 0.1% (v/v) TFA in 100% H_2O; B: 0.1% (v/v) TFA in 100% CH_3CN. Column: Sepachrom Robusta C18 column (10 µm, 250 x 21.2 mm). Flow rate: 10 mL/min. λ 220 nm.**

7.4.3. Peptide Immobilisation

7.4.3.1. Peptide Immobilisation via Thiol-Maleimide Chemistry

Plain PLGA scaffolds were first activated by incubation in a solution of EDC (2 mM) and NHS (5 mM) in MES buffer (0.1 M, pH 5–6) for 2 h at room temperature. Following activation, scaffolds were gently rinsed and subsequently immersed in a solution of a heterobifunctional maleimide-PEG-amine linker (10 molar equivalents relative to the calculated molar quantity of PLGA carboxyl groups) in MES buffer containing 5 µL DIPEA. The reaction was allowed to proceed overnight (16–18 h) at room temperature. Scaffolds were then thoroughly washed with deionised water to remove unreacted linker.

Cysteine-modified peptides (P1–P5) were dissolved in 1× PBS (pH 7.4) containing TCEP (2 molar equivalents relative to the peptide) as a reducing agent to prevent disulfide bond formation. The peptide solutions were stirred for 30 min at room temperature. The maleimide-functionalised scaffolds were immersed in the respective peptide solutions (using 3 molar equivalents of peptide relative to the calculated quantity of PLGA) and incubated for 4 h at room temperature to facilitate thiol–maleimide Michael addition. Following immobilisation, the peptide-conjugated scaffolds (designated P1-scaffold, P2-scaffold, etc.) were removed from the peptide solutions and washed gently with PBS (2×). The initial and post-immobilisation peptide solutions were retained for indirect quantification.

7.4.4. Physiochemical Characterisations of Peptide Immobilised Scaffolds

7.4.4.1. Morphological Evaluations

The morphology and fibre diameter of the peptide-immobilised scaffolds were evaluated by SEM as described in Section 7.4.1.2.

7.4.4.2. *Quantification of Peptide Immobilisation*

Peptide conjugation was quantified indirectly by analytical RP-HPLC using an Agilent 1260 Infinity system equipped with a C18 reversed-phase column (150 × 4.6 mm, 5 µm). The mobile phase consisted of Solvent A (H_2O + 0.1% TFA) and Solvent B (ACN + 0.1% TFA). The gradient program was as follows: 5% B at 0 min, linear increase to 70% B at 20 min, linear increase to 90% B at 25 min, and return to 5% B at 30 min. The flow rate was 0.8 mL/min, column temperature was 25 °C, and detection was at $\lambda = 220$ nm. [196]

Calibration curves for each peptide (P1–P5) were constructed by injecting standard solutions of known concentration (25–500 µg/mL in PBS) and plotting the integrated peak area (AUC) versus concentration. The concentration of peptide remaining in the supernatant after immobilisation was determined by HPLC, and the amount of peptide conjugated was calculated by subtraction:

Peptide Conjugated (µg) = $(C_{\text{initial}} - C_{\text{final}}) \times V_{\text{reaction}}$

Conjugation Efficiency (%) = [Conjugated Peptide (nmol) / PLGA Scaffold (nmol)] × 100

where PLGA Scaffold (nmol) = [Average Scaffold Weight (g) / MW of PLGA (66,000 g/mol)] × 10^9.

7.4.4.3. *Relative Water Absorption Capacity*

Circular specimens of plain PLGA scaffolds and peptide-immobilised scaffolds (P1-scaffold, P2-scaffold, P3-scaffold, P4-scaffold, and P5-scaffold) with a diameter of 15 mm were dried in a desiccator for at least 72 h to remove residual moisture. The initial dry weight (W_0) of each scaffold was recorded. Scaffolds were then immersed in deionised water (MQ water) for 24 h at room temperature. After gently blotting the scaffold surfaces with filter paper to remove superficial water, the hydrated weight (W_1) was recorded. The relative water absorption capacity was calculated using the following equation:

Relative Water Absorption (%) = $[(W_1 – W_0) / W_0] \times 100$

Measurements were performed in triplicate, and results were expressed as mean ± standard deviation.

7.4.4.4. *Surface Wettability (statistic Water Contact Angle)*

The surface wettability of plain and peptide-immobilised scaffolds was evaluated by static water contact angle measurements using the sessile drop method. Scaffold specimens were affixed to a flat glass slide to ensure a planar surface. A droplet of deionised water (5 µL) was carefully deposited onto the scaffold surface using a microsyringe. Images of the droplet profile were captured immediately after deposition using a digital camera equipped with a macro lens. The contact angle was determined by image analysis using ImageJ software with the DropSnake plugin. Measurements were performed on at least five different locations per scaffold type, and results were expressed as mean ± standard deviation.

7.4.5. *In Vitro* Biological Evaluation on Normal Human Dermal Fibroblasts (nHDFs)

Normal human dermal fibroblasts (nHDFs) were cultured in complete culture medium consisting of Dulbecco's Modified Eagle Medium (DMEM) high glucose supplemented with 10% (v/v) fetal bovine serum (FBS) and 1% (v/v) penicillin–streptomycin. Cells were maintained at 37 °C in a humidified incubator with 5% CO_2 and were passaged at 80–90% confluency.

7.4.5.1. Cytotoxicity Evaluation of Soluble Peptides (P1, P2, P3, and P5)

The intrinsic cytotoxicity of the soluble peptides was evaluated on nHDFs prior to scaffold immobilisation studies. nHDFs were seeded in standard 96-well plates at a density of 1×10^4

cells per well in complete culture medium and incubated overnight to allow for proper adherence. Peptide stock solutions were prepared under sterile conditions and diluted in complete culture medium to final concentrations ranging from 8 to 400 µM. Prior to treatment, the cell monolayers were gently washed twice with sterile PBS to remove non-adherent or dead cells. The cells were then exposed to the diluted peptide solutions (100 µL/well) and incubated for 24 h at 37 °C.

Following the 24 h incubation period, cell viability was assessed using the MTT (3-(4,5-dimethylthiazol-2-yl)-2,5-diphenyltetrazolium bromide) assay. MTT reagent (0.5 mg/mL final concentration in serum-free medium) was added to each well, and the plates were incubated for 3 h at 37 °C. The resulting formazan crystals were dissolved in DMSO (100 µL/well), and the absorbance was measured at 570 nm using a microplate reader. Cell viability was expressed as a percentage relative to untreated control cells (defined as 100% viability). Experiments were performed in triplicate.

7.4.5.2. Cell Viability and Morphology on Peptide-Immobilised Scaffolds

To investigate the interaction between fibroblast cells and peptide-functionalised surfaces, nHDFs were cultured directly on selected peptide-immobilised scaffolds (P1-scaffold, P2-scaffold, and P3-scaffold). Scaffold specimens were first sterilised by exposure to UV radiation for 1 h per side in a laminar flow biosafety cabinet. Sterilised scaffolds were placed in sterile cell crowns (Scaffdex) to prevent floating during incubation and transferred to the wells of a 24-well culture plate.

nHDFs were seeded onto the scaffold surfaces at a density of 5×10^3 cells per scaffold in complete culture medium and incubated for 72 h at 37 °C with 5% CO_2. After the incubation period, cell viability was assessed qualitatively using an Invitrogen™ Live/Dead™

viability/cytotoxicity staining kit according to the manufacturer's protocol. [197–199] Stained scaffolds were imaged using a confocal laser scanning microscope.

In parallel experiments, the cell morphology and cytoskeletal organisation were evaluated by fluorescence staining. Cells cultured on scaffolds for 72 h were fixed with 4% paraformaldehyde in PBS for 15 min, permeabilised with 0.1% Triton X-100 in PBS for 5 min, and blocked with 1% bovine serum albumin (BSA) in PBS for 30 min. F-actin filaments were stained with Alexa Fluor™ 488-conjugated phalloidin, and nuclei were counterstained with DAPI (4',6-diamidino-2-phenylindole). Stained scaffolds were imaged using a confocal laser scanning microscope.

7.4.6. *In Vitro* Biological Evaluation on Human Umbilical Vein Endothelial Cells (HUVECs)

Immortalised human umbilical vein endothelial cells (HUVECs) were cultured in endothelial cell growth medium (EGM-2) supplemented with the EGM-2 BulletKit (Lonza) containing 2% FBS, growth factors, and antibiotics. Cells were maintained at 37 °C in a humidified incubator with 5% CO_2 and were passaged at 70–80% confluency.

7.4.6.1. Cytotoxicity and Proliferation Assessment of Soluble Peptides (P1, P2, and P3)

To evaluate the dose-dependent effects of soluble peptides P1, P2, and P3 on HUVEC viability and proliferation, cells were seeded in 96-well plates at a density of 3×10^3 cells per well and incubated for 3 days to allow for attachment and establishment of logarithmic growth. Peptide stock solutions were prepared in sterile PBS and diluted in EGM-2 complete medium to final concentrations ranging from 8 to 400 μM (corresponding to approximately 10–200 μg/mL, depending on peptide molecular weight). All peptide solutions were filter-sterilised (0.22 μm) prior to use. HUVECs were gently washed twice with sterile PBS and subsequently treated with the peptide-containing media (100 µL/well). Cells were incubated for 24 and 72 h, with a medium change after 24 h for the 72 h time point. Following the respective incubation periods, the peptide solutions were aspirated, cells were washed twice with PBS, and viability was assessed using the MTT assay as described in Section 7.4.5.1. Cells treated with fresh complete medium without peptides served as the untreated control. Experiments were performed in triplicate.

7.4.6.2. Cytotoxicity and Proliferation Assessment of Scaffold Extracts

To evaluate the potential release of cytotoxic or inhibitory substances from the peptide-immobilised scaffolds (including acidic PLGA degradation products), an extract-based cytotoxicity assay was performed on HUVECs. HUVECs were seeded in 96-well plates at a density of 3×10^3 cells per well and incubated for 3 days to establish a confluent monolayer. Scaffold specimens (P1-scaffold, P2-scaffold, and plain PLGA control) were sterilised by UV irradiation (35 min per side, total exposure 70 min), followed by gentle washing with 70% ethanol (2×) and sterile PBS (2×). The sterilised scaffolds were immersed in EGM-2 complete culture medium at a concentration of 5 mg fibre mass per mL medium and incubated for 3 days at 37 °C under gentle agitation to obtain the scaffold extracts. Culture medium incubated under identical conditions without scaffolds served as the control extract. Prior to treatment, the HUVEC monolayers were washed twice with sterile PBS. Cells were then exposed to the scaffold extracts or control medium (100 µL/well) and incubated for 24 and 72 h. Following the incubation periods, cell viability was assessed using the MTT assay as previously described. Viability was expressed as a percentage relative to cells treated with the control extract. Experiments were performed in triplicate.

7.5. Instrumentation and Software

7.5.1. Analytical and Semi-Preparative RP-HPLC

Analytical and semi-preparative reverse-phase high-performance liquid chromatography (RP-HPLC) was performed on a Jasco LC-NetII/ADC system equipped with a PU-4180 quaternary pump, an AS-4050 autosampler, and an MD-4010 photodiode array (PDA) detector. Data acquisition and analysis were performed using ChromNAV 2.0 software.

7.5.1. Mass Spectrometry (ESI-MS)

Electrospray ionisation mass spectrometry (ESI-MS) was performed on either a Fisons MD800 single quadrupole spectrometer or a Finnigan LCQ Fleet ion trap spectrometer (Thermo Scientific). Samples were dissolved in H_2O/ACN (1:1 v/v) containing 0.1% formic acid and infused directly into the ion source.

7.5.2. Fourier-Transform Infrared Spectroscopy (FTIR)

FTIR spectra were acquired on a PerkinElmer Spotlight 400 FT-IR spectrophotometer equipped with a diamond crystal Attenuated Total Reflection (ATR) accessory. Data processing and spectral deconvolution were performed using OriginPro 2021 software (OriginLab Corporation).

7.5.3. Dynamic Light Scattering (DLS)

DLS measurements were performed using a Malvern Zetasizer Nano ZS instrument (Malvern Panalytical Ltd.). Data acquisition and analysis were performed using Zetasizer Software 7.13.

7.5.4. Circular Dichroism (CD) Spectroscopy

CD spectra were recorded on a Jasco J-815 spectropolarimeter equipped with a Peltier temperature controller. Data were processed using Spectra Manager™ II software.

7.5.5. Rheology

Rheological measurements were performed using a TA Instruments Discovery HR-30 rheometer. Data acquisition and analysis were performed using TRIOS Software v5.1.

7.5.6. Scanning Electron Microscopy (SEM)

SEM imaging for Projects 1 and 2 was performed using either a JEOL JSM-IT500 or a Phenom-World ProX scanning electron microscope. SEM imaging for Project 3 was performed using a Tescan Mira3 XMU scanning electron microscope. Image analysis for fibre diameter quantification was performed using ImageJ software (NIH, USA).

7.5.7. Confocal Microscopy

Confocal laser scanning microscopy was performed using a Leica TCS SP8 or Zeiss LSM 880 microscope. Image processing and analysis were performed using ImageJ (Fiji) software.

7.5.8. 3D Bioprinting

3D printing feasibility tests were performed using a BioX 3D bioprinter (CELLINK).

7.5.9. Mechanical Testing

Uniaxial tensile testing of electrospun scaffolds was performed using a Mark-10 Tensile Tester (Series 5) equipped with a 50 N load cell. Data were acquired and analysed using MESURgauge software.

7.6. Statistical Analysis

All quantitative data are presented as mean ± standard deviation (SD) unless otherwise stated. Statistical analyses were performed using GraphPad Prism software (Version 9). Comparisons between two groups were performed using an unpaired Student's t-test. Comparisons among multiple groups were performed using one-way or two-way analysis of variance (ANOVA) followed by appropriate post-hoc tests (Tukey's or Šídák's multiple comparisons test).

Statistical significance was defined as follows: ns, not significant ($p \geq 0.05$); *$p < 0.05$; **$p < 0.01$; ***$p < 0.001$; ****$p < 0.0001$.

8. References:

(1) Exploring the World of Functional Materials. In *Functional Materials from Carbon, Inorganic, and Organic Sources*; Woodhead Publishing, 2023; pp 1–19. https://doi.org/10.1016/B978-0-323-85788-8.00014-8.

(2) Yorke, S. K.; Yang, Z.; Wiita, E. G.; Kamada, A.; Knowles, T. P. J.; Buehler, M. J. Design and Sustainability of Polypeptide Material Systems. *Nat Rev Mater* **2025**, *10* (10), 750–768. https://doi.org/10.1038/s41578-025-00793-3.

(3) Nath Das, T.; Ramesh, A.; Ghosh, A.; Moyra, S.; Kumar Maji, T.; Ghosh, G. Peptide-Based Nanomaterials and Their Diverse Applications. *Nanoscale Horizons* **2025**, *10* (2), 279–313. https://doi.org/10.1039/D4NH00371C.

(4) Li, T.; Lu, X.-M.; Zhang, M.-R.; Hu, K.; Li, Z. Peptide-Based Nanomaterials: Self-Assembly, Properties and Applications. *Bioactive Materials* **2022**, *11*, 268–282. https://doi.org/10.1016/j.bioactmat.2021.09.029.

(5) Kumaraswamy, P.; Sethuraman, S.; Yakhmi, J. V.; Krishnan, U. M. Hierarchical Self-Assembled Peptide Nano-Ensembles. In *Handbook of Nanomaterials Properties*; Bhushan, B., Luo, D., Schricker, S. R., Sigmund, W., Zauscher, S., Eds.; Springer: Berlin, Heidelberg, 2014; pp 247–284. https://doi.org/10.1007/978-3-642-31107-9_23.

(6) Hao, Z.-W.; Zhang, Z.-Y.; Wang, Z.-P.; Wang, Y.; Chen, J.-Y.; Chen, T.-H.; Shi, G.; Li, H.-K.; Wang, J.-W.; Dong, M.-C.; Hong, L.; Li, J.-F. Bioactive Peptides and Proteins for Tissue Repair: Microenvironment Modulation, Rational Delivery, and Clinical Potential. *Mil Med Res* **2024**, *11*, 75. https://doi.org/10.1186/s40779-024-00576-x.

(7) Edwards-Gayle, C. J. C.; Hamley, I. W. Self-Assembly of Bioactive Peptides, Peptide Conjugates, and Peptide Mimetic Materials. *Organic & Biomolecular Chemistry* **2017**, *15* (28), 5867–5876. https://doi.org/10.1039/c7ob01092c.

(8) Oliver-Cervelló, L.; Martin-Gómez, H.; Gonzalez-Garcia, C.; Salmeron-Sanchez, M.; Ginebra, M.-P.; Mas-Moruno, C. Protease-Degradable Hydrogels with Multifunctional Biomimetic Peptides for Bone Tissue Engineering. *Front. Bioeng. Biotechnol.* **2023**, *11*. https://doi.org/10.3389/fbioe.2023.1192436.

(9) Marchesan, S.; Vargiu, A. V.; Styan, K. E. The Phe-Phe Motif for Peptide Self-Assembly in Nanomedicine. *Molecules* **2015**, *20* (11), 19775–19788. https://doi.org/10.3390/molecules201119658.

(10) Wang, J.; Liu, K.; Xing, R.; Yan, X. Peptide Self-Assembly: Thermodynamics and Kinetics. *Chemical Society Reviews* **2016**, *45* (20), 5589–5604. https://doi.org/10.1039/C6CS00176A.

(11) Selegård, R.; Aronsson, C.; Brommesson, C.; Dånmark, S.; Aili, D. Folding Driven Self-Assembly of a Stimuli-Responsive Peptide-Hyaluronan Hybrid Hydrogel. *Sci Rep* **2017**, *7* (1), 7013. https://doi.org/10.1038/s41598-017-06457-9.

(12) Wu, E.; Ellis, A. S.; Bell, K.; Moss, D. L.; Landry, S. J.; Hristova, K.; Wimley, W. C. pH-Responsive Peptide Nanoparticles Deliver Macromolecules to Cells via Endosomal Membrane Nanoporation. *ACS Nano* **2024**, *18* (50), 33922–33936. https://doi.org/10.1021/acsnano.4c07525.

(13) Gentile, L.; Frohm, B.; Malmendal, A.; Åkerfeldt, K. S.; Olsson, U.; Linse, S. Charge Regulation in Peptide Self-Assembly and Hydrogelation. *Journal of Colloid and Interface Science* **2025**, *700*, 138615. https://doi.org/10.1016/j.jcis.2025.138615.

(14) Samdin, T. D.; Wang, X.; Fichman, G.; Schneider, J. P. Exploring the Temperature Dependence of β-Hairpin Peptide Self-Assembly. *Faraday Discuss.* **2025**, *260* (0), 113–131. https://doi.org/10.1039/D5FD00018A.

(15) Zhang, S.; Chen, C.; Li, Z. Effects of Molecular Weight on Thermal Responsive Property of Pegylated Poly-l-Glutamates. *Chin J Polym Sci* **2013**, *31* (2), 201–210. https://doi.org/10.1007/s10118-013-1218-7.

(16) Huang, R.; Wang, Y.; Qi, W.; Su, R.; He, Z. Temperature-Induced Reversible Self-Assembly of Diphenylalanine Peptide and the Structural Transition from Organogel to Crystalline Nanowires. *Nanoscale Res Lett* **2014**, *9* (1), 653. https://doi.org/10.1186/1556-276X-9-653.

(17) Canchi, D. R.; García, A. E. Cosolvent Effects on Protein Stability. *Annual Review of Physical Chemistry* **2013**, *64* (Volume 64, 2013), 273–293. https://doi.org/10.1146/annurev-physchem-040412-110156.

(18) Li, H.; Qian, X.; Mohanram, H.; Han, X.; Qi, H.; Zou, G.; Yuan, F.; Miserez, A.; Liu, T.; Yang, Q.; Gao, H.; Yu, J. Self-Assembly of Peptide Nanocapsules by a Solvent Concentration Gradient. *Nat. Nanotechnol.* **2024**, *19* (8), 1141–1149. https://doi.org/10.1038/s41565-024-01654-w.

(19) Sun, X.; Wu, B.; Li, N.; Liu, B.; Li, S.; Ma, L.; Zhang, H. Influence of Electrostatic Interactions on the Self-Assembly of Charged Peptides. *Gels* **2025**, *11* (1). https://doi.org/10.3390/gels11010080.

(20) Ghosh, G.; Fernández, G. pH- and Concentration-Dependent Supramolecular Self-Assembly of a Naturally Occurring Octapeptide. *Beilstein J. Org. Chem.* **2020**, *16* (1), 2017–2025. https://doi.org/10.3762/bjoc.16.168.

(21) Muraoka, T.; Koh, C. Y.; Cui, H.; Stupp, S. I. Light-Triggered Bioactivity in Three Dimensions. *ANGEW CHEM (INT ED ENGL)* **2009**, *48* (32), 5946–5949. https://doi.org/10.1002/anie.200901524.

(22) Ross, A.; Sauce-Guevara, M. A.; Alarcon, E. I.; Mendez-Rojas, M. A. Peptide Biomaterials for Tissue Regeneration. *Front. Bioeng. Biotechnol.* **2022**, *10*. https://doi.org/10.3389/fbioe.2022.893936.

(23) Mishra, A.; Loo, Y.; Deng, R.; Chuah, Y. J.; Hee, H. T.; Ying, J. Y.; Hauser, C. A. E. Ultrasmall Natural Peptides Self-Assemble to Strong Temperature-Resistant Helical Fibers in Scaffolds Suitable for Tissue Engineering. *Nano Today* **2011**, *6* (3), 232–239. https://doi.org/10.1016/j.nantod.2011.05.001.

(24) Marchesan, S.; Waddington, L.; Easton, C. D.; Winkler, D. A.; Goodall, L.; Forsythe, J.; Hartley, P. G. Unzipping the Role of Chirality in Nanoscale Self-Assembly of Tripeptide Hydrogels. *Nanoscale* **2012**, *4* (21), 6752–6760. https://doi.org/10.1039/C2NR32006A.

(25) Marchesan, S.; Easton, C. D.; Styan, K. E.; Waddington, L. J.; Kushkaki, F.; Goodall, L.; McLean, K. M.; Forsythe, J. S.; Hartley, P. G. Chirality Effects at Each Amino Acid Position on Tripeptide Self-Assembly into Hydrogel Biomaterials. *Nanoscale* **2014**, *6* (10), 5172–5180. https://doi.org/10.1039/C3NR06752A.

(26) *Tripeptide self-assembled hydrogels: unexpected twists of chirality - PubMed*. https://pubmed.ncbi.nlm.nih.gov/22159641/ (accessed 2026-03-06).

(27) Green, H.; Ochbaum, G.; Gitelman-Povimonsky, A.; Bitton, R.; Rapaport, H. RGD-Presenting Peptides in Amphiphilic and Anionic β-Sheet Hydrogels for Improved Interactions with Cells. *RSC Adv* *8* (18), 10072–10080. https://doi.org/10.1039/c7ra12503h.

(28) Martin, C.; Oyen, E.; Mangelschots, J.; Bibian, M.; Haddou, T. B.; Andrade, J.; Gardiner, J.; Mele, B. V.; Madder, A.; Hoogenboom, R.; Spetea, M.; Ballet, S. Injectable Peptide Hydrogels for Controlled-Release of Opioids. *Med. Chem. Commun.* **2016**, *7* (3), 542–549. https://doi.org/10.1039/C5MD00440C.

(29) Bertouille, J.; Van Lommel, R.; Aerts, R.; Dockx, L.; Mangialetto, J.; Van den Brande, N.; Willaert, R. G.; De Proft, F.; Hennecke, U.; Martin, C.; Herrebout, W.; Jansen, T. L. C.; Cunha, A. V.; Ballet, S. A Comparative Study between Phenylglycine and Phenylalanine Derived Peptide Hydrogels: Towards Atomic Elucidation. *Materials Today Chemistry* **2025**, *44*, 102593. https://doi.org/10.1016/j.mtchem.2025.102593.

(30) Heremans, J.; Chevillard, L.; Mannes, M.; Mangialetto, J.; Leroy, K.; White, J. F.; Lamouroux, A.; Vinken, M.; Gardiner, J.; Van Mele, B.; Van den Brande, N.; Hoogenboom, R.; Madder, A.; Caveliers, V.; Mégarbane, B.; Hernot, S.; Ballet, S.; Martin, C. Impact of Doubling Peptide Length on *in Vivo* Hydrogel Stability and Sustained Drug Release. *Journal of Controlled Release* **2022**, *350*, 514–524. https://doi.org/10.1016/j.jconrel.2022.08.027.

(31) Vu, H.; Peeters, E.; Hofkens, K.; Vandemeulebroecke, K.; T'Sas, S.; Martin, C.; Ballet, S.; Hoogenboom, R.; Goossens, S.; Lammens, T.; Trimpont, M. V.; Madder, A. Peptide Hydrogels as Slow-Release Formulations of Protein Therapeutics: Case Study of Asparaginase-Loaded Hydrogels. *Biomater. Sci.* **2025**, *13* (15), 4139–4152. https://doi.org/10.1039/D5BM00138B.

(32) Hartgerink, J. D.; Beniash, E.; Stupp, S. I. Self-Assembly and Mineralization of Peptide-Amphiphile Nanofibers. *Science* **2001**, *294* (5547), 1684–1688. https://doi.org/10.1126/science.1063187.

(33) Webber, M. J.; Tongers, J.; Renault, M.-A.; Roncalli, J. G.; Losordo, D. W.; Stupp, S. I. Development of Bioactive Peptide Amphiphiles for Therapeutic Cell Delivery. *Acta Biomaterialia* **2010**, *6* (1), 3–11. https://doi.org/10.1016/j.actbio.2009.07.031.

(34) Silva, G. A.; Czeisler, C.; Niece, K. L.; Beniash, E.; Harrington, D. A.; Kessler, J. A.; Stupp, S. I. Selective Differentiation of Neural Progenitor Cells by High-Epitope Density Nanofibers. *Science* **2004**, *303* (5662), 1352–1355. https://doi.org/10.1126/science.1093783.

(35) Mata, A.; Geng, Y.; Henrikson, K. J.; Aparicio, C.; Stock, S. R.; Satcher, R. L.; Stupp, S. I. Bone Regeneration Mediated by Biomimetic Mineralization of a Nanofiber Matrix. *Biomaterials* **2010**, *31* (23), 6004–6012. https://doi.org/10.1016/j.biomaterials.2010.04.013.

(36) Bioactive Scaffolds with Enhanced Supramolecular Motion Promote Recovery from Spinal Cord Injury. *Science*.

(37) Mondal, T.; Chatterjee, A.; Hansda, B.; Mondal, B.; Sen, P.; Banerjee, A. Cationic and Amphiphilic Peptide-Based Hydrogels with Dual Activities as Anticancer and Antibacterial Agents. *Soft Matter* **2024**, *20* (6), 1236–1244. https://doi.org/10.1039/D3SM01291C.

(38) *Aromatic π–π Interactions in Self-assembled Nanostructured Materials | Springer Nature Link*. https://link.springer.com/chapter/10.1007/978-981-96-9342-9_3 (accessed 2026-03-10).

(39) Rosa, M.; Gallo, E.; Pellegrino, P.; Mercurio, F. A.; Leone, M.; Cascione, M.; Carrese, B.; Morelli, G.; Accardo, A.; Diaferia, C. Inclusion of Cationic Amphiphilic Peptides

in Fmoc-FF Generates Multicomponent Functional Hydrogels. *ACS Appl. Bio Mater.* **2025**, *8* (1), 488–502. https://doi.org/10.1021/acsabm.4c01409.

(40) Yueze, W.; Dayong, H.; Wanhai, X. The Design of Programmable Peptide-Coupled AIEgens in Biomedical Applications. In *Encyclopedia of Aggregation-Induced Emission*; Springer, Singapore, 2025; pp 1–12. https://doi.org/10.1007/978-981-97-1574-9_113-1.

(41) *Fluorescent β-Sheet-Based Peptide Hydrogels with Aggregation-Enhanced Emission Properties - Bertouille - 2025 - European Journal of Organic Chemistry - Wiley Online Library*. https://chemistry-europe.onlinelibrary.wiley.com/doi/10.1002/ejoc.202500730 (accessed 2026-02-10).

(42) Antoniou, A. I.; Pesenti, M.; Crespi, S.; Shenoy, D. S.; Penconi, M.; Bossi, A.; Pellegrino, S. Aggregation-Induced Enhanced Emission of Tetraphenylethene-Phenylalanine Hybrids: Synthesis and Characterization. *J. Org. Chem.* **2024**, *89* (7), 4733–4740. https://doi.org/10.1021/acs.joc.3c02969.

(43) Yeh, M.-Y.; Huang, C.-W.; Chang, J.-W.; Huang, Y.-T.; Lin, J.-H.; Hsu, S.-M.; Hung, S.-C.; Lin, H.-C. A Novel Nanostructured Supramolecular Hydrogel Self-Assembled from Tetraphenylethylene-Capped Dipeptides. *Soft Matter* **2016**, *12* (30), 6347–6351. https://doi.org/10.1039/C6SM00755D.

(44) Mei, L.; He, S.; Zhang, L.; Xu, K.; Zhong, W. Supramolecular Self-Assembly of Fluorescent Peptide Amphiphiles for Accurate and Reversible pH Measurement. *Org. Biomol. Chem.* **2019**, *17* (4), 939–944. https://doi.org/10.1039/C8OB02983K.

(45) Bertouille, J.; Mashweu, A. R.; De Beer, F. J.; Yvanoff, C.; Willaert, R. G.; Ballet, S.; Martin, C.; Azov, V. A.; Hennecke, U. Fluorescent β-Sheet-Based Peptide Hydrogels with Aggregation-Enhanced Emission Properties. *European Journal of Organic Chemistry* **2025**, *28* (34), e202500730. https://doi.org/10.1002/ejoc.202500730.

(46) Impresari, E.; Bossi, A.; Lumina, E. M.; Ortenzi, M. A.; Kothuis, J. M.; Cappelletti, G.; Maggioni, D.; Christodoulou, M. S.; Bucci, R.; Pellegrino, S. Fatty Acids/Tetraphenylethylene Conjugates: Hybrid AIEgens for the Preparation of Peptide-Based Supramolecular Gels. *Front. Chem.* **2022**, *10*. https://doi.org/10.3389/fchem.2022.927563.

(47) Antoniou, A. I.; Pesenti, M.; Crespi, S.; Shenoy, D. S.; Penconi, M.; Bossi, A.; Pellegrino, S. Aggregation-Induced Enhanced Emission of Tetraphenylethene-Phenylalanine Hybrids: Synthesis and Characterization. *J. Org. Chem.* **2024**, *89* (7), 4733–4740. https://doi.org/10.1021/acs.joc.3c02969.

(48) Subbalakshmi, C.; Basak, P.; Nagaraj, R. Self-Assembly of t-Butyloxycarbonyl Protected Dipeptide Methyl Esters Composed of Leucine, Isoleucine, and Valine into Highly Organized Structures from Alcohol and Aqueous Alcohol Mixtures. *Peptide Science* **2017**, *108* (6), e23033. https://doi.org/10.1002/bip.23033.

(49) Krishnan, Y.; Sampath, S. Biopolymers and Synthetic Polymeric Materials in Wound Healing: Cellular Mechanisms and Therapeutic Potential. *Discov Mater* **2025**, *5* (1), 254. https://doi.org/10.1007/s43939-025-00435-z.

(50) *New trends in the development of multifunctional peptides to functionalize biomaterials - Oliver-Cervelló - 2022 - Journal of Peptide Science - Wiley Online Library*. https://onlinelibrary.wiley.com/doi/10.1002/psc.3335?msockid=21c0d55e971767632d3ac5b896a5665f (accessed 2026-03-02).

(51) Valiente-Alandi, I.; Schafer, A. E.; Blaxall, B. C. Extracellular Matrix-Mediated Cellular Communication in the Heart. *Journal of Molecular and Cellular Cardiology* **2016**, *91*, 228–237. https://doi.org/10.1016/j.yjmcc.2016.01.011.

(52) Pang, X.; He, X.; Qiu, Z.; Zhang, H.; Xie, R.; Liu, Z.; Gu, Y.; Zhao, N.; Xiang, Q.; Cui, Y. Targeting Integrin Pathways: Mechanisms and Advances in Therapy. *Sig Transduct Target Ther* **2023**, *8* (1), 1–42. https://doi.org/10.1038/s41392-022-01259-6.

(53) Dhavalikar, P.; Robinson, A.; Lan, Z.; Jenkins, D.; Chwatko, M.; Salhadar, K.; Jose, A.; Kar, R.; Shoga, E.; Kannapiran, A.; Cosgriff-Hernandez, E. Review of Integrin-Targeting Biomaterials in Tissue Engineering. *Adv Healthcare Materials* **2020**, *9* (23), 2000795. https://doi.org/10.1002/adhm.202000795.

(54) Chai, Y.; Long, Y.; Dong, X.; Liu, K.; Wei, W.; Chen, Y.; Qiu, T.; Dai, H. Improved Functional Recovery of Rat Transected Spinal Cord by Peptide-Grafted PNIPAM Based Hydrogel. *Colloids and Surfaces B: Biointerfaces* **2022**, *210*, 112220. https://doi.org/10.1016/j.colsurfb.2021.112220.

(55) Zhou, F.; Wen, M.; Zhou, P.; Zhao, Y.; Jia, X.; Fan, Y.; Yuan, X. Electrospun Membranes of PELCL/PCL-REDV Loading with miRNA-126 for Enhancement of Vascular Endothelial Cell Adhesion and Proliferation. *Materials Science and Engineering: C* **2018**, *85*, 37–46. https://doi.org/10.1016/j.msec.2017.12.005.

(56) Ha, M. Y.; Yang, D. H.; You, S. J.; Kim, H. J.; Chun, H. J. In-Situ Forming Injectable GFOGER-Conjugated BMSCs-Laden Hydrogels for Osteochondral Regeneration. *npj Regen Med* **2023**, *8* (1), 1–13. https://doi.org/10.1038/s41536-022-00274-z.

(57) Li, X.-J.; Sun, Y.-T.; Yin, L.; Zhang, X.-J.; Yang, Y.; Paul Fawcett, J.; Cui, Y.-M.; Gu, J.-K. Quantitation of Bivalirudin, a Novel Anticoagulant Peptide, in Human Plasma by LC–MS/MS: Method Development, Validation and Application to Pharmacokinetics. *Journal of Pharmaceutical Analysis* **2013**, *3* (1), 1–8. https://doi.org/10.1016/j.jpha.2012.10.006.

(58) Wang, G.; Yuan, N.; Li, N.; Wei, Q.; Qian, Y.; Zhang, J.; Qin, M.; Wang, Y.; Dong, S. Vascular Endothelial Growth Factor Mimetic Peptide and Parathyroid Hormone (1–34) Delivered via a Blue-Light-Curable Hydrogel Synergistically Accelerate Bone Regeneration. *ACS Appl. Mater. Interfaces* **2022**, *14* (31), 35319–35332. https://doi.org/10.1021/acsami.2c06159.

(59) Fu, X.; Wang, J.; Cai, H.; Jiang, H.; Han, S. C16 Peptide and Ang-1 Improve Functional Disability and Pathological Changes in an Alzheimer’s Disease Model Associated with Vascular Dysfunction. *Pharmaceuticals* **2022**, *15* (4), 471. https://doi.org/10.3390/ph15040471.

(60) Ramovs, V.; te Molder, L.; Sonnenberg, A. The Opposing Roles of Laminin-Binding Integrins in Cancer. *Matrix Biology* **2017**, *57–58*, 213–243. https://doi.org/10.1016/j.matbio.2016.08.007.

(61) Kreidberg, J. A.; Donovan, M. J.; Goldstein, S. L.; Rennke, H.; Shepherd, K.; Jones, R. C.; Jaenisch, R. Alpha 3 Beta 1 Integrin Has a Crucial Role in Kidney and Lung Organogenesis. *Development* **1996**, *122* (11), 3537–3547. https://doi.org/10.1242/dev.122.11.3537.

(62) Couvelard, A.; Bringuier, A.-F.; Dauge, M.-C.; Nejjari, M.; Darai, E.; Benifla, J.-L.; Feldmann, G.; Henin, D.; Scoazec, J.-Y. Expression of Integrins during Liver Organogenesis in Humans. *Hepatology* **1998**, *27* (3), 839. https://doi.org/10.1002/hep.510270328.

(63) Lora, J. M.; Rowader, K. E.; Soares, L.; Giancotti, F.; Zaret, K. S. A3β1-Integrin as a Critical Mediator of the Hepatic Differentiation Response to the Extracellular Matrix. *Hepatology* **1998**, *28* (4), 1095–1104. https://doi.org/10.1002/hep.510280426.

(64) Georges-Labouesse, E.; Mark, M.; Messaddeq, N.; Gansmüller, A. Essential Role of A6 Integrins in Cortical and Retinal Lamination. *Current Biology* **1998**, *8* (17), 983–986. https://doi.org/10.1016/S0960-9822(98)70402-6.

(65) Fujiwara, H.; Kataoka, N.; Honda, T.; Ueda, M.; Yamada, S.; Nakamura, K.; Suginami, H.; Mori, T.; Maeda, M. Physiological Roles of Integrin A6β1 in Ovarian Functions. *Hormone Research* **2004**, *50* (Suppl. 2), 25–29. https://doi.org/10.1159/000053120.

(66) Álvarez, Z.; Kolberg-Edelbrock, A. N.; Sasselli, I. R.; Ortega, J. A.; Qiu, R.; Syrgiannis, Z.; Mirau, P. A.; Chen, F.; Chin, S. M.; Weigand, S.; Kiskinis, E.; Stupp, S. I. Bioactive Scaffolds with Enhanced Supramolecular Motion Promote Recovery from Spinal Cord Injury. *Science* **2021**, *374* (6569), 848–856. https://doi.org/10.1126/science.abh3602.

(67) Clauder, F.; Czerniak, A. S.; Friebe, S.; Mayr, S. G.; Scheinert, D.; Beck-Sickinger, A. G. Endothelialization of Titanium Surfaces by Bioinspired Cell Adhesion Peptide Coatings. *Bioconjugate Chem.* **2019**, *30* (10), 2664–2674. https://doi.org/10.1021/acs.bioconjchem.9b00573.

(68) Hubbell, J. A.; Massia, S. P.; Desai, N. P.; Drumheller, P. D. Endothelial Cell-Selective Materials for Tissue Engineering in the Vascular Graft Via a New Receptor. *Nat Biotechnol* **1991**, *9* (6), 568–572. https://doi.org/10.1038/nbt0691-568.

(69) Massia, S. P.; Hubbell, J. A. Vascular Endothelial Cell Adhesion and Spreading Promoted by the Peptide REDV of the IIICS Region of Plasma Fibronectin Is Mediated by Integrin Alpha 4 Beta 1. *Journal of Biological Chemistry* **1992**, *267* (20), 14019–14026. https://doi.org/10.1016/S0021-9258(19)49672-5.

(70) Lin, Q.-K.; Hou, Y.; Ren, K.-F.; Ji, J. Selective Endothelial Cells Adhesion to Arg-Glu-Asp-Val Peptide Functionalized Polysaccharide Multilayer. *Thin Solid Films* **2012**, *520* (15), 4971–4978. https://doi.org/10.1016/j.tsf.2012.03.041.

(71) Wei, Y.; Ji, Y.; Xiao, L.-L.; Lin, Q.; Xu, J.; Ren, K.; Ji, J. Surface Engineering of Cardiovascular Stent with Endothelial Cell Selectivity for *in Vivo* Re-Endothelialisation. *Biomaterials* **2013**, *34* (11), 2588–2599. https://doi.org/10.1016/j.biomaterials.2012.12.036.

(72) Shi, C.; Li, Q.; Zhang, W.; Feng, Y.; Ren, X. REDV Peptide Conjugated Nanoparticles/pZNF580 Complexes for Actively Targeting Human Vascular Endothelial Cells. *ACS Appl. Mater. Interfaces* **2015**, *7* (36), 20389–20399. https://doi.org/10.1021/acsami.5b06286.

(73) Qi, P.; Maitz, M. F.; Huang, N. Surface Modification of Cardiovascular Materials and Implants. *Surface and Coatings Technology* **2013**, *233*, 80–90. https://doi.org/10.1016/j.surfcoat.2013.02.008.

(74) Mahara, A.; Somekawa, S.; Kobayashi, N.; Hirano, Y.; Kimura, Y.; Fujisato, T.; Yamaoka, T. Tissue-Engineered Acellular Small Diameter Long-Bypass Grafts with Neointima-Inducing Activity. *Biomaterials* **2015**, *58*, 54–62. https://doi.org/10.1016/j.biomaterials.2015.04.031.

(75) Sun, X.; He, M.; Wang, L.; Luo, L.; Wang, J.; Xiao, J. Luminescent Biofunctional Collagen Mimetic Nanofibers. *ACS Omega* **2019**, *4* (15), 16270–16279. https://doi.org/10.1021/acsomega.9b00740.

(76) Ha, M. Y.; Yang, D. H.; You, S. J.; Kim, H. J.; Chun, H. J. In-Situ Forming Injectable GFOGER-Conjugated BMSCs-Laden Hydrogels for Osteochondral Regeneration. *npj Regen Med* **2023**, *8* (1), 2. https://doi.org/10.1038/s41536-022-00274-z.

(77) Clark, A. Y.; Martin, K. E.; García, J. R.; Johnson, C. T.; Theriault, H. S.; Han, W. M.; Zhou, D. W.; Botchwey, E. A.; García, A. J. Integrin-Specific Hydrogels Modulate Transplanted Human Bone Marrow-Derived Mesenchymal Stem Cell Survival, Engraftment, and Reparative Activities. *Nat Commun* **2020**, *11* (1), 114. https://doi.org/10.1038/s41467-019-14000-9.

(78) Wang, L.; Xin, X.; Li, P.; Dou, J.; Han, X.; Shen, J.; Yuan, J. Stepwise Immobilization of Keratin-Dopamine Conjugates and Gold Nanoparticles on PET Sheets for Potential Vascular Graft with the Catalytic Generation of Nitric Oxide. *Colloids and Surfaces B: Biointerfaces* **2021**, *205*, 111855. https://doi.org/10.1016/j.colsurfb.2021.111855.

(79) Chernonosova, V. S.; Gostev, A. A.; Chesalov, Y. A.; Karpenko, A. A.; Karaskov, A. M.; Laktionov, P. P. Study of Hemocompatibility and Endothelial Cell Interaction of Tecoflex-Based Electrospun Vascular Grafts. *International Journal of Polymeric Materials and Polymeric Biomaterials* **2019**, *68* (1–3), 34–43. https://doi.org/10.1080/00914037.2018.1525721.

(80) Xing, Z.; Wu, S.; Zhao, C.; Bai, Y.; Jin, D.; Yin, M.; Liu, H.; Fan, Y. Vascular Transplantation with Dual-Biofunctional ePTFE Vascular Grafts in a Porcine Model. *Journal of Materials Chemistry B* **2021**, *9* (36), 7409–7422. https://doi.org/10.1039/D1TB01398J.

(81) Du, P.; Li, X.; Sun, L.; Pan, Y.; Zhu, H.; Li, Y.; Yang, Y.; Wei, X.; Jing, C.; Chen, H.; Shi, Q.; Li, W.; Zhao, L. Improved Hemocompatibility by Modifying Acellular Blood Vessels with Bivalirudin and Its Biocompatibility Evaluation. *Journal of Biomedical Materials Research Part A* **2022**, *110* (3), 635–651. https://doi.org/10.1002/jbm.a.37316.

(82) Sun, Q.; Si, J.; Zhao, L.; Wei, T.; Wang, T.; Li, F.; Li, Y.; Shafiq, M.; Wang, L.; Liu, R.; Zhi, D.; Wang, K. Direct Thrombin Inhibitor-Bivalirudin Improved the Hemocompatibility of Electrospun Polycaprolactone Vascular Grafts. *Composites Part B: Engineering* **2022**, *234*, 109702. https://doi.org/10.1016/j.compositesb.2022.109702.

(83) Yan, H.; Cheng, Q.; Si, J.; Wang, S.; Wan, Y.; Kong, X.; Wang, T.; Zheng, W.; Rafique, M.; Li, X.; He, J.; Midgley, A. C.; Zhu, Y.; Wang, K.; Kong, D. Functionalization of in Vivo Tissue-Engineered Living Biotubes Enhance Patency and Endothelization without the Requirement of Systemic Anticoagulant Administration. *Bioactive Materials* **2023**, *26*, 292–305. https://doi.org/10.1016/j.bioactmat.2023.03.003.

(84) Koster, A.; Faraoni, D.; Levy, J. H. Argatroban and Bivalirudin for Perioperative Anticoagulation in Cardiac Surgery. *Anesthesiology* **2018**, *128* (2), 390–400. https://doi.org/10.1097/ALN.0000000000001976.

(85) Mezu-Ndubuisi, O. J.; Maheshwari, A. The Role of Integrins in Inflammation and Angiogenesis. *Pediatr Res* **2021**, *89* (7), 1619–1626. https://doi.org/10.1038/s41390-020-01177-9.

(86) D'Andrea, L. D.; Iaccarino, G.; Fattorusso, R.; Sorriento, D.; Carannante, C.; Capasso, D.; Trimarco, B.; Pedone, C. Targeting Angiogenesis: Structural Characterization and Biological Properties of a de Novo Engineered VEGF Mimicking Peptide. *Proceedings of the National Academy of Sciences* **2005**, *102* (40), 14215–14220. https://doi.org/10.1073/pnas.0505047102.

(87) Pal, A.; Smith, C. I.; Palade, J.; Nagaraju, S.; Alarcon-Benedetto, B. A.; Kilbourne, J.; Rawls, A.; Wilson-Rawls, J.; Vernon, B. L.; Nikkhah, M. Poly(N-Isopropylacrylamide)-Based Dual-Crosslinking Biohybrid Injectable Hydrogels for Vascularization. *Acta Biomaterialia* **2020**, *107*, 138–151. https://doi.org/10.1016/j.actbio.2020.02.041.

(88) Kokubo, T.; Uchida, H.; Choi, E. T. Integrin Avβ3 as a Target in the Prevention of Neointimal Hyperplasia. *Journal of Vascular Surgery* **2007**, *45* (6, Supplement), A33–A38. https://doi.org/10.1016/j.jvs.2007.02.069.

(89) Bishop, G. G.; McPherson, J. A.; Sanders, J. M.; Hesselbacher, S. E.; Feldman, M. J.; McNamara, C. A.; Gimple, L. W.; Powers, E. R.; Mousa, S. A.; Sarembock, I. J. Selective Avβ3-Receptor Blockade Reduces Macrophage Infiltration and Restenosis After Balloon Angioplasty in the Atherosclerotic Rabbit. *Circulation* **2001**, *103* (14), 1906–1911. https://doi.org/10.1161/01.CIR.103.14.1906.

(90) Guermonprez, P.; Valladeau, J.; Zitvogel, L.; Théry, C.; Amigorena, S. Antigen Presentation and T Cell Stimulation by Dendritic Cells. *Annual Review of Immunology* **2002**, *20* (Volume 20, 2002), 621–667. https://doi.org/10.1146/annurev.immunol.20.100301.064828.

(91) Renner, G.; Noulet, F.; Mercier, M.-C.; Choulier, L.; Etienne-Selloum, N.; Gies, J.-P.; Lehmann, M.; Lelong-Rebel, I.; Martin, S.; Dontenwill, M. Expression/Activation of A5β1 Integrin Is Linked to the β-Catenin Signaling Pathway to Drive Migration in Glioma Cells. *Oncotarget* **2016**, *7* (38), 62194–62207. https://doi.org/10.18632/oncotarget.11552.

(92) Lv, X.; Li, Z.; Guan, J.; Hu, S.; Zhang, J.; Lan, Y.; Zhao, K.; Lu, H.; Song, D.; He, H.; Gao, F.; He, W. Porcine Hemagglutinating Encephalomyelitis Virus Activation of the Integrin A5β1-FAK-Cofilin Pathway Causes Cytoskeletal Rearrangement To Promote Its Invasion of N2a Cells. *Journal of Virology* **2019**, *93* (5), 10.1128/jvi.01736-18. https://doi.org/10.1128/jvi.01736-18.

(93) Oh, S.-H.; Kim, J.-W.; Kim, Y.; Lee, M. N.; Kook, M.-S.; Choi, E. Y.; Im, S.-Y.; Koh, J.-T. The Extracellular Matrix Protein Edil3 Stimulates Osteoblast Differentiation through the Integrin A5β1/ERK/Runx2 Pathway. *PLOS ONE* **2017**, *12* (11), e0188749. https://doi.org/10.1371/journal.pone.0188749.

(94) López-Luppo, M.; Catita, J.; Ramos, D.; Navarro, M.; Carretero, A.; Mendes-Jorge, L.; Muñoz-Cánoves, P.; Rodriguez-Baeza, A.; Nacher, V.; Ruberte, J. Cellular Senescence Is Associated With Human Retinal Microaneurysm Formation During Aging. *Invest. Ophthalmol. Vis. Sci.* **2017**, *58* (7), 2832–2842. https://doi.org/10.1167/iovs.16-20312.

(95) Di Maggio, N.; Martella, E.; Frismantiene, A.; Resink, T. J.; Schreiner, S.; Lucarelli, E.; Jaquiery, C.; Schaefer, D. J.; Martin, I.; Scherberich, A. Extracellular Matrix and A5β1 Integrin Signaling Control the Maintenance of Bone Formation Capacity by Human Adipose-Derived Stromal Cells. *Sci Rep* **2017**, *7* (1), 44398. https://doi.org/10.1038/srep44398.

(96) Diaz, C.; Neubauer, S.; Rechenmacher, F.; Kessler, H.; Missirlis, D. Recruitment of Avβ3 Integrin to A5β1 Integrin-Induced Clusters Enables Focal Adhesion Maturation and Cell Spreading. *J Cell Sci* **2020**, *133* (1), jcs232702. https://doi.org/10.1242/jcs.232702.

(97) Hanna, C. C.; Kriegesmann, J.; Dowman, L. J.; Becker, C. F. W.; Payne, R. J. Chemical Synthesis and Semisynthesis of Lipidated Proteins. *Angewandte Chemie International Edition* **2022**, *61* (15), e202111266. https://doi.org/10.1002/anie.202111266.

(98) Ward, B. P.; Ottaway, N. L.; Perez-Tilve, D.; Ma, D.; Gelfanov, V. M.; Tschöp, M. H.; DiMarchi, R. D. Peptide Lipidation Stabilizes Structure to Enhance Biological Function. *Molecular Metabolism* **2013**, *2* (4), 468–479. https://doi.org/10.1016/j.molmet.2013.08.008.

(99) Vicente-Garcia, C.; Colomer, I. Lipopeptides as Tools in Catalysis, Supramolecular, Materials and Medicinal Chemistry. *Nat Rev Chem* **2023**, *7* (10), 710–731. https://doi.org/10.1038/s41570-023-00532-8.

(100) W. Hamley, I. Lipopeptides: From Self-Assembly to Bioactivity. *Chemical Communications* **2015**, *51* (41), 8574–8583. https://doi.org/10.1039/C5CC01535A.

(101) Qiu, Z.; Zheng, X.; Pan, S.; Zhong, Y.; Chen, X.; Wen, X.; Chen, X.; Li, S.; Cheng, H.; Chen, X. Stearic Acid-Modified PSMA-Targeting Peptide–Drug Conjugate for Long-Acting Prostate Cancer Therapy. *Chem Sci*. https://doi.org/10.1039/d5sc08259e.

(102) Palladino, P.; Castelletto, V.; Dehsorkhi, A.; Stetsenko, D.; Hamley, I. W. Conformation and Self-Association of Peptide Amphiphiles Based on the KTTKS Collagen Sequence. *Langmuir* **2012**, *28* (33), 12209–12215. https://doi.org/10.1021/la302123h.

(103) Budin, I.; Prwyes, N.; Zhang, N.; Szostak, J. W. Chain-Length Heterogeneity Allows for the Assembly of Fatty Acid Vesicles in Dilute Solutions. *Biophys J* **2014**, *107* (7), 1582–1590. https://doi.org/10.1016/j.bpj.2014.07.067.

(104) White, P.; Collins, J.; Cox, Z.; Corp, C. Comparative Study of Conventional and Microwave Assisted Synthesis.

(105) Singh, S. K.; Collins, J. M. New Developments in Microwave–Assisted Solid Phase Peptide Synthesis. In *Peptide Synthesis: Methods and Protocols*; Hussein, W. M., Skwarczynski, M., Toth, I., Eds.; Springer US: New York, NY, 2020; pp 95–109. https://doi.org/10.1007/978-1-0716-0227-0_6.

(106) *Mechanistic Studies of the Triggered Release of Liposomal Contents by Matrix Metalloproteinase-9 | Journal of the American Chemical Society*. https://pubs.acs.org/doi/10.1021/ja801548g (accessed 2026-03-19).

(107) AD-0178 Determination of Protein Secondary Structures Using FTIR Spectroscopy. https://www.shimadzu.com/an/sites/shimadzu.com.an/files/pim/pim_document_file/applications/application_note/13324/apa218043.pdf (accessed 2026-03-19).

(108) Vicente-Garcia, C.; Colomer, I. Lipopeptides as Tools in Catalysis, Supramolecular, Materials and Medicinal Chemistry. *Nat Rev Chem* **2023**, *7* (10), 710–731. https://doi.org/10.1038/s41570-023-00532-8.

(109) The IKVAV Peptide: A Technical Guide to Sequence, Structure, and Function.

(110) Das, U.; Hariprasad, G.; Ethayathulla, A. S.; Manral, P.; Das, T. K.; Pasha, S.; Mann, A.; Ganguli, M.; Verma, A. K.; Bhat, R.; Chandrayan, S. K.; Ahmed, S.; Sharma, S.; Kaur, P.; Singh, T. P.; Srinivasan, A. Inhibition of Protein Aggregation:

Supramolecular Assemblies of Arginine Hold the Key. *PLoS One* **2007**, *2* (11), e1176. https://doi.org/10.1371/journal.pone.0001176.

(111) Ng, Y. K.; Konermann, L. Mechanism of Protein Aggregation Inhibition by Arginine: Blockage of Anionic Side Chains Favors Unproductive Encounter Complexes. *J. Am. Chem. Soc.* **2024**, *146* (12), 8394–8406. https://doi.org/10.1021/jacs.3c14180.

(112) Yan, X.; Lin, L.; Li, S.; Wang, W.; Chen, B.; Jiang, S.; Liu, S.; Ma, X.; Yu, X. Arginine-Rich Peptide Based Nanoparticles with Bridge-like Structure: Enhanced Cell Penetration and Tumor Therapy Effect. *Chemical Engineering Journal* **2020**, *395*, 125171. https://doi.org/10.1016/j.cej.2020.125171.

(113) Makowska, M.; Kosikowska-Adamus, P.; Zdrowowicz, M.; Wyrzykowski, D.; Prahl, A.; Sikorska, E. Lipidation of Naturally Occurring α-Helical Antimicrobial Peptides as a Promising Strategy for Drug Design. *International Journal of Molecular Sciences* **2023**, *24* (4). https://doi.org/10.3390/ijms24043951.

(114) Castelletto, V.; Hamley, I. W.; Whitehouse, C.; Matts, P. J.; Osborne, R.; Baker, E. S. Self-Assembly of Palmitoyl Lipopeptides Used in Skin Care Products. *Langmuir* **2013**, *29* (29), 9149–9155. https://doi.org/10.1021/la401771j.

(115) Erdemli, Ö.; Tezcaner, A. Hydrogels as Extracellular Matrix Mimics. In *Hydrogels and Bioinks in Tissue Engineering*; Hasirci, N., Hasirci, V., Eds.; Springer Nature Switzerland: Cham, 2025; pp 107–126. https://doi.org/10.1007/978-3-031-90966-5_7.

(116) Sui, J.; Pragnere, S.; A. Kurniawan, N. Revisiting the Biophysical Aspects of Extracellular-Matrix-Mimicking Hydrogels: What Cells See vs. What Cells Feel. *Biomaterials Science* **2025**, *13* (19), 5297–5324. https://doi.org/10.1039/D5BM00210A.

(117) Li, L.; Wang, S.; Chen, Y.; Dong, S.; Zhang, C.; Liao, L.; Zhang, W. Hydrogels Mimicking the Viscoelasticity of Extracellular Matrix for Regenerative Medicine: Design, Application, and Molecular Mechanism. *Chemical Engineering Journal* **2024**, *498*, 155206. https://doi.org/10.1016/j.cej.2024.155206.

(118) *Self-assembling Peptide Hydrogels as Extracellular Matrix-Mimicking Scaffolds for Tissue Regeneration in Chronic-Degenerative Diseases | Springer Nature Link*. https://link.springer.com/chapter/10.1007/978-3-031-29360-3_11 (accessed 2026-03-17).

(119) Tan, D.-H.; Chang, C.-Y.; Huang, Y.-C.; Lin, M.-F.; Su, W.-F. Biomimicking Extracellular Matrix Fabricated from Alginate-Polypeptide Hydrogel with Aligned Fibrous Structure. *Colloids and Surfaces A: Physicochemical and Engineering Aspects* **2025**, *727*, 138120. https://doi.org/10.1016/j.colsurfa.2025.138120.

(120) Lin, B. F.; Megley, K. A.; Viswanathan, N.; Krogstad, D. V.; Drews, L. B.; Kade, M. J.; Qian, Y.; Tirrell, M. V. pH-Responsive Branched Peptide Amphiphile Hydrogel Designed for Applications in Regenerative Medicine with Potential as Injectable Tissue Scaffolds. *J. Mater. Chem.* **2012**, *22* (37), 19447–19454. https://doi.org/10.1039/C2JM31745A.

(121) Sun, W.; Gregory, D. A.; Zhao, X. Designed Peptide Amphiphiles as Scaffolds for Tissue Engineering. *Advances in Colloid and Interface Science* **2023**, *314*, 102866. https://doi.org/10.1016/j.cis.2023.102866.

(122) Younis, M.; Tabish, T. A.; Firdharini, C.; Aslam, M.; Khair, M.; Anjum, D. H.; Yan, X.; Abbas, M. Self-Assembled Peptide-Based Fibrous Hydrogel as a Biological

Catalytic Scaffold for Nitric Oxide Generation and Encapsulation. *ACS Appl. Mater. Interfaces* **2025**, *17* (19), 27964–27973. https://doi.org/10.1021/acsami.5c03250.

(123) Binaymotlagh, R.; Chronopoulou, L.; Palocci, C. Peptide-Based Hydrogels: Template Materials for Tissue Engineering. *J Funct Biomater* **2023**, *14* (4), 233. https://doi.org/10.3390/jfb14040233.

(124) Knight, C. G.; Morton, L. F.; Onley, D. J.; Peachey, A. R.; Messent, A. J.; Smethurst, P. A.; Tuckwell, D. S.; Farndale, R. W.; Barnes, M. J. Identification in Collagen Type I of an Integrin Alpha2 Beta1-Binding Site Containing an Essential GER Sequence. *J Biol Chem* **1998**, *273* (50), 33287–33294. https://doi.org/10.1074/jbc.273.50.33287.

(125) Knight, C. G.; Morton, L. F.; Peachey, A. R.; Tuckwell, D. S.; Farndale, R. W.; Barnes, M. J. The Collagen-Binding A-Domains of Integrins A1β1 and α2β1Recognize the Same Specific Amino Acid Sequence, GFOGER, in Native (Triple-Helical) Collagens *. *Journal of Biological Chemistry* **2000**, *275* (1), 35–40. https://doi.org/10.1074/jbc.275.1.35.

(126) Clark, A. Y.; Martin, K. E.; García, J. R.; Johnson, C. T.; Theriault, H. S.; Han, W. M.; Zhou, D. W.; Botchwey, E. A.; García, A. J. Integrin-Specific Hydrogels Modulate Transplanted Human Bone Marrow-Derived Mesenchymal Stem Cell Survival, Engraftment, and Reparative Activities. *Nat Commun* **2020**, *11* (1), 114. https://doi.org/10.1038/s41467-019-14000-9.

(127) Sipilä, K. H.; Drushinin, K.; Rappu, P.; Jokinen, J.; Salminen, T. A.; Salo, A. M.; Käpylä, J.; Myllyharju, J.; Heino, J. Proline Hydroxylation in Collagen Supports Integrin Binding by Two Distinct Mechanisms. *Journal of Biological Chemistry* **2018**, *293* (20), 7645–7658. https://doi.org/10.1074/jbc.RA118.002200.

(128) Lukomski, S.; Nakashima, K.; Abdi, I.; Cipriano, V. J.; Shelvin, B. J.; Graviss, E. A.; Musser, J. M. Identification and Characterization of a Second Extracellular Collagen-Like Protein Made by Group AStreptococcus: Control of Production at the Level of Translation. *Infection and Immunity* **2001**, *69* (3), 1729–1738. https://doi.org/10.1128/iai.69.3.1729-1738.2001.

(129) Humtsoe, J. O.; Kim, J. K.; Xu, Y.; Keene, D. R.; Höök, M.; Lukomski, S.; Wary, K. K. A Streptococcal Collagen-like Protein Interacts with the A2β1 Integrin and Induces Intracellular Signaling*. *Journal of Biological Chemistry* **2005**, *280* (14), 13848–13857. https://doi.org/10.1074/jbc.M410605200.

(130) Lukomski, S.; Nakashima, K.; Abdi, I.; Cipriano, V. J.; Ireland, R. M.; Reid, S. D.; Adams, G. G.; Musser, J. M. Identification and Characterization of Thescl Gene Encoding a Group A StreptococcusExtracellular Protein Virulence Factor with Similarity to Human Collagen. *Infection and Immunity* **2000**, *68* (12), 6542–6553. https://doi.org/10.1128/iai.68.12.6542-6553.2000.

(131) Aerssens, D.; Theppawong, A.; Vu, H.; Rigole, P.; Troys, M. V.; Coenye, T.; Hoogenboom, R.; Ballet, S.; Martin, C.; Madder, A. A Short Amphipathic Peptide-Based Injectable Hydrogel with Antibacterial Properties. *RSC Adv.* **2025**, *15* (30), 24566–24574. https://doi.org/10.1039/D5RA03481G.

(132) Impresari, E.; Bossi, A.; Lumina, E. M.; Ortenzi, M. A.; Kothuis, J. M.; Cappelletti, G.; Maggioni, D.; Christodoulou, M. S.; Bucci, R.; Pellegrino, S. Fatty Acids/Tetraphenylethylene Conjugates: Hybrid AIEgens for the Preparation of Peptide-Based Supramolecular Gels. *Frontiers in Chemistry* **2022**, *10*.

(133) Colombo, E.; Aydın, E. M.; Canıtez, İ. S.; Polito, L.; Penconi, M.; Bossi, A.; Impresari, E.; Passarella, D.; Dallavalle, S.; Athanassopoulos, C. M.; Pellegrino, S.; Şahin, I. D.;

Christodoulou, M. S. Tetraphenylethylene-Based Photoluminescent Self-Assembled Nanoparticles: Preparation and Biological Evaluation. *ACS Med. Chem. Lett.* **2023**, *14* (10), 1472–1477. https://doi.org/10.1021/acsmedchemlett.3c00396.

(134) *Lipopeptide Hydrogel Possesses Adjuvant-Like Properties for the Delivery of the GPC-3 Peptide-derived Antigen - Mathes - 2025 - Advanced Functional Materials - Wiley Online Library*. https://advanced.onlinelibrary.wiley.com/doi/10.1002/adfm.202413870 (accessed 2025-06-24).

(135) Tan, T.; Hou, Y.; Shi, J.; Wang, B.; Zhang, Y. Biostable Hydrogels Consisting of Hybrid β-Sheet Fibrils Assembled by a Pair of Enantiomeric Peptides. *Materials Today Bio* **2024**, *25*, 100961. https://doi.org/10.1016/j.mtbio.2024.100961.

(136) Raeburn, J.; Pont, G.; Chen, L.; Cesbron, Y.; Lévy, R.; Adams, D. J. Fmoc-Diphenylalanine Hydrogels: Understanding the Variability in Reported Mechanical Properties. *Soft Matter* **2012**, *8* (4), 1168–1174. https://doi.org/10.1039/C1SM06929B.

(137) Bertouille, J.; Van Lommel, R.; Aerts, R.; Dockx, L.; Mangialetto, J.; Van den Brande, N.; Willaert, R. G.; De Proft, F.; Hennecke, U.; Martin, C.; Herrebout, W.; Jansen, T. L. C.; Cunha, A. V.; Ballet, S. A Comparative Study between Phenylglycine and Phenylalanine Derived Peptide Hydrogels: Towards Atomic Elucidation. *Materials Today Chemistry* **2025**, *44*, 102593. https://doi.org/10.1016/j.mtchem.2025.102593.

(138) *Insight into the self-assembly and gel formation of a bioactive peptide derived from bovine casein - ScienceDirect*. https://www.sciencedirect.com/science/article/pii/S2667160323000157#sec0002 (accessed 2025-06-24).

(139) *Forging out-of-equilibrium supramolecular gels | Nature Synthesis*. https://www.nature.com/articles/s44160-024-00623-4#Sec4 (accessed 2025-06-24).

(140) *The Use of Circular Dichroism in the Investigation of Protein Structure and Function | Bentham Science*. https://www.eurekaselect.com/article/26718 (accessed 2026-03-19).

(141) Migliore, M.; Bonvicini, A.; Tognetti, V.; Guilhaudis, L.; Baaden, M.; Oulyadi, H.; Joubert, L.; Ségalas-Milazzo, I. Characterization of β-Turns by Electronic Circular Dichroism Spectroscopy: A Coupled Molecular Dynamics and Time-Dependent Density Functional Theory Computational Study. *Phys. Chem. Chem. Phys.* **2020**, *22* (3), 1611–1623. https://doi.org/10.1039/C9CP05776E.

(142) Sivagnanam, S.; Arul, A.; Ghosh, S.; Dey, A.; Ghorai, S.; Das, P. Concentration-Dependent Fabrication of Short-Peptide-Based Different Self-Assembled Nanostructures with Various Morphologies and Intracellular Delivery Property. *Materials Chemistry Frontiers* **2019**, *3* (10), 2110–2119. https://doi.org/10.1039/C9QM00363K.

(143) Pentlavalli, S.; Coulter, S. M.; An, Y.; Cross, E. R.; Sun, H.; Moore, J. V.; Sabri, A. B.; Greer, B.; Vora, L.; McCarthy, H. O.; Laverty, G. D-Peptide Hydrogels as a Long-Acting Multipurpose Drug Delivery Platform for Combined Contraception and HIV Prevention. *Journal of Controlled Release* **2025**, *379*, 30–44. https://doi.org/10.1016/j.jconrel.2024.12.052.

(144) Heino, J.; Siljamäki, E. Integrins A1β1 and A2β1: The Generalist Collagen Receptors. In *Integrins in Health and Disease: Key Effectors of Cell-Matrix and Cell-Cell Interactions*; Gullberg, D., Eble, J. A., Eds.; Springer International Publishing: Cham, 2023; pp 3–25. https://doi.org/10.1007/978-3-031-23781-2_1.

(145) Mhanna, R.; Öztürk, E.; Vallmajo-Martin, Q.; Millan, C.; Müller, M.; Zenobi-Wong, M. GFOGER-Modified MMP-Sensitive Polyethylene Glycol Hydrogels Induce Chondrogenic Differentiation of Human Mesenchymal Stem Cells. *Tissue Eng Part A* **2014**, *20* (7–8), 1165–1174. https://doi.org/10.1089/ten.tea.2013.0519.

(146) Reynolds, N. P.; Adamcik, J.; Berryman, J. T.; Handschin, S.; Zanjani, A. A. H.; Li, W.; Liu, K.; Zhang, A.; Mezzenga, R. Competition between Crystal and Fibril Formation in Molecular Mutations of Amyloidogenic Peptides. *Nat Commun* **2017**, *8* (1), 1338. https://doi.org/10.1038/s41467-017-01424-4.

(147) *Modular bioink for 3D printing of biocompatible hydrogels: sol–gel polymerization of hybrid peptides and polymers - RSC Advances (RSC Publishing)*. https://pubs.rsc.org/en/content/articlelanding/2017/ra/c6ra28540f (accessed 2026-01-05).

(148) Matson, J. B.; Zha, R. H.; Stupp, S. I. Peptide Self-Assembly for Crafting Functional Biological Materials. *Curr Opin Solid State Mater Sci* **2011**, *15* (6), 225–235. https://doi.org/10.1016/j.cossms.2011.08.001.

(149) Hartgerink, J. D.; Beniash, E.; Stupp, S. I. Self-Assembly and Mineralization of Peptide-Amphiphile Nanofibers. *Science* **2001**, *294* (5547), 1684–1688. https://doi.org/10.1126/science.1063187.

(150) Cui, H.; Webber, M. J.; Stupp, S. I. Self-Assembly of Peptide Amphiphiles: From Molecules to Nanostructures to Biomaterials. *Peptide Science* **2010**, *94* (1), 1–18. https://doi.org/10.1002/bip.21328.

(151) Paramonov, S. E.; Jun, H.-W.; Hartgerink, J. D. Self-Assembly of Peptide−Amphiphile Nanofibers: The Roles of Hydrogen Bonding and Amphiphilic Packing. *J. Am. Chem. Soc.* **2006**, *128* (22), 7291–7298. https://doi.org/10.1021/ja060573x.

(152) Pavani, P.; Kumar, K.; Rani, A.; Venkatesu, P.; Lee, M.-J. The Influence of Sodium Phosphate Buffer on the Stability of Various Proteins: Insights into Protein-Buffer Interactions. *Journal of Molecular Liquids* **2021**, *331*, 115753. https://doi.org/10.1016/j.molliq.2021.115753.

(153) Rad-Malekshahi, M.; Lempsink, L.; Amidi, M.; Hennink, W. E.; Mastrobattista, E. Biomedical Applications of Self-Assembling Peptides. *Bioconjugate Chem.* **2016**, *27* (1), 3–18. https://doi.org/10.1021/acs.bioconjchem.5b00487.

(154) Yan, C.; Pochan, D. J. Rheological Properties of Peptide-Based Hydrogels for Biomedical and Other Applications. *Chemical Society Reviews* **2010**. https://doi.org/10.1039/B919449P.

(155) Reyes, C. D.; García, A. J. A2β1 Integrin-Specific Collagen-Mimetic Surfaces Supporting Osteoblastic Differentiation. *Journal of Biomedical Materials Research Part A* **2004**, *69A* (4), 591–600. https://doi.org/10.1002/jbm.a.30034.

(156) De Maeseneer, T.; Cauwenbergh, T.; Gardiner, J.; White, J. F.; Thielemans, W.; Martin, C.; Moldenaers, P.; Ballet, S.; Cardinaels, R. Peptide Sequence Variations Govern Hydrogel Stiffness: Insights from a Multi-Scale Structural Analysis of H-FQFQFK-NH2 Peptide Derivatives. *Macromolecular Bioscience* **2024**, *24* (8), 2300579. https://doi.org/10.1002/mabi.202300579.

(157) Zhang, N.-Y.; Hu, X.-J.; An, H.-W.; Liang, J.-X.; Wang, H. Programmable Design and Self Assembly of Peptide Conjugated AIEgens for Biomedical Applications. *Biomaterials* **2022**, *287*, 121655. https://doi.org/10.1016/j.biomaterials.2022.121655.

(158) Bera, S.; Mondal, S.; Xue, B.; Shimon, L. J. W.; Cao, Y.; Gazit, E. Rigid Helical-like Assemblies from a Self-Aggregating Tripeptide. *Nat. Mater.* **2019**, *18* (5), 503–509. https://doi.org/10.1038/s41563-019-0343-2.

(159) Zhang, L.; Li, Y.; Mu, G.; Yang, L.; Ren, C.; Wang, Z.; Guo, Q.; Liu, J.; Yang, C. Structure of Self-Assembled Peptide Determines the Activity of Aggregation-Induced Emission Luminogen-Peptide Conjugate for Detecting Alkaline Phosphatase. *Anal. Chem.* **2022**, *94* (4), 2236–2243. https://doi.org/10.1021/acs.analchem.1c04936.

(160) Gao, Y.; Wang, L.; Zhang, X.; Zhou, Z.; Shen, X.; Hu, H.; Sun, R.; Tang, J. Advances in Self-Assembled Peptides as Drug Carriers. *Pharmaceutics* **2023**, *15* (2). https://doi.org/10.3390/pharmaceutics15020482.

(161) Tallawi, M.; Rosellini, E.; Barbani, N.; Cascone, M. G.; Rai, R.; Saint-Pierre, G.; Boccaccini, A. R. Strategies for the Chemical and Biological Functionalization of Scaffolds for Cardiac Tissue Engineering: A Review. *J. R. Soc. Interface.* **2015**, *12* (108), 20150254. https://doi.org/10.1098/rsif.2015.0254.

(162) Xia, D.; Chen, J.; Zhang, Z.; Dong, M. Emerging Polymeric Biomaterials and Manufacturing Techniques in Regenerative Medicine. *Aggregate* **2022**, *3* (5), e176. https://doi.org/10.1002/agt2.176.

(163) Rickel, A. P.; Deng, X.; Engebretson, D.; Hong, Z. Electrospun Nanofiber Scaffold for Vascular Tissue Engineering. *Materials Science and Engineering: C* **2021**, *129*, 112373. https://doi.org/10.1016/j.msec.2021.112373.

(164) Bucci, R.; Vaghi, F.; Erba, E.; Romanelli, A.; Gelmi, M. L.; Clerici, F. Peptide Grafting Strategies before and after Electrospinning of Nanofibers. *Acta Biomaterialia* **2021**, *122*, 82–100. https://doi.org/10.1016/j.actbio.2020.11.051.

(165) Onak Pulat, G.; Tatar, A. G.; Usta, Y. H.; Karaman, O. Improved Endothelial Cell Proliferation on Laminin-Derived Peptide Conjugated Nanofibrous Microtubes Using Custom Made Bioreactor. *International Advanced Researches and Engineering Journal* **2022**, *6* (3), 220–226. https://doi.org/10.35860/iarej.1096616.

(166) Asakura, T.; Hayashi, T.; Tanaka, T.; Tatematsu, K.; Sezutsu, H. Promotion of Endothelialization of Silk Functionalized with IKVAV Peptide and Production of Silk Containing IKVAV-REDV Sequence by Transgenic Silkworms. *J Biomater Appl* **2025**, *40* (3), 402–418. https://doi.org/10.1177/08853282251345003.

(167) Grant, D. S.; Kinsella, J. L.; Fridman, R.; Auerbach, R.; Piasecki, B. A.; Yamada, Y.; Zain, M.; Kleinman, H. K. Interaction of Endothelial Cells with a Laminin A Chain Peptide (SIKVAV) in Vitro and Induction of Angiogenic Behavior in Vivo. *Journal Cellular Physiology* **1992**, *153* (3), 614–625. https://doi.org/10.1002/jcp.1041530324.

(168) Chen, S.; Zhang, M.; Shao, X.; Wang, X.; Zhang, L.; Xu, P.; Zhong, W.; Zhang, L.; Xing, M.; Zhang, L. A Laminin Mimetic Peptide SIKVAV-Conjugated Chitosan Hydrogel Promoting Wound Healing by Enhancing Angiogenesis, Re-Epithelialization and Collagen Deposition. *J. Mater. Chem. B* **2015**, *3* (33), 6798–6804. https://doi.org/10.1039/C5TB00842E.

(169) Song, Y.; Li, Y.; Zheng, Q. Angiogenesis Induced by IKVAV-Containing Amphiphile Peptide in Vivo. *J. Wuhan Univ. Technol.-Mat. Sci. Edit.* **2010**, *25* (5), 803–806. https://doi.org/10.1007/s11595-010-0096-x.

(170) Asakura, T.; Shimokawatoko, H.; Nakazawa, Y. Characterization and Promotion of Endothelialization of Bombyx Mori Silk Fibroin Functionalized with REDV Peptide. *International Journal of Biological Macromolecules* **2024**, *261*, 129746. https://doi.org/10.1016/j.ijbiomac.2024.129746.

(171) Mahara, A.; Li, M.; Ohya, Y.; Yamaoka, T. Small-Diameter Synthetic Vascular Graft Immobilized with the REDV Peptide Reduces Early-Stage Fibrin Clot Deposition and Results in Graft Patency in Rats. *Biomacromolecules* **2020**, *21* (8), 3092–3101. https://doi.org/10.1021/acs.biomac.0c00457.

(172) Zhou, J.; Wang, M.; Wei, T.; Bai, L.; Zhao, J.; Wang, K.; Feng, Y. Endothelial Cell-Mediated Gene Delivery for In Situ Accelerated Endothelialization of a Vascular Graft. *ACS Appl. Mater. Interfaces* **2021**, *13* (14), 16097–16105. https://doi.org/10.1021/acsami.1c01869.

(173) Ohya, Y.; Nishimura, K.; Sumida, H.; Yoshizaki, Y.; Kuzuya, A.; Mahara, A.; Yamaoka, T. Cellular Attachment Behavior on Biodegradable Polymer Surface Immobilizing Endothelial Cell-Specific Peptide. *Journal of Biomaterials Science, Polymer Edition* **2020**, *31* (11), 1475–1488. https://doi.org/10.1080/09205063.2020.1762325.

(174) Mansour, A.; Darwiche, W.; Yaker, L.; Da Nascimento, S.; Gomila, C.; Rossi, C.; Jung, V.; Sonnet, P.; Kamel, S.; Guerrera, I. C.; Boullier, A.; Ausseil, J. GFOGER Peptide Modifies the Protein Content of Extracellular Vesicles and Inhibits Vascular Calcification. *Front. Cell Dev. Biol.* **2020**, *8*, 589761. https://doi.org/10.3389/fcell.2020.589761.

(175) Malcor, J.-D.; Hunter, E. J.; Davidenko, N.; Bax, D. V.; Cameron, R.; Best, S.; Sinha, S.; Farndale, R. W. Collagen Scaffolds Functionalized with Triple-Helical Peptides Support 3D HUVEC Culture. *Regenerative Biomaterials* **2020**, *7* (5), 471–482. https://doi.org/10.1093/rb/rbaa025.

(176) Reyes, C. D.; García, A. J. Engineering Integrin-specific Surfaces with a Triple-helical Collagen-mimetic Peptide. *J Biomedical Materials Res* **2003**, *65A* (4), 511–523. https://doi.org/10.1002/jbm.a.10550.

(177) Ichise, S. F.; Takeuchi, S.; Aoki, S.; Kuroda, K. C.; Nose, H.; Masuda, R.; Koide, T. Development of a Collagen-like Peptide Polymer via End-to-End Disulfide Cross-Linking and Its Application as a Biomaterial. *Acta Biomaterialia* **2019**, *94*, 361–371. https://doi.org/10.1016/j.actbio.2019.06.010.

(178) Turner, K. R.; Adams, C.; Staelens, S.; Deckmyn, H.; San Antonio, J. Crucial Role for Endothelial Cell A2β1 Integrin Receptor Clustering in Collagen-Induced Angiogenesis. *The Anatomical Record* **2020**, *303* (6), 1604–1618. https://doi.org/10.1002/ar.24277.

(179) García, J. R.; Clark, A. Y.; García, A. J. Integrin-specific Hydrogels Functionalized with VEGF for Vascularization and Bone Regeneration of Critical-size Bone Defects. *J Biomedical Materials Res* **2016**, *104* (4), 889–900. https://doi.org/10.1002/jbm.a.35626.

(180) Sun, Q.; Si, J.; Zhao, L.; Wei, T.; Wang, T.; Li, F.; Li, Y.; Shafiq, M.; Wang, L.; Liu, R.; Zhi, D.; Wang, K. Direct Thrombin Inhibitor-Bivalirudin Improved the Hemocompatibility of Electrospun Polycaprolactone Vascular Grafts. *Composites*

Part B: Engineering **2022**, *234*, 109702. https://doi.org/10.1016/j.compositesb.2022.109702.

(181) Yang, Z.; Tu, Q.; Maitz, M. F.; Zhou, S.; Wang, J.; Huang, N. Direct Thrombin Inhibitor-Bivalirudin Functionalized Plasma Polymerized Allylamine Coating for Improved Biocompatibility of Vascular Devices. *Biomaterials* **2012**, *33* (32), 7959–7971. https://doi.org/10.1016/j.biomaterials.2012.07.050.

(182) Shammas, N. W. Bivalirudin: Pharmacology and Clinical Applications. *Cardiovascular Drug Reviews* **2006**, *23* (4), 345–360. https://doi.org/10.1111/j.1527-3466.2005.tb00177.x.

(183) Nomizu, M.; Kuratomi, Y.; Song, S.-Y.; Ponce, M. L.; Hoffman, M. P.; Powell, S. K.; Miyoshi, K.; Otaka, A.; Kleinman, H. K.; Yamada, Y. Identification of Cell Binding Sequences in Mouse Laminin Γ1 Chain by Systematic Peptide Screening. *Journal of Biological Chemistry* **1997**, *272* (51), 32198–32205. https://doi.org/10.1074/jbc.272.51.32198.

(184) Ponce, M. L.; Nomizu, M.; Kleinman, H. K. An Angiogenic Laminin Site and Its Antagonist Bind through the Avβ3 and Α5β1 Integrins. *The FASEB Journal* **2001**, *15* (8), 1389–1397. https://doi.org/10.1096/fj.00-0736com.

(185) Chen, H.; Fu, X.; Jiang, J.; Han, S. C16 Peptide Promotes Vascular Growth and Reduces Inflammation in a Neuromyelitis Optica Model. *Front. Pharmacol.* **2019**, *10*, 1373. https://doi.org/10.3389/fphar.2019.01373.

(186) Malinda, K. M.; Wysocki, A. B.; Koblinski, J. E.; Kleinman, H. K.; Ponce, M. L. Angiogenic Laminin-Derived Peptides Stimulate Wound Healing. *The International Journal of Biochemistry & Cell Biology* **2008**, *40* (12), 2771–2780. https://doi.org/10.1016/j.biocel.2008.05.025.

(187) Zachman, A. L.; Crowder, S. W.; Ortiz, O.; Zienkiewicz, K. J.; Bronikowski, C. M.; Yu, S. S.; Giorgio, T. D.; Guelcher, S. A.; Kohn, J.; Sung, H.-J. Pro-Angiogenic and Anti-Inflammatory Regulation by Functional Peptides Loaded in Polymeric Implants for Soft Tissue Regeneration. *Tissue Engineering Part A* **2013**, *19* (3–4), 437–447. https://doi.org/10.1089/ten.tea.2012.0158.

(188) Zachman, A. L.; Wang, X.; Tucker-Schwartz, J. M.; Fitzpatrick, S. T.; Lee, S. H.; Guelcher, S. A.; Skala, M. C.; Sung, H.-J. Uncoupling Angiogenesis and Inflammation in Peripheral Artery Disease with Therapeutic Peptide-Loaded Microgels. *Biomaterials* **2014**, *35* (36), 9635–9648. https://doi.org/10.1016/j.biomaterials.2014.08.011.

(189) Yalcin Enis, I.; Gok Sadikoglu, T. Design Parameters for Electrospun Biodegradable Vascular Grafts. *Journal of Industrial Textiles* **2018**, *47* (8), 2205–2227. https://doi.org/10.1177/1528083716654470.

(190) Kowalska, M.; Bąchor, R. Catch, Modify and Analyze: Methods of Chemoselective Modification of Cysteine-Containing Peptides. *Molecules* **2022**, *27* (5). https://doi.org/10.3390/molecules27051601.

(191) Zhang, C.; Welborn, M.; Zhu, T.; Yang, N. J.; Santos, M. S.; Van Voorhis, T.; Pentelute, B. L. π-Clamp-Mediated Cysteine Conjugation. *Nature Chem* **2016**, *8* (2), 120–128. https://doi.org/10.1038/nchem.2413.

(192) LeBel, R. G.; Goring, D. A. I. Density, Viscosity, Refractive Index, and Hygroscopicity of Mixtures of Water and Dimethyl Sulfoxide. *J. Chem. Eng. Data* **1962**, *7* (1), 100–101. https://doi.org/10.1021/je60012a032.

(193) McMurry, J. E. Carbonyl-Coupling Reactions Using Low-Valent Titanium. *Chem. Rev.* **1989**, *89* (7), 1513–1524. https://doi.org/10.1021/cr00097a007.

(194) Chu, N.-T.; Chakravarthy, R. D.; Shih, N.-C.; Lin, Y.-H.; Liu, Y.-C.; Lin, J.-H.; Lin, H.-C. Fluorescent Supramolecular Hydrogels Self-Assembled from Tetraphenylethene (TPE)/Single Amino Acid Conjugates. *RSC Adv.* **2018**, *8* (37), 20922–20927. https://doi.org/10.1039/C8RA02296H.

(195) Schneider, C. A.; Rasband, W. S.; Eliceiri, K. W. NIH Image to ImageJ: 25 Years of Image Analysis. *Nat Methods* **2012**, *9* (7), 671–675. https://doi.org/10.1038/nmeth.2089.

(196) Peqini, K.; Attanasio, S.; Feni, L.; Cappelletti, G.; Pellegrino, S. Breaking down and Building up Alpha-synuclein: An Insight on Its N-terminal Domain. *Journal of Peptide Science* **2024**, *30* (4), e3556. https://doi.org/10.1002/psc.3556.

(197) *LIVE/DEAD Cell Imaging Kit (488/570) - IT*. https://www.thermofisher.com/uk/en/home/references/protocols/cell-and-tissue-analysis/protocols/live-dead-cell-imaging-kit-488-570.html (accessed 2025-12-17).

(198) *DAPI Counterstaining Protocols - IT*. https://www.thermofisher.com/uk/en/home/references/protocols/cell-and-tissue-analysis/dapi-protocol/basic-dapi-counterstaining-protocols.html (accessed 2026-01-08).

(199) *Actin Staining Protocol - IT*. https://www.thermofisher.com/uk/en/home/references/protocols/cell-and-tissue-analysis/microscopy-protocol/actin-staining-protocol.html (accessed 2026-01-08).

9. Supplementary Data

RP-HPLC chromatograms and MS-ESI analyses

DS02 (Stearic acid-IKVAV-NH_2)

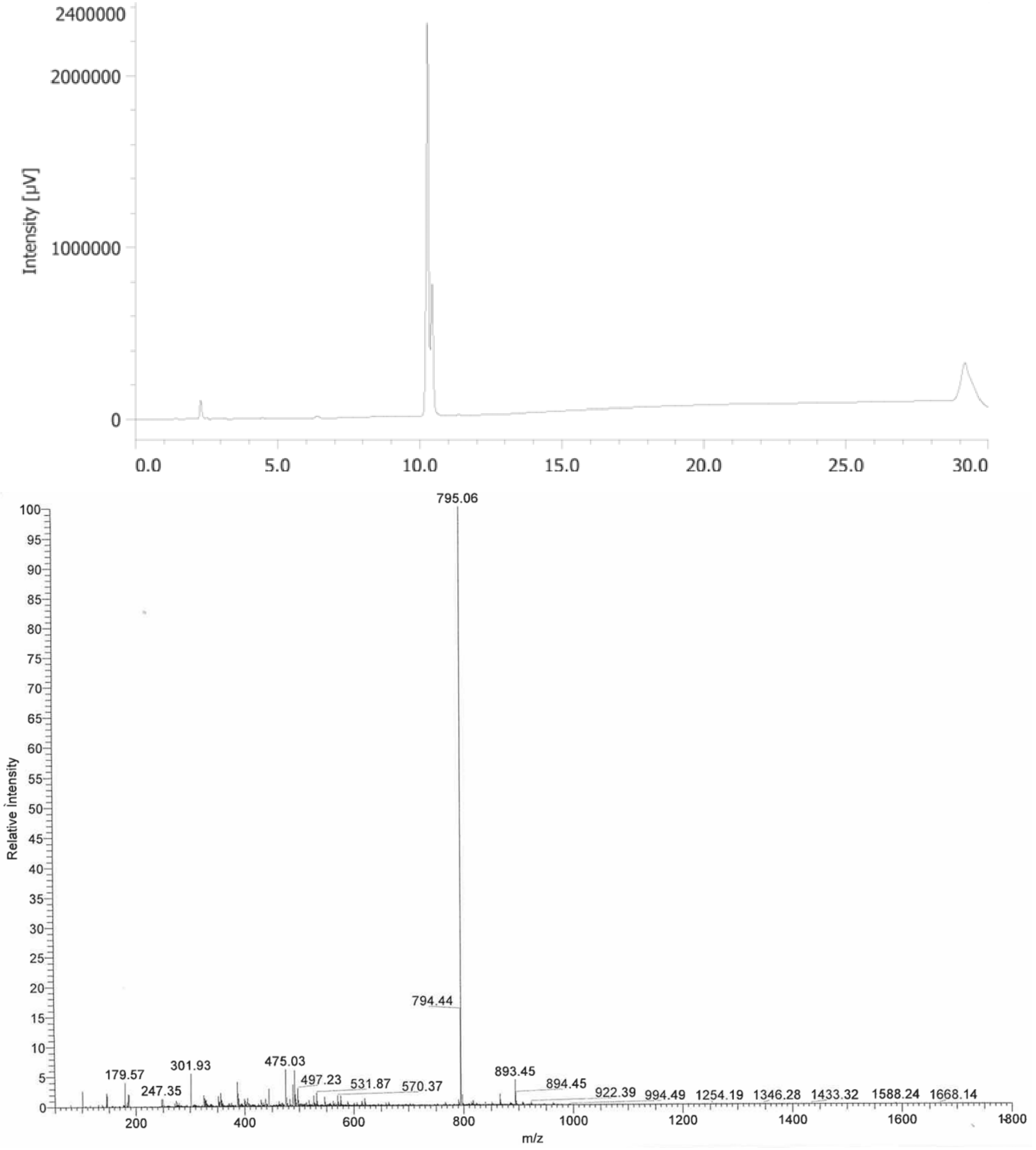

Figure 34 UV chromatogram and ESI-MS spectrum of DS02. Gradient: 20-100% of B in A in 20 min. 0.8 mL/min. A: 0.1% TFA in 100% H2O: B: 0.1% TFA in CH_3CN. The peaks signed correspond to: [M+H]+ (795.06 m/z)

DS04 (Stearic acid-REDV-NH_2)

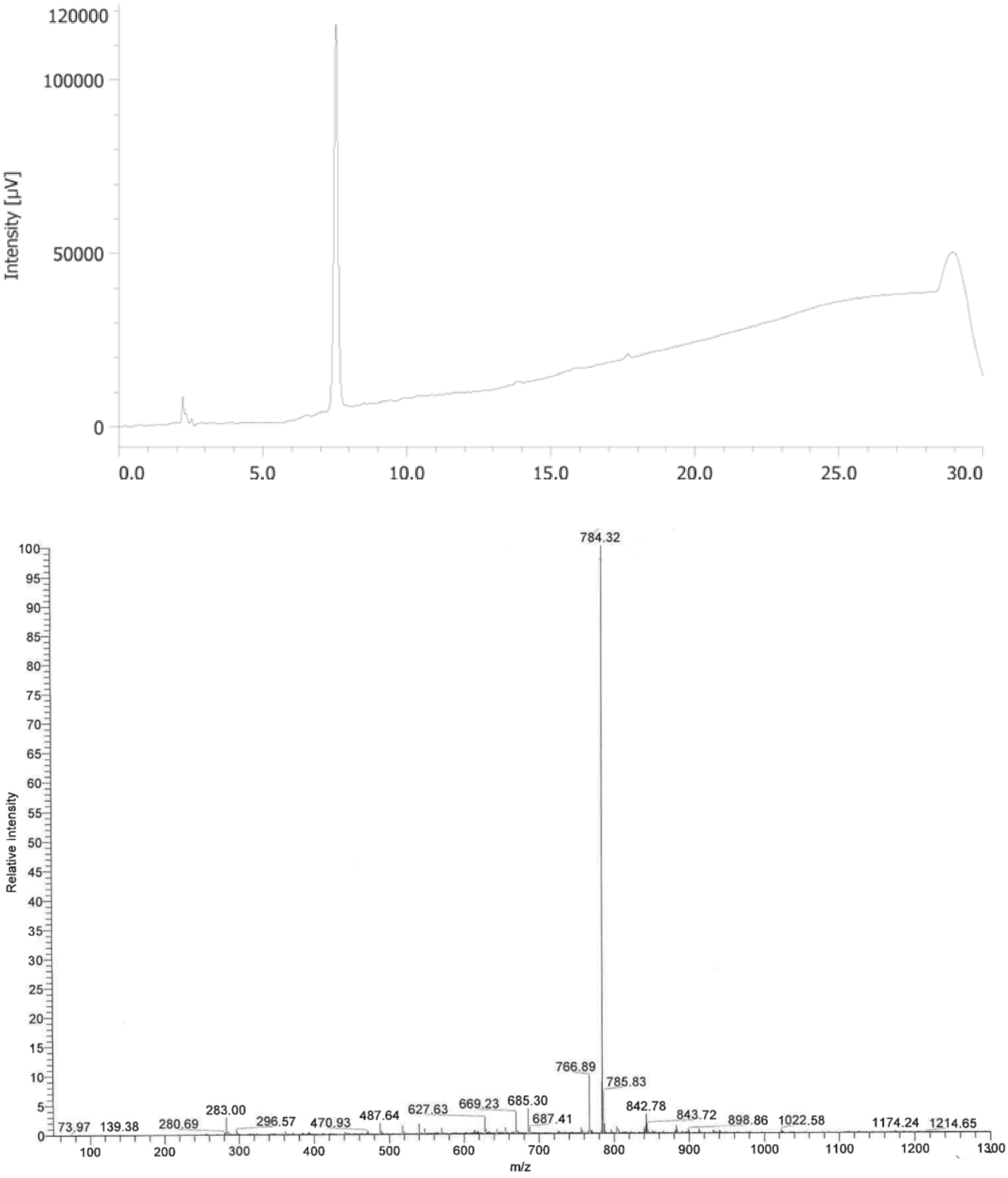

Figure 35 UV chromatogram and ESI-MS spectrum of DS04. Gradient: 20-100% of B in A in 20 min. 0.8 mL/min. A: 0.1% TFA in 100% H2O: B: 0.1% TFA in CH_3CN. The peaks signed correspond to: [M+H]+ (784.32 m/z)

DS08 (Stearic acid-GFOGER-NH_2)

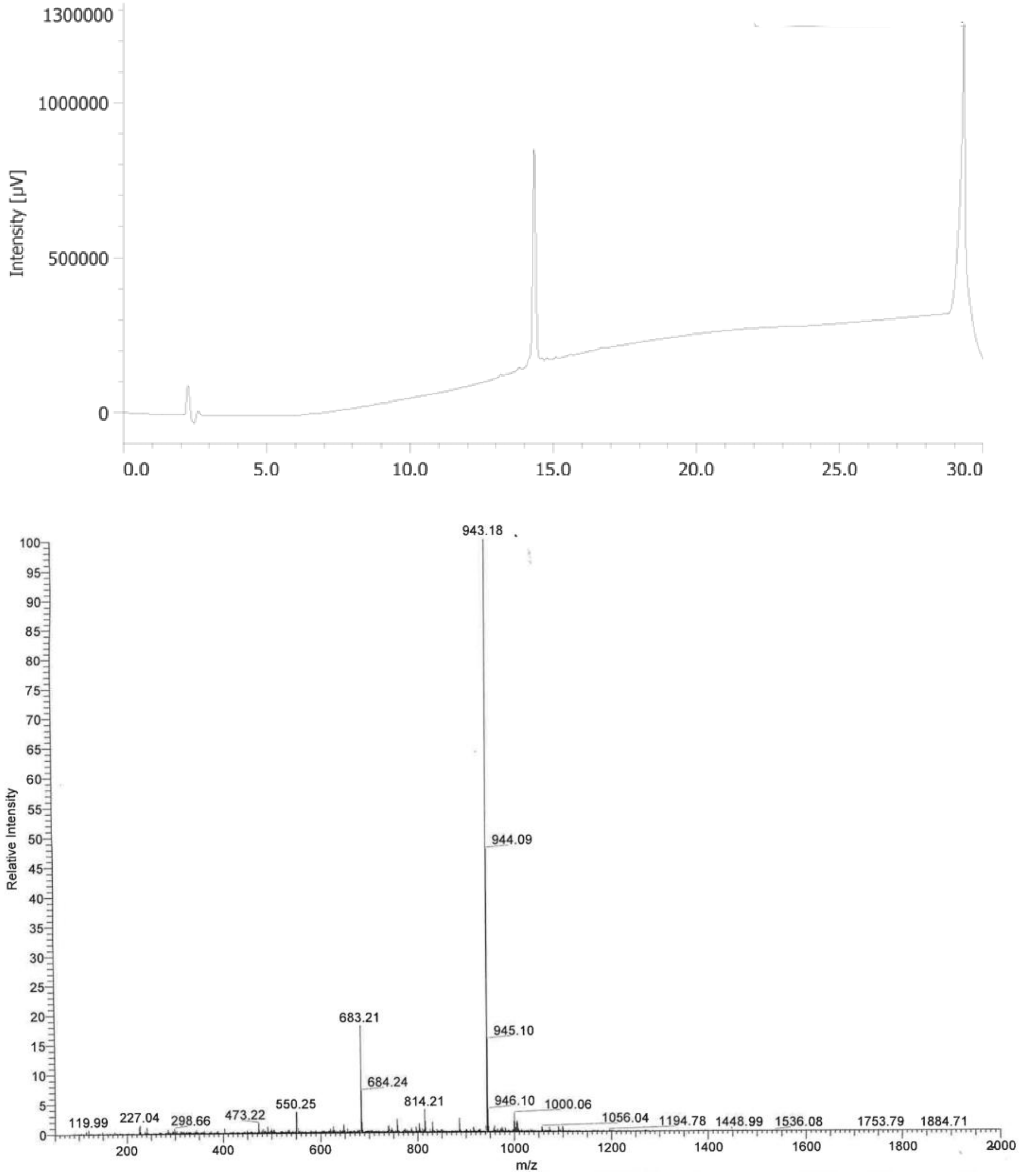

Figure 36 UV chromatogram and ESI-MS spectrum of DS08. Gradient: 20-100% of B in A in 20 min. 0.8 mL/min. A: 0.1% TFA in 100% H2O: B: 0.1% TFA in CH_3CN. The peaks signed correspond to: $[M+H]^+$ (943.18 m/z)

DS10 (Stearic acid-fPRP-NH_2)

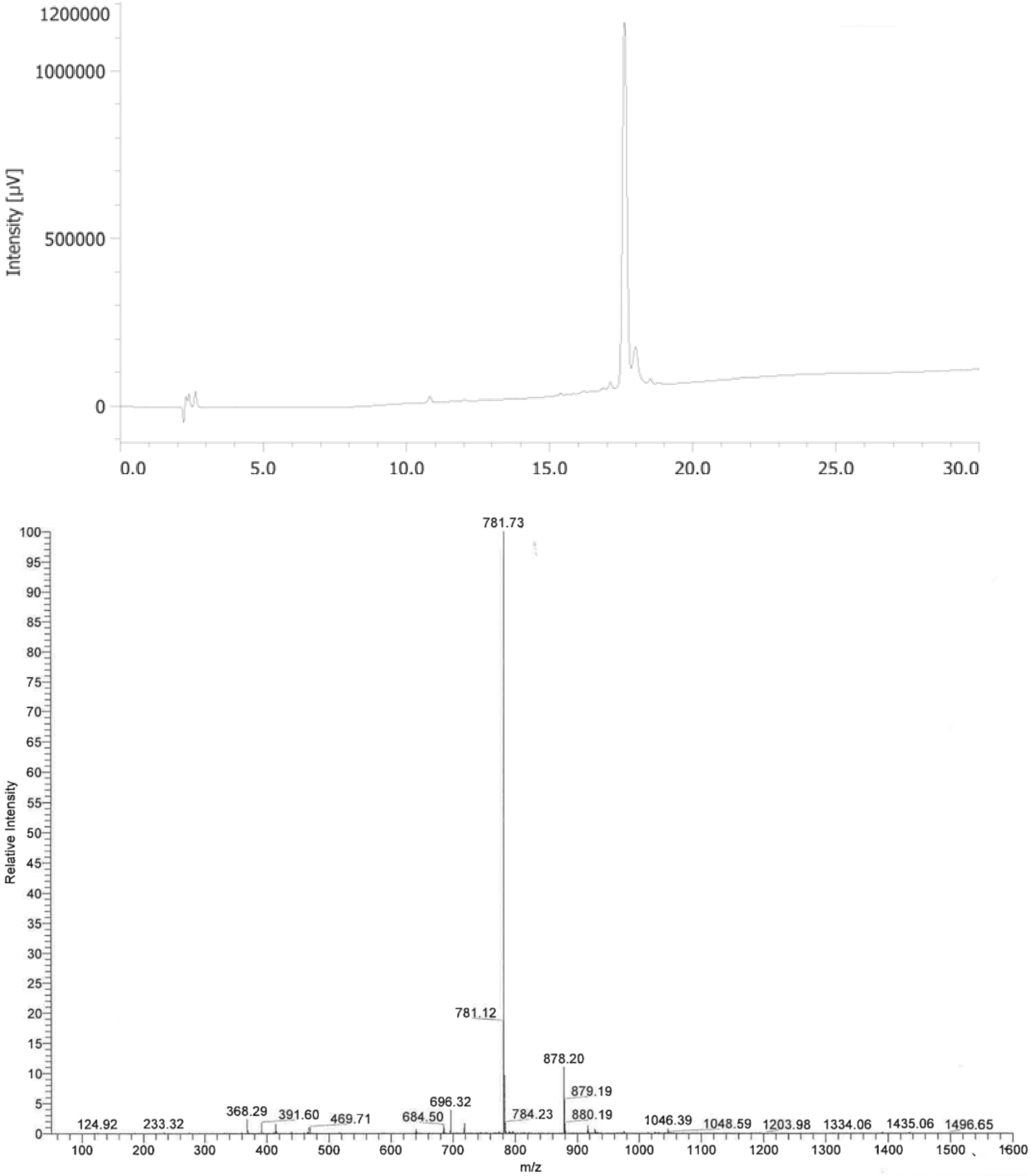

Figure 37 UV chromatogram and ESI-MS spectrum of DS10. Gradient: 20-100% of B in A in 20 min. 0.8 mL/min. A: 0.1% TFA in 100% H2O: B: 0.1% TFA in CH_3CN. The peaks signed correspond to: [M+H]+ (781.73 m/z)

DS12 (Stearic acid-KLTWQELYQLKYKGI-NH_2)

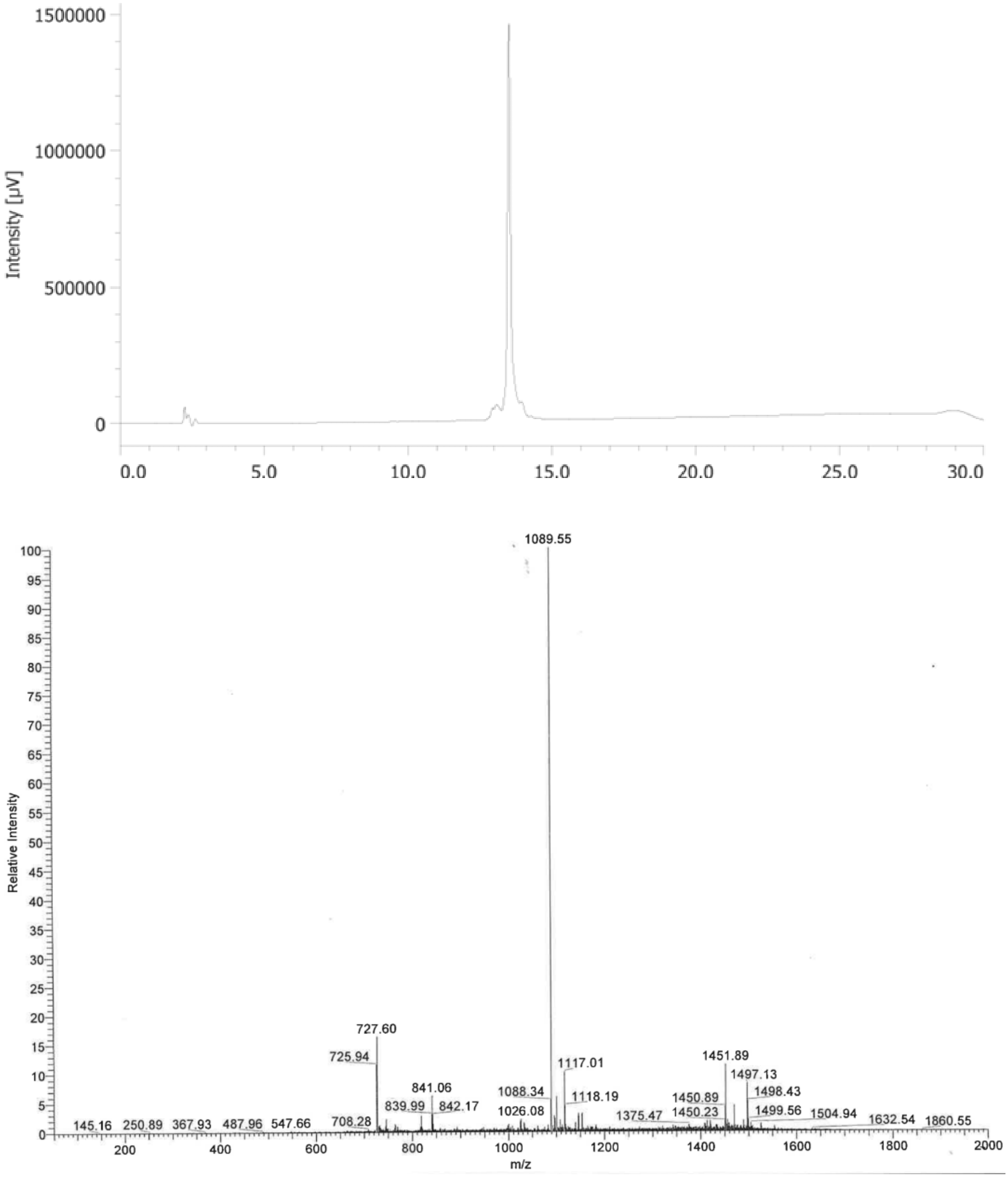

Figure 38 UV chromatogram and ESI-MS spectrum of DS12. Gradient: 20-100% of B in A in 20 min. 0.8 mL/min. A: 0.1% TFA in 100% H2O: B: 0.1% TFA in CH_3CN. The peaks signed correspond to: [M+2H]2+ (1089.55 m/z) and [M+3H]3+ (727.60 m/z)

DS14 (Stearic acid-KAFDITYVRLKF-NH_2)

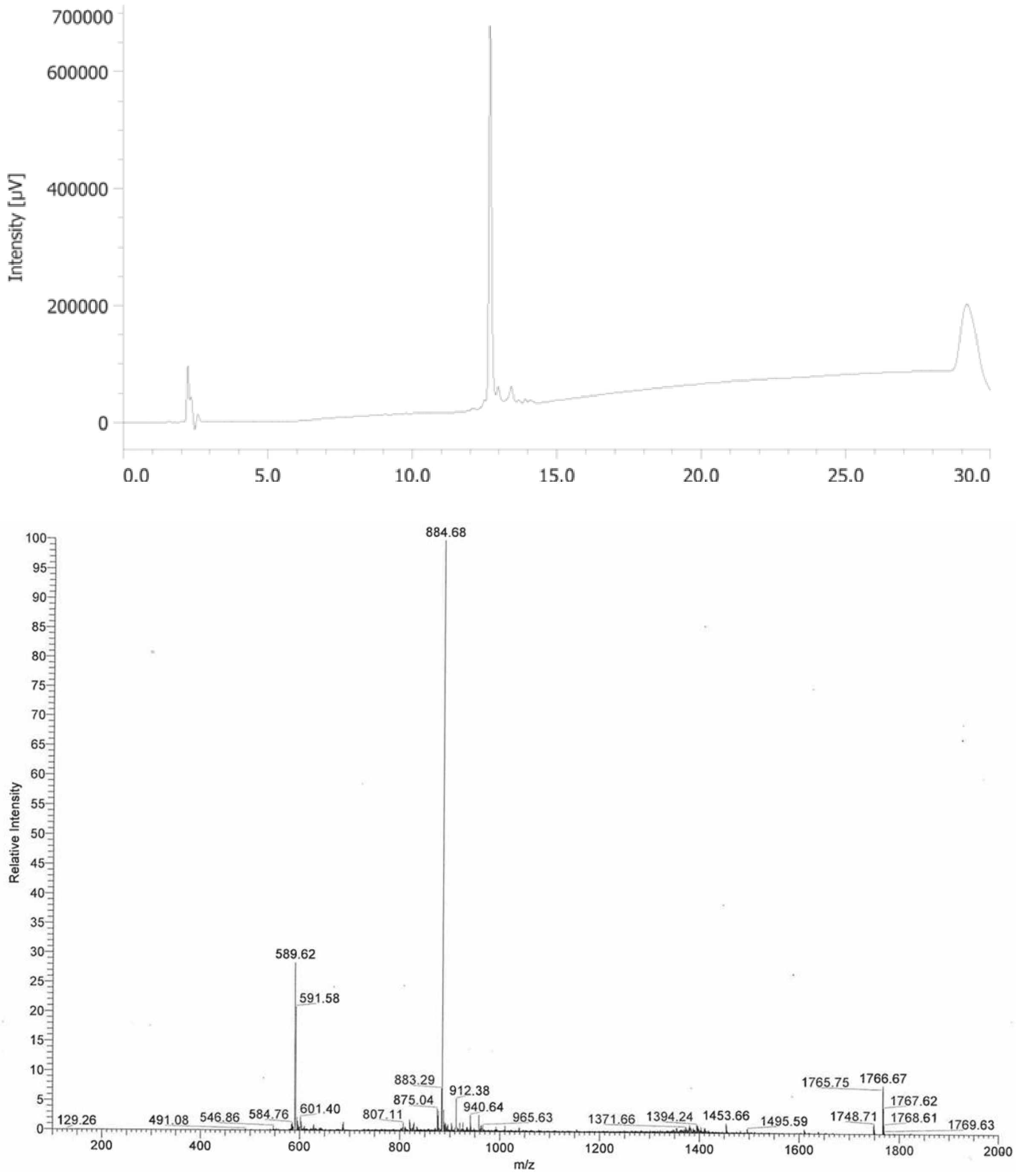

Figure 39 UV chromatogram and ESI-MS spectrum of DS14. Gradient: 20-100% of B in A in 20 min. 0.8 mL/min. A: 0.1% TFA in 100% H2O: B: 0.1% TFA in CH_3CN. The peaks signed correspond to: [M+2H]+2 (884.68 m/z) and [M+3H]+3 (589.62 m/z)

DS33 (FQFQFKGFPGER-NH_2)

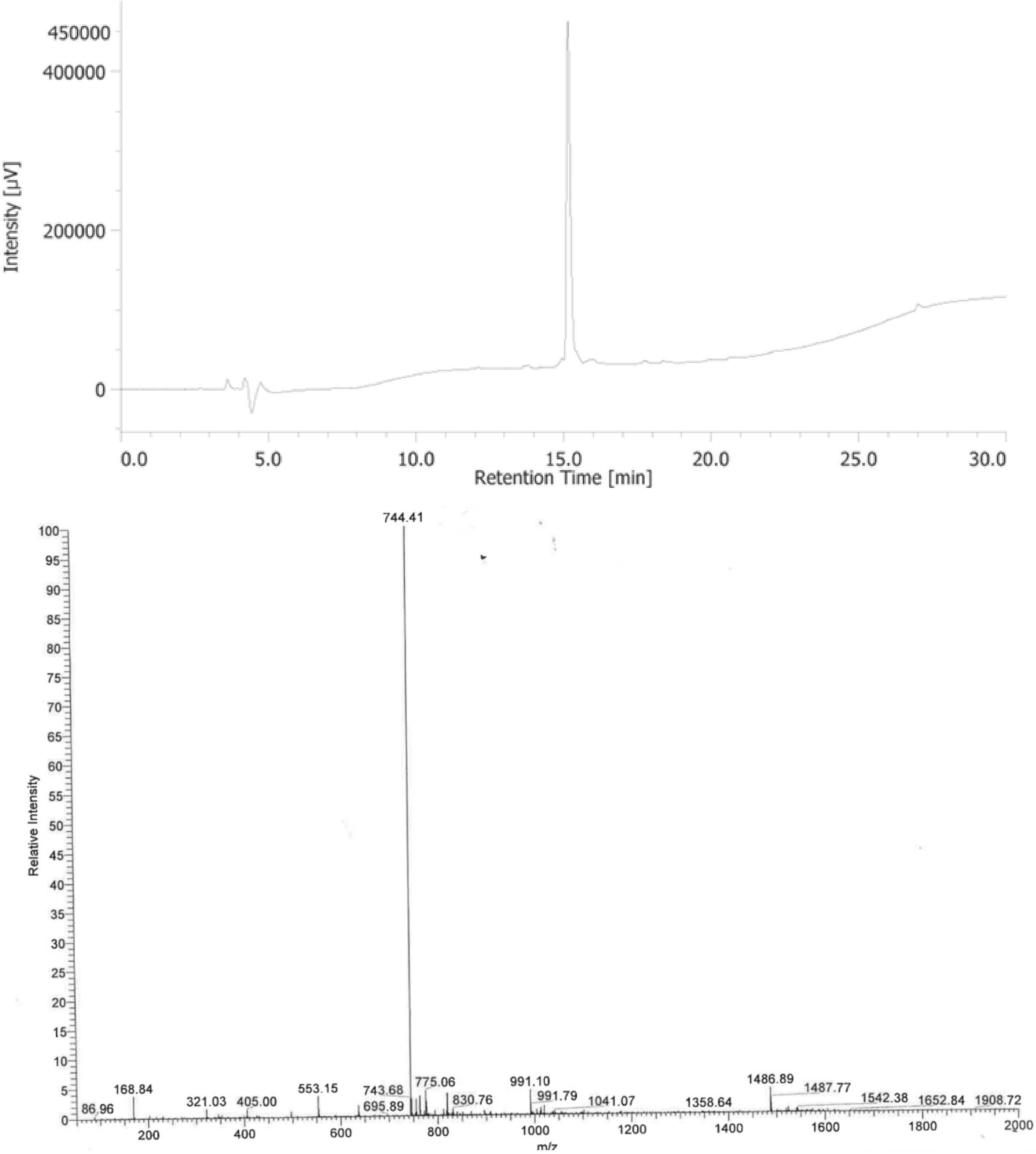

Figure 40 UV chromatogram and ESI-MS spectrum of DS33. Gradient: 5-70% of B in A in 20 min. 0.8 mL/min. A: 0.1% TFA in 100% H2O: B: 0.1% TFA in CH_3CN. The peaks signed correspond to: [M+2H]2+ (744.41 m/z)

DS34 (Stearic acid-FQFQFKGFPGER-NH_2)

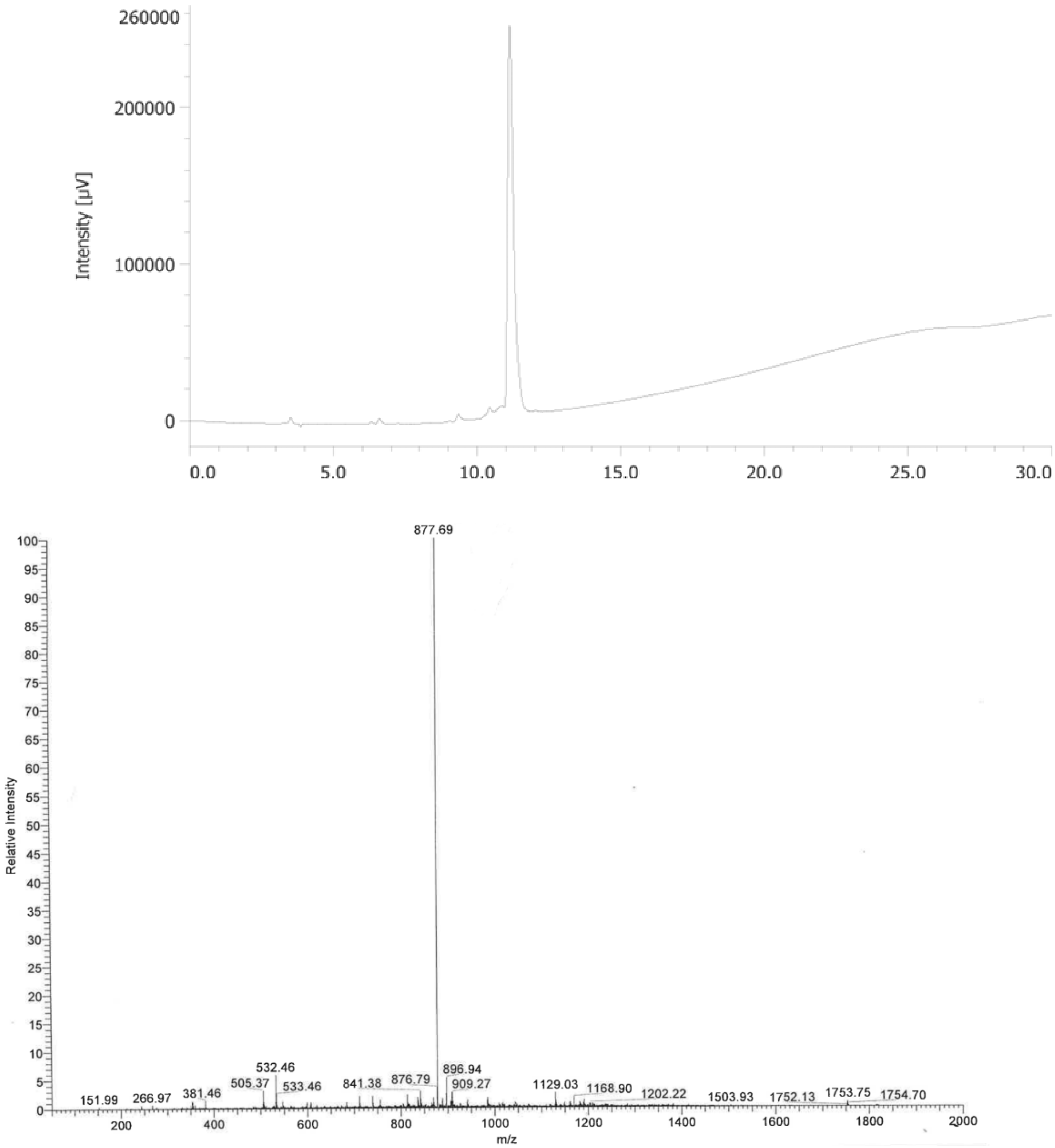

Figure 41 UV chromatogram and ESI-MS spectrum of DS34. Gradient: 20-100% of B in A in 20 min. 0.8 mL/min. A: 0.1% TFA in 100% H2O: B: 0.1% TFA in CH_3CN. The peaks signed correspond to: [M+2H]2+ (877.69 m/z)

DS35 (FQFQFKGFOGER-NH_2)

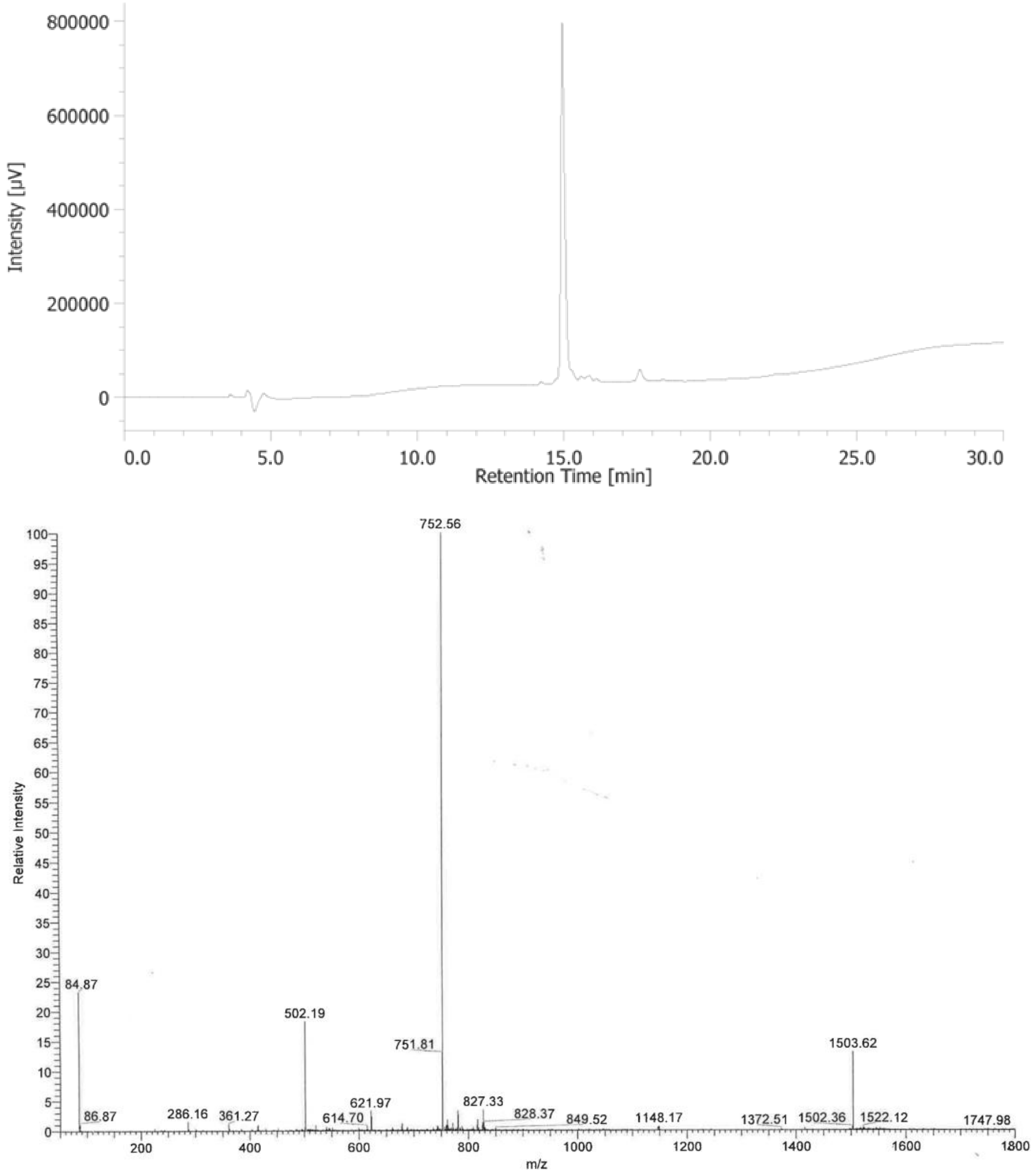

Figure 42 UV chromatogram and ESI-MS spectrum of DS35. Gradient: 5-70% of B in A in 20 min. 0.8 mL/min. A: 0.1% TFA in 100% H2O: B: 0.1% TFA in CH_3CN. The peaks signed correspond to: [M+H]+ (1503.62 m/z), [M+2H]2+ (752.56 m/z), and [M+3H]3+ (502.19 m/z)

DS36 (Stearic acid-FQFQFKGFOGER-NH_2)

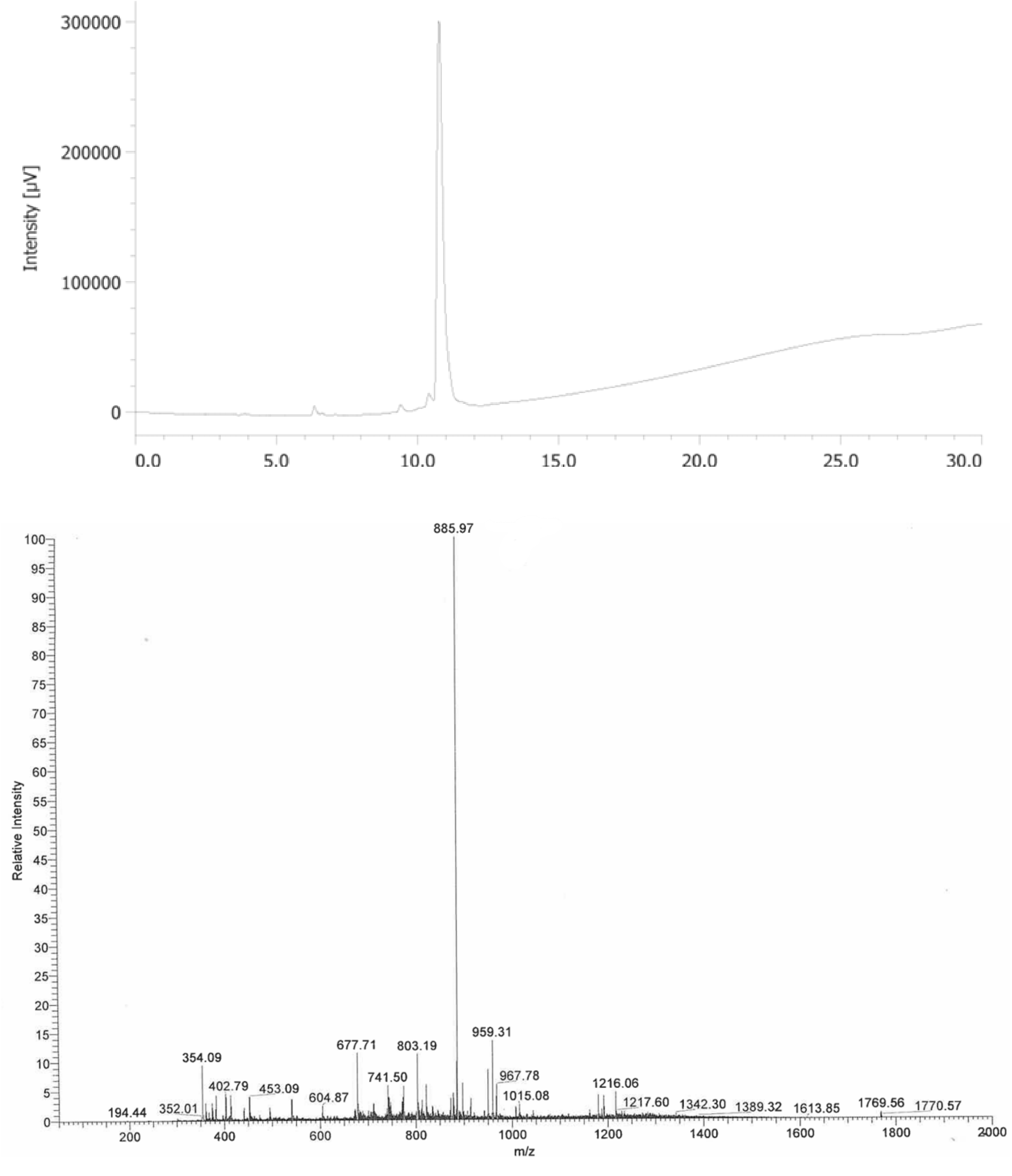

Figure 43 UV chromatogram and ESI-MS spectrum of DS36. Gradient: 20-100% of B in A in 20 min. 0.8 mL/min. A: 0.1% TFA in 100% H2O: B: 0.1% TFA in CH_3CN. The peaks signed correspond to: [M+2H]2+ (885.97 m/z)

TPE 08 (TPE acid-GFOGER-NH_2)

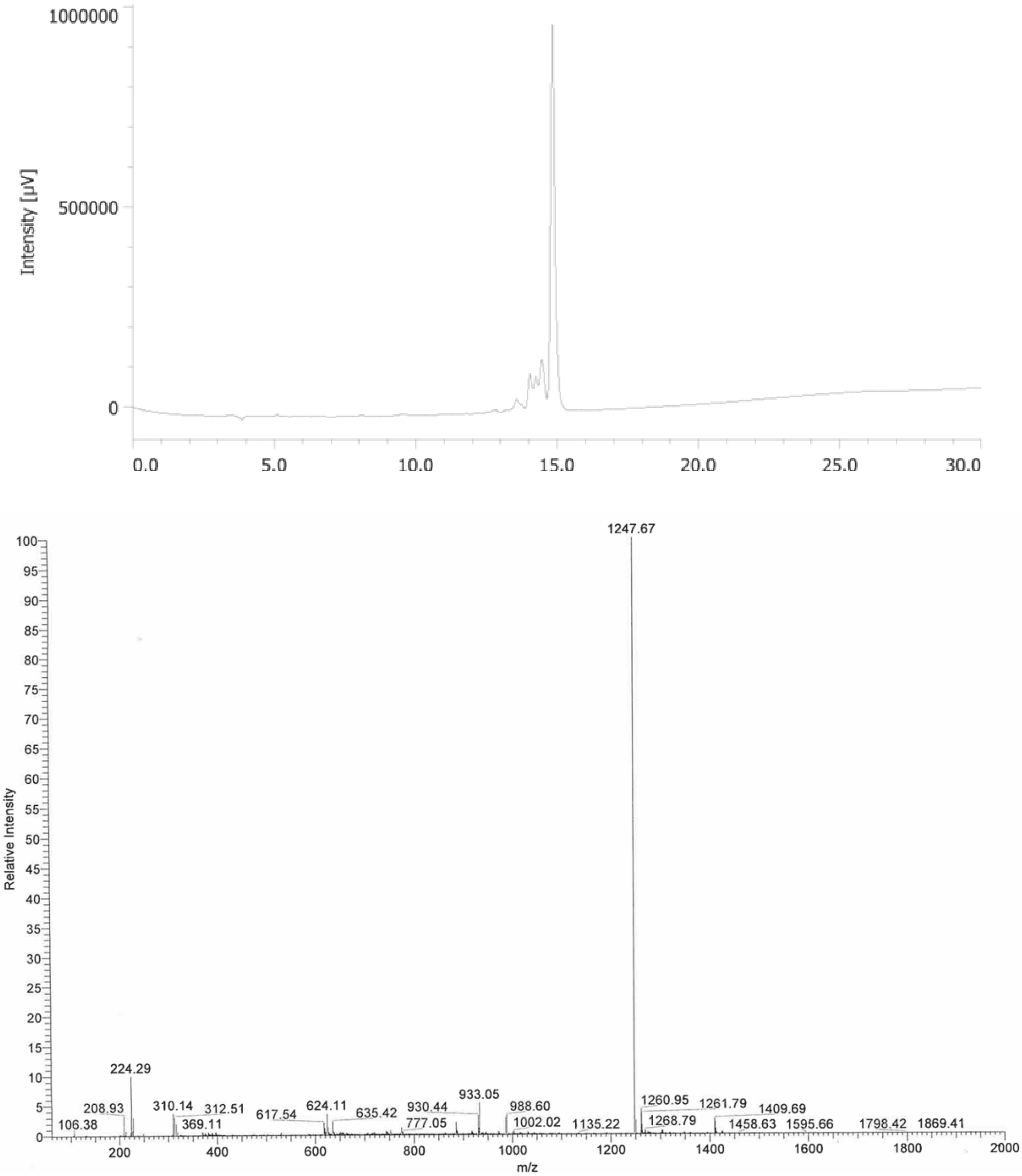

Figure 44 UV chromatogram and ESI-MS spectrum of TPE 08. Gradient: 20-100% of B in A in 20 min. 0.8 mL/min. A: 0.1% TFA in 100% H2O: B: 0.1% TFA in CH_3CN. The peaks signed correspond to: [M+H]+ (1247.67 m/z)

TPE 38 (TPE acid-GFPGER-NH_2)

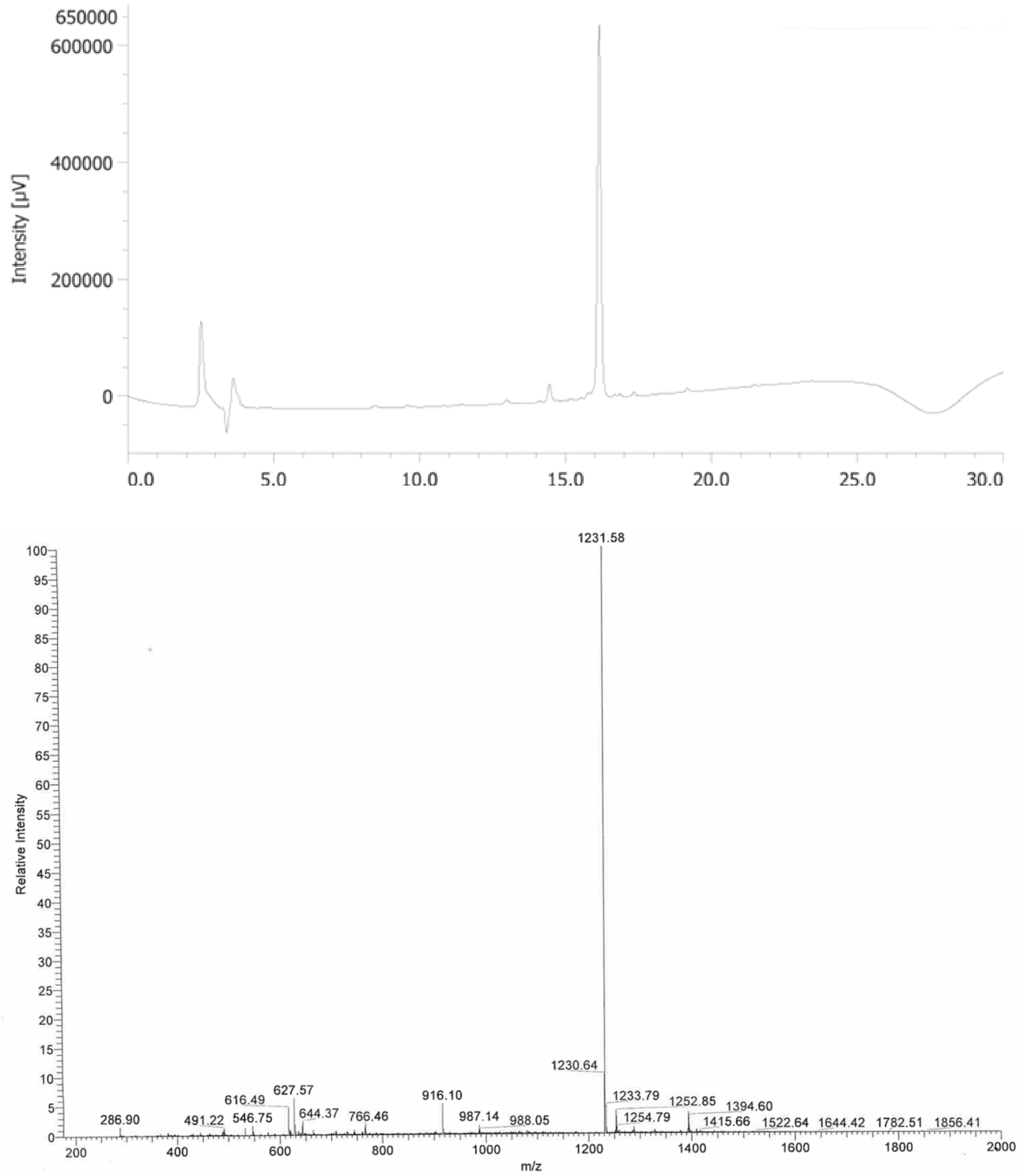

Figure 45 UV chromatogram and ESI-MS spectrum of TPE 38. Gradient: 20-100% of B in A in 20 min. 0.8 mL/min. A: 0.1% TFA in 100% H2O: B: 0.1% TFA in C_H3CN. The peaks signed correspond to: [M+H]+ (1231.58 m/z)

P1 (CIKVAV-NH$_2$)

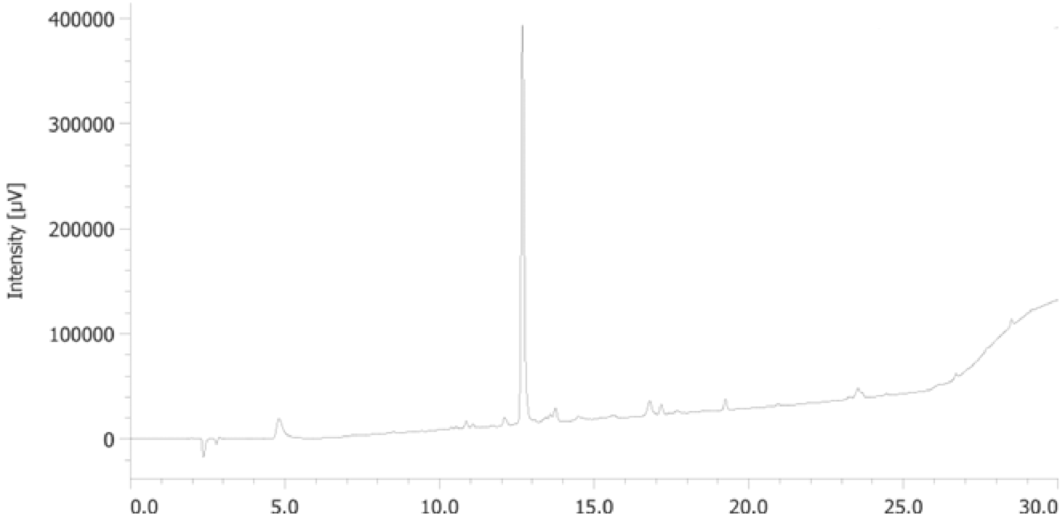

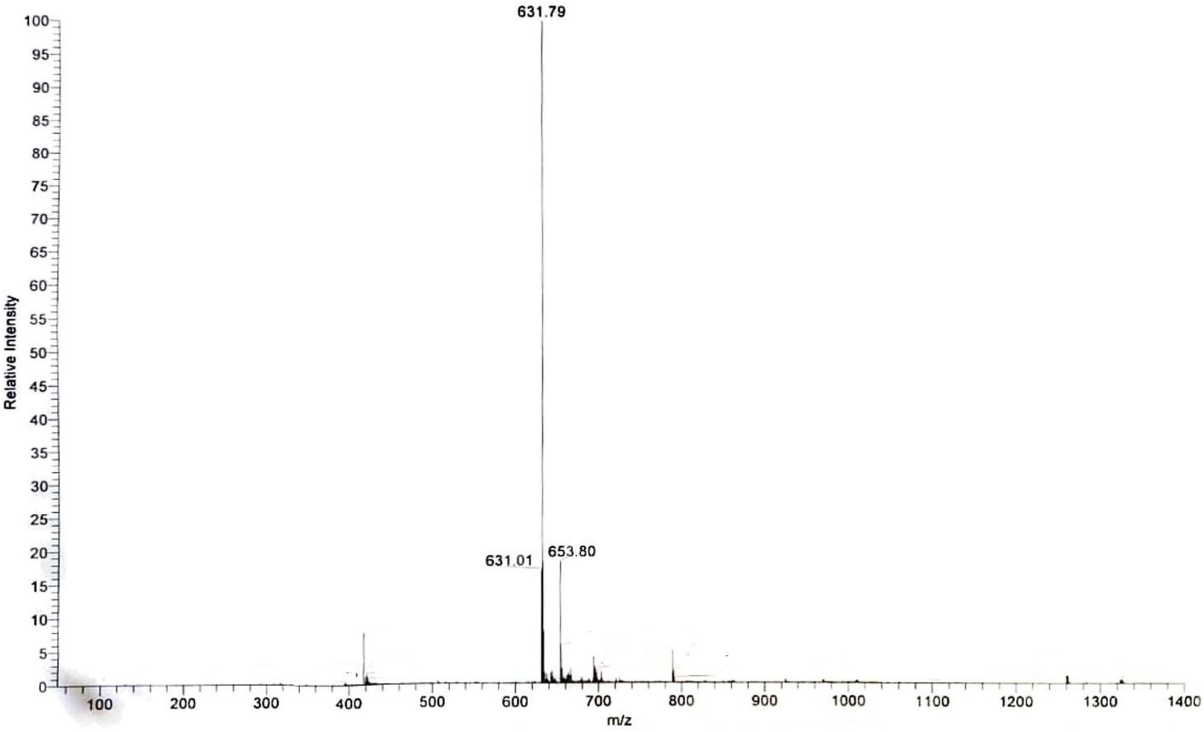

Figure 46 UV chromatogram and ESI-MS spectrum of P1. Gradient: 5-70% of B in A in 20 min. 0.8 mL/min. A: 0.1% TFA in 100% H2O: B: 0.1% TFA in CH$_3$CN. The peaks signed correspond to: [M+H]+ (631.79 m/z) and [M+Na]+ (653.80 m/z)

P2 (CREDV-NH_2)

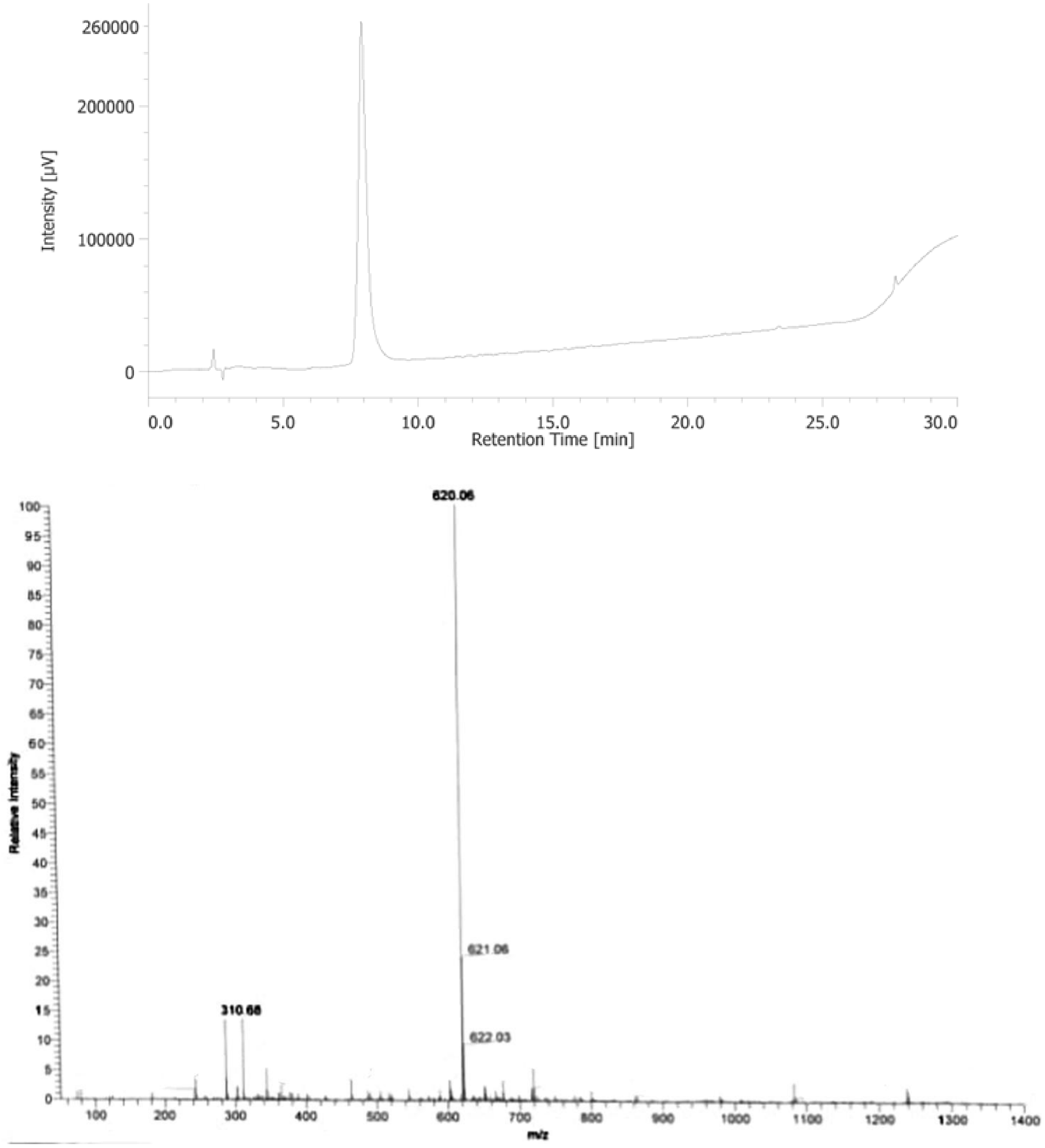

Figure 47 UV chromatogram and ESI-MS spectrum of P2. Gradient: 5-70% of B in A in 20 min. 0.8 mL/min. A: 0.1% TFA in 100% H2O: B: 0.1% TFA in CH_3CN. The peaks signed correspond to: [M+H]+ (620.08 m/z) and [M+2H]2+ (310.66 m/z)

P3 (CGFOGER-NH_2)

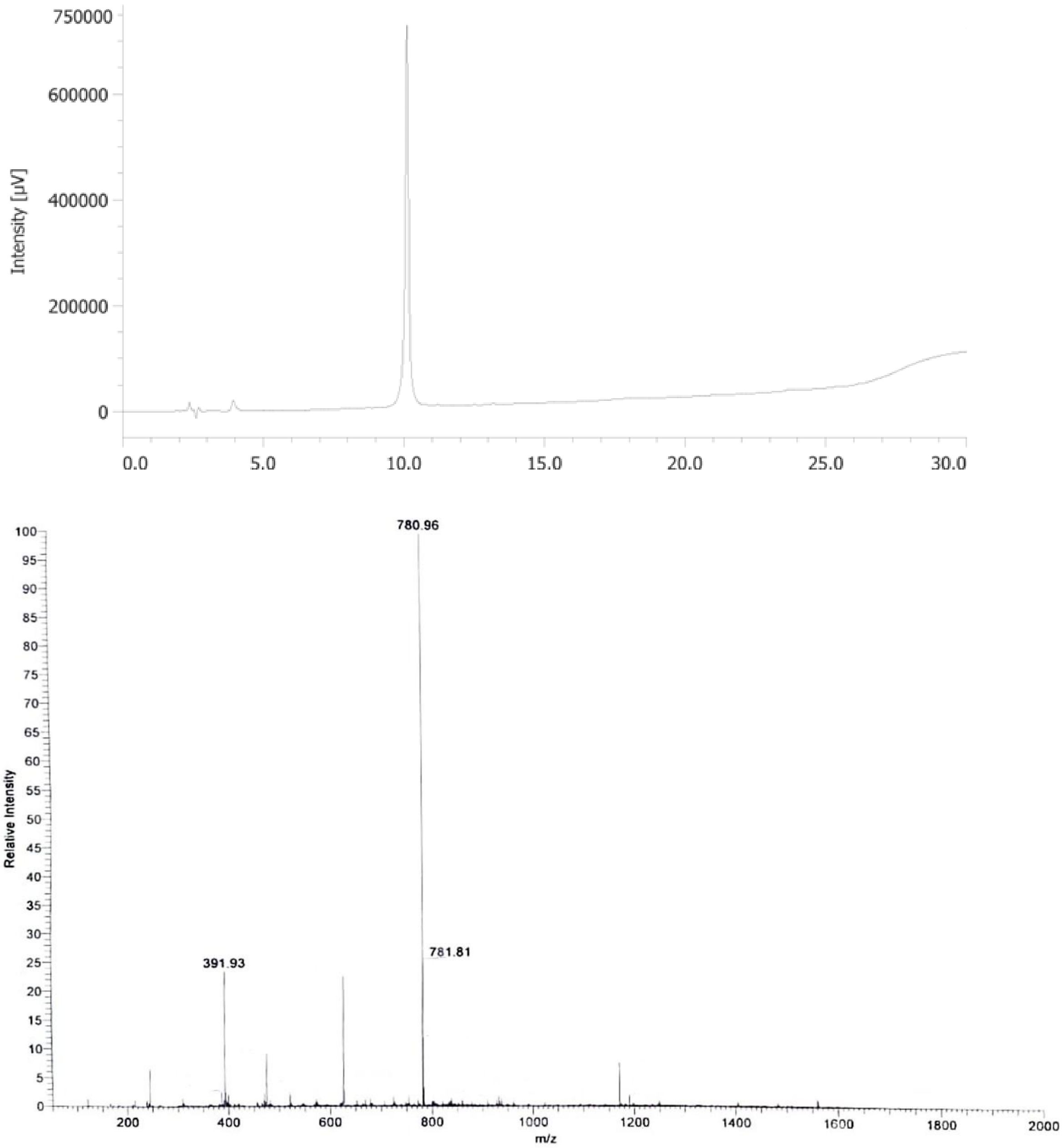

Figure 48 UV chromatogram and ESI-MS spectrum of P3. Gradient: 5-70% of B in A in 20 min. 0.8 mL/min. A: 0.1% TFA in 100% H2O: B: 0.1% TFA in CH_3CN. The peaks signed correspond to: [M+H]+ (780.96 m/z) and [M+2H] 2+ (391.93 m/z)

P4 (CfPRP-NH₂)

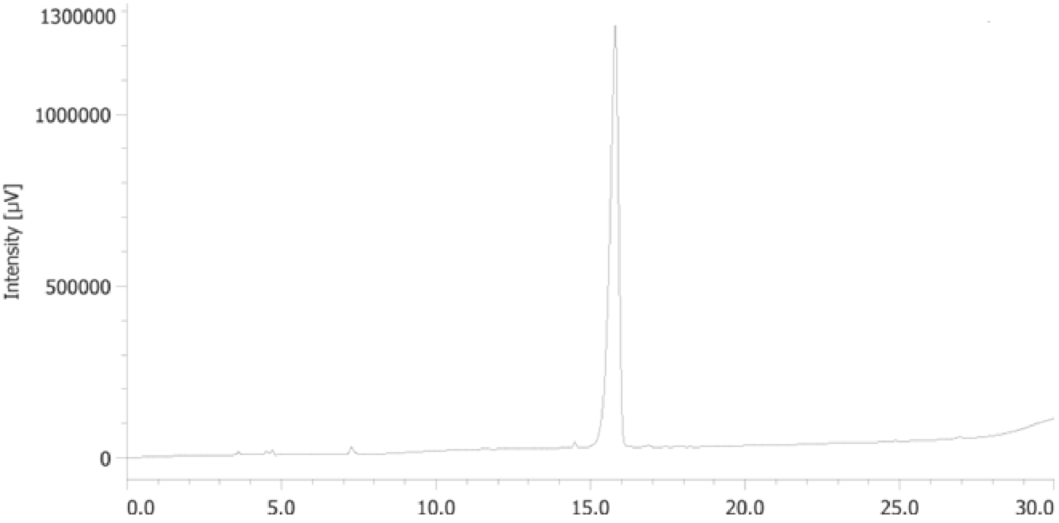

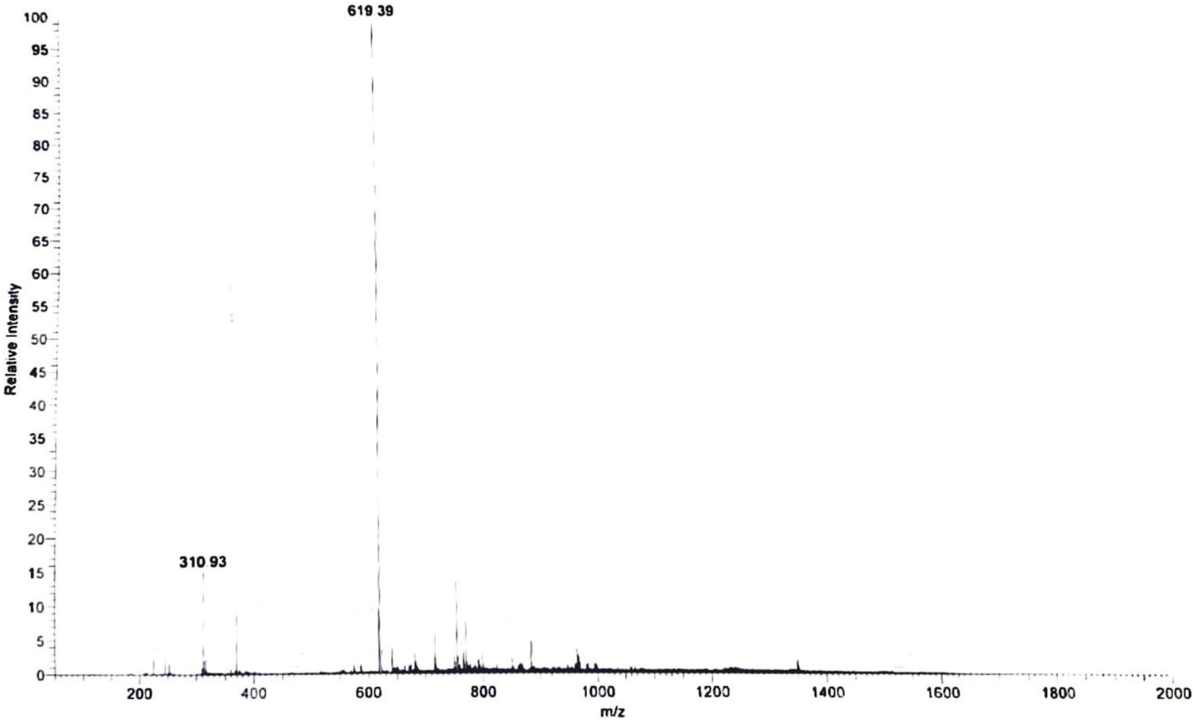

Figure 49 UV chromatogram and ESI-MS spectrum of P4. Gradient: 5-70% of B in A in 20 min. 0.8 mL/min. A: 0.1% TFA in 100% H2O: B: 0.1% TFA in CH_3CN. The peaks signed correspond to: [M+H]+ (619.39 m/z) and [M+2H]2+ (310.93 m/z)

P5 (CKAFDITYVRLKF-NH_2)

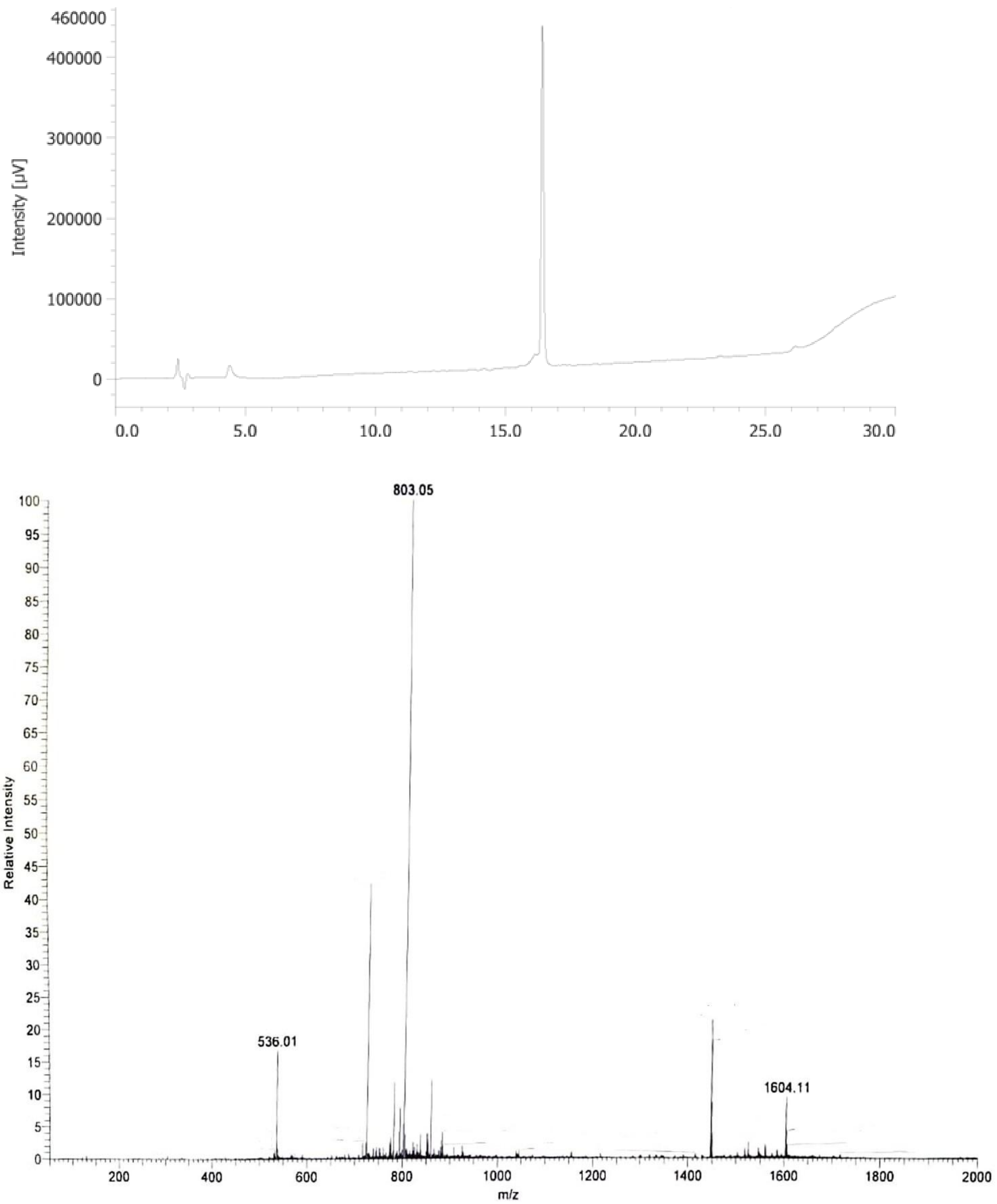

Figure 50 UV chromatogram and ESI-MS spectrum of P5. Gradient: 5-70% of B in A in 20 min. 0.8 mL/min. A: 0.1% TFA in 100% H2O: B: 0.1% TFA in CH_3CN. The peaks signed correspond to: [M+H]+ (1604.11 m/z), [M+2H]2+ (803.05 m/z) and [M+3H]3+ (536.01 m/z)

ATR-FTIR spectra

DS02 (Stearic acid-IKVAV-NH_2)

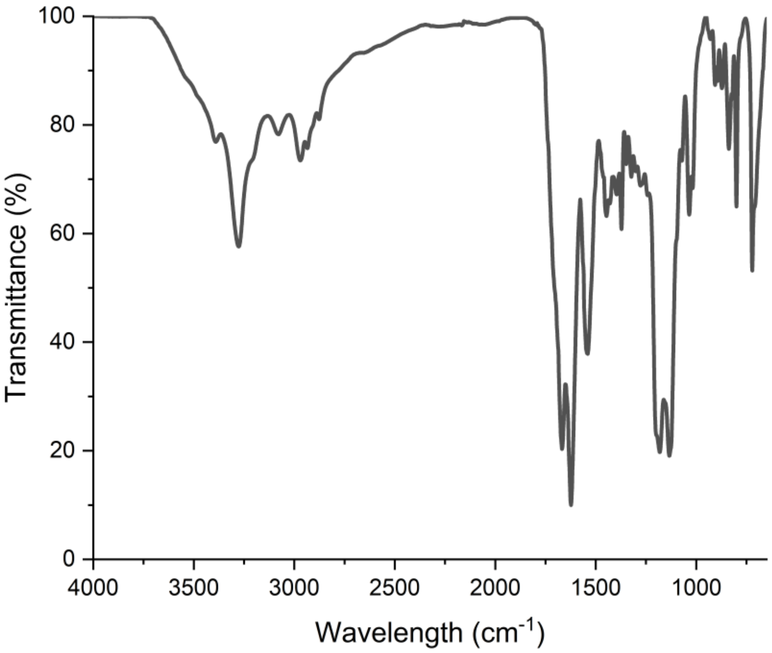

Figure 51 ATR-FTIR spectra of DS02(Stearic acid-IKVAV-NH_2) in solid state

DS04 (Stearic acid-REDV-NH_2)

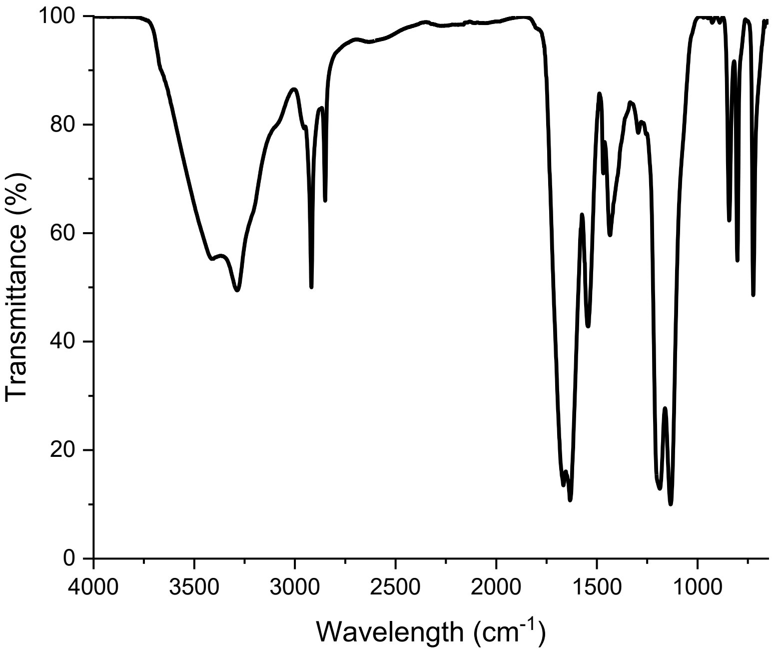

Figure 52 ATR-FTIR spectra of DS04 (Stearic acid-REDV-NH₂) in solid state

DS08 (Stearic acid-GFOGER-NH₂)

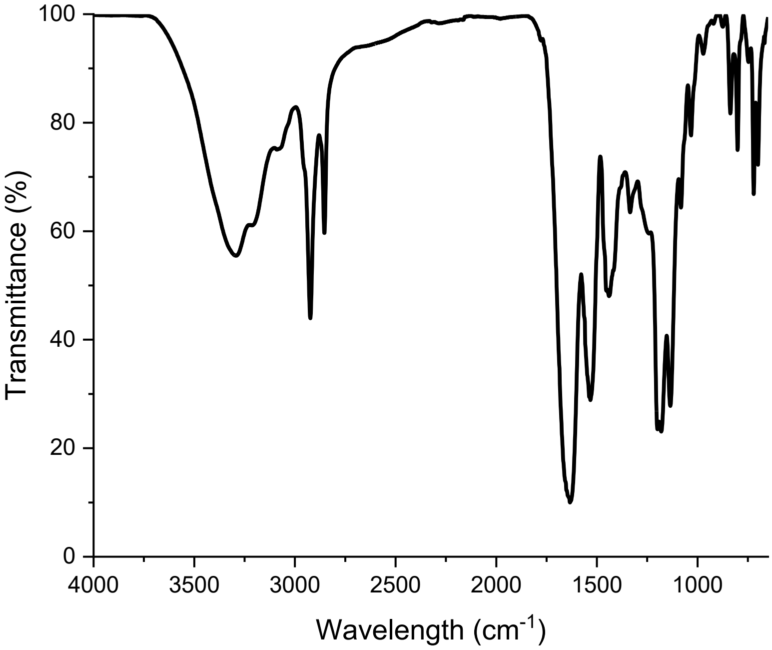

Figure 53 ATR-FTIR spectra of DS08(Stearic acid-GFOGER-NH₂) in solid state

DS10(Stearic acid-fPRP-NH₂)

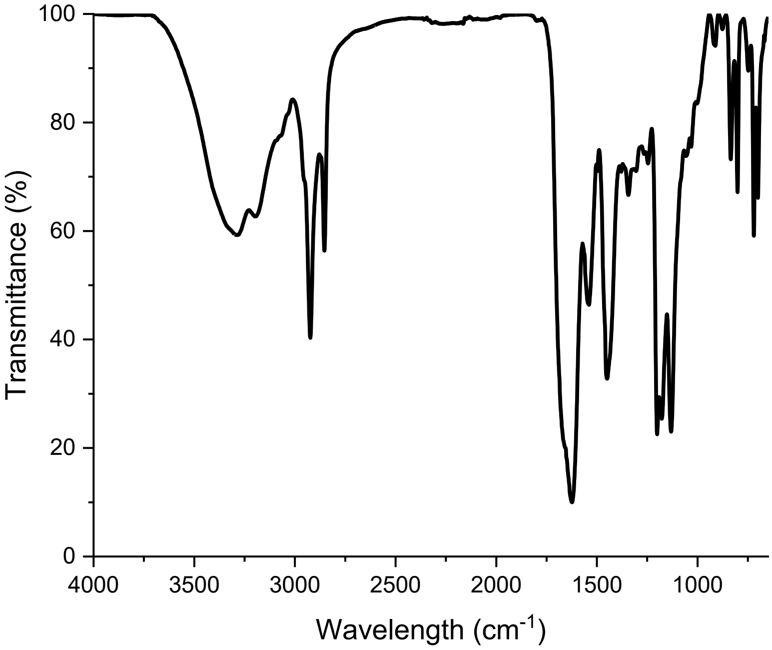

Figure 54 ATR-FTIR spectra of DS10(Stearic acid-fPRP-NH$_2$) in solid state

DS12 (Stearic acid-KLTWQELYQLKYKGI-NH$_2$)

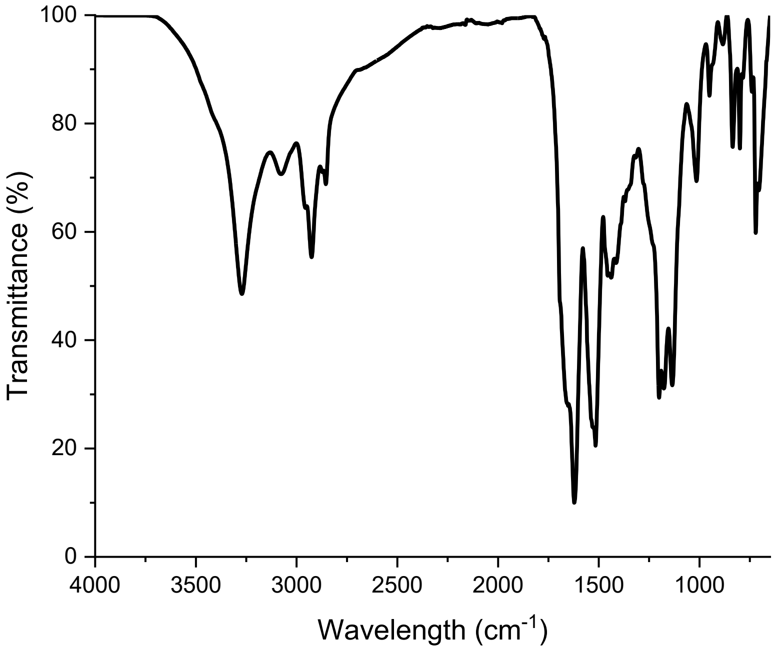

Figure 55 ATR-FTIR spectra of DS12 (Stearic acid-KLTWQELYQLKYKGI-NH$_2$) in solid state

DS14 (Stearic acid-KAFDITYVRLKF-NH$_2$)

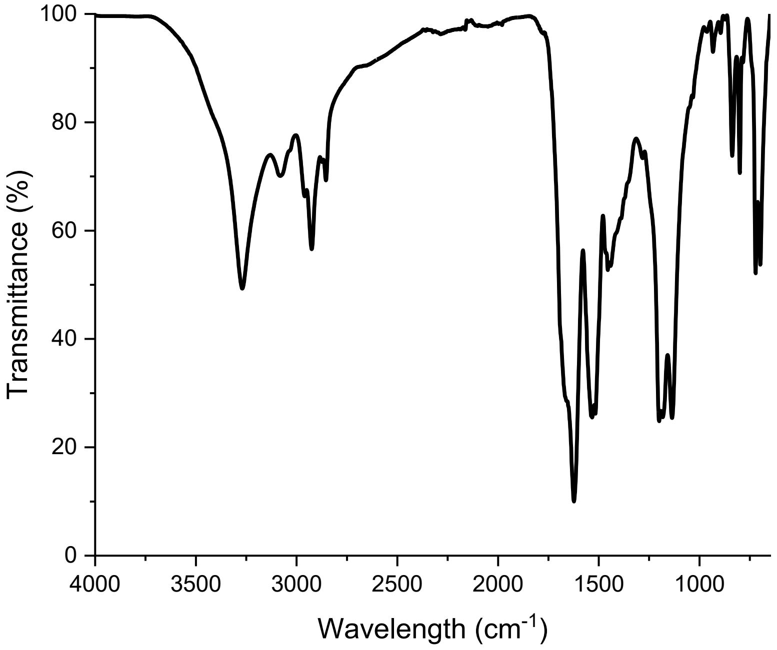

Figure 56 ATR-FTIR spectra of DS14 (Stearic acid-KAFDITYVRLKF-NH₂) in solid state

DS33 (FQFQFKGFPGER-NH₂)

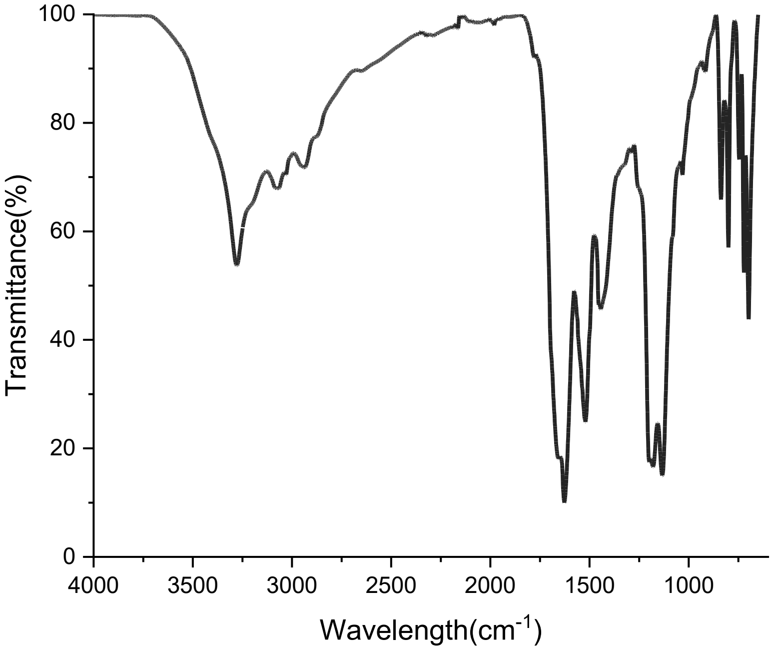

Figure 57 ATR-FTIR spectra of DS33 (FQFQFKGFPGER-NH₂) in solid state

DS34 (Stearic acid-FQFQFKGFPGER-NH₂)

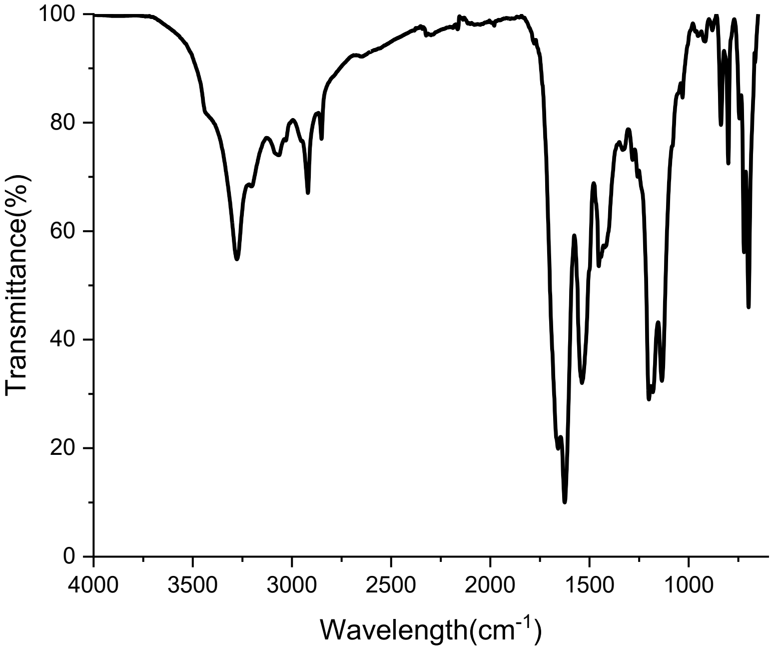

Figure 58 ATR-FTIR spectra of DS34 (Stearic acid-FQFQFKGFPGER-NH₂) in solid state

DS35 (FQFQFKGFOGER-NH$_2$)

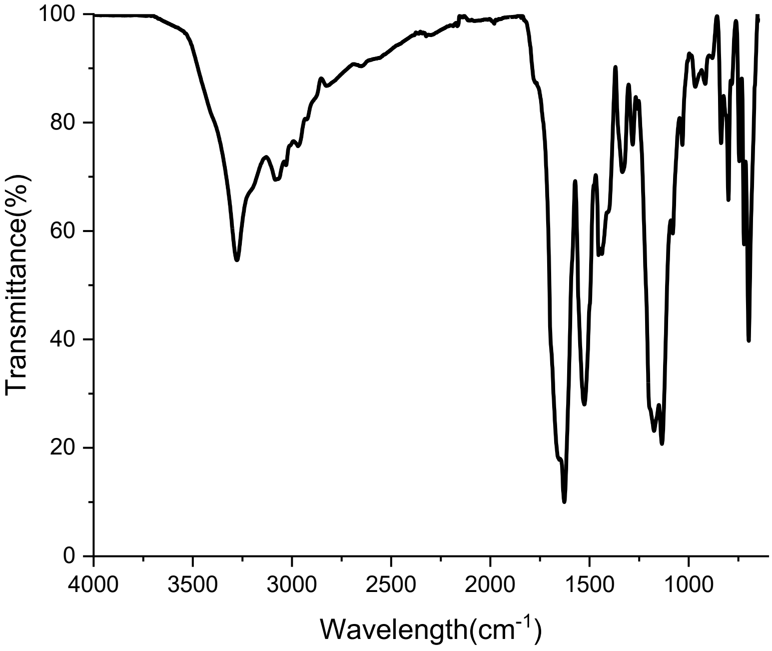

Figure 59 ATR-FTIR spectra of DS35 (FQFQFKGFOGER-NH$_2$) in solid state

DS36 (Stearic acid-FQFQFKGFOGER-NH$_2$)

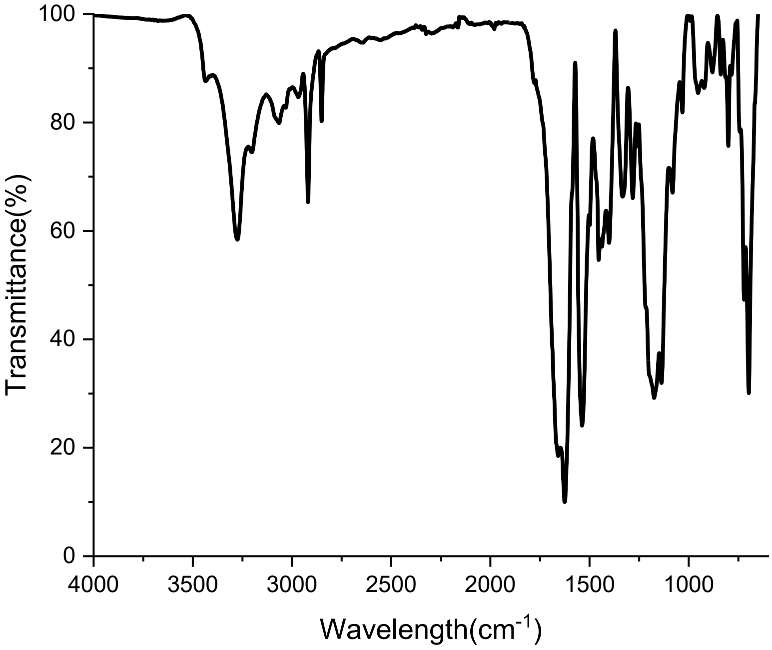

Figure 60 ATR-FTIR spectra of DS36 (Stearic acid-FQFQFKGFOGER-NH$_2$) in solid state

TPE 08 (TPE acid-GFOGER-NH_2)

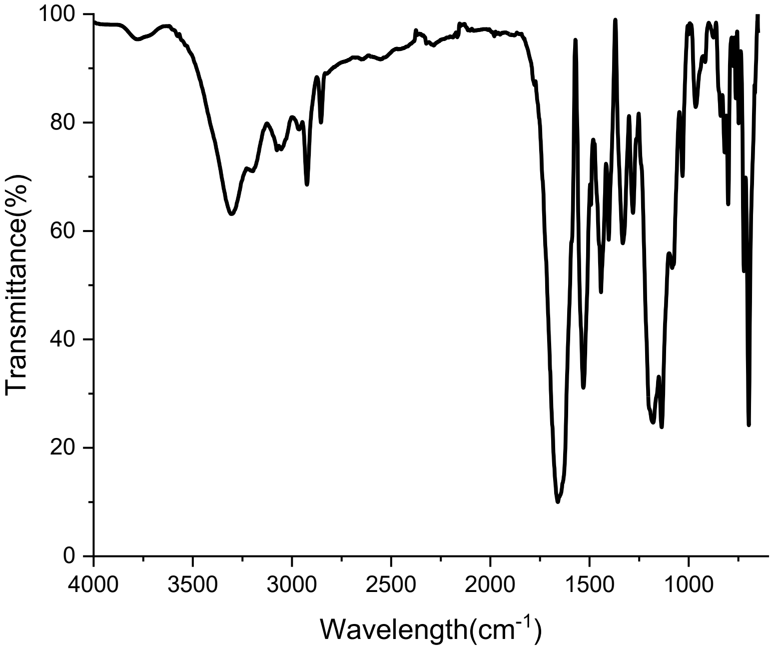

Figure 61 ATR-FTIR spectra of TPE 08(TPE acid-GFOGER-NH_2) in solid state

TPE 38 (TPE acid-GFPGER-NH_2)

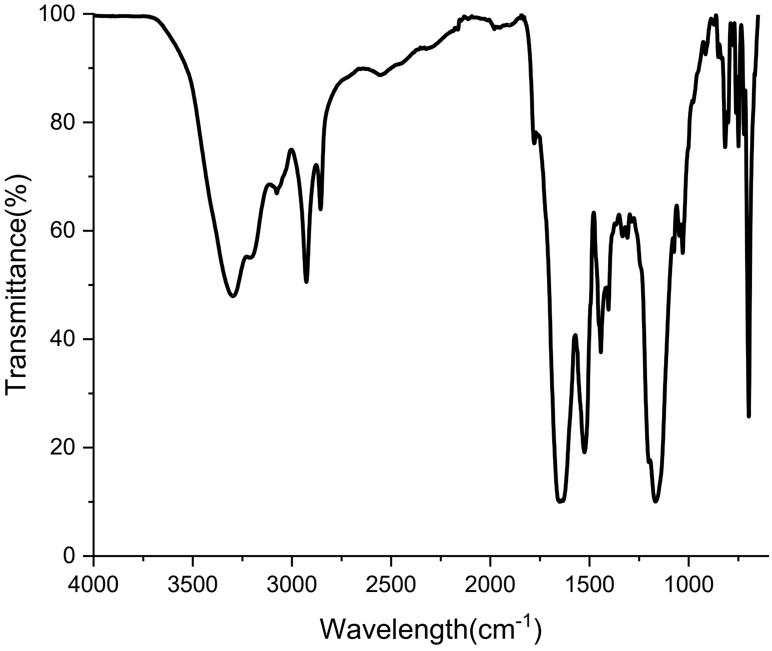

Figure 62 ATR-FTIR spectra of TPE 38 (TPE acid-GFPGER-NH_2) in solid state